Thèse n° 9378

Computational studies for the description of electronic and optical properties for photocatalysis in Metal Organic Frameworks

Présentée le 7 décembre 2021

Faculté des sciences de base
Laboratoire de simulation moléculaire
Programme doctoral en chimie et génie chimique

pour l'obtention du grade de Docteur ès Sciences

par

Andres Adolfo ORTEGA GUERRERO

Acceptée sur proposition du jury

Prof. A. Züttel, président du jury
Prof. B. Smit, directeur de thèse
Dr L. Gagliardi, rapporteuse
Dr B. Curchod, rapporteur
Dr A.-C. Corminbœuf, rapporteuse

École
polytechnique
fédérale
de Lausanne

2021

Acknowledgements

The ending of a Ph.D. is considered an individual accomplishment, yet this affirmation is far from reality. This four-year journey brought many challenges and difficulties. Here, I would like to thank all the persons who have supported me. This thesis would never have been possible without them.

I would like to start expressing my gratitude to my supervisor, Prof. Berend Smit, for giving me the opportunity and support of conducting exciting research projects with all the freedom I could imagine. Having you as my supervisor comes with learning other skills of great importance for a scientist as the formulation of scientific questions, communication, and most importantly writing skills. Although there is plenty of room for improvement in the latter one, I will always remember the importance of: "having a good story flow".

During my Ph.D., I had the opportunity to work with excellent scientists from which I learned a lot. Knowing them had a great impact on the development of this thesis as well. Ivano Tavernelli (IBM) for our collaboration, advice, and discussion during the time we worked. Gloria Capano, thank you so much for inspiring me to work in photocatalysis and for all the knowledge you gave me in computational chemistry. Maria Fumanal, thank you for all the long theoretical and critical discussions, support, advice, and remarks which were essential in this work.

I am very grateful to all the members of my thesis jury for accepting the evaluation of this work: Prof. Andreas Züttel, president of the jury, Prof. Laura Gagliardi (The University of Chicago), Prof. Basile Curchod (Durham University), and Prof. Clémence Corminboeuf (EPFL).

Thank you to our administrative assistant, Evelyn Ludi, for always uplifting us and being available for us at any time. I would like to thank all the LSMO group. Thank you to all my colleagues: Özge, Leopold, Sasha, Daniele, Mohamad, Henglu, Miriam, Sauradeep, Raffaella, and Elias. Many thanks to Pelin for our enjoyable collaboration in the last year, I learned many experimental aspects involved in our study. I also would like to thank you Mish for our nice collaboration, it is a great pleasure. Thank you, Kevin, for the collaborations, and for always being available for our long talks and discussions. I have a great time working with you in the LSMO group.

I would like to thank my parents, Beatriz and Adolfo, and my sister, Luz Carime; your encouragement, your values, and your love are essential in every step of my life. Finally, to my

beautiful fiancé Rajrupa. Thank you for being with me during this four-year journey. You were an unofficial supervisor to me with endless patience and support motivating me to give my best every day. I love you

Andres Ortega-Guerrero

Lausanne, October 14th 2021 Andrés

Abstract

Metal-organic frameworks(MOFs) are promising materials for photocatalytic applications. MOFs modular and porosity structure provides a platform to assemble photo-active and catalytic-sites building block units that can offer unique photo-physics. This feature is of great interest for H_2 evolution photocatalytic applications. However, MOFs current photocatalysts do not meet the industrial need for their implementation as a technology due to performance limitations. Thus, elucidating and predicting the optical properties of MOFs will have wide implications in the development of MOF-based photocatalysts. Computational studies can be of great aid for the discovery of MOFs photocatalyst. Yet, this is a challenging task for computational chemistry given the complexity of the photophysical properties, the inorganic-organic nature, the number of atoms, and the unit cell size of MOFs. The principal goal of this thesis is the study MOFs photophysical properties for predicting their feasibility for photocatalytic applications. Density functional theory (DFT) and linear-response time-dependent DFT (LR-TDDFT) formalisms are used for the description of the light absorption, charge separation, and charge transfer properties of MOFs. We first address the dependence of the ligand in the UV/Vis optical absorption of porphyrin-based MOFs. The characterization of the excited states of the porphyrin ligands in MOFs requires an appropriate approximation for the description in periodic crystal MOFs. The selection of proper functionals and approximations within DFT/TDDFT calculations is necessary to overcome the erroneous description of properties like excitonic effects, optical transitions, and gap-renormalization. Later, we continue with the study of the charge separation in a porphyrin ruthenium-based MOF. We describe the importance of missing coordinated solvents anions in the metal node for the stability and charge transfer mechanism in the material. Within this study, we computed electron-hole interacting energy indicating a low electron-hole recombination rate. We next introduce a computational strategy to describing the long-lived electron-hole pairs and the long-rage charge transfer in MOFs. This description can be depicted by computing charge transfer numbers and the effective mass of carriers, respectively. This methodology can correctly predict the charge separation and the effective mass of 15 representative MOF structures promising for photocatalysis in agreement with the literature. Finally, we present an experimental and theoretical combined study investigation towards optimal photocatalytic hydrogen evolution reaction (HER) in MOFs. Isostructural pyrene-based MOFs with different

transition metals allowed us a proper comparison. This study highlights the interplay between tunning electronic properties and crystal morphology on the photocatalytic HER performance of the MOFs. These results presented in this thesis can be exploited and transfer to the study of other MOFs for HER photocatalysis.

Zusammenfassung

Metallorganische Gerüstverbindungen (MOFs) sind vielversprechende Materialien für photokatalytische Anwendungen. Die modulare und poröse Struktur von MOFs bietet eine Plattform zum Zusammenbau photoaktiver und katalytischer Zentren-Bausteineinheiten, die eine einzigartige Photophysik bieten können. Diese Eigenschaft ist von großem Interesse für photokatalytische Anwendungen der H2-Entwicklung. Die derzeitigen Photokatalysatoren der MOFs erfüllen jedoch aufgrund von Leistungseinschränkungen nicht den industriellen Bedarf für ihre Implementierung als Technologie. Daher wird die Aufklärung und Vorhersage der optischen Eigenschaften von MOFs weitreichende Auswirkungen auf die Entwicklung von MOF-basierten Photokatalysatoren haben. Computergestützte Studien können bei der Entdeckung von MOFs-Photokatalysatoren eine große Hilfe sein. Angesichts der Komplexität der photophysikalischen Eigenschaften, der anorganisch-organischen Natur, der Anzahl der Atome und der Elementarzellengröße von MOFs ist dies jedoch eine Herausforderung für die Computerchemie. Das Hauptziel dieser Arbeit ist die Untersuchung der photophysikalischen Eigenschaften von MOFs, um ihre Machbarkeit für photokatalytische Anwendungen vorherzusagen. Dichtefunktionaltheorie (DFT) und zeitabhängige DFT (LR-TDDFT)-Formalismen mit linearer Antwort werden zur Beschreibung der Lichtabsorption, Ladungstrennung und Ladungsübertragungseigenschaften von MOFs verwendet. Wir befassen uns zunächst mit der Abhängigkeit des Liganden bei der optischen UV/Vis-Absorption von Porphyrin-basierten MOFs. Die Charakterisierung der angeregten Zustände der Porphyrinliganden in MOFs erfordert eine geeignete Näherung für die Beschreibung in periodischen Kristall-MOFs. Die Auswahl geeigneter Funktionale und Näherungen innerhalb von DFT/TDDFT-Rechnungen ist notwendig, um die fehlerhafte Beschreibung von Eigenschaften wie exzitonischen Effekten, optischen Übergängen und Lücken-Renormierung zu überwinden. Später fahren wir mit der Untersuchung der Ladungstrennung in einem Porphyrin-Ruthenium-basierten MOF fort. Wir beschreiben die Bedeutung fehlender koordinierter Lösungsmittelanionen im Metallknoten für die Stabilität und den Ladungstransfermechanismus im Material. In dieser Studie haben wir die Elektron-Loch-Wechselwirkungsenergie berechnet, was auf eine niedrige Elektron-Loch-Rekombinationsrate hinweist. Als nächstes stellen wir eine Computerstrategie zur Beschreibung der langlebigen Elektron-Loch-Paare und des langreichweitigen Ladungstransfers in MOFs vor. Diese Beschreibung kann durch Berechnung der Ladungsübertragungszahlen bzw. der effektiven Masse der Ladungsträger dargestellt werden. Diese Methode kann in

Übereinstimmung mit der Literatur die Ladungstrennung und die effektive Masse von 15 repräsentativen MOF-Strukturen, die für die Photokatalyse vielversprechend sind, korrekt vorhersagen. Schließlich präsentieren wir eine experimentelle und theoretische kombinierte Studienuntersuchung zur optimalen photokatalytischen Wasserstoffentwicklungsreaktion (HER) in MOFs. Isostrukturelle Pyren-basierte MOFs mit verschiedenen Übergangsmetallen ermöglichten uns einen richtigen Vergleich. Diese Studie beleuchtet die Wechselwirkung zwischen der Abstimmung elektronischer Eigenschaften und der Kristallmorphologie auf die photokatalytische HER-Leistung der MOFs. Die in dieser Dissertation präsentierten Ergebnisse können verwertet und auf die Untersuchung anderer MOFs für die HER-Photokatalyse übertragen werden.

Contents

List of Figures

List of Tables

Introduction

Our modern society is facing aggravating energy and environmental problems as fossil fuel depletion and global warming. The constant effort from scientists and engineers all over the world is concentrated on finding new materials and technologies for renewable sources of energy. Among these technologies, a promising and sustainable strategy is to exploit the energy coming from the sunlight and transform it into chemical energy. This strategy uses the unique class of chemical transformations trigger by light, known as photocatalysis. This field is inspired by the naturally occurring photosynthesis where plants using the sunlight transform water and carbon dioxide into oxygen and sugars, which are stored and used for metabolic activities (chemical energy). Similarly, renewable energy photocatalytic applications' ultimate aim is to efficiently produce H_2 at a large scale via water splitting. In this regard, hydrogen is a promising clean fuel candidate since its consumption in a fuel cell produces water. The scope of photocatalysis can address numerous environmental problems such as CO_2 reduction, degradation of organic pollutants, and disinfection of viruses and bacteria[45].

The concept of photocatalysis was established by the discoveries from Boddy[15] and Honda and Fujishima[59] on the photocatalytic properties of TiO_2 under ultraviolet (UV) light illumination. Subsequently, longstanding scientific efforts have focused on the discovery of efficient H_2 photocatalysts. This has led to the investigation of the photocatalytic principles of semiconductors, molecular photocatalysts, quantum dots, two-dimensional (2D) materials, and porous materials[217]. Although these different materials can present specific mechanisms[78], a photocatalytic process generally has four fundamental steps (Figure 1): (i) light absorption, (ii) charge separation, (iii) charge transfer, and (iv) catalytic reaction. An ideal photocatalyst should efficiently combine the performance of these steps. For instance, for practical applications, the material light absorption should have a high absorbance coefficient and be within the visible frequencies. The latter characteristic is ideal since most of the solar spectra are at that frequency range. Additionally, the excited state of the material should guarantee a long lifetime for the charge separation of the photo-generated carriers (electron and hole), as well as their subsequent migrations. Finally, these photo-generated carriers should efficiently reach the active sites for the reaction. The active sites can intrinsically be part of the material or a co-catalyst to reduce the activation energy barrier of the reaction. Such requirements posses significant challenges in material considerations. These challenges can be charge recombination, degradation, water instability, among others. As the example

mention above, TiO_2 has different limitations for water splitting application due to its inefficient exploitation of visible light, charge recombination, and aggregation[78]. In this context, the optimally tuning of the electronic properties is essential to enhance the behavior of the fundamental steps. Such understanding is a challenge for the discovery of new materials for photocatalytic applications.

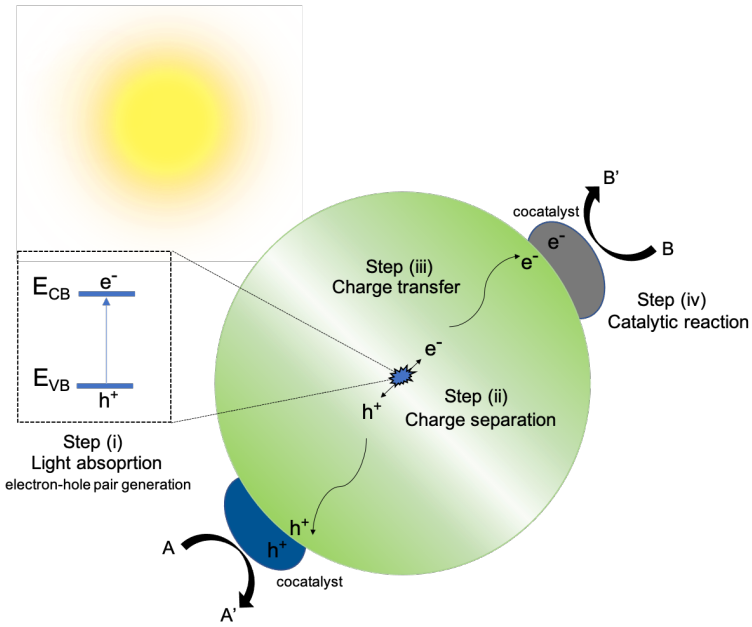

Figure 1 – Schematic illustration of the photocatalysis fundamental steps. (i) Light absorption, photo excitation of an electron from the valence band E_{VB} to the conduction band E_{CB} generating a electron-hole pair. (ii) Charge separation, exciton dissociation. (iii) Charge migration and (iv) Catalytic reaction, oxidation (involving the holes) and reduction (involving the electrons) at the active sites (cocatalyst).

Among the very long list of materials considered for photocatalysis, one kind of material stands out as a promising route to tune their electronic and optical properties known as Metal-Organic Frameworks(MOFs). MOFs are a relatively new kind of porous material with a hybrid organic-inorganic nature[222]. MOFs are a three-dimensional (or two-dimensional) class of materials consisting of self-assembled metal ions (or clusters) coordinated to organic molecules known as ligands (Figure 2). Such crystals can offer unique photophysics with the selection of their building units. In this regard, the MOFs structure provides a platform to assemble photo-active building and active site units in porous and highly periodic crystals.

Owing to their structural and chemical versatility, MOFs are promising candidates in different applications such as selective gas storage and adsorption[119], catalysis[225], chemical sensing and detection[147], biomedical applications[215], and photocatalysis[120, 211]. In the context of photocatalysis, the electronic and optical properties of MOFs are determined by the combination of their components (metal and organic ligands) as well as their structural topology. Yet, the definition of their electronic properties is not trivial leading to MOFs presenting

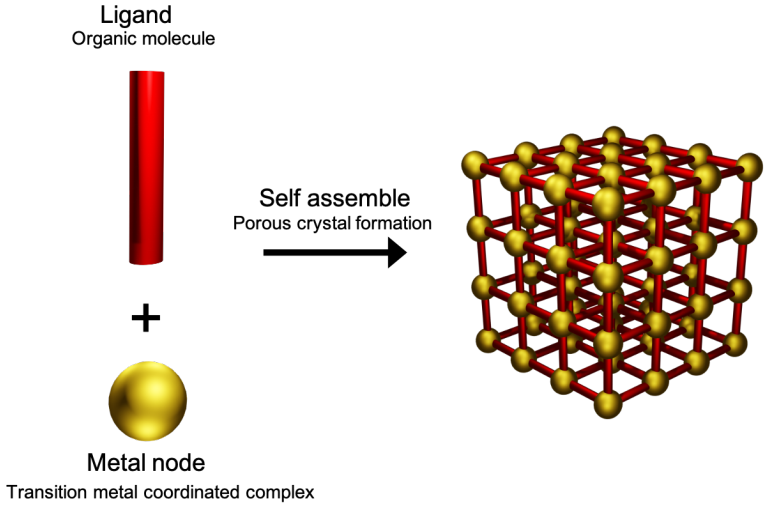

Figure 2 – Schematic representation of a MOF.

metallic[37, 212], semiconducting, and isolating characteristics[180]. Likewise, the optical properties of MOFs are governed as well by their structural components and their interactions. The presence of orbitals from the organic ligands and metal nodes lying close to the band structure edges (Valence and Conductance bands) can promote the presence of ligand-to-metal charge transfer (LMCT) or metal-to-ligand charge transfer (MLCT) states. This aspect is an advantage of MOFs for photocatalysis since the excited states of the photo-generated carriers can promote spatial charge separation leading to long life states.

Directly related to its structure, MOFs offer different properties of importance for photocatalysis as the porous characteristics provide a large surface area and can potentially offer rich surface active sites[203]. In the context of all these unique photophysical properties of MOFs, they can potentially exhibit advantages in comparison with traditional semiconductors given the MOFs' versatility. However, the photocatalytic efficiency of MOFs has not met the current needs. Current research efforts are focus on the optimization of MOFs to enhance their performance. Thus, the prediction of photophysical properties of MOFs for photocatalysis is essential to aid the discovery of new materials. Therefore, this thesis focuses on the understanding and prediction of photophysical properties of MOFs involving the fundamental steps of photocatalysis via computational chemistry.

While computational studies have been conducted to facilitate the discovery of MOFs for applications like gas storage and separations[207, 4, 6], photocatalysis applications represent a computational challenge for existing methods. Considering the size of a MOF crystal, Density Functional Theory (DFT) in many cases is the selected method for studying the electronic properties of MOFs due to its favorable scaling of demand on computational resources. The theory comes from Hohenberg-Kohn[92] and Kohn-Sham[105] theorems which establish an approximation for the solution of the ground state Schrodinger equation by using the electronic density of the system. A well-known limiting factor of DFT is the approximation of the

exchange-correlation functional for the proper description of the electronic problem. Different approximations have been implemented to minimize errors. MOFs electronic properties are not indifferent to this approximation. The presence of transition metals complexes in their structure is also challenging for DFT methods. Likewise, the photophysical properties of MOFs involving photo-initiated processes require the description of the excited states. Excited states calculations present their challenges, state of art methods are limited to a few atoms required for accurate description. For the case of DFT, it requires time-dependent methods for the description of excited-state phenomena[187]. One approach is the use of Linear-Response Time-Dependent DFT(LR-TDDFT)[28]. As in the case of DFT, LR-TDDFT as well as susceptible to the approximations used. Thus, this thesis aims to investigate the descriptors of MOFs for photocatalysis using the DFT/LR-TDDFT approaches as well as the importance of the approximation used on the prediction of the electronic and photophysical properties.

Under the desire of optimizing the fundamental photocatalytic steps, this thesis has addressed main principles, features, and strategies involving the prediction of these steps via ab-initio simulations. The different chapters of the thesis address the three first fundamental steps light-harvesting, charge separation and charge mobility in different studies conducted on photo-active MOFs. More specifically, **Chapter 1** highlights the importance of photosensitizers as porphyrin molecules in MOFs to improve the light-harvesting properties and how the organic ligand can impose the UV/Vis absorption properties of the MOFs. Likewise, it addresses the challenges and artifacts from DFT/LR-TDDFT to predict fundamental and optical bandgaps, capture excitonic effects, and gap-renormalization of MOFs crystals.

In **Chapter 2**, the photo-induced charge-transfer mechanism of a porphyrin ruthenium-based MOF is described based on the anions (Cl^- or OH^-) coordinated to the structure. The study involves the description of the charge transfer mechanisms and the interaction energy of the photo-generated electron-hole carriers for the charge separation in the systems. The description of the photophysical properties of the system was modeled with the full periodic and representative cluster models of the MOF. The latter one facilitated the used of more accurate approximations to describe charge transfer states, challenging within the TDDFT scope.

Chapter 3 is focused on the third fundamental step of photocatalysis, charge mobility. This chapter describes a cost-effective computational strategy to address long-lived electron-hole pairs and long-range charge transport in MOFs. The former relies on the prediction of charge separation while the latter relies on the charge mobility of the material. This strategy was tested in a group of 15 MOF structures. Charge mobility criteria are deduced from the curvature at the extrema of the band structure since it is related to the effective mass values of the carriers (electrons and holes). The larger the curvature the higher the charge carrier mobility.

Chapter 4 presents a combined experimental and theoretical synergy toward optimal electronic properties for hydrogen evolution reaction photocatalysis in isoreticular MOFs. Using the different computational strategies described in the previous chapters, the computational

studies aided in the understanding of the electronic and photophysical properties of the materials. The combination with experimental characterization and analysis led to address challenging parameters for computational chemistry. The importance of structural properties such as shape and size of the crystals where influential in the performance of the photocatalytic activity.

Finally, **Chapter 5** gives a general conclusion of this thesis and a discussion of the future research for the prediction of MOF photocatalytic properties. Accurate description of excited states for MOFs via computational chemistry is an active field of research. Therefore, new computational methodologies are required to explore MOFs' photochemical and photophysical properties.

1 From Isolated Porphyrin Ligands to Periodic Al-PMOF: A Comparative Study of the Optical Properties using DFT/TDDFT[a]

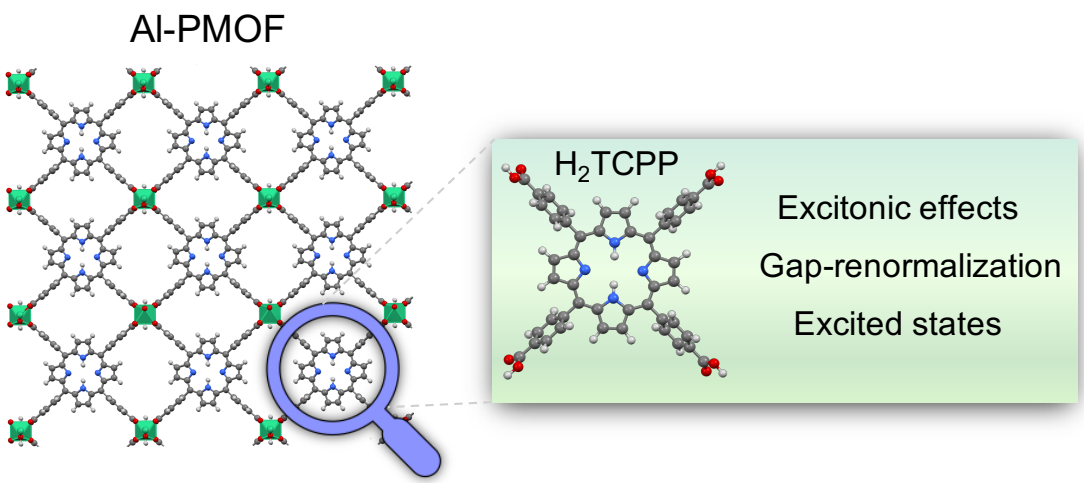

[a]postprint version of the article published as: Andres Ortega-Guerrero, Maria Fumanal, Gloria Capano, and Berend Smit The Journal of Physical Chemistry C 2020 124 (39), 21751-21760 DOI: 10.1021/acs.jpcc.0c06885. A O-G conduced all the calculation and analysed the data and together with M.F. and B.S. wrote the manuscript with the contribution from all authors.

Abstract

The use of photosensitizers as organic ligands in Metal-Organic Frameworks (MOFs) is a common practice to engineer their UV/Vis optical absorption. For instance, MOFs consisting of porphyrin ligands usually inherit their light-harvesting properties and thus follow the Gouterman model in which the low-lying excitations correspond to $\pi \rightarrow \pi^*$ transitions. However, the characterization of the excited states of porphyrin ligands in MOFs requires an appropriate description of the periodic crystal including the metal nodes and inter-molecular interactions. Here, we investigate the UV/Vis absorption properties of the porphyrin-MOF Al-PMOF and two metallated forms, Zn-Al-PMOF and Co-Al-PMOF, and of their corresponding isolated porphyrin ligands using DFT/TDDFT simulations with PBE, PBE0, and CAM-B3LYP functionals. Our results indicate that hybrid functionals are necessary to capture the proper nature of the transitions and the excitonic effects of the optical and fundamental gaps in porphyrin molecules and porphyrin-MOFs that PBE functional fails to describe. Likewise, the simulations show that a wrong representation of some excitations can be obtained depending on the functional and when the Tamm-Dancoff approximation is used. Finally, our results show that PBE and PBE0 functionals are not able to capture the gap-renormalization when going from the isolated molecules to the periodic crystals. Overall, the nature of the optical transitions, the excitonic effects, and the gap-renormalization are important features to assess in the prediction of optical properties in MOF crystals that require considering proper functionals and approximations to overcome the main failures of DFT/TDDFT calculations.

1.1 Introduction

Metal-Organic frameworks (MOFs) have attracted significant attention as materials with the potential to be exploited in optical applications[211, 40]. The modular inorganic-organic nature and the topology of their crystal structure make MOFs prospect materials for designing novel systems with unique photophysical and photochemical properties. Inorganic nodes and organic ligands can interact in a manner that the overall electronic structure is different from the sum of the initial components. In this regard, MOFs offer the advantage of tunability since their properties can be easily modified by the selection and/or modification of its constituent units[143]. The incorporation of photosensitizers as ligands in MOFs is of interest for improving the visible-light absorption profile. Such property can be beneficial in applications for light-harvesting and photocatalysis. [177, 53]. Inspired by the natural photosynthesis that occurs in highly ordered chlorophyll complexes, the incorporation of porphyrins in MOFs has been a recurrent strategy to exploit their optical properties [178, 113, 52]. This strategy has also being used in dye-sensitized solar cells, where the molecular engineered of porphyrin-based compounds improved the light-harvesting properties[130].

Porphyrin MOFs have been synthesized using different transition metal nodes attempting to encompass the optical properties of porphyrin ligands within a porous framework[96, 52]. Rosseinsky and coworkers synthesized a porphyrin MOF with Al(III) at the metal nodes named

Al-PMOF (Figure 1.1a) which was found to be water-stable[51]. This material presents visible-light-driven hydrogen generation when combined with ethylenediaminetetracetic acid and Pt nanoparticles. Porphyrins can easily coordinate metal ions, yielding to metallated-porphyrins that can boost the catalytic activity. With this purpose, Al-PMOF has been also reported in different metallated forms such as Zn-Al-PMOF[51] and Co-Al-PMOF[107, 122] aiming to modify the catalytic and photophysical properties of the material. In previous studies, the ground state electronic properties of Al-PMOF have been extensively analyzed indicating that the frontier crystal orbitals of the material are centered on the porphyrin ligands[79, 7]. For that reason, even though Al-PMOF is composed of porphyrin ligands and Al nodes, the optical properties of this MOF have been mainly attributed to the porphyrin ligands[51] assuming that the interaction with the metal-nodes and between porphyrin ligands is minor. In this context, the optical properties of porphyrin molecules have been studied in both computational and experimental studies but a detailed analysis of the role of the metal-ligand and ligand-ligand interactions in the excited states and optical absorption properties of porphyrin-MOF materials is still missing. Certainly, excited-state phenomena in MOFs are not restricted solely to the ligands, where the interaction with the metal nodes can also lead to low-lying charge-transfer excited states[113, 150]. Moreover, the crystal embedding may have a strong effect on the ligands properties and thus, it is necessary to apply computational approximations that are capable to describe this effect in periodic MOFs. The optimum design of MOFs with desired optical properties requires ultimately the understanding and prediction of their excited states, which in conjunction with other theoretical descriptors will define the final photophysical and photochemical properties of the material[208, 61]. For this reason, an accurate description of their electronic and optical properties is needed.

Both the fundamental and the optical gap are of special interest in studying the optical properties of MOFs. The fundamental gap, E_{fund}, is the difference between the first ionization potential and the first electron affinity in both molecules and solids [109, 8]. The position of these energy levels is of great importance for photocatalytic applications as they determine the capabilities of the system to promote a given reaction upon excitation [61]. The optical gap, E_{opt}, which is defined as the difference between the energies of the lowest dipole-allowed excited state and the ground state[109]. The optical band gap can be determined experimentally as the onset of the UV/Vis spectrum. Both band gaps can be in principle predicted by Density Functional Theory (DFT). In the case of a molecule, the E_{fund} can be directly obtained as the difference between the eigenvalues of the highest occupied molecular orbital (HOMO) and the lowest unoccupied molecular orbital (LUMO) energies. For the case of solids, it is the difference between the highest occupied crystal orbital (HOCO) and the lowest unoccupied crystal orbital (LUCO) energies. The frontier crystal orbital energies can be obtained from the highest and lowest energies from a band structure calculation of the material, respectively. These can be directly computed at the Γ-point in the Brillouin Zone if these are located in this point [8]. Unfortunately, the previous statements only holds for the exact exchange-correlation(XC) functional, while in practice we can only use approximations for this functional[9, 14]. It is noteworthy to mention that GGA functionals cannot provide the

correct fundamental gap and global hybrid functionals usually also lead to an underestimated frontier orbital energy gap (especially in organic molecules)[9, 14]. The optical gap can be predicted using the eigenvalues obtained from DFT by its linear-response time-dependent DFT (LR-TDDFT) extension. Within TDDFT it is possible to derive the excitation energies of the system as the poles of the response function. The optical gap is then considered as the fist dipole-allowed excitation energy obtained by LR-TDDFT[98, 109, 169, 14]. The solution of the linear-response can be done by solving the Casida equations including forward and backward transitions [29] or by the Tamm-Dancoff approximation (TDA) [90] that discards the backward transitions. The TDA has the advantage of being computationally simpler and has been shown to ameliorate some drawbacks of conventional TDDFT such as the triplet instability problem [155]. As in the case of the fundamental gap, the optical gap prediction is also susceptible to the approximations used to solve the exchange-correlation functional[131].

In this work, we perform a comprehensive study of the optical properties of the isolated porphyrin ligand and the porphyrin-MOF crystal of Al-PMOF by DFT and LR-TDDFT computations. We aim to evaluate the effect of the crystal embedding of the porphyrin ligands in MOFs. To do so, we study the performance of different DFT/TDDFT approximations in both isolated porphyrin ligands and periodic porphyrin-MOFs. We consider the isolated porphyrin ligand meso-Tetra(4-carboxyphenyl)porphine (TCPP) and the Zn(II) and Co(II) metallated forms (Figure 1.1b) to assess the effect of metallation on the optical properties of porphyrin Al-PMOF. This choice allows us to compare two model cases TPCC and Zn(II)-TPCC of porphyrin with a closed-shell electronic configuration, with a challenging open-shell system, Co(II)-TPCC, characterized by a partially occupied d-shell. First, we analyze the isolated porphyrin ligands to determine the characteristic excited state features as predicted by different functionals and considering full LR-TDDFT and TDA implementations. We then study the properties of Al-PMOF material and the two different metallated forms Zn-Al-PMOF and Co-Al-PMOF at the same level of theory than the isolated systems. Aiming to compare the isolated and periodic systems, we use a computational setup based on a basis set and functionals that can be used in both periodic MOFs and isolated molecules. Finally, we perform a comparative analysis of the results of the periodic systems and the isolated ligands and discuss the performance and limitations of DFT to address the optical properties of porphyrin-MOFs.

1.2 Computational details

1.2.1 Molecular systems

The three porphyrin molecules, meso-Tetra(4-carboxyphenyl)porphine H_2TCPP, Zn(II) meso-Tetra(4-carboxyphenyl)porphine ZnTCPP, and Co(II) meso-Tetra(4-carboxyphenyl)porphine CoTCPP, were optimized using DFT with PBE[158], PBE0,[159, 1] and CAM-B3LYP[214] implemented in Gaussian 16[56]. The 6-31G* basis set[164] was used for H, C, N, and O, while the LANL2DZ basis set with pseudopotentials was employed for Zn and Co[167]. We restrict our analysis to double-ζ with polarization basis set in order to fairly compare the results with

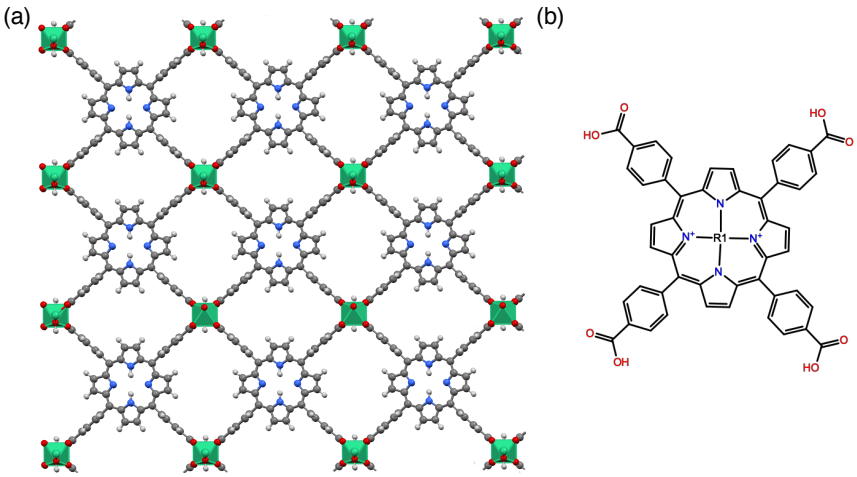

Figure 1.1 – (a) Al-based porphyrin framework structure of Al-PMOF. Oxygen atoms are shown in red, hydrogen in white, carbon in gray, and titanium in green. (b) Isolated porphyrin ligand of Al-PMOF, the center of the porphyrin R_1 can coordinated in order to have meso- Tetra (4-carboxyphenyl) porphine (H_2TCPP), Zn(II) meso- Tetra (4- carboxyphenyl) porphine (ZnTCPP) and Co(II) meso- Tetra (4- carboxyphenyl) porphine (CoTCPP).

the calculations in periodic calculations performed also with double-ζ polarization basis set. The optimization procedure was set to tight along with a super fine grid for the two-electron integrals. The optical absorption spectra were computed considering the full formulation of the Casida equations and the Tamm-Dancoff approximation using linear response TDDFT with the three different functionals.

1.2.2 Periodic Systems

Starting from the known experimental single-crystal X-ray structure [51], the periodic structures for the aluminium porphyrin MOF (Al-PMOF) and the ones with Zn (Zn-Al-PMOF) and Co (Co-Al-PMOF) were fully optimized using DFT implemented in the CP2K code[97, 111]. The structures were optimized using the PBE XC functional with the D3 dispersion correction[71]. The electronic and optical properties of the MOFs were also studied with PBE0 functional[75]. The PBE calculations are conducted using a 1 x 2 x 1 supercell. For Co-Al-PMOF, we used an anti-ferromagnetic singlet orientation of the spin and the DFT+U scheme, where a Hubbard effective potential is added to the d orbitals of the Co atoms. The Löwdin population analysis method[127] was used along with a Hubbard correction U_{eff} value of 3.5 eV. This U-value corrects the nature of the crystal orbitals in Co-Al-PMOF to the same symmetry of the ones obtained with PBE0. In addition, we also fully optimized the H_2TCPP, ZnTCPP, and CoTCPP isolated molecules in CP2K to properly compare the fundamental and optical gap values obtained for the periodic MOF counterparts. In this case, the DFT+U method was used to compute its electronic ground state of CoTCPP. Calculations with CP2K used the QUICKSTEP program and mixed Gaussian and plane wave basis sets in combination with Goedecker-Teter-

Hutter (GTH) pseudopotentials[69]. The efficient orbital transformation (OT) method[188] was used for the optimization of the wave function. The double-ζ polarization MOLOPT basis sets were used to describe H, O and N atoms, while a triple-ζ was used for Zn, Al, and Co atoms. In addition, for the PBE0 calculations, the auxiliary MOLOPT-ADMM basis functions[74] were used: cFIT8 for Al, cFIT11 for Zn and Co, and pFIT3 for non-metal atoms. The Truncated Coulomb operator with a long-range correction was employed for the Hartree-Fock exchange of hybrid calculations. The truncation radius is half of the smallest edge of the unit cell, and the long-range part of the exchange is computed using the PBE exchange. A plane-wave energy cutoff of 600 Ry was used, and the calculations were at the gamma point. The density of states and the crystal orbitals were computed using the PBE0 XC functional along with D3 dispersion correction using 1 x 2 x 1 supercell structures. The UV/Vis absorption spectra of the MOFs was computed using the PBE functional for Al-PMOF and Zn-Al-PMOF while DFT+U was used for Co-Al-PMOF using the LR-TDDFT implementation of CP2K. The optical gaps of the three materials were computed as well with PBE0. When applying LR-TDDFT using PBE0 the long-range correction is excluded according to the CP2K implementation.

1.3 Results and discussion

1.3.1 Molecular systems

The study of optical absorption properties in MOF can be performed considering full periodic boundary conditions [5, 27] or using a representative cluster model [88, 43, 205]. In the case of Al-PMOF that corresponds to the isolated porphyrin ligands. The excited states of porphyrin molecules can be explained by the Gouterman four-orbital model [70]. According to this model, the excitations are characterized by $\pi \rightarrow \pi^*$ transitions from the HOMO, HOMO-1 to the LUMO, LUMO+1 orbitals. Figure 1.2 shows the frontier orbitals of H_2TCPP localized in the porphyrin core of the molecule and have the same symmetry of the Gouterman model. Although, porphyrin is only the macrocycle of H_2TCPP, the presence of the carboxyphenyl groups does not affect frontier orbitals from the porphyrin group. Porphyrins absorb strongly in the 400-450 nm range (Soret or B band) and weakly in the 500–700 nm region (Q band) [115].

In general, the DFT packages available for periodic calculations implement LR-TDDFT solving the Casida equations within the Tamm-Dancoff approximation (TDA). In contrast, quantum chemistry software used for studying isolated molecular systems and cluster models implements both the full representation of the Casida equations and TDA. In order to determine the relevance of the TDA approach in the study of porphyrin ligands, we computed the UV/Vis spectra using both full LR-TDDFT and TDA on the isolated molecules and compared them with the experimental results. In this way, we can fairly compare with the TDA absorption spectra of the periodic systems, which is shown in the next section.

Figure 1.3 shows the different spectra of H_2TCPP, ZnTCPP, and CoTCPP molecules computed with the full LR-TDDFT and TDA using PBE, PBE0, and CAM-B3LYP functional. In this figure,

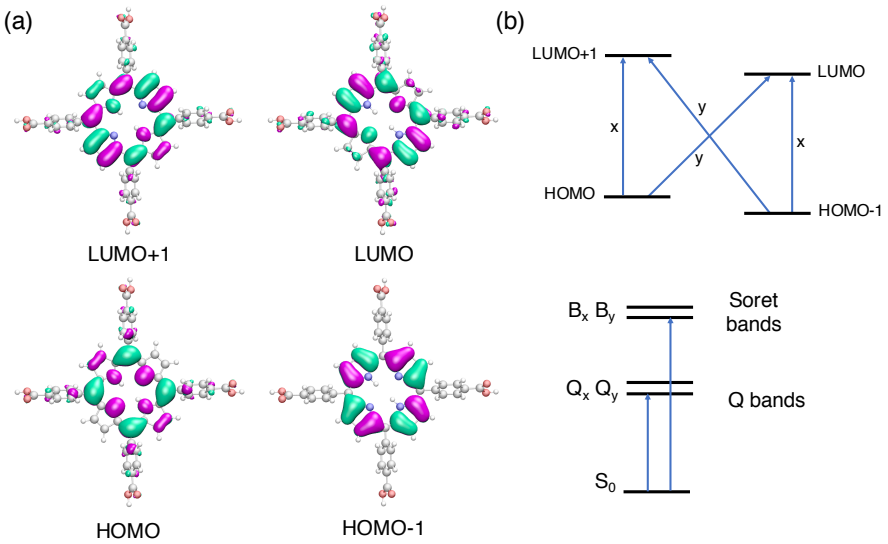

Figure 1.2 – (a) H_2TCPP π and π^* frontier edge molecular orbitals involved in the Q and Sored bands transitions. (b) Gouterman four orbital model transitions and excited states.

we also compare the compute spectra with the experimental ones. It is important to mention that the experimental Q bands in H_2TCPP are four while in ZnTCPP are two. The difference comes from the metallation with the Zn ion which increases the symmetry from D_{2h} to D_{4h} point group in the porphyrin macrocycle[218, 10]. This change in symmetry causes a degeneracy of the LUMO and LUMO+1 orbitals in ZnTCPP. For the case of H_2TCPP, there are two separate Q band excitations that further split into four due to vibrational coupling while ZnTCPP should have two degenerate Q bands that split due to vibrational coupling. For the case of CoTCPP, the Q bands do not further split as much as ZnTCPP and are observed as one single Q band. In the absence of vibrational coupling, the Q bands appear as double and single peaks in the TDDFT calculations for H_2TCPP and ZnTCPP, respectively.

To discuss the results, we should make a difference between H_2TCPP and ZnTCPP, which are closed-shell systems, and CoTCPP which is an open-shell system with a partially occupied d-shell. For H_2TCPP and ZnTCPP, the three XC functionals describe the frontier molecular orbitals as in the Gouterman-model (Figures 1.7 and 1.8) and only differ by their Kohn-Sham energy gap (Tables 1.2 and 1.4). The three functionals predict with good accuracy the position of the Q bands in comparison with the experimental spectra (Figure 1.3). The use of TDA or the full Casida formalism have a small impact on the positioning of the Q bands. In particular, the Q bands when evaluated with the TDA are slightly blue-shifted with respect to their position when using the full Casida formalism, regardless of the XC functional used. Similarly, the use of a pure hybrid XC PBE0 and a range-separated XC CAM-B3LYP results in the Q bands only slightly blue-shifted with respect to the PBE results. Thus, the performance of PBE on the prediction of the optical gap (Q Bands) in porphyrin molecules is rather good, as has been previously reported [109]. Although PBE predicts the optical gap with good accuracy, the value

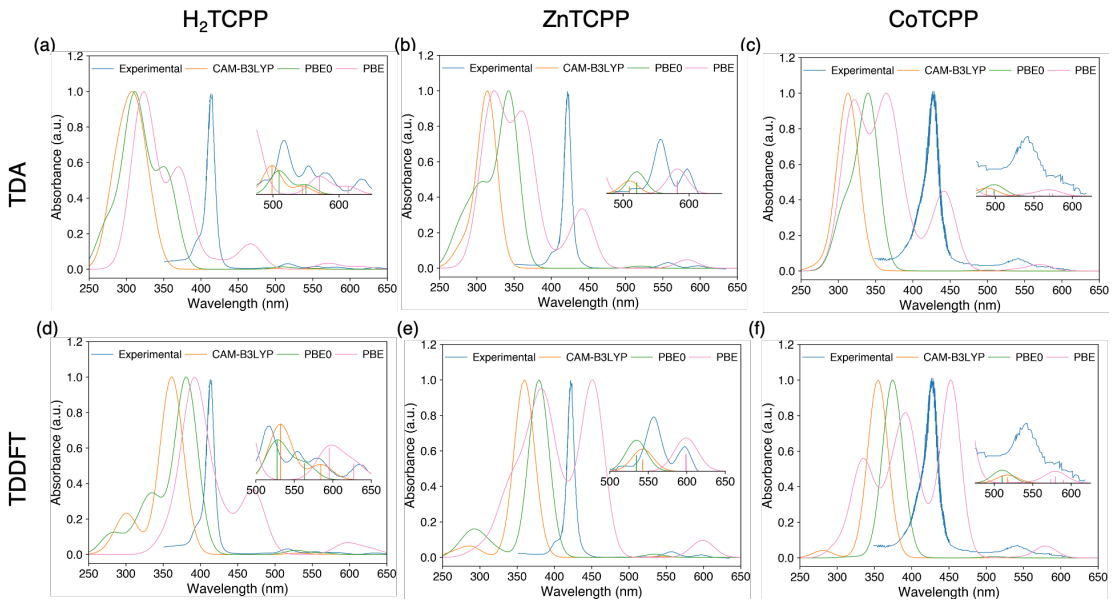

Figure 1.3 – Comparison of the experimental UV/Vis absorption spectra and the TDDFT calculations using different XC functionals of the porphyrin molecules. The upper row considers the Tamm-Dancoff approximation while the lower row the full solution of the Casida equations for (a) and (d) H_2TCPP, (b) and (e) ZnTCPP, (c) and (f) CoTCPP, respectively. The theoretical UV/Vis spectra are normalized and generated using a Gaussian line shape convolution with a half-width of 0.07 eV. Experimental spectra of H_2TCPP and ZnTCPP are taken from ref. [165] and CoTCPP are taken from ref. [179] Insets: enlarged spectra of the Q bands.

obtained is larger than the PBE fundamental gap, which indicates a misrepresentation of the excitonic effects[98, 109]. Given the local excitation nature of the Q bands ($\pi \rightarrow \pi^*$), this will imply a repulsive interaction between the electron and hole. This artifact is preserved in all the PBE calculations with TDA and full TDDFT (Tables 1.2, 1.3, 1.4 and 1.5). The use of hybrid or range-separated XC functionals corrects this artifact resulting in larger fundamental gap predictions and therefore, attractive excitonic effects (Tables 1.2 and 1.4). Another feature observed in the PBE spectra is the presence of additional excitations between the Soret band and Q bands. According to the Gouterman model, the Soret excitations should be predicted right after the Q bands. However, H_2TCPP and ZnTCPP UV/Vis spectra using PBE predict additional absorption peaks providing a wrong description of the experimental spectrum. These additional peaks appear as a result of a strong underestimation of charge-transfer (CT) states within TDDFT[112] evaluated with a pure GGA functional. These excitations correspond to CT transition from the porphyrin macrocycle to the phenyl orbitals of the molecule, which is observed in both TDA and full-Casida formalism calculations. Due to the artificial underestimation of the CT states within PBE, the Soret band shows a mixture of orbital contributions and thus has been analyzed using Natural transition orbitals (NTO) to assign the peaks(Figures 1.15, 1.16, 1.20 and 1.20).

In contrast, PBE0 and CAM-B3LYP functionals show the proper description of the excitations

of the porphyrin molecules within the UV/Vis range in good agreement with the experimental measurements[49, 16]. In both molecules, the Soret band appears as the third excitation in the full Casida TDDFT calculations (Table 1.2 and 1.4). When using TDA with PBE0 the previous statement only holds for ZnTCPP but not for H_2TCPP. For the latter, additional excitations of CT character from the porphyrin to the phenyl groups appear below in energy (Figure 1.14). These additional excitations observed in H_2TCPP with PBE0 and TDA remain when larger basis set are considered as well (Figure 1.4). Although PBE0 functional can still be susceptible to CT artifacts in TDDFT[112], an over-stabilization of the CT states is only observed with TDA applied to the H_2TCPP ligand. This error is not observed with CAM-B3LYP in any case. Altogether, the spectra predicted with the three XC functionals for H_2TCPP and ZnTCPP showed the Soret band less blue-shifted with respect to the experiments when using the full-Casida TDDFT formalism instead of the TDA. Despite that the TDA has been found to very accurate when used to organic molecules[32], our calculations show a significant improvement of the porphyrin UV/Vis spectrum when using the full TDDFT approach. Yet, it is important to mention that the TDA does not fail in the description of the porphyrin excitations. The failure of TDA to fully recover the appropriate ordering and energetics of the CT and local states of porphyrin molecules suggests that important electronic correlation is missing when neglecting the backward contributions to the transitions[13].

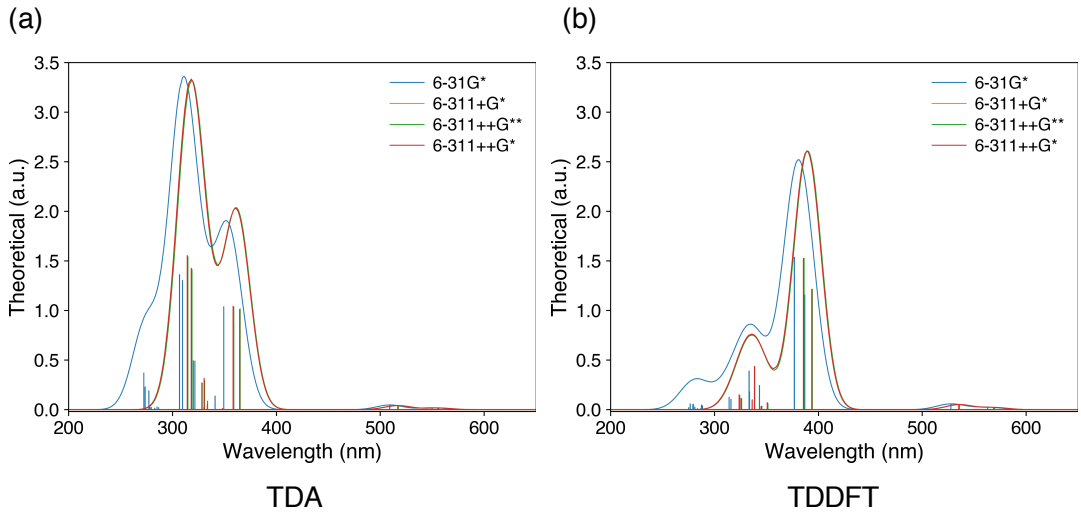

Figure 1.4 – H_2TCPP UV/Vis spectra computed at the PBE0 using different basis set with (a) TDA and (b) full Casida TDDFT formalism.

The description of the UV/Vis properties of CoTCPP is a bigger challenge for both DFT and TDDFT. In particular, the ground state properties must be computed by DFT using an unrestricted Kohn-Sham formalism. Unrestricted DFT and TDDFT calculations for open-shell systems are susceptible to spin-contamination from having α and β electrons treated independently[28]. In addition, Co(II) has a partially occupied d-shell, whose electrons are highly correlated. These challenges lead to the necessity of using more accurate and computationally demanding functionals to ensure an appropriate description of the ground state and usually

imply highly demanding TDDFT calculations including a large number of excitations.

First, we consider the description of the ground state properties of CoTCPP. The PBE calculations of CoTCPP suffer from a high self-interaction error and result in frontier molecular orbitals that do not follow the Gouterman model (Figure 1.9). This error mainly originates from the presence of an unpaired electron in the d-shell of the Cobalt atom and can be partially fixed by considering a hybrid functional. Indeed, the PBE0 and CAM-B3LYP functionals reduced the self-interaction error and predicted the frontier molecular orbitals of CoTCPP in agreement with the Gouterman model (Figure 1.10). Remarkably, the calculations performed with PBE also alter the molecular structure of CoTCPP, which shows a distorted non-planar shape of the porphyrin macrocycle in contrast to the planar structure obtained with PBE0 and CAM-B3LYP(Figure 1.11). This effect is not observed in H_2HTCPP and ZnTCPP during the geometry optimization using the three functionals which yield to similar structures.

Second, we analyse the optical absorption properties of CoTCPP. Figures 1.3c and 1.3f show the TDDFT UV/Vis spectra compared with the experimental measurement using TDA and the full-Casida formalism, respectively. Like in the case of H_2TCPP and ZnTCPP, the UV/Vis spectra of CoTCPP computed with the hybrid and range-separated functionals show good agreement with the experimental spectra, being the TDA spectra slightly blue-shifted with respect to the full-Casida approach in all cases. On the other hand, the PBE calculations predict that the lowest excitations correspond to d-d transition (with an almost zero oscillator strength) instead of the Q bands (Tables 1.6 and 1.7). However, the Q bands appear after this d-d excitations and have a higher oscillator strength as shown in the UV/Vis spectra (Figures 1.3c). Although PBE fails to properly describe the ground properties of CoTCPP, it predicts the Q bands in agreement with the Gouterman-model and with the experimental wavelength, while still suffers from the same problems encountered in H_2TCPP and ZnTCPP showing additional excitations between the Q bands and Soret Band. Moreover, the PBE results shows large spin contamination in the low lying transitions up to values of the squared of the total spin angular momentum (S^2) of 1.5 (being ideally 0.75) (Table 1.6 and 1.7).

The LR-TDDFT calculations using hybrid and range-separated functionals entail a larger computational cost for CoTCPP than for H_2TCPP and ZnTCPP. As previously mentioned, the use of unrestricted TDDFT in conjunction with a partially occupied d-shell requires to include a higher number of excitations than in the restricted TDDFT case whith either a purely organic or fully occupied d-shell system. The first 10 excitations in CoTCPP computed with PBE0 and CAM-B3LYP functionals are all dark excitation (oscillator strength equals to zero), mostly including low energy d-d local excitations. Excitations S_{11} and S_{12} correspond to the Q bands of the porphyrin and thus properly represent the optical gap with negligible spin contamination (Table 1.6 and 1.7). As in the case of H_2TCPP and ZnTCPP, the NTO analysis of the full-Casida TDDFT calculations shows that both PBE0 and CAM-B3LYP functionals describe properly the Soret bands in CoTCPP. However, the NTO analysis of the TDA results obtained with CAM-B3LYP shows that the some d orbitals of Co(II) are involved in one of the Soret bands transition (Figure 1.21) thus misrepresenting the character of this excitation. Overall our results suggest

that the full Casida formulation should be considered when studying the optical UV/Vis excitations of porphyrin ligands instead of TDA. According to our calculations, we encounter some additional excitations (H_2TCPP) and the wrong description of the orbitals of the Soret band (CoTCPP) when using this approximation. It is noteworthy to mention that the last statement only holds for the basis set we consider here. Despite that GGA functionals are able to properly predict the Q bands of porphyrin ligands, these functionals have important issues to correctly account for the excitonic effects in the E_{opt} and may over-stabilize charge-transfer states between the porphyrin and its substituent units in the UV/Vis spectrum.

MOFs systems containing porphyrins have the additional challenge of addressing the optical properties in periodic boundary conditions plus the presence of the transition metal nodes. Herein, we considered Al-PMOF built from aluminium metal nodes connected to porphyrin ligands in a 3D network (Figure 1.1a). The optimization in periodic boundary conditions of Al-PMOF using PBE functional with D3 dispersion correction shows good agreement with the unit cell parameters published experimentally[80, 51]. Figure 1.5 shows the projected density of states of Al-PMOF, as well as the systems where the porphyrin is metallated with Zinc (Zn-Al-PMOF) and Cobalt (Co-Al-PMOF) at the PBE0 theory level. The band gaps are 2.81, 2.93 and 3.12 eV for Al-PMOF, Zn-Al-PMOF and Co-Al-PMOF, respectively. The valence and conduction bands of the three MOFs are mainly dominated by crystal orbitals localized on the porphyrin ligands. The band edge crystal orbitals have the same symmetry(π and π^*) as the ones of the isolated molecules(Figure 1.23 and 1.24). Likewise, these orbitals are highly localized presenting minimal dispersion[180, 80]. The region above the first conduction band has a strong contribution from the phenyl groups of the ligand including the carboxylic groups. The electronic properties of Al-PMOF, Zn-Al-PMOF, and Co-Al-PMOF depicts a material where its electronic and optical properties are highly dominated by the porphyrin ligands[80]. There are not major changes in the electronic properties of the material after changing the metal center of the porphyrin molecule (Figure 1.5).

Calculations performed for Al-PMOF and Zn-Al-PMOF with PBE0 result in same band edge orbitals than the ones obtained with PBE considering the opening of the band gap in the hybrid calculations (Figure 1.27). However, in the case of Co-Al-PMOF, the description of the frontier orbitals remains challenging using PBE due to important self-interaction error effects[47]. As previously mentioned, these arise from the presence of Co(II) with an unpaired electron in the porphyrin ligand. In particular, the use of GGA functionals leads to a misrepresentation of the LUMO, which is the d_{z^2} orbital of the Cobalt ion instead of the π^* orbital of the porphyrin (Figure 1.25) as observed for the isolate CoTCPP molecule. Likewise, the use of a hybrid functional corrects the description of frontier orbitals of CoTCPP in Co-Al-PMOF, placing the d_{z^2} orbital of the Cobalt ion at higher energies (Figure 1.10). Interestingly, the CoTCPP ligand in Co-Al-PMOF does not display a non-planar shape when optimized with PBE (Figure 1.11). Instead, the presence of the aluminium backbone and the confined environment promotes a more planar structure in agreement with the experimental structure.

Taking into account our analysis on the use of PBE and PBE0 XC functionals to describe

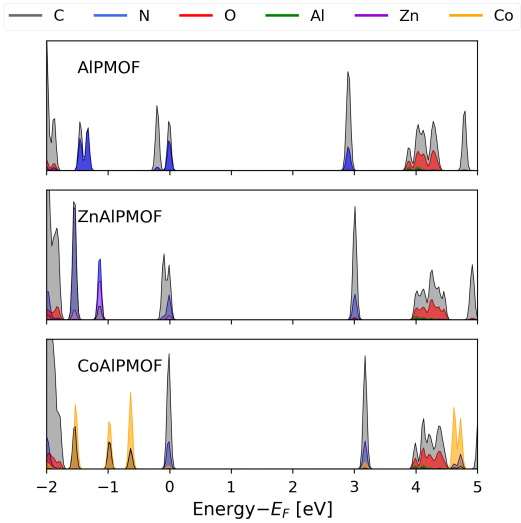

Figure 1.5 – Projected density of states of Al-PMOF, Zn-Al-PMOF, and Co-Al-PMOF using PBE0 XC functional.

the electronic and structural properties of porphyrin-MOF, in the following we are going to focus on the study of their optical absorption properties. Since Co-Al-PMOF ground state is misrepresented with PBE, we use DFT+U calculations to correct the energy and character of its frontier crystal orbitals. A Hubbard U_{eff} =3.5 eV corrects the crystal orbitals in Co-Al-PMOF resulting in symmetries similar to the ones obtained with PBE0 (Figure 1.28 and 1.26). The DOS obtained with DFT+U display the correct band edges of the material as the ones obtained from PBE0 being slightly less localized (Figure 1.26). Figure 1.6 shows the comparison between the TDDFT with TDA computed spectra and the experimental UV/Vis spectra of Al-PMOF, Zn-Al-PMOF, and Co-Al-PMOF. We used PBE for Al-PMOF and ZnAlMOF while DFT+U method was used for Co-Al-PMOF. The periodic TDDFT with TDA calculations predict the Q bands in agreement with the experimental measurements. These Q bands have a 100% contribution from the band edge orbitals following the Gouterman four-orbital model. Additional excitations between the Soret and Q bands were also observed, as in the case of the isolated molecules. These additional excitations between the Soret and Q band do not correspond to transitions between the band edges orbitals exclusively. Instead, these transitions involve orbitals also from the phenyl group being of the same nature as the ones observed for the isolated molecules using PBE functional. Likewise, the highest absorption peak obtained for the periodic MOFs is not entirely described by the Gouterman four-orbital of the Soret band, instead it shows less than a 50% contribution of the π and π^* orbitals. The UV/Vis calculations spectra of the three MOFs are qualitatively similar to the experimental measurements. Yet, there are many additional transitions wrongly describing the character of the excitations in the entire UV/Vis spectra. The comparison of the experimental UV/Vis spectra of the molecules and periodic MOFs shows small differences around the Soret band (Figures 1.3 and 1.6). In the case of the molecular structures, we evaluate the

effect of using the TDA in the theoretical UV/Vis calculation, which yields to blue-shifted spectra, while the full Casida formalism leads to UV/Vis spectra closer to the experimental measurements (Figure 1.3). For that reason, we ascribe the blue-shift shift obtained in the periodic materials mainly to the use of TDA. PBE is the most common functional for the calculation of the UV/Vis spectra of periodic MOFs[190, 27] since its computational cost allows to obtain the necessary number of excitations to cover the UV/Vis range. Based on our results, this functional has important difficulties to describe the upper region of the UV/Vis spectra in porphyrin MOFs, while predicts properly the Q bands of Al-PMOF and its metallated counterparts. The performance of the functional and the TDA approximation could be the source of important artifacts when studying MOFs containing porphyrin or ligands affected by the approximations since software for periodic systems rely on TDA for TDDFT calculations.

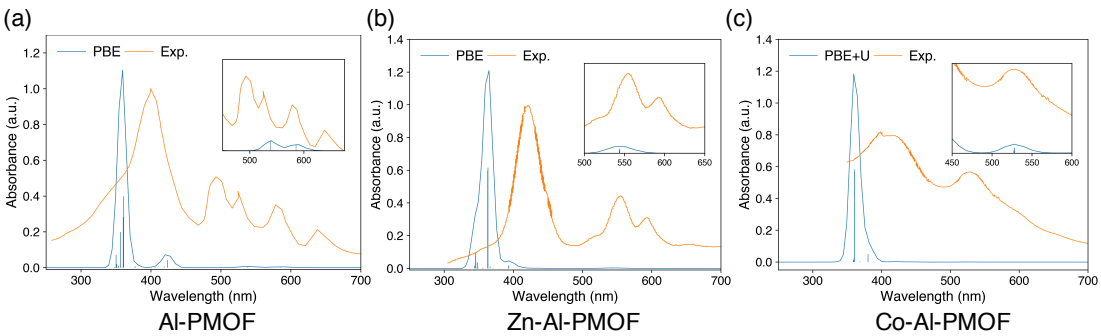

Figure 1.6 – Comparison of the experimental UV/Vis absorption spectra and the periodic TDDFT calculations using a 1 x 2 x 1 supercell of (a) Al-PMOF and (b) Zn-Al-PMOF using the PBE XC functional, and (c) Co-Al-PMOF using the PBE+U XC functional with U_{eff} = 3.5 eV. The theoretical UV/Vis spectra are normalized and generated using a Gaussian line shape convolution with a half-width of 0.07 eV. Al-PMOF and Zn-Al-PMOF UV/Vis spectra is taken from ref. [51], while Co-Al-PMOF is taken from ref. [122]. Insets: enlarged spectra of the Q bands.

1.4 Molecular vs periodic systems

According to the calculations of the isolated porphyrin molecules, a proper description of the UV/Vis spectra in porphyrin-MOFs requieres a hybrid functional. However, computing the necessary number of excitations to cover the full range of the UV/Vis spectra using a hybrid functional is computationally too demanding. Instead, we computed the necessary excitations in the lower energy range to evaluate the Q bands energies in the three porphyrin-MOF materials using PBE0, which correspond to excitations localized in the porphyrin macrocycle. We have computed the E_{opt} from TDDFT with TDA calculation as the first dipole allowed excitation. Table 1.1 shows a comparison of E_{fund} and E_{opt} computed with PBE and PBE0 XC functionals in the periodic MOFs and the isolated porphyrin ligands, except for Co-Al-PMOF and CoTCPP for which DFT+U was used instead of PBE. The values of E_{fund} and E_{opt} of the isolated porphyrin molecules shown in Table 1.1 were recomputed with CP2K to properly

	PBE		PBE0	
System	E_{fund} [eV]	E_{opt} [eV]	E_{fund} [eV]	E_{opt} [eV]
Al-PMOF	1.820	2.110	2.879	1.801
Zn-Al-PMOF	1.960	2.140	2.993	1.930
Co-Al-PMOF*	2.082	2.348	3.161	1.898
H_2TCPP	1.798	2.068	2.929	1.861
ZnTCPP	1.893	2.197	3.037	1.975
CoTCPP*	2.049	2.290	3.202	2.099

* The PBE results are from PBE+U calculations.

Table 1.1 – Comparison of the Fundamental Gap (E_{fund}) and Optical gap (E_{opt}) of the MOFs and isolated ligands using PBE and PBE0 calculations.

compare with the periodic calculations. It can be seen that the use of hybrid functionals increases the E_{fund} from the underestimated values obtained with PBE. Moreover, the E_{fund} have a similar value when computed in the periodic MOF and the associated isolated ligands, when using both PBE and PBE0 functionals. The results shows no major differences from computing E_{fund} for the isolated porphyrin molecule or from the periodic MOF. Considering that the frontier crystal orbital of the porphyrin-MOFs are of the same nature as in the Gouterman-model in isolated porphyrin molecules, that implies that neither PBE and PBE0 functionals are able to capture the gap re-normalization of going from an isolated molecule to a periodic crystal[182, 169, 14, 109]. This re-normalization implies that the fundamental gap of an isolated molecule should be wider than the one of the same molecule as part of a periodic crystal. Although the last statement generally applies strongly to organic crystals, MOFs can inherit similar behavior given the limited electronic coupling and localized nature of their orbitals. In the case of the E_{opt}, the calculations using PBE on the periodic MOFs show the same behavior of their isolated ligand counterparts resulting in higher E_{opt} than the ones of their obtained for E_{fund}. This artifact from DFT/TDDFT using GGA functionals in porphyrins is reduced when a hybrid functional is used [98]. The PBE0 calculations show large E_{fund} than reduced E_{opt} depicting properly the excitonic effect nature of the Q Bands of both periodic MOFS and isolated ligands. The values of E_{opt} from PBE0 calculation are smaller than the PBE ones like it is observed in the isolated molecule calculations. Overall, Table 1.1 shows no significant differences in the E_{fund} and E_{opt} between calculations of the isolated molecules or the periodic MOFs. This last observation is in agreement with the nature of the electronic and optical properties of Al-PMOF being directed dominated by the porphyrin ligands.

Excitonic effects and gap-renormalization represent major challenges for the accurate prediction of the electronic and optical properties of MOFs. In general, experimental measurements of band gaps in MOFs are limited to the optical band gaps[212]. Usually, DFT calculations conducted in MOFs use the Kohn-Sham values to be compared with the reported values of experimental measurements of the optical gap, and this comparison is in principle incorrect. We said in principle, since in experimental conditions there are more effects to consider, as thermal effects and the quantum motion of the nuclei affecting both E_{fund} and E_{opt}[204, 27].

In the field of bulk inorganic semiconductors, such comparison can hold given that excitonic effects are usually small, making the energy difference between E_{fund} and E_{opt} negligible. The strategy to overcome such challenges (gap-renormalization and excitonic effects) in organic crystals is to include the effect of the dielectric response along with optimally-tuned range-separated functionals by enforcing the Koopmans' condition[169, 182]. In the case of MOFs, these calculations can be computationally demanding given the number of atoms and size of the unit cell. However such calculations are required to properly described their electronic and optical properties of MOFs. Here, we use a truncated and long-corrected PBE0 functional that, despite not being optimized, is capable to describe the excitonic effects in Al-PMOF and its metallated forms due to the strong localization of the frontier crystal orbitals in the porphyrin ligands.

1.5 Conclusions

In this work, we have performed DFT and TDDFT calculations of Al-PMOF, Zn-Al-PMOF, and Co-Al-PMOF to asses the performance of different computational approximations to predict their electronic and optical absorption properties. To do so, we have first considered the isolated porphyrin ligands of the three periodic MOFs and analyzed their ground state and excited state properties as obtained with PBE, PBE0 and CAM-B3LYP functionals. Our calculations reveal that different artifacts are obtained with the PBE functional. First, additional absorption bands are shown between the Soret and Q bands in the UV/Vis spectrum ascribed to charge transfer transitions from the porphyrin to its phenyl substituent. Second, the computed optical gap is larger than the fundamental gap thus resulting in a wrong representation of the excitonic effects. For that reason, we conclude that to study UV/Vis spectra in porphyrins and to correctly describe their optical excitations at least a hybrid functional is required. Evaluation of the optical spectra with the full-Casida formalism or TDA shows that TDA tends to predict a blue-shifted spectra and in some cases, additional excitations (H_2TCPP) and the wrong description of the orbitals of the Soret band (CoTCPP) are obtained. According to our calculations, the full-formalism shows better agreement with the experimental UV/Vis measurements and predicts the correct ordering and character of the states. This discrepancies between full TDDFT and TDA suggest that the electronic correlation of the backward excitations is important for the simulation of optical properties in porphyrins. The same conclusions apply for periodic porphyrin-MOFs. Our results show that the optical properties of Al-PMOF and its two metallated forms, Zn-Al-PMOF and Co-Al-PMOF, follow the Gouterman four-orbital model [70] in which the lowest excitations are characterized by $\pi \rightarrow \pi^*$ transitions between the frontier crystal orbitals localized in the porphyrin ligands. Remarkably, both PBE and PBE0 functionals lead to an accurate prediction of the optical gap. However, both fail to capture the gap re-normalization of going from an isolated molecule to a periodic crystal.

It is important to note that the above results can be translated to other MOFs. The presence of localized orbitals from the organic ligands at the band structure edges of the MOF is a

common feature, which is obtained when the orbitals of the metal-nodes are too high in energy with respect to the orbitals of the ligand. In such case, the ligand strongly influences the optical properties of the material. Thus, the performance of the DFT/TDDFT approximations observed to describe the isolated ligands is translated to the periodic MOF. This may include a wrong representation of the excitonic effects and the character of the lowest excited states. The presence of additional ligands and transition metals with low-lying energy levels represent a major challenge for TDDFT when charge-transfer states are accessible. Additionally, calculations performed for periodic MOFs and isolated ligands may suffer from a wrong gap-renormalization description when using traditional functionals available for solids such as PBE and PBE0.

1.6 Supplemantary Materials

1.6.1 Molecules Orbitals

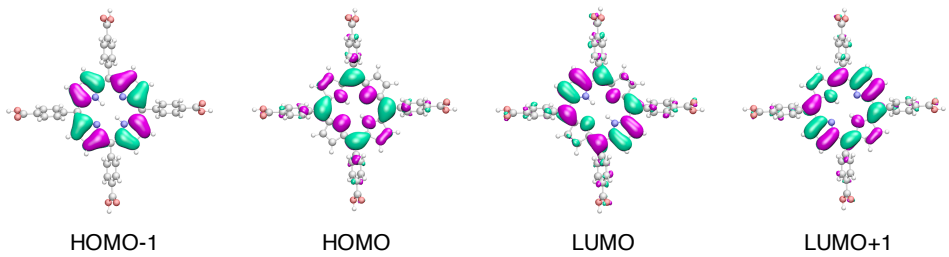

Figure 1.7 – H_2TCPP Molecular Orbitals at the PBE/PBE0/CAM-B3LYP theory level. The three different functionals presented the same symmetry orbitals.

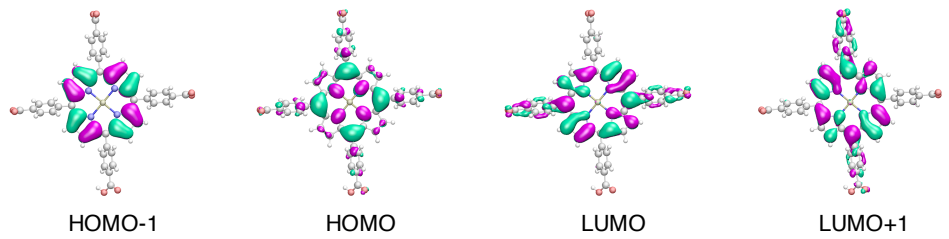

Figure 1.8 – ZnTCPP Molecular Orbitals at the PBE/PBE0/CAM-B3LYP theory level. The three different functionals presented the same symmetry orbitals.

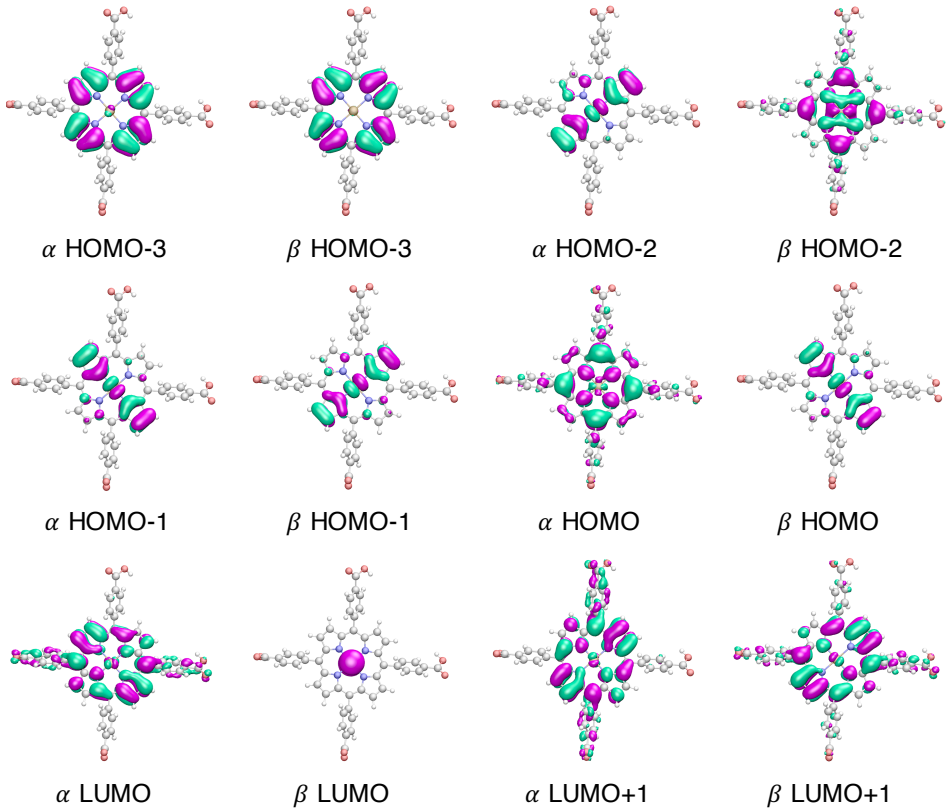

Figure 1.9 – CoTCPP Molecular Orbitals at the PBE theory level.

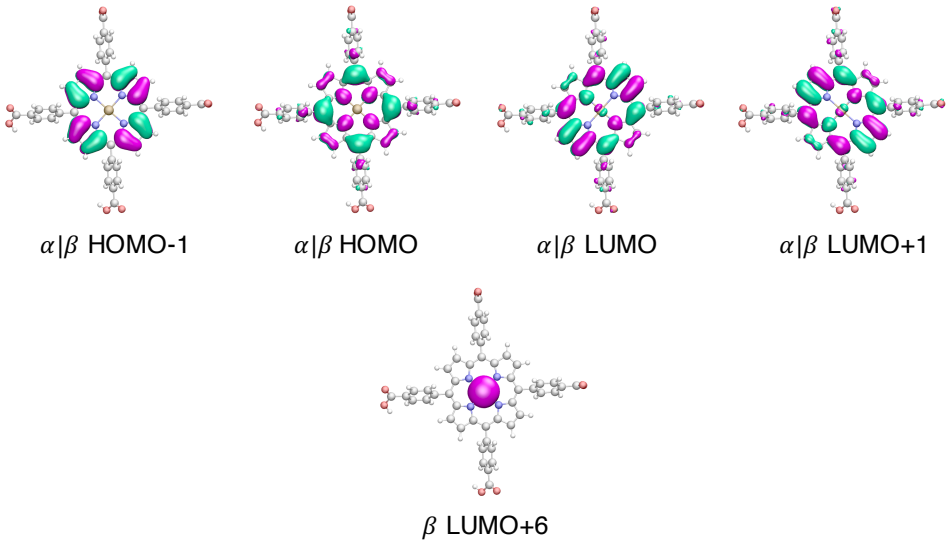

Figure 1.10 – CoTCPP Molecular Orbitals at the PBE0/CAM-B3LYP theory level. These two functionals functionals presented the same symmetry orbitals.

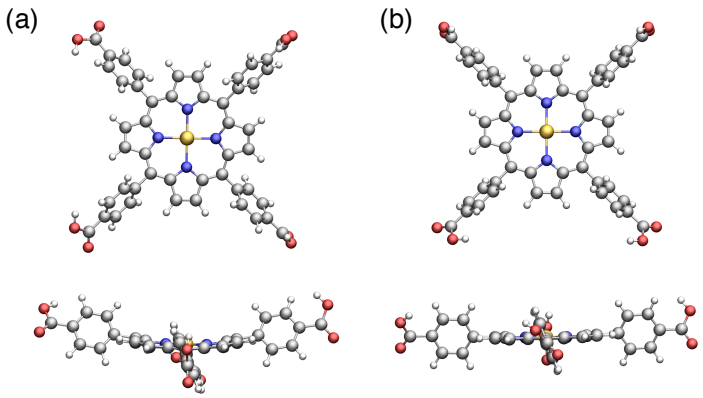

Figure 1.11 – CoTCPP top and lateral view of the geometry optimization structure in Gaussian 16 using (a) PBE and (b) PBE0 functionals.

1.6.2 TDDFT Molecules results

The column Character of the tables relates the nature of the orbitals involved in the excitation. Q and B represent excitations of the Q and the Soret bands nature, respectively, according to the Gouterman model. B is selected as the excitation with the highest oscillator strength value. d-d represents an excitations involving d orbitals in the metalated porphyrin. Mix represent a transition with multiple orbitals involved. The Orbitals column of the table should be associated with the figures 1.7, 1.8, 1.9 and 1.10. We included the Kohn-Sham bandgap (E_g) for each functional to highlight the excitonic effect. For the case CoTCPP, the square of the total spin momentum (S^2) is included since is an open-shell system.

Excitation	f [b]	nm	eV	Character	Orbitals [c]
PBE (E_g = 1.753 eV)					
S_1	0.0502	627.03	1.9773	Q	H-1 → L ; H → L+1
S_2	0.1006	595.24	2.0829	Q	H-1 → L+1 ; H → L
S_{23}	0.5944	391.99	3.1630	B	H-1 → L ; H → L+1
S_{24}	0.6215	389.93	3.1797	B	H-1 → L+1 ; H → L
PBE0 (E_g = 2.904 eV)					
S_1	0.0240	562.89	2.2026	Q	H-1 → L ; H → L+1
S_2	0.0577	527.55	2.3502	Q	H-1 → L+1 ; H → L
S_3	1.1535	386.90	3.2046	B	H-1 → L ; H → L+1
S_4	1.5367	376.84	3.2901	B	H-1 → L+1 ; H → L
CAM-B3LYP (E_g = 4.421 eV)					
S_1	0.0070	584.44	2.1214	Q	H-1 → L ; H → L+1
S_2	0.0255	531.86	2.3312	Q	H-1 → L+1 ; H → L
S_3	1.4521	366.78	3.3803	B	H-1 → L ; H → L+1
S_4	1.8684	357.44	3.4687	B	H-1 → L+1 ; H → L

Table 1.2 – H_2TCPP full Casida TDDFT formalism main excitations using different XC functionals results. Gaussian 16 calculations.

PBE (E_g = 1.753 eV)					
Excitation	f	nm	eV	Character	Orbitals
S_1	0.0443	613.83	2.0199	Q	H-1 → L ; H → L+1
S_2	0.1007	570.58	2.1729	Q	H-1 → L+1 ; H → L
S_{61}	1.1101	323.96	3.8272	B	H-1 → L ; H → L+1
S_{62}	1.4355	323.69	3.8304	B	H-1 → L+1 ; H → L
PBE0 (E_g = 2.904 eV)					
S_1	0.0190	549.90	2.2547	Q	H-1 → L ; H → L+1
S_2	0.0473	509.09	2.4354	Q	H-1 → L+1 ; H → L
S_{15}	1.3031	309.64	4.0041	B	H → L ; H-1 → L+1
S_{16}	1.3607	306.75	4.0418	B	H → L+1 ; H-1 → L
CAM-B3LYP (E_g = 4.421 eV)					
S_1	0.0055	544.42	2.2774	Q	H-1 → L ; H → L+1
S_2	0.0189	498.54	2.4870	Q	H-1 → L+1 ; H → L
S_3	1.4646	327.67	3.7838	B	H-1 → L ; H → L+1
S_5	3.2791	309.21	4.0097	B	H-1 → L+1 ; H → L

Table 1.3 – H_2TCPP TDA TDDFT formalism main excitations using different XC functionals results. Gaussian 16 calculations.

PBE (E_g = 1.810 eV)					
Excitation	f	nm	eV	Character	Orbitals
S_1	0.0579	599.17	2.0693	Q	H-1 → L+1 ; H → L
S_2	0.0583	598.70	2.0709	Q	H-1 → L ; H → L+1
S_4	0.5379	452.29	2.7412	Mix	
S_5	0.5786	452.10	2.7424	Mix	
PBE0 (E_g = 3.032 eV)					
S_1	0.0283	534.55	2.3194	Q	H-1 → L+1 ; H → L
S_2	0.0275	534.40	2.3201	Q	H-1 → L ; H → L+1
S_3	1.5569	379.37	3.2682	B	H-1 → L+1 ; H → L
S_4	1.5571	379.18	3.2698	B	H-1 → L ; H → L+1
CAM-B3LYP (E_g = 4.642 eV)					
S_1	0.0070	542.61	2.2850	Q	H-1 → L ; H → L+1
S_2	0.0078	542.51	2.2854	Q	H → L ; H-1 → L+1
S_3	1.7298	359.82	3.4457	B	H-1 → L+1 ; H → L
S_4	1.7348	359.69	3.4470	B	H-1 → L ; H → L+1

Table 1.4 – ZnTCPP full Casida TDDFT formalism results using different XC functionals. Gaussian 16 calculations.

PBE (E_g = 1.810 eV)					
Excitation	f	nm	eV	Character	Orbitals
S_1	0.0544	582.59	2.1282	Q	H-1 → L ; H → L
S_2	0.0553	582.12	2.1299	Q	H-1 → L ; H → L+1
S_{36}	0.4950	361.58	3.4290	Mix	
S_{72}	0.4013	319.81	3.8768	Mix	
PBE0 (E_g = 3.032 eV)					
S_1	0.0235	520.54	2.3818	Q	H-1 → L+1 ; H → L
S_2	0.0229	520.44	2.3823	Q	H-1 → L ; H → L+1
S_3	1.7421	343.59	3.6084	B	H-1 → L+1 ; H → L
S_4	1.7934	343.26	3.61200	B	H-1 → L ; H → L+1
CAM-B3LYP (E_g = 4.642 eV)					
S_1	0.0050	509.57	2.4331	Q	H-1 → L ; H → L+1
S_2	0.0056	509.50	2.4335	Q	H → L ; H-1 → L+1
S_3	2.8553	314.30	3.944	B	H-1 → L+1 ; H → L
S_4	2.8575	314.13	3.9469	B	H-1 → L ; H → L+1

Table 1.5 – ZnTCPP TDA TDDFT formalism results using different XC functionals. Gaussian 16 calculations.

Excitation	f	nm	eV	Character	Orbitals	S^2
PBE (E_g = 1.168 eV)						
S_3	0.0002	1067.21	1.1618	d-d	β H-2 → β L	0.777
S_{17}	0.0137	613.54	2.1013	Q	α H → α L ; α H → α L+2	1.543
S_{18}	0.0317	613.25	2.1395	Q	α H → α L+1 ; β H-2 → β L+1	1.041
S_{19}	0.0188	389.60	2.1625	Q	α H → α L+1 ; β H-2 → β L+1	1.296
S_{47}	0.2414	451.18	2.7480	Mix		1.306
S_{106}	0.2525	397.51	3.1190	Mix		1.097
PBE0 (E_g = 3.183 eV)						
S_{11}	0.0094	510.43	2.42904	Q	H-1 → L ; H-1 → L+1 H → L; H → L+1	0.759
S_{12}	0.0111	510.26	2.4298	Q	H-1 → L ; H-1 → L+1 H → L; H → L+1	0.758
S_{28}	1.2275	375.06	3.3057	B	H-1 → L ; H-1 → L+1 H → L; H → L+1	0.871
S_{29}	1.3054	374.18	3.3135	B	H-1 → L ; H-1 → L+1 H → L; H → L+1	0.849
CAM-B3LYP (E_g = 4.566 eV)						
S_{11}	0.0006	517.74	2.3947	Q	H-1 → L ; H-1 → L+1 H → L; H → L+1	0.756
S_{12}	0.0012	517.36	2.3965	Q	H-1 → L ; H-1 → L+1 H → L; H → L+1	0.756
S_{26}	1.4614	355.15	3.4911	B	H-1 → L ; H-1 → L+1 H → L; H → L+1	0.820
S_{27}	1.5602	354.68	3.4957	B	H-1 → L ; H-1 → L+1 H → L; H → L+1	0.758

Table 1.6 – CoTCPP full Casida TDDFT formalism results using different XC functionals. Gaussian 16 calculations.

Excitation	f	nm	eV	Character	Orbitals	S^2
PBE (E_g = 1.168 eV)						
S_3	0.0002	1057.82	1.1721	d-d	β H-2 → β L	0.777
S_{17}	0.0201	574.22	2.1592	Q	α H → α L ; α H → α L+2	1.531
S_{20}	0.0256	570.22	2.1743	Q	α H → α L+1 ; β H-2 → β L+1	1.190
S_{49}	0.1806	444.64	2.7884	Mix		1.306
S_{266}	0.3349	318.13	3.8973	Mix		1.138
PBE0 (E_g = 3.183 eV)						
S_{11}	0.0080	498.50	2.4872	Q	H-1 → L ; H-1 → L+1 H → L; H → L+1	0.759
S_{12}	0.0094	498.23	2.4885	Q	H-1 → L ; H-1 → L+1 H → L; H → L+1	0.759
S_{35}	1.6301	341.28	3.6330	B	H-1 → L ; H-1 → L+1 H → L; H → L+1	0.767
S_{36}	1.6461	340.26	3.6438	B	H-1 → L ; H-1 → L+1 H → L; H → L+1	0.767
CAM-B3LYP (E_g = 4.566 eV)						
S_{11}	0.0002	488.74	2.5368	Q	H-1 → L ; H-1 → L+1 H → L; H → L+1	0.755
S_{12}	0.0006	488.44	2.5384	Q	H-1 → L ; H-1 → L+1 H → L; H → L+1	0.755
S_{24}	2.5729	312.91	3.9622	B	H-1 → L ; H-1 → L+1 H → L; H → L+1	0.766
S_{35}	2.5570	312.76	3.9642	B	H-1 → L ; H-1 → L+1 H → L; H → L+1	0.769

Table 1.7 – CoTCPP TDA TDDFT formalism results using different XC functionals. Gaussian 16 calculations.

1.7 Natural Transition Orbital Analysis

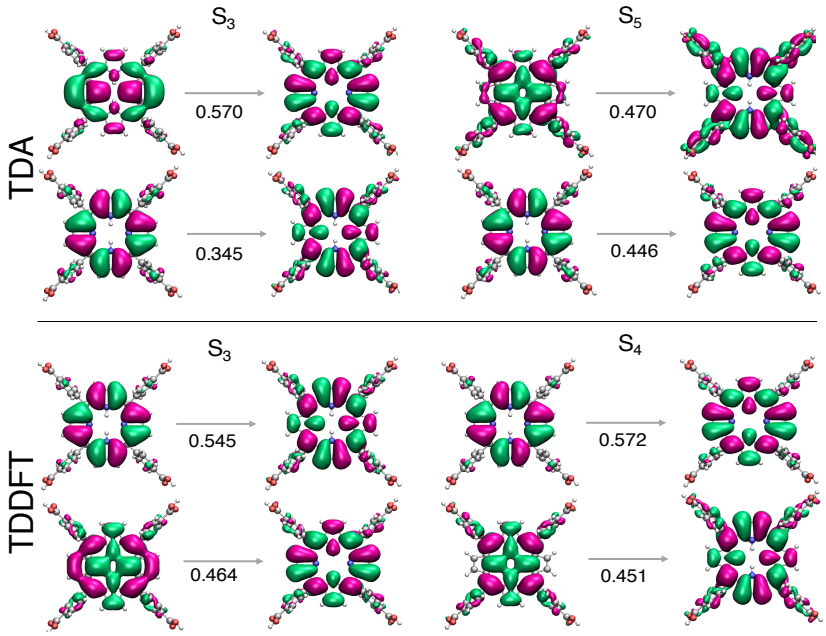

Figure 1.12 – H_2TCPP NTO analysis of the Soret bands at the CAM-B3LYP level using TDA vs full Casida TDDFT calculations.

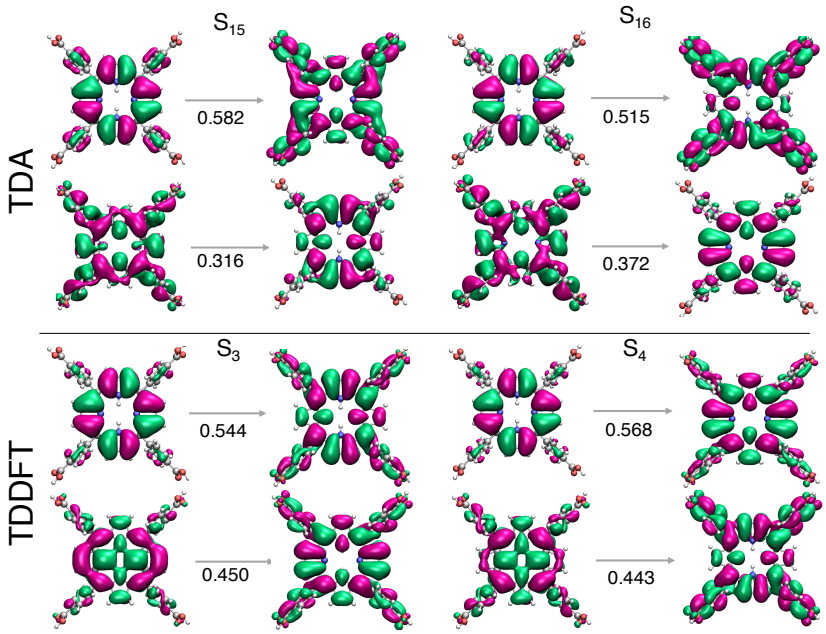

Figure 1.13 – H_2TCPP NTO analysis of the Soret bands at the PBE0 level using TDA vs full Casida TDDFT calculations.

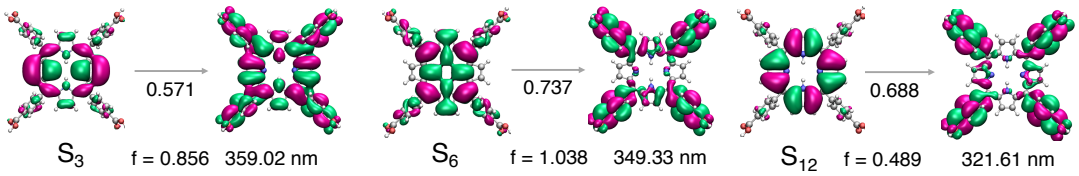

Figure 1.14 – H_2TCPP NTO analysis of the additional excitations between Q and B bands at the PBE0 level using TDA.

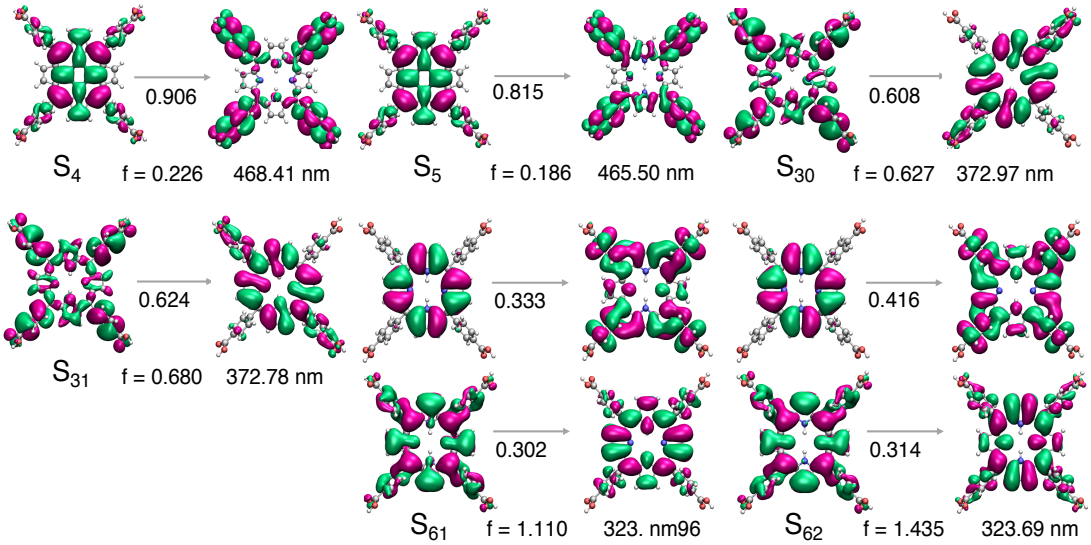

Figure 1.15 – H_2TCPP NTO analysis of the main excitations at the PBE level using TDA.

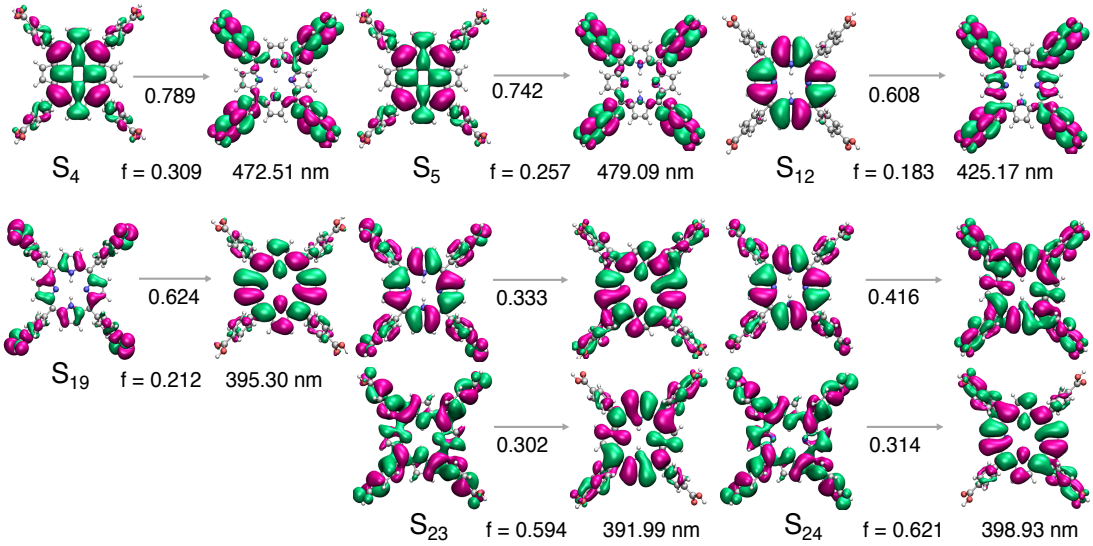

Figure 1.16 – H_2TCPP NTO analysis of the main excitations at the PBE level using full Casida TDDFT approach.

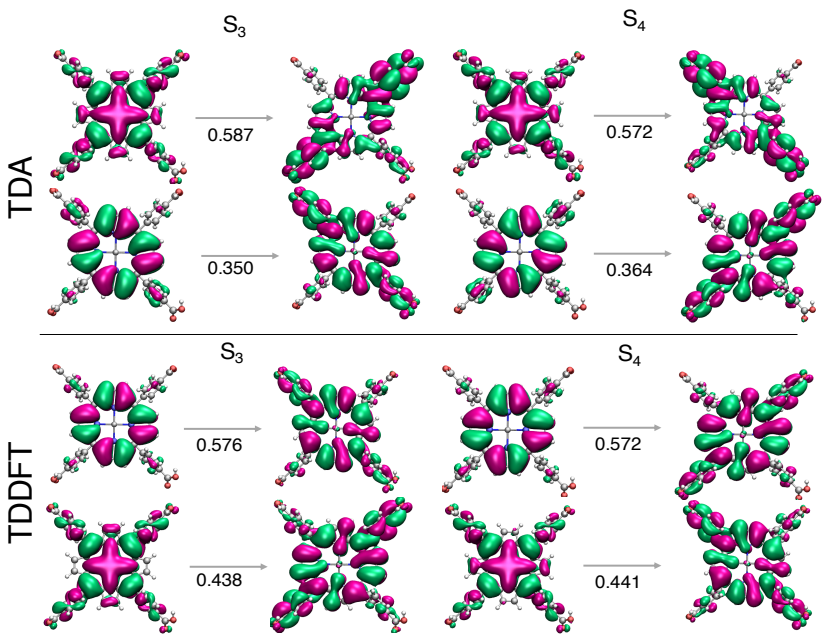

Figure 1.17 – ZnTCPP NTO analysis of the Soret bands at the PBE0 level using TDA vs full Casida TDDFT calculations.

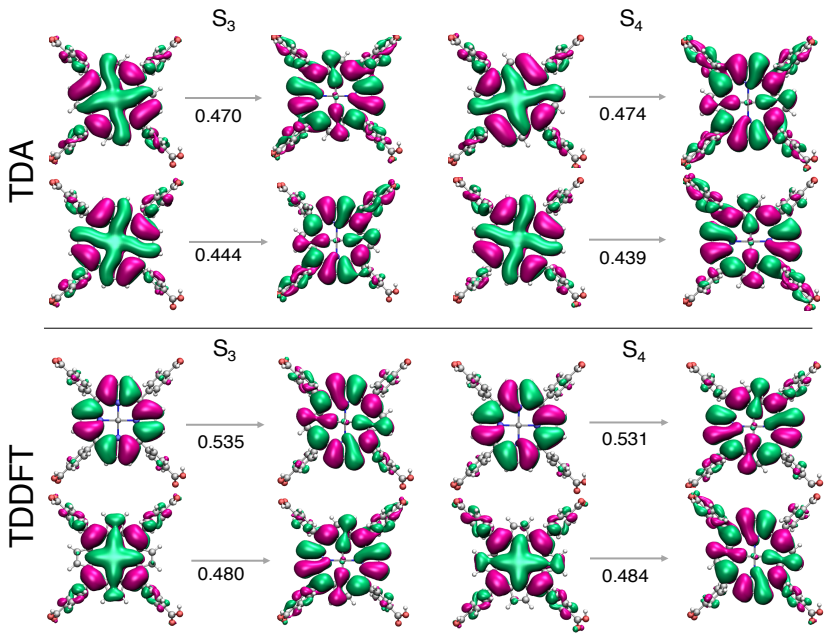

Figure 1.18 – ZnTCPP NTO analysis of the Soret bands at the CAM-B3LYP level using TDA vs full Casida TDDFT calculations.

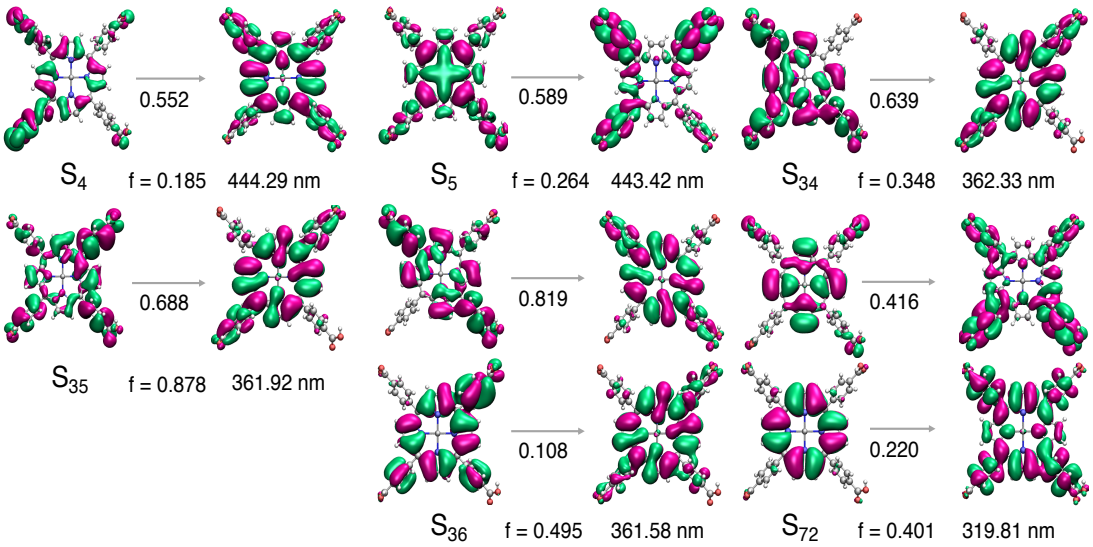

Figure 1.19 – ZnTCPP NTO analysis of the main excitations at the PBE level using TDA.

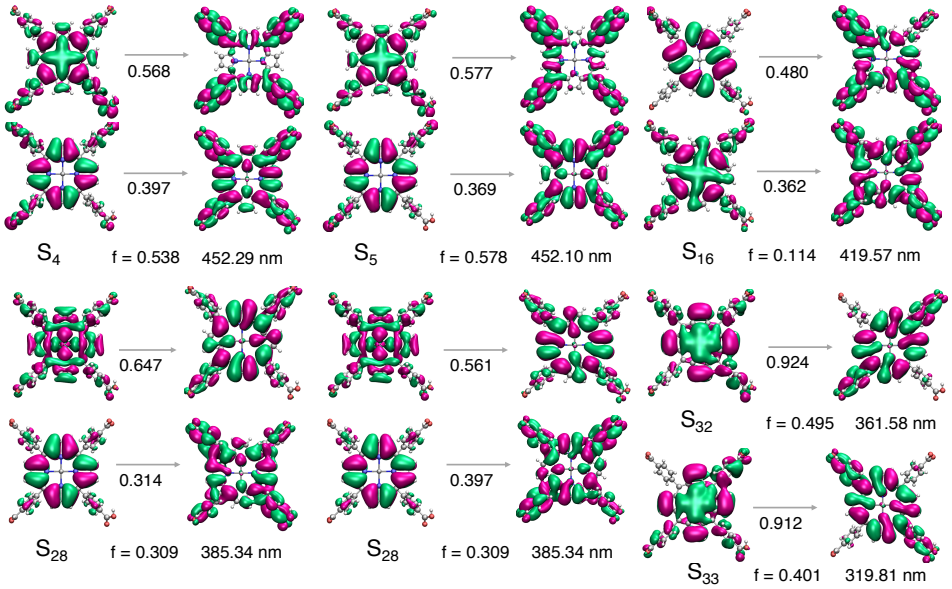

Figure 1.20 – ZnTCPP NTO analysis of the main excitations at the PBE level using full Casida TDDFT approach.

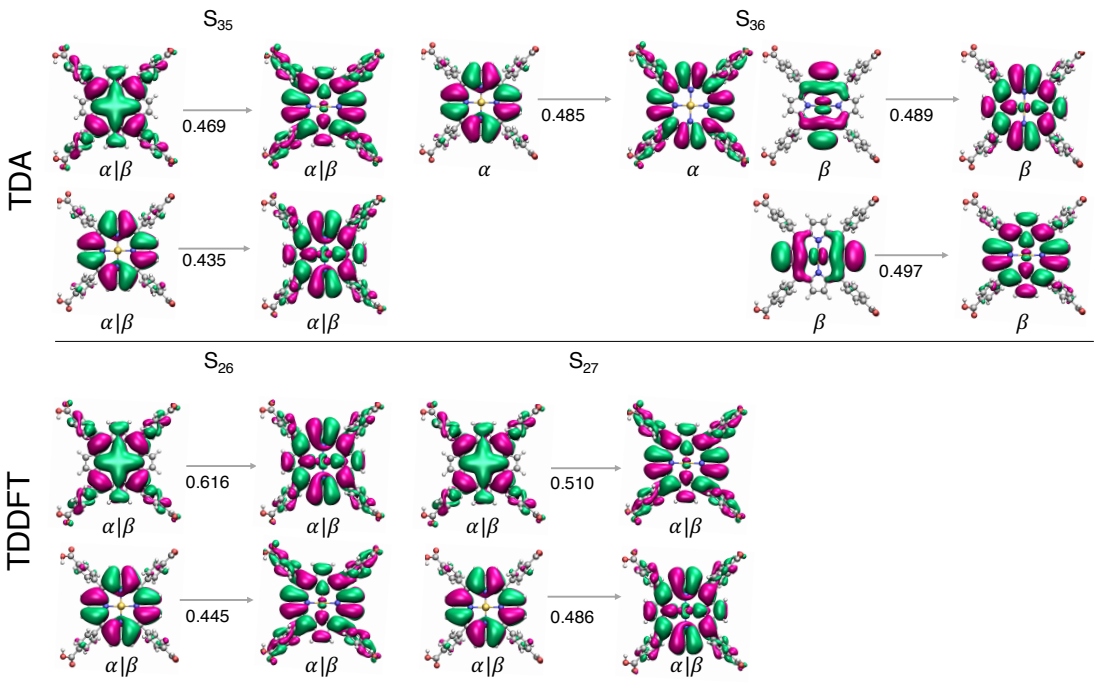

Figure 1.21 – CoTCPP NTO analysis of the Soret bands at the CAM-B3LYP level using TDA vs full Casida TDDFT calculations.

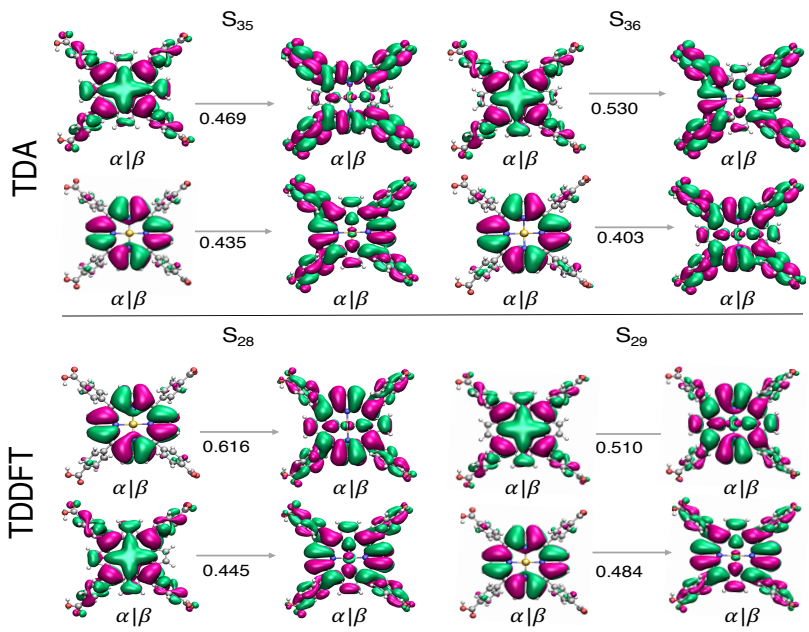

Figure 1.22 – CoTCPP NTO analysis of the Soret bands at the PBE0 level using TDA vs full Casida TDDFT calculations.

1.7.1 Periodic MOF results

The crystal orbitals used are only represented in the central porphyrin of the unit cell for clarity.

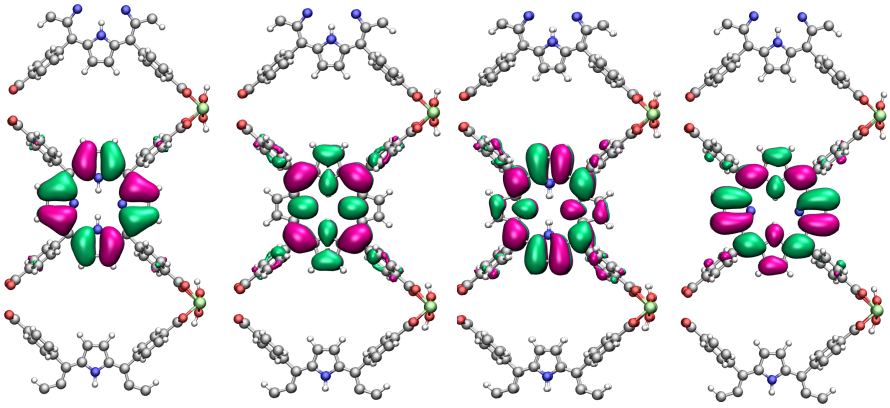

HOCO-7 HOCO-6 HOCO-5 HOCO-4 | HOCO-3 HOCO-2 HOCO-1 HOCO | LUCO LUCO+1 LUCO+4 LUCO+5 | LUCO+2 LUCO+3 LUCO+6 LUCO+7

Figure 1.23 – Al-PMOF Crystal Orbitals at the PBE0 theory level. We have use one representation for the same crystal orbital symmetry.

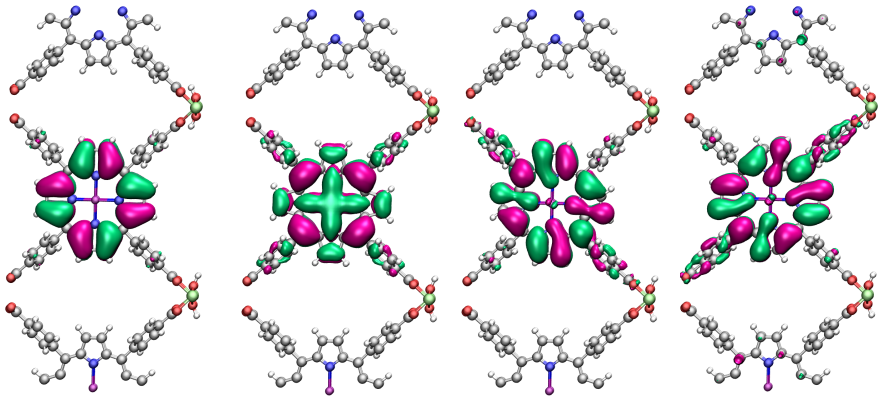

HOCO-7 HOCO-6 HOCO-5 HOCO-4 | HOCO-3 HOCO-2 HOCO-1 HOCO | LUCO LUCO+1 LUCO+4 LUCO+5 | LUCO+2 LUCO+3 LUCO+6 LUCO+7

Figure 1.24 – Zn-Al-PMOF Crystal Orbitals at the PBE0 theory level. We have use one representation for the same crystal orbital symmetry.

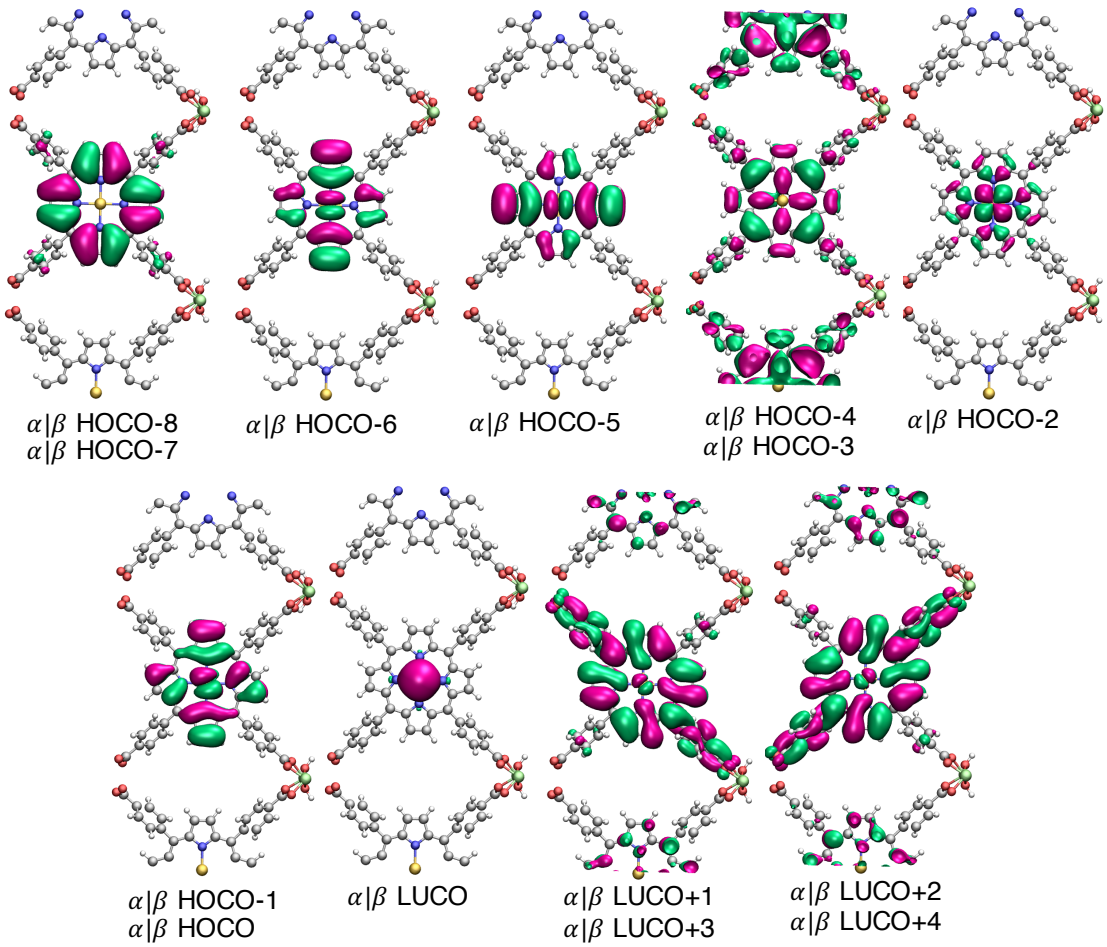

Figure 1.25 – Co-Al-PMOF Crystal Orbitals at the PBE theory level. We have use one representation for the same crystal orbital symmetry.

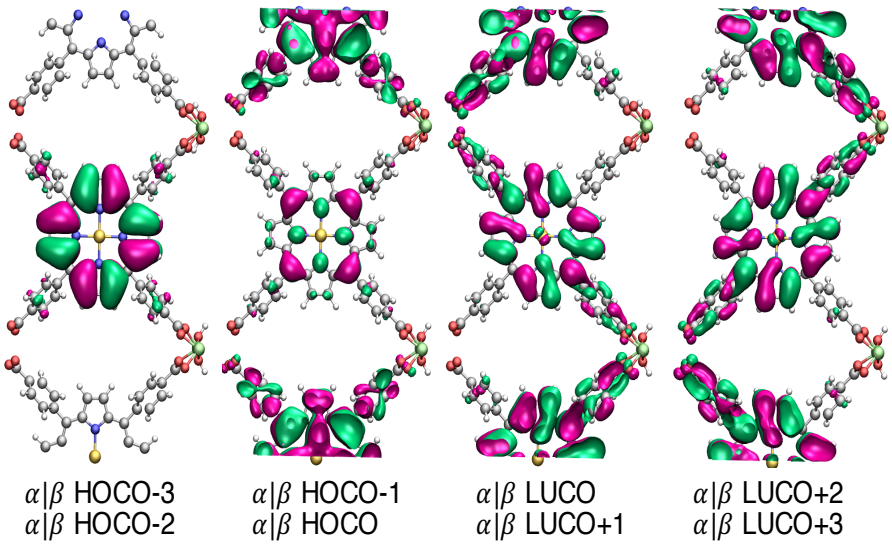

Figure 1.26 – Co-Al-PMOF Crystal Orbitals at the PBE+U (U_{eff} = 3.5 eV) and PBE0 theory level. We have use one representation for the same crystal orbital symmetry. These two functionals functionals presented the same symmetry orbitals.

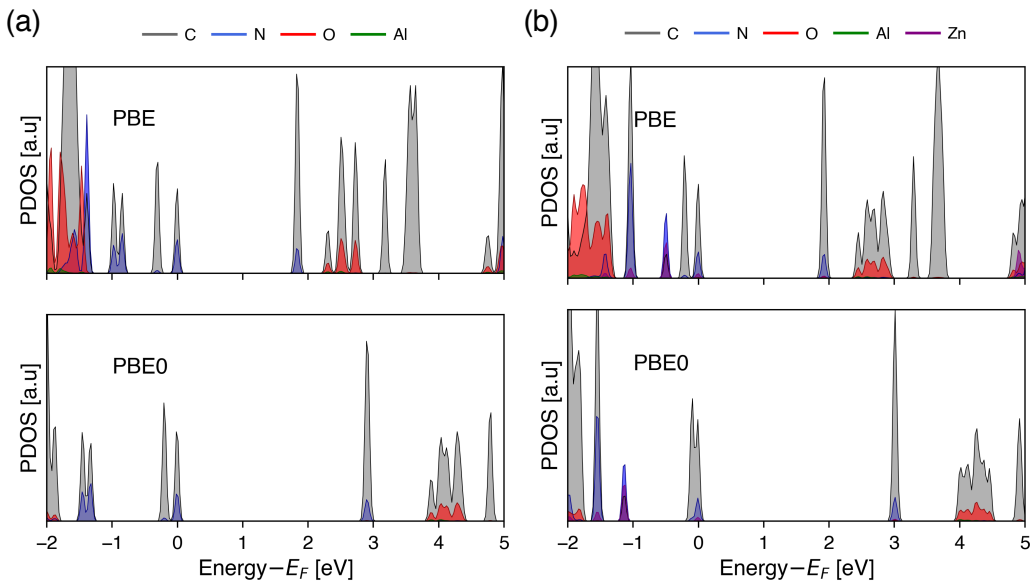

Figure 1.27 – Projected density of states of (a) Al-PMOF and (b) Zn-Al-PMOF using PBE and PBE0 XC functionals.

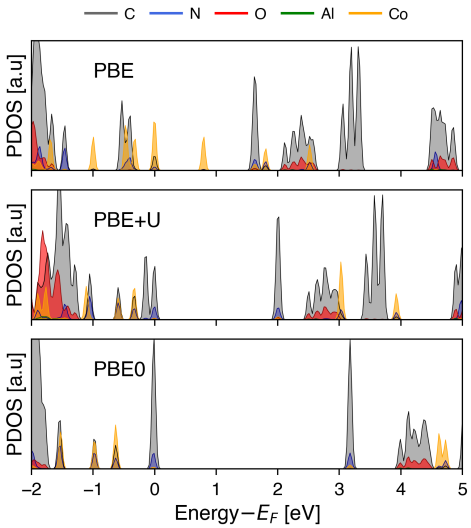

Figure 1.28 – Projected density of states of Co-Al-PMOF using PBE, PBE+U and PBE0 XC functionals.

2 Insights into the electronic properties and charge transfer mechanism of a porphyrin ruthenium-based Metal-Organic Framework

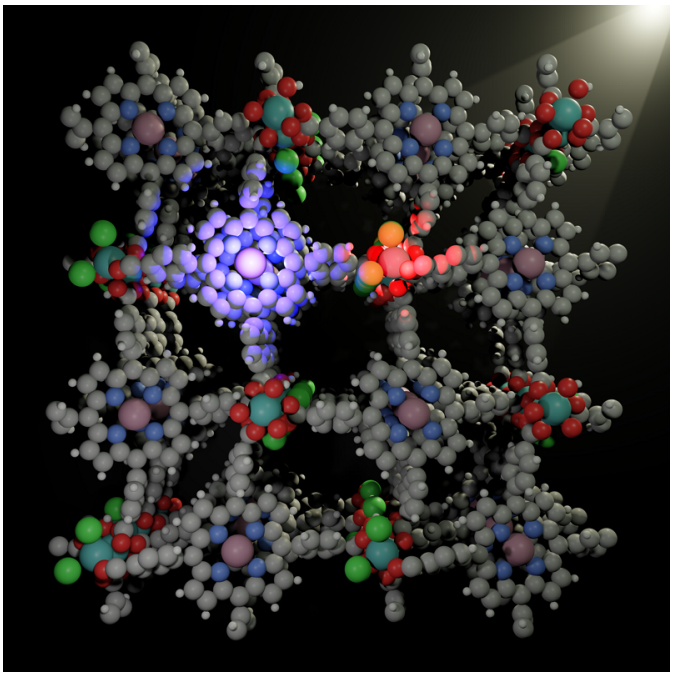

[a] postprint version of the article published as: Andres Ortega-Guerrero, Maria Fumanal, Gloria Capano, Ivano Tavernelli, and Berend Smit Chemistry of Materials 2020 32 (10), 4194-4204 DOI: 10.1021/acs.chemmater.0c00356. A O-G conduced all the calculations and analysed the data and together with M.F. and B.S. wrote the manuscript with the contribution from all authors.

2.1 Abstract

Recently, a porphyrin ruthenium-based MOF (Ru-TBP-Zn) has shown highly efficient co-catalyst-free photocatalytic hydrogen evolution reaction(HER) under visible light in neutral water. However, a detailed molecular understanding of the electronic and optical properties is missing. In this work, we have conducted Density Functional Theory (DFT) simulations to study these properties in Ru-TBP-Zn. Our DFT calculations indicate instability in the experimentally reported structure of Ru-TBP-Zn. Such instability is resolved by proposing two structural models where Cl^- or OH^- anions are coordinated with the metal backbone of Ru-TBP-Zn. Based on these models, the electronic and optical properties in Ru-TBP-Zn are analyzed. UV/Vis spectra calculations allow identifying the importance of the charge-transfer bands. According to our simulations, two possible charge transfer mechanism can co-exist: the direct photo-induced electron transfer from the porphyrin to the ruthenium upon light absorption, and the relaxation from the optically excited porphyrin to the low-lying ligand-to-metal charge-separated state. The interaction energy of the photo-generated electron-hole carriers is computed considering hole-phonon-electron contributions according to the polaron model. Our calculations predict a repulsive electron-hole interacting energy indicating a low electron-hole recombination rate, which is a prerequisite for multi-electron transfer processes such as HER. The understanding of the electronic properties and charge transfer mechanism in Ru-TBP-Zn paves the way for designing efficient porphyrin-based MOFs for photocatalysis.

2.2 Introduction

Hydrogen production is a promising technology that has attracted attention as an environmentally safe energy source [196, 152]. Metal-organic frameworks (MOFs) based catalysts are promising candidates for photocatalytic applications, including electrocatalytic, photocatalytic, and chemocatalytic HER[224]. The unique characteristics of MOFs are related to their porous structure and the tunability of their modular chemical structure, which offers an almost unlimited number of combinations of organic ligands and metal centres. In the context of the development of novel efficient photocatalytic materials, MOFs offer the versatility of combining an organic photosensitizer with an inorganic semiconductor [195]. This ensures the visible light absorption of the material and facilitate the transfer of the light-generated electrons to the nearby metal nodes [195]. For instance, the optical properties of the photocatalytic Ti-based MIL-125 MOF can be tuned through organic linker functionalization [58]. The incorporation of $BDC-(NH_2)_2^{-2}$ (BDC = benzene 1,4-dicarboxylate) linkers shifts the absorption profile into the visible region. The new material known as MIL-125-NH_2, has shown remarkable H_2 generation when combined with nickel phosphide (Ni_2P) nanoparticles, enhancing the photocatalytic activity of this system [100]. MIL-125-NH_2 demonstrates the importance of the linker selection in the photophysical properties in MOF. Therefore, a common strategy to improve the absorption profile of MOFs is the use of chromophores such as porphyrin, with absorption spectra in the visible region. As an example, the well-known

aluminum porphyrin-based MOF (Al-PMOF) has been shown to undergo HER under visible light illumination when combined with platinum nanoparticles as co-catalyst [79]. In this context, the photophysical properties of MOF-based photo-catalysts can be improved by the successful combination of light-harvesting linkers with appropriate metal nodes.

To promote photocatalytic activity, the metal nodes could function as a mediator of the electron transfer process towards the surface of a co-catalyst, or ideally act themselves as the catalytic centers in a co-catalyst-free setup [128, 192, 196]. Within this strategy, Lan *et al.* [113] reported two new MOFs, Ru-TBP, and Ru-TBP-Zn, based on diruthenium secondary building units and porphyrin-derived tetracarboxylate ligands (Figure 2.1). These MOFs have been designed for HER to exploit the light-harvesting and catalytic properties of porphyrin and ruthenium, respectively. Remarkably, it was reported that Ru-TBP-Zn is capable of efficient visible-light-driven HER in neutral water[113]. To unravel the light-harvesting mechanism Lan *et al.* [113] compared the cyclic voltammograms and photoluminescence of the MOF with the isolated Ru paddle wheel and porphyrin ligands. Based on the similarities of the cyclic voltammograms and spectra Lan *et al.* concluded that the MOF has a similar mechanism as the isolated Ru paddle wheel, namely a multi-electron injection from the porphyrin group to the Ru backbone of the MOF. However, a detailed molecular understanding of the porphyrin-to-ruthenium charge transfer mechanism from quantum mechanical simulations is still missing. In this work, we develop a theoretical framework that allows us to systematically study the different mechanisms of charge transfer for this large open-shell system.

For the Ru-TBP-Zn system, like in many other MOFs, the XRD data do not allow for a full assignment of the structure. Our calculations suggest two possible crystal structures of Ru-TBP-Zn. More importantly, the different structural and electronic properties of the proposed materials have a profound impact on the electron transfer mechanism, and hence on their photocatalytic activity. Interestingly, our calculations indicate that the different possible mechanisms of charge transfer should also become detectable experimentally. However, with the help of our simulations, we are now in the position of determining, in a systematic way, the electronic and structural changes undergoing the electron transfer process with atomistic resolution.

2.3 Results and discussion

2.3.1 Ru-TBP-Zn Structure

The reported structure of Ru-TBP and Ru-TBP-Zn have a rod-like backbone composed by Ru(III) atoms in two coordination environments: one is tetrahedrally coordinated to four carboxylate oxygen atoms, and the other is octahedrally coordinated to four carboxylate oxygen atoms and two water molecules[113] (Figure 2.1). The porphyrin ligands in Ru-TBP have a Ru(III) metal centre coordinated with DMF, whereas the porphyrin group in Ru-TBP-Zn has a Zn(II) metal centre. Both materials have a formula of $[Ru_2(TBP{-}Ru{-}DMF)(H_2O)_2]Cl_3$

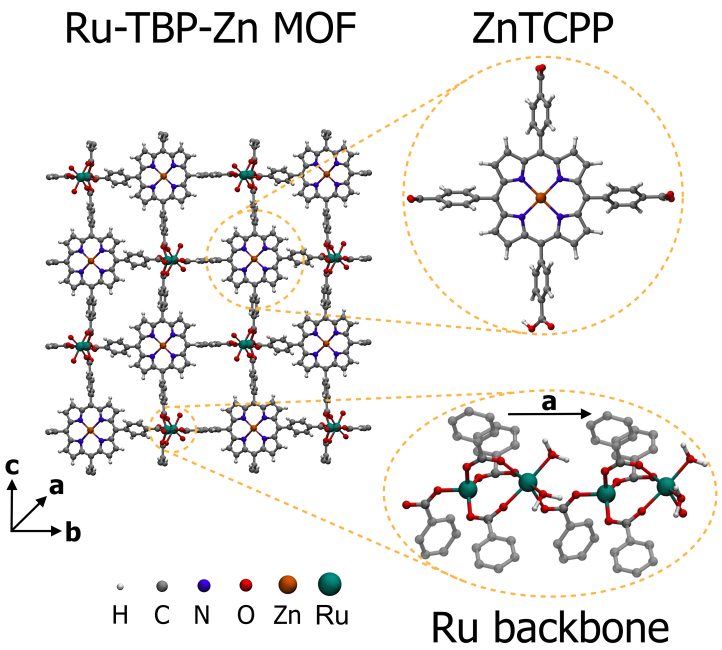

Figure 2.1 – Molecular representations of the Ru-TBP-Zn MOF composed of Zinc(II) meso-tetra(4-carboxyl-phenyl) porphyrin (ZnTCPP) ligands and one-dimensional ruthenium backbones view along the a- axis. Color code: H white, C grey, N blue, O red, Zn brown, Ti green.

and $[Ru_2(TBP{-}Zn)(H_2O)_2]Cl_2$, respectively. The Cl^- ions are present to compensate for the charge of the Ru(III) atoms, however, as is common in these materials they were not resolved by single-crystal X-ray powder diffraction (XRD)[113]. The crystallographic unit cells of Ru-TBP and Ru-TBP-Zn are composed of two porphyrins and two Ru dimers, which results in a total charge of +6 and +4, respectively, according to X-ray absorption near edge structure (XANES) measurement of the oxidation state[113].

PBE, PBESol, and PBE0 DFT calculations including D3-BJ Grimme dispersion correction were conducted to optimize the atomic coordinates and cell parameters of Ru-TBP and Ru-TBP-Zn (See Methods). Considering that Ru-TBP and Ru-TBP-Zn are isostructural[113], the Ru-TBP-Zn structure was modeled based on the crystal structure reported of Ru-TBP. The calculations with charged systems without the inclusion of counterions did not yield stable structures. Implicit Cl^- ions were included for additional cell optimization calculations, but similar instabilities were obtained. In particular, the Ru-Ru distance is reduced considerably and the carboxylate groups of the tetrahedral Ru(III) atom adopt a trigonal bipyramidal geometry. The use of GGA and hybrid functionals during optimization led to an unreasonable reduction of the box volume (by more than 60% the volume), together with a distortion of the cell parameters (as the structure is not stable).

It is quite common in MOFs that the resolved crystal structures (available through the databases) are not exactly equivalent to the ones obtained from and energy minimization using DFT. One typically observes a small shift in the positions of the hydrogen atoms and (small) changes

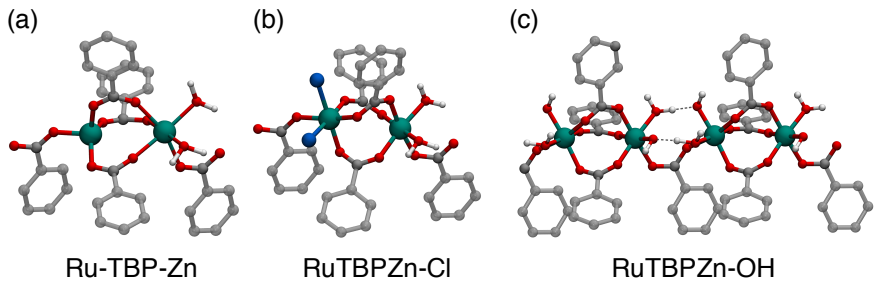

Figure 2.2 – Backbone coordination structures (a) XRD Ru-TBP-Zn. One Ru is tetrahedrally coordinated to four carboxylate oxygen atoms and the other Ru is octahedrally coordinated to four carboxylate oxygen atoms and two water molecules. (b) RuTBPZn-Cl and (c) RuTBPZn-OH systems proposed in this work. The tetrahedrally ruthenium atom is completed by Cl and OH anions, respectively. Oxygen atoms are shown in red, hydrogen in white, chlorine in blue, carbon in gray, and ruthenium in cyan. Hydrogen atoms in the aromatic rings are omitted for clarity.

in the cell parameters. However, in our case, we could not obtain a stable structure for Ru-TBP-Zn, despite the attempts described above. In general, Ru(III) coordination systems do not present a coordination number of 4; instead, they present a coordination number of 6[114]. This raises the question of whether Ru(III) is stable in tetrahedral coordination. A simple way to address this question is to search in the Cambridge Crystallographic Data Centre (CCDC)[72] for similar structures. If Ru(III) is stable in tetrahedral coordination, one would expect to find many occurrences. However, only two examples of MOF materials in the CCDC were found to have a Ru atom in tetrahedral-like coordination.

The two examples are the current material of study (Ru-TBP) and a Zn-MOF with a partial site-selective post-synthetic modification of one Zn atom for Ru[11]. During the post-synthetic modification the tetrahedral Zn(II) node was replaced by Fe^{3+}, Cu^{2+}, Co^{2+}, and also Ru^{3+} metal ions. However, Bajpai *et al.* [11] reported that in the case of Fe^{3+} and Ru^{3+}, there must necessarily be a counter-chloride anion, which is not observed by XRD. If this counter ion would have been observable in the XRD, we most likely would have not identified this structure. Altogether, our DFT calculations and the lack of previously reported Ru(III) structures with a coordination number of 4, indicate that the tetrahedral coordination of Ru(III) in Ru-TBP MOF is unstable.

The average Ru-Ru bond distances of paddlewheel complexes are within 2.2 and 2.5Å[186]. Based on the Ru-Ru distance of the backbone (3.84 Å) of Ru-TBP, the Ru dimer is not in a paddlewheel configuration, instead, the Ru dimer in the unit cell can be stabilized by solvent molecules or counterions. We considered the experimental stoichiometry of Ru-TBP-Zn ($[Ru_2(TBP{-}Zn)(H_2O)_2]Cl_2$), including two Cl^- ions[113]. This structure, named RuTBPZn-Cl, is obtained by changing the tetrahedral Ru(III) atom coordination into an octahedral form. The Cl anions in the Ru-TBP-Zn unit cell were placed such that each ruthenium dimer is symmetrical to each other. As an alternative structure, we also considered the possible ligand

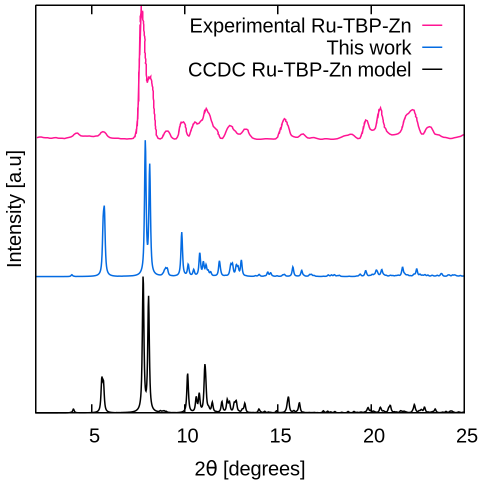

Figure 2.3 – PXRD patterns: experimental Ru-TBP-Zn measurements from Lan *et al.* [113](pink), the simulated pattern of our proposed structure RuTBPZn-Cl (blue), and the simulated pattern of Ru-TBP-Zn structure (black) from Lan *et al.* To clarify, the latter is a model using the reported experimental structure of Ru-TBP as starting configuration, due to both structures are isostructural.

substitution of the two chloride ions with OH groups, named RuTBPZn-OH. Although, the initial configuration has both OH groups located in the same Ru atom, during the geometry and cell optimizations a proton transfer between the two Ru-centers occurs. In this case, the most energetically stable configuration for RuTBPZn-OH is where each Ru(III) is octahedrally coordinated to four carboxylic groups, one water, and one OH group. As a consequence, a hydrogen-bond network along the ruthenium backbone chain is formed. Figures 2.2b and 2.2c show the backbone coordination structures of RuTBPZn-Cl and RuTBPZn-OH proposed in this work. It is important to highlight the decision on the proposed models is to solve the instability of Ru-TBP-Zn structure found in our DFT calculations. We consider Cl^- ions as they appear in the experimental stoichiometry. Also, the possible exchange of Cl^- by OH^- ions is considered as the system is immersed in neutral water. These ions balance the charge of the system and complete the octahedral coordination of the Ru atoms. We did not consider any other anionic ligands, based on the reactants and solvents present in the synthesis protocol of Ru-TBP-Zn. However, other anionic ligands could in principle be coordinated to the Ru backbone to stabilize the system. Figure 2.3 shows the comparison between the Powder X-ray diffraction (PXRD) profiles of the reported experimental structure of Ru-TBP-Zn (Experimental measurement and the computed one), and our proposed structures. It can be observed that the peaks between 5 and 10 degrees in our structures present a good agreement with the experimental measurements. The two high peaks around 7.5 degrees are closer to each other after the inclusion of the Cl or OH ligands to the ruthenium cluster, in contrast to the experimental proposed structure of Ru-TBP-Zn, which shows slightly more separated peaks. Since both models (RuTBPZn-Cl and RuTBPZn-OH) are based on the completion of the Ru backbone of the experimentally reported structure, negligible differences are obtained

between the PXRD calculations of these models and the computed one from the structured of Ru-TPZ-Zn deposited in CCDC. Overall, our DFT calculations indicate that both RuTBPZn-Cl and RuTBPZn-OH structures are stable and are in good agreement with the experimental PXRD pattern of Ru-TBP-Zn[113] (see Figure 2.3). Table 2.1 presents a comparison between the cell parameters of the experimental structure of Ru-TBP and the results of our DFT calculations. A small contraction of the cell volume is observed between the experimental and the optimized structures (less than 5%), both PBE and PBE0 functionals lead to an average difference of 2.5% in unit cell volume. This is the effect of the known under/over estimation of DFT functionals missing expansive thermal effects[136].

Table 2.1 – Experimental lattice parameters of RuTBP, and calculated lattice parameters for RuTBPZn-Cl and RuTBPZn-OH at the PBE and PBE0 theory level

Source	Volume (Å^3)	a (Å)	b (Å)	c (Å)	α (°)	β (°)	γ(°)
RuTBP							
CCDC model	4554	8.732	22.947	22.807	90.743	93.980	92.211
RuTBPZn-Cl							
PBE	4219	8.743	21.723	22.255	87.691	92.399	90.988
PBE0	4176	8.684	21.738	22.148	87.638	91.321	89.653
RuTBPZn-OH							
PBE	4209	8.631	21.891	22.303	87.686	91.260	90.701
PBE0	4155	8.566	21.812	22.266	88.021	91.759	90.539

The relative stability between the RuTBPZn-Cl and RuTBPZn-OH MOF structures was computed considering the appropriate balance between the energies of the MOFs and the isolated ligands (OH and Cl ions, respectively). RuTBPZn-OH structure is predicted to be −2.59 eV more stable than RuTBPZn-Cl, for each Cl^- to OH^- ion exchange. It is noteworthy that the RuTBPZn-OH system has a hydrogen bonds network along the ruthenium backbone (Figure 2.2c) which might increase the ground state stability of this system. The simulations and the PXRD comparison suggest that Ru-TBP-Zn MOF is a dynamic system where solvent interaction might play a key role in the stability and structure of the system. Our simulations highlight the importance of analyzing the metal coordination environment in MOFs and help in determining possible completion models of the Ru backbone structure of Ru-TBP-Zn.

2.3.2 Electronic properties

The presence of open-shell Ru(III) atoms in the structure of the Ru-TBP-Zn requires the definition of the total magnetization of the unit cell. The ground state spin configuration was determined by testing different total magnetization and orientation in RuTBPZn-Cl. Because of the one-dimensional pattern of the ruthenium backbone (See Figure 2.1), a supercell along vector a is required to account for the magnetic interactions between consecutive ruthenium dimers. Figure 2.4 shows the different cases considered. The energy difference between the different magnetic configurations is of the order of 30 meV (Table 2.3). Cases 1 and 2 in Figure 2.4 are the most stable ones. Additionally, we considered cases were Ru(III) atoms

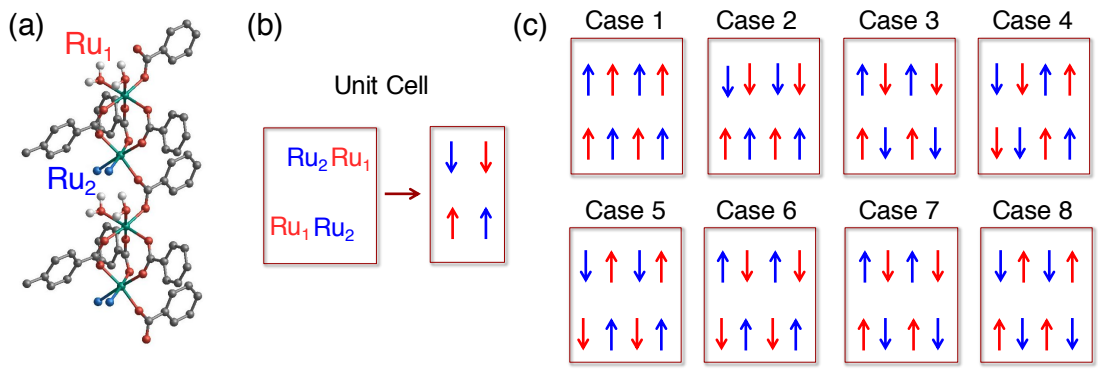

Figure 2.4 – (a) RuTBPZn-Cl ruthenium backbone in 2x1x1 supercell. Ru_1 (red) and Ru_2 (blue) are the two coordination environments, with H_2O and Cl^- ions, respectively. (b) Spin configuration in a single unit cell. (c) Spin configuration cases tested with the 2x1x1 supercell.

were assumed to be in a high-spin (HS) state; however, these were discarded since they are energetically unfavorable in comparison with the low spin (LS) state of Ru(III). The HS-LS energy difference of Ru(III) was of the order of 5 eV. In the following, we have selected the lowest energy magnetic state, which is the antiferromagnetic singlet orientation shown in Case 2 of Figure 2.4. We did not further consider Case 1 due to its large associated magnetic moment and to the lack of experimental studies of the magnetic properties on Ru-TBP-Zn that would support such exceptional large magnetization.

To analyze the electronic properties of RuTBPZn-Cl and RuTBPZn-OH structures we use PBE0 hybrid functional. Although hybrid functionals offer an accurate prediction of the electronic structure properties of materials[64], the fraction of the Hartree-Fock (HF) exchange is a tuning parameter[108, 133]. To prevent any artifact from our results, we optimized the percentage of HF exchange where generalized Koopmans' condition is enforced [133](See Supporting Information). The amount of HF exchange to be corrected is almost negligible and has no significant effects on the description of the projected-density-of-states (PDOS) of RuTBPZn-Cl and RuTBPZn-OH, displayed in Figure 2.5a. It can be seen that both in RuTBPZn-Cl and RuTBPZn-OH, the porphyrin molecules contribute to the valence band maximum (VBM). On the one hand, the valence band of RuTBPZn-Cl presents an energy gap between the states associated with the ruthenium backbone and the ones localized on the porphyrin ligands. On the other hand, in RuTBPZn-OH the ruthenium-backbone valence states mix with the porphyrin local states. The conduction band of RuTBPZn-Cl shows two main bands fully localized in the Ru backbone (Figure 2.8). In contrast, the CBM of RuTBPZn-OH is a mixture between Porphyrin and Ru-backbone partially localized orbitals (Figure 2.9). Interestingly, the Cl^- to OH^- functionalization of the Ru-backbone in Ru-TBP-Zn leads to an increase of the electronic bandgap of the material while functionalizing the organic ligands in previously reported MOFs has the opposite effect[86, 209, 166]. In the latter, the valence band orbitals localized on the organic ligands are affected by the functionalization, while the orbitals from the transition metals remain mainly unperturbed. In contrast, in Ru-TBP-Zn, the Cl^- to

OH^- functionalization affects the Ru-backbone orbitals, which mainly constribute to the conduction band and leaves the porphyrin bands unaffected. The difference in the localization nature of the PDOS of RuTBPZn-Cl and RuTBPZn-OH is thus attributed to the ligand exchange from Cl^- to OH^- that is directly affecting the ligand-field on the ruthenium atoms. In the case of RuTBPZn-Cl, the Ru orbitals appear well below in energy than the porphyrin orbitals. In the case of RuTBPZn-OH, despite that the Ru orbitals remain below the porphyrin orbitals, they are mixed with the porphyrin orbitals. This can be associated with the different electronegativity of both ligands (Cl^- and OH^- ions) and the hydrogen bond network along the backbone present in RuTBPZn-OH. The electronic bandgap predicted for RuTBPZn-Cl and RuTBPZN-OH is 2.03 and 2.75 eV, respectively, both in agreement with described semiconducting nature of Ru-TBP-Zn in the visible range observed by Lan *et al.* [113].

The unique electronic properties of Ru-TBP-Zn can be rationalized based on its PDOS. In particular, because of the presence of Ru-backbone states within the porphyrin states in the conduction band. This feature is not common in porphyrin MOFs. Usually, in porphyrin MOFs, the electronic and optical properties are mainly determined by the properties of the porphyrin linker as in the case of Al-PMOF[79, 7] and PCN-222[44]. The d^5 electronic configuration of Ru(III) ions with one unpaired electron, and the rod-like structure of the Ru backbone results in low-lying Ru-backbone localized states that dominate the CBM of the PDOS of Ru-TBP-Zn. Similar findings have been reported as well by the doping of Fe(III) in the Al-backbone of Al-PMOF[7].

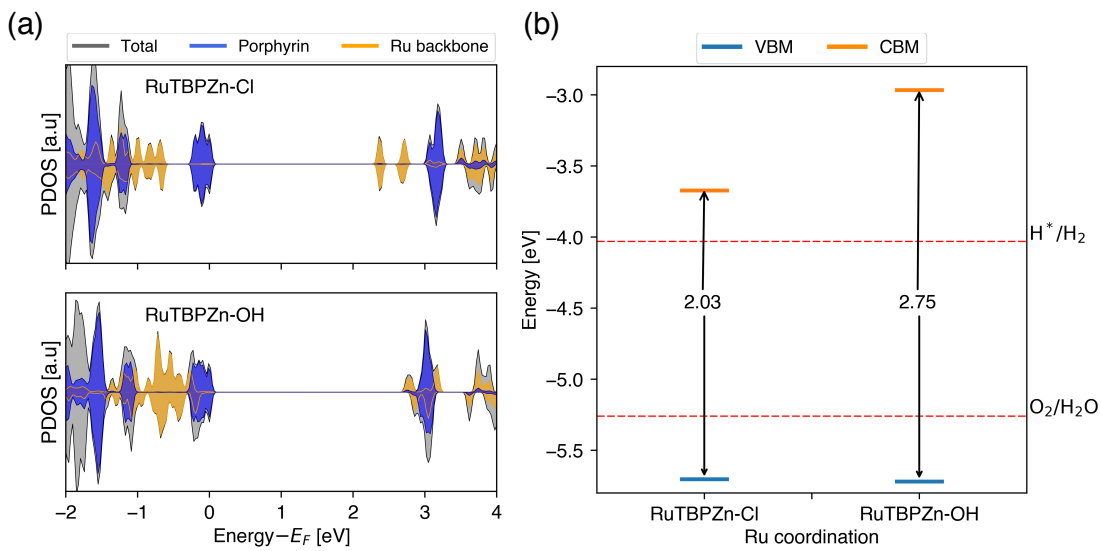

Figure 2.5 – (a) Projected spin density of states of RuTBPZn-Cl and RuTBPZn-OH , alpha and beta spin electrons are in the top and bottom, respectively. (b) Energy diagrams of Bandgaps and the band edge positions with respect to the vacuum potential computed at the pore centre. The dashed lines are redox potentials of water splitting. PBE0 where generalized Koopmans' condition is enforced was used for RuTBPZn-Cl and RuTBPZn-OH.

The total or partial spatial localization of the VBM and CBM in the porphyrin and Ru-backbone,

respectively, allows anticipating a low-lying ligand-to-metal charge transfer (LMCT) excitation from porphyrin to Ru-backbone in both RuTBPZn-OH and RuTBPZn-Cl. These results are in agreement with the luminescence and time-resolved photoluminescence experiments by Lan *et al.* [113]. This charge transfer excitation will promote spatial electron-hole separation via the injection of an electron from the porphyrin to the Ru(III), following the mechanism proposed for the catalytic cycle of HER in Ru-TBP-Zn[113]. To address the photo-redox capabilities of RuTBPZn-Cl and RuTBPZn-OH, we compared the position of their band edges with the redox potential for water photolysis[191, 91] (see Figure 2.5b). Since the experiments on Ru-TBP-Zn were conducted on neutral water [113], we consider the hydrogen evolution reaction (HER) and oxygen evolution reaction (OER) levels located at −4.0 and −5.26 eV, respectively. Our calculations show the CBM above the HER level and the VBM below the OER level, making both systems thermodynamically suitable for photocatalytic water splitting in a neutral pH environment, in agreement with the efficient visible-light-driven HER observed in Ru-TBP-Zn[113].

2.3.3 Optical properties

The photocatalytic process at the basis of the conversion of solar energy into a chemical fuel (such as molecular hydrogen) begins with photon absorption. Light absorption properties in MOF can be usually determined by the photophysical properties of its ligands. Ru-TBP-Zn has porphyrin ligands which are natural photosensitizers with light absorption in the visible region[115]. To understand the optical excitations in Ru-TBP-Zn, we have computed the first 35 excitations of RuTBPZn-Cl and RuTBPZn-OH using linear-response time-dependent DFT(LR-TDDFT) with PBE0 functional optimized to satisfy Koopman's condition. The calculated vertical excitations energies and their oscillator strengths in the two periodic systems are collected in Table 2.5 and 2.6. In both systems, the main character of the first optically active excitations is ligand centered porphyrin-to-porphyrin. The excited states of porphyrin molecules can be explained by the Gouterman four-orbital model [70]. According to this model, the excitations are characterized by $\pi \rightarrow \pi^*$ transitions from the HOMO, HOMO-1 to the LUMO, LUMO+1 orbitals in the isolated porphyrin molecule. Porphyrins absorb strongly in the 400–450 nm range (Soret or B band) and weakly in the 500–700 nm region (Q band)[115]. Our LR-TDDFT periodic calculations show that RuTBPZn-Cl and RuTBPZn-OH first absorption band has the same character as the Q bands in porphyrin. This agrees with the experimental UV/Vis optical spectra of Ru-TBP-Zn where the character of the optical gap is associated with the porphyrin Q bands. Additionally, RuTBPZn-Cl presents low-lying charge transfer excitations from the porphyrin to the Ru orbitals after the Q bands (See Table 2.5 and Figure 2.8), the energy of which is close to the value of the Kohn-Sham band gap predicted from the ground state calculations. The presence of low-lying charge-transfer states agrees with the proposed photocatalytic cycle where the porphyrin ligand is excited and can transfer one electron to the ruthenium dimer [113]. In contrast, RuTBPZn-OH does not present low-lying charge transfer excitations within the explored energy range. Note that the lowest $\pi \rightarrow \pi^*$ porphyrin transitions in RuTBPZn-Cl and RuTBPZn-OH appear lower

in energy than the $\pi \rightarrow Ru$ charge-transfer excitations, despite being the conduction band contribution of the porphyrin higher in energy than that of the Ru-backbone (Figure 2.5a and Figure 2.14). This highlights the importance of considering excitonic effects when addressing local and charge-transfer excited states in molecular-based systems such as MOFs. Excitonic effects are particularly strong in organic molecules[109]. The optical gap in porphyrin ligands described by $\pi \rightarrow \pi^*$ transitions , presents a big reduction due to excitonic attraction between the photo-generated electron and hole[109].

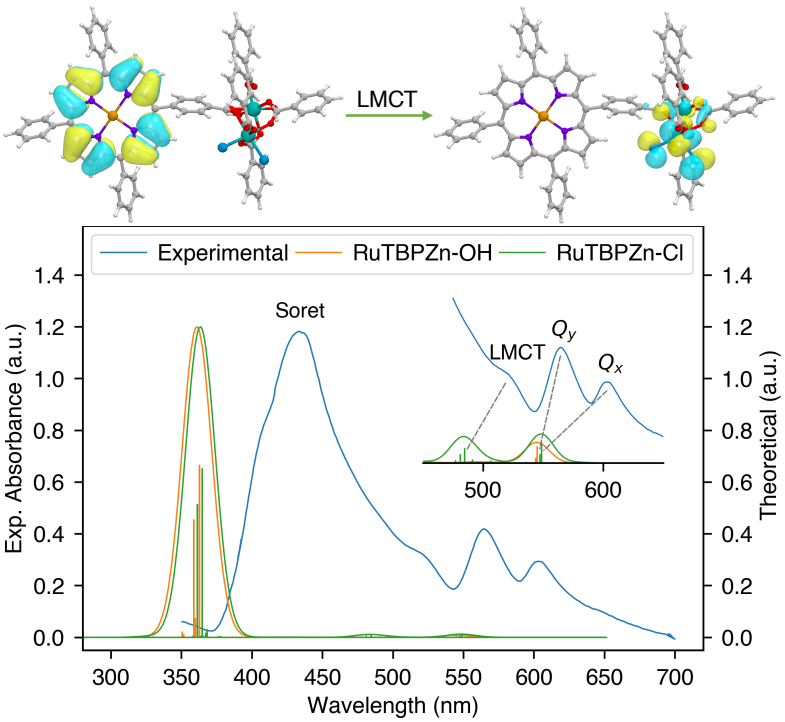

Figure 2.6 – Experimental UV-visible absorption spectra of Ru-TBP-Zn (blue) (taken from [113]) compared with the CAM-B3LYP TDDFT calculations on the cluster models for RuTBZn-OH (Orange) and RuTBPZn-Cl (Green). Inset: enlarged spectra of the Q and LMCT bands.(Molecular orbitals of the corresponding LMCT state).

In order to access the full optical spectra, reduced-size representative models of RuTBPZn-Cl and RuTBPZn-OH were used. Cluster models can significantly reduce the computational cost and allow the use of a high level of theory to describe the optical properties of MOFs[145, 87, 209]. The representative models consist of a porphyrin ligand with a ruthenium dimer of the backbone (Figure 2.13). The comparison of the PDOS between the cluster models and the periodic systems validate the transferability of the results (Figure 2.14). Considering the known failures of TDDFT with charge-transfer excitations, we used the CAM-B3LYP functional to compute absorption spectra. This functional can capture the physics of charge screening and therefore is intrinsically better suited for describing charge-transfer states[109]. Figure 2.6 presents a comparison of the reported experimental UV/Vis optical spectra of Ru-TBP-Zn[113] and the LR-TDDFT calculations on the RuTBPZn-Cl and RuTBPZn-OH clusters models at

the CAM-B3LYP level. The theoretical spectra are normalized to match the experimental Soret peak absorbance (maximum peak). It can be seen that the LR-TDDFT optical spectra are blue-shifted in comparison with the experimental ones. The difference between the experimental and LR-TDDFT spectra for the absorbance of the Soret and Q bands originated due to two factors. First, the molecule-like behaviour of a cluster model in comparison with the periodic MOF structure. Second, the use of the CAM-B3LYP functional in the calculations(See Supporting Information). However, by using this functional, we avoid any misinterpretation of the calculated ordering of the excitation states with the experiments [112]. The nature of the most intense excitations is summarize in Table 2.7 and 2.8. The most intense peak at 363 nm is associated with the porphyrin Soret band, while the lowest peak located at 548 nm corresponds to the two degenerate porphyrin Q bands. The latter will split only when considering vibrational coupling, giving rise to the two non-degenerate bands shown in the experimental absorption spectra[121]. A close inspection of the experimental optical spectra shows an additional peak around 520 nm in between the porphyrin Soret and Q bands. The calculations suggest that the broadening of the Soret band and this additional peak originate from a charge transfer excitation from the porphyrin to the Ru dimer (Figure 2.6 and Table 2.7). In particular, the RuTBPZn-Cl cluster model predicts a charge transfer band with an oscillator strength of the same order as the Q bands. Figure 2.6 depicts the orbitals associated with the charge transfer state. The RuTBPZn-OH cluster model does not show any optical active charge transfer band in the UV/Vis range, in agreement with the calculations performed for the periodic crystals. This can be explained by the energy shift of the conduction band associated with the Ru-backbone upon Cl^- to OH^- substitution (Figure 2.5a and Figure 2.14), which results in a destabilization of the charge transfer state to higher energies. Overall, the LR-TDDFT calculations suggest two different charge transfer mechanism in our proposed models. In the case of the RuTBPZn-Cl system, a porphyrin-to-Ru electron transfer can occur as a direct photo-induced charge transfer generating charge carriers via light absorption. In contrast, the electron transfer will be promoted in RuTBPZn-OH only via non-adiabatic relaxation of the optically excited porphyrin[41]. Note that although the charge transfer state is higher in energy at the optimized geometry, structural relaxation following photo-excitation may lead to stabilization and eventually to a crossing with the lower-lying intra-porphyrin excitations. Taking into account that Ru-TBP-Zn MOF is a dynamic system, our results indicate that both charge transfer mechanisms can take place in this material. It is worth mentioning that the optical spectrum of Ru-TBP-Zn differs from other porphyrin-based MOF thanks to the appearance of low-lying ruthenium orbitals within the conduction band. Whereas porphyrin-MOFs present the UV/Vis spectra dominated by porphyrin Soret and Q bands[79, 116, 44], Ru-TBP-Zn has a significant broadening of the spectrum with a characteristic charge transfer peak in the visible range (See Figure 2.6 - LMCT band).

2.3.4 Electron-hole relaxation

Photon absorption on photo-catalytic materials results in optical excitation in which electrons in the valence band are excited to the conduction band, generating electron-hole pairs[196].

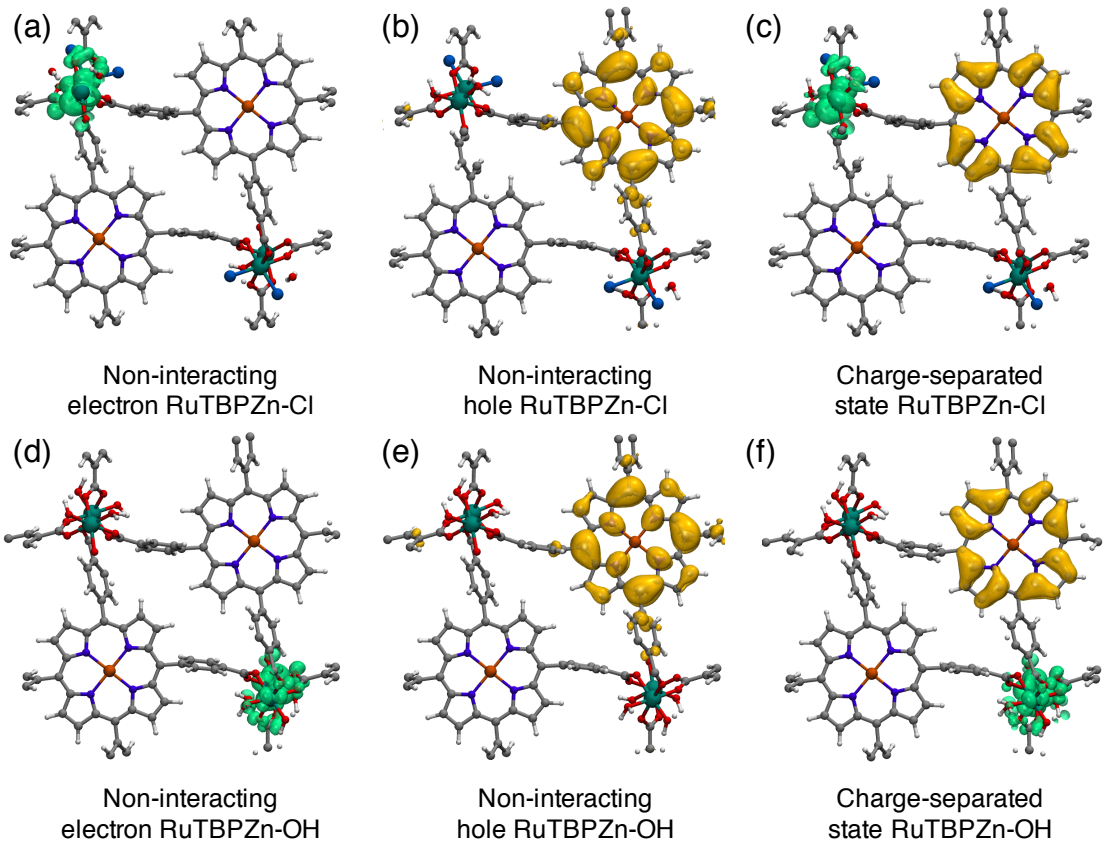

Figure 2.7 – Isosurface representation of the densities of the electron (green) and hole (orange) in RuTBPZn-Cl and RuTBPZn-OH. (a) , (b) , (d) and (e) are the non-interacting polaron geometry relaxations. (c) and (d) are the interacting electron-hole calculations, calculated using CDFT.

The response of the material to these photo-generated charges is a deformation of the lattice to screen them. The electron and the hole in a polar material interact with each other via an electron-phonon-hole mediated interaction (polaronic exciton [2]). A significant contribution to the interaction between such photo-generated carriers results from interference between their structural atomic relaxation patterns. As a result, oppositely charged polarons may experience an intermediate-range repulsion, this effect can be very important for the recombination kinetics of electrons and holes[48] their lifetime[138]. To study the interaction energy of the charge-transfer state between the porphyrin and the ruthenium backbone in Ru-TBP-Zn, we have study the non-interacting and interacting polarons. The interaction of the photogenerated carriers is estimated as

$$E_{int} = E_{e-h} - (E_{e^-} + E_{h^+}) \tag{2.1}$$

where E_{e^-} and E_{h^+} are the relaxation energies of the non-interacting electron and hole polarons, respectively, computed in two independent setups. E_{e-h} is the relaxation energy of

the photo-excited state where the electron and hole polarons are now interacting [82, 73]. All relaxation energies are calculated as the energy difference between the relaxed and unrelaxed structures. Note that E_{e^-} and E_{h^+} correspond to the polaron binding energy where the energies have not been corrected for finite-size effects. Finite-size effects are expected to be small in our case since the dependence of the binding energy on the lattice constant L goes as $1/\epsilon_0 L$ where ϵ_0 is the static dielectric constant[106]. We also consider supercell calculations, which confirm our interpretation based on the minimal setups (See Supporting Information). We have studied the hole polaron (electron removal) and the electron polaron (electron addition) in RuTBPZn-Cl and RuTBPZn-OH by performing full structure geometrical relaxations of the charged systems. These polarons represent the non-interacting charge carriers of the polaronic excited state in the Ru-TBP-Zn. Figures 2.7a and 2.7d, and Figures 2.7b and 2.7e show the isosurface electronic density of the electron and hole injections calculations, respectively, computed for RuTBPZn-Cl and RuTBPZn-OH. In both systems, the electron charge localizes in the Ru backbone, and the hole charge localized in the porphyrin ligand. The localization of the electron polaron in the ruthenium backbone could be beneficial for photo-conduction since it has been observed that photo-conductivity in MOFs arises mainly from rod-like structures along the inorganic building unit[197]. Similarly, in Figure 2.7c and 2.7f we show the isodensity representation of the interacting electron-hole density wavefunction (in the neutral system) in RuTBPZn-Cl and RuTBPZn-OH, respectively. Both systems were optimized using constraint DFT (CDFT) through localizing the hole in the porphyrin ligand and the electron in the ruthenium atom, leading to a charge-separated state. Table 2.2 summarizes the relaxation and interaction energy of the photoexcited charge carriers. On the one side, the results predict an attractive interaction ($-0.252\ eV$) between the charge carriers in RuTBPZn-OH that will favour the electron-hole recombination. In contrast, the computed interaction energy of the electron-hole pair is repulsive in RuTBPZn-Cl (0.160 eV), promoting a long-lived polaron.

Table 2.2 – Relaxation energy of the hole polaron E_{h^+}, electron polaron E_{e^-}, the electron-hole pair E_{e-h}, and the interaction energy E_{int} of the electron hole charge carriers evaluated in the periodic and cluster model systems.

	MOF RuTBPZn		Cluster RuTBPZn	
Energy eV \ System	Cl	OH	Cl	OH
E_{h^+}	-0.190	-0.407	-0.960	-0.097
E_{e^-}	-0.217	-0.471	-1.188	-0.735
E_{e-h}	-0.247	-1.130	-0.441	-0.946
E_{int}	0.160	-0.252	1.707	-0.114

The interaction energy of the photo-excited charge carriers was also computed using the reduced-size representative clusters to confirm the nature (attractive versus repulsive) of the electron-hole interaction (see Figure 2.18). In that case, E_{e-h} was computed as a geometry relaxation of the LMCT (from the porphyrin to the Ru dimer) excited state within the TDDFT framework[62, 171], which allows the simulation of the interacting electron-hole pair. The results are collected in Table 2.2. RuTBPZn-OH cluster model results in an attractive electron-hole interaction ($-0.114\ eV$) while the RuTBPZn-Cl cluster model results in a re-

pulsive interaction (1.707 eV), in agreement with the periodic calculations described above. Altogether, the repulsive interaction of the photo-generated charge carriers predicted for RuTBPZn-Cl can be associated with a long electron-hole lifetime beneficial for multi-electron transfer processes, such as HER [152]. In addition to the charge carrier localization in the ruthenium backbone, these characteristics will significantly promote the catalytic process in comparison to other systems.

2.4 Conclusions

Motivated by the recent synthesis of a porphyrin ruthenium-based MOF (Ru-TBP-Zn) capable of photocatalytic HER in neutral water [113], we report ab-initio simulations that provide fundamental insights into the unique electronic and optical properties of this material. Our computational study showed that the experimental structure was incomplete. We propose two possible structures, which differ in the type of anion coordinated to the Ru ion in the Ru-TBP-Zn backbone, and which are both in agreement with the available experimental data. Interestingly, the nature of the anion (Cl^- versus OH^-) has an impact on the charge transfer mechanism. In the case of RuTBPZn-OH, electron injection from the porphyrin to the Ru backbone will occur via non-adiabatic relaxation of the optically excited porphyrin. On the other hand, in RuTBPZn-Cl, a photo-induced electron transfer from the porphyrin to the ruthenium backbone might also happen, which reduces the recombination probability. In addition, our calculations showed that the electron-hole interaction in RuTBPZn-OH is attractive, while it is repulsive in RuTBPZn-Cl. From a catalytic point of view, both the repulsive electron-hole interaction as well as the photo-induced electron transfer mechanism make the RuTBPZn-Cl a better catalyst. Therefore, we expect that the performance of the material will increase if one can ensure, e.g., through ion exchange, that OH ligands in the ruthenium backbone are replaced by Cl^- ions.

Our study reveals that the optical and electronic properties in Ru-TBP-Zn are different from “normal" porphyrin MOFs. In most porphyrin MOFs these properties are dominated by the porphyrin unit only. Our study shows that in Ru-TBP-Zn the interplay between the ruthenium backbone and the porphyrin changes the electronic and optical properties in such a way that makes the material better for photocatalysis. The key design criterion is to ensure that frontier bands of the metal are placed below the ones of the conduction band of porphyrin and hence facilitating the electron transfer to the ruthenium backbone. With this understanding, we can envision the creation of similar “electron catchers" in other porphyrin systems.

2.5 Methods

2.5.1 Models

Starting from the known experimental single-crystal X-ray structure of RuTBP[113], the two periodic structures of Ru-TBP-Zn with complete coordination, namely RuTBPZn-Cl and

RuTBPZn-OH, were built by adding two Cl^- and two OH^- ions, respectively, to the coordination of the tetrahedral Ru atom. Additionally, the Ru atom coordinated with Dimethylformamide in the porphyrin ligands was replace by Zn ions.

2.5.2 Periodic simulations

The two periodic structures were fully optimized using periodic DFT implemented in the CP2K code[97, 111]. The optimized structures were obtained using a three-stage protocol: First we optimized the geometry following the atomic gradients on the potential energy surface, then we performed a short MD (Molecular Dynamics) simulation to make sure that the system did not get trapped in a local minimum[148], and finally we optimized the cell parameters along with all atomic coordinates. The MD consisted of 100 steps of 0.5 fs each in a canonical ensemble at 300K using the CSVR thermostat[21]. PBE[158] and PBE0[1, 75] exchange-correlation functionals with DFT-D3 van der Waals corrections with Becke-Johnson damping were used throughout[176]. The Truncated Coulomb operator with a long-range correction was employed for the Hartree-Fock exchange. The truncation radius is half of the smallest edge of the unit cell, and the long-range part of the exchange is computed using the PBE exchange. The CP2K calculations used mixed Gaussian and plane-wave basis sets in combination with Goedecker-Teter-Hutter (GTH) pseudopotentials[69]. The double-ζ polarization MOLOPT basis sets were used to describe H, C, N, O and Cl atoms, while a triple-ζ was used for Zn, and Ru atoms. PBESol functional[161] was considered as well for the cell optimization of the experimental proposed structure. In addition, for the PBE0 calculations, the auxiliary MOLOPT-ADMM basis functions[74] were used: cFIT11 for Zn and Ru, and pFIT3 for non-metal atoms. A plane-wave energy cutoff of 600 Ry was used, and the calculations were done using the gamma point over the irreducible Brillouin zone.

We optimized the percentage of HF exchange where generalized Koopmans' condition is enforced in our systems [133](See Supporting Information). The description of the Density of states and band gap is computed for 2 x 1 x 1 supercell structures. To align the conduction and valence band energies with vacuum, the methodology proposed by Butler *et al* [22] was used to calculate the vacuum level in the periodic systems. This method consists of evaluating the average potential within a small sphere at the pore centre.

LR-TDDFT scheme including the Tamm-Dancoff approximation[90] was used to predict the excited state properties of the periodic systems using the unit cell. The HF percentage used in these calculations is the one found with the Koopmans' condition for the unit cell studies (Figure 2.11a and Figure 2.12a). Given the CP2K implementation, the long-range correction is not included with the LR-TDDFT module. Due to the large computational cost of using a hybrid XC functional, only the first 35 states were computed.

Constrained DFT (CDFT) simulations were used to obtain the non-interacting hole polaron and interacting charge-separation states in the periodic systems. The geometry optimizations were performed using the Becke density partitioning scheme [93]. The Becke cell boundaries

are adjusted to lead to physical partial charges. For Ru, Cl, O and Zn the Shannon & Prewitt's ionic radii was used (0.82, 0.99, 0.60 and 0.74 Å) [172]. For C and N the covalent radii were used (0.77 and 0.75 Å). Two kinds of H atoms were defined: the first one is for H atoms in the metal cluster (H_2O and OH), and the rest involving the organic ligand. The former used the ionic radius while the later the covalent one.

The calculations on the electron-hole relaxations were conducted on the single unit cell to reduce the computational cost. The non-interacting polarons are obtained considering charged periodic systems where the charge is neutralized by a charge background that does not affect the charges and forces. The non-interacting hole polaron has one constraint defined as the porphyrin having one unpaired alpha electron (therefore leaving a hole in beta). CDFT was used in this case to localize the hole in a single porphyrin ligand. All atoms of the porphyrin were considered when defining the constraint. The interacting charge-separated state has two constraints: one porphyrin has a hole, while the ruthenium cluster has an extra electron. A screening threshold of 10^{-7} was employed to construct the Gaussian confinement cavity. The constraint convergence criterion was set to 10^{-2} e. Element cutoff radii were set to 3.5 Å for all elements.

2.5.3 Cluster simulations

From the optimized crystal structures of RuTBPZn-Cl and RuTBPZn-OH, two representative model clusters containing one single porphyrin ligand and one dimer Ru cluster were defined. These clusters were designed to preserve a good representation of the electronic properties of the periodic system. To mimic the solid-state framework, constrained geometry calculations were performed where the aromatic C atoms and two carboxylic groups from the ruthenium backbone are held fixed. DFT geometry optimization calculations on the clusters were performed in Gaussian 16.0[56], using the PBE0 XC functional. The 6-31G* basis set[164] was used for H, C, N, O, and Cl, while the LANL2DZ basis set[83] with pseudopotentials was employed for Ru and Zn. The absorption spectrum was computed considering the full linear response TDDFT using the CAM-B3LYP XC functional[214]. Natural Transition Orbitals (NTO) analysis[129] was conducted to have a better understanding of the optical excitations and their character.

2.6 Supporting Information

2.6.1 Ground state magnetization

The proper spin configuration was determined by testing different total magnetization and orientation. The presence of 1D Ru channels in the system requires the consideration of a supercell.

Table 2.3 – Differences of the electronic energy of the spin-configuration states considered at the PBE and PBE0 levels of theory, for the 2x1x1 supercell of RuTBPZn-Cl.

System	PBE [meV]	PBE0 [meV]
Case 1	0.18	6.33
Case 2	0.00	0.00
Case 3	367.9	17.3
Case 4	80.4	28.3
Case 5	312.3	14.2
Case 6	365.7	54.1
Case 7	215.5	8.7
Case 8	370.3	13.67

2.6.2 Ground state orbitals

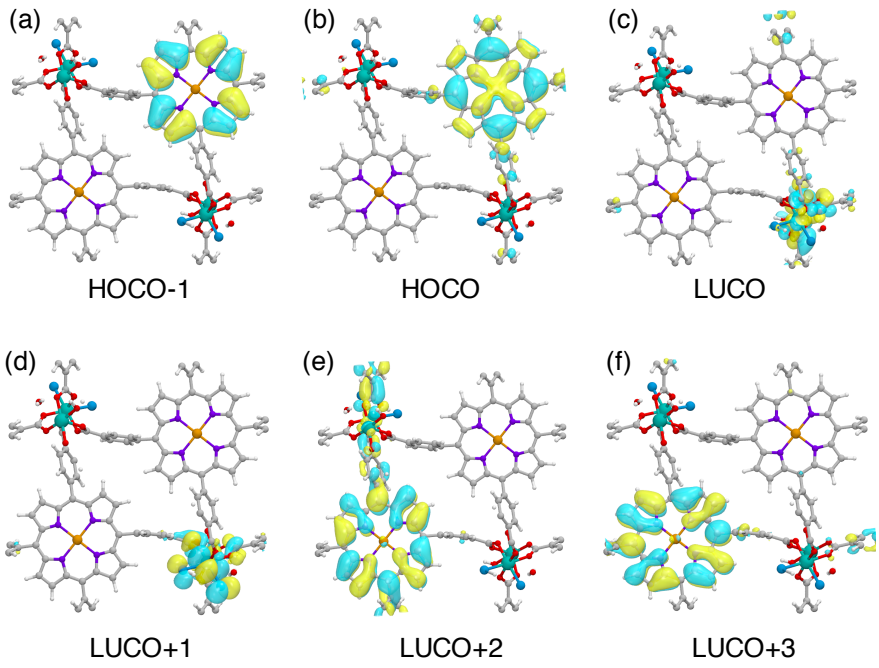

Figure 2.8 – RuTBPZn-Cl Crystal Orbitals.

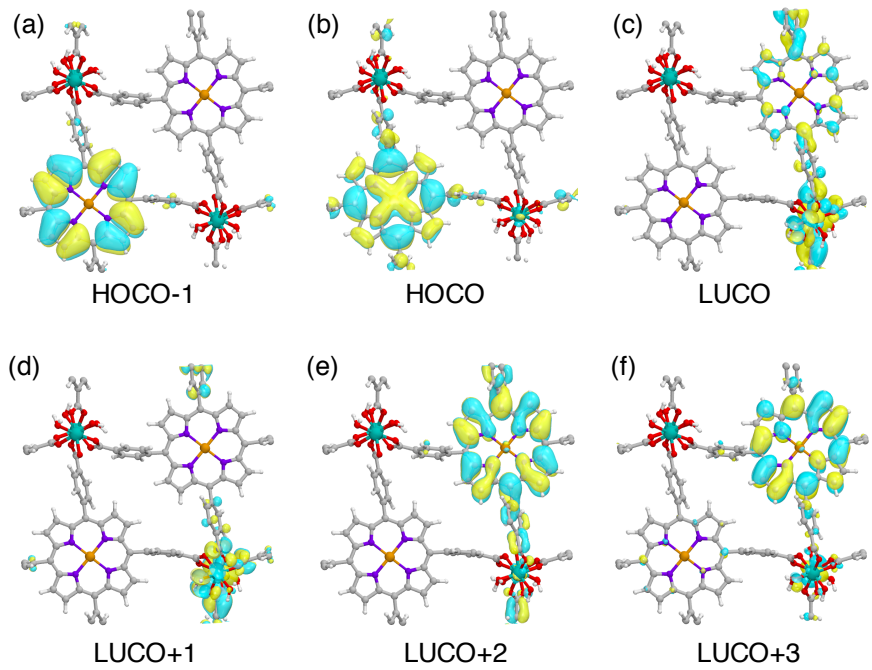

Figure 2.9 – RuTBPZn-OH Crystal Orbitals.

2.6.3 Exchange correlation functional test

The partial density of states (PDOS) using different exchange-correlation (XC) functionals of RuTBPZn-Cl and RuTBPZn-OH models is displayed in Figure 2.10. The PBE functional predicts the properties of the system as a metallic material. The strong correlation nature of the d electrons in Ru influences the electronic properties, that PBE is not able to describe. This failure of generalized gradient approximations(GGA) functionals, as PBE, has been observed in metal oxides[132], such as Iron Oxides. One corrective approach is the use of the DFT+U scheme where a Hubbard effective potential can be added to the d orbitals of the Ru atoms. Single point calculations test using DFT+U were used to study the density of states. The Hubbard correction U_{eff} was only applied to the Ru atoms using a value of 4.10 eV. This U-value was taken from ref. [168] which is used to describe Ru(III) atoms. For these calculations, the Lowdin orbital method is used. Figure 2.10 shows the effect of the DFT+U method. In RuTBPZn-Cl, the porphyrin molecules contribute to the valence band maximum (VBM) while the Ru backbone contributes to the conduction band minimum (CBM). In contrast, the CBM is a mixture between porphyrin and Ru backbone orbitals in RuTBPZn-OH. Despite the bandgap correction of the DFT+U method, a limitation emerges since the correction only affects Ru d-orbitals leaving the porphyrin orbitals unaffected. To overcome such limitation, we considered the use of hybrid functionals. We have used PBE0 and optimized the percentage of the Hartree-Fock (HF) percentage where the generalized Koopmans' condition is enforced in our systems [133](See Koopmans-based HF percentage determination, Supporting information). The amount of HF exchange to be corrected is almost negligible and has no main effect on the

description of the DOS in our system.

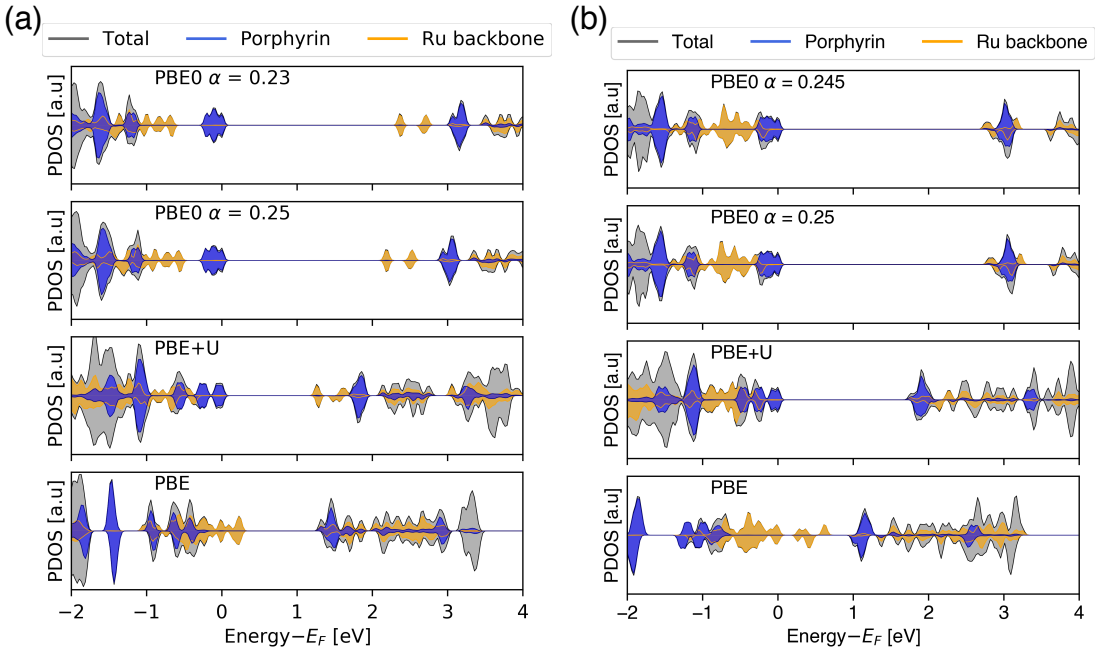

Figure 2.10 – Density of state calculated using different exchange correlation functionals. (a) RuTBPZn-Cl , (b) RuTBPZn-OH.

2.6.4 Koopmans-based HF percentage determination

For the proper description of the electronic properties of the periodic systems, the generalized Koopmans' condition is enforced [160]. For our calculations, we consider the implementation of PBE0-TC-LRC in CP2K[75]. Which contains a parameter α corresponding to the fraction of Hartree Fock exchange. To determine the α parameter we used the method describe by G. Miceli *et al* (2018) [133]. Since the Koopmans' condition stays that the ionization potential of a system with N electron is identical to the electron affinity of the system with $N-1$ electrons. Two geometry optimization injecting a hole and electron in the periodic systems were considered. To impose localized electronic states, the optimization was conducted using an α parameter of 0.45. Using the relaxed structures, single-point calculations using different α values were considered to enforce the Koopmans' condition.

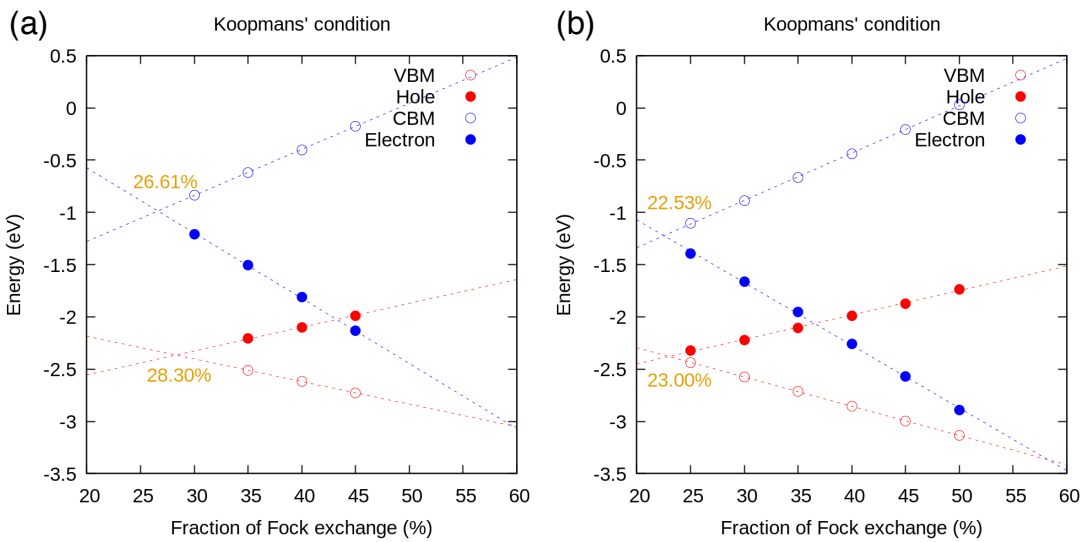

Figure 2.11 – Band edges and single-particle electron polaron (blue) and hole polaron (red) in RuTBPZn-Cl as a function of the Hartree-Fock exchange α used in the PBE0-TC-LRC. The intersection points are the α values for the Koopmans' condition. The dashed lines are extrapolations of energy levels to regions where the charge is not well localized. Using the (a) unit cell and (b) considering a 2 x 1 x 1 supercell extending the ruthenium backbone.

The α parameter to enforce the Koopmans' condition is determined as an average between the $\alpha_{electron}$ and α_{hole}. The calculations performed on the unit cell show the same behavior and a value of 0.275. The supercell calculations presented a value of 0.23 and 0.245 for RuTBPZn-Cl and RuTBPZn-OH, respectively. The description of the Density of states and Bandgap will be reported using the values obtained from the supercell calculations, while the geometry relaxations and LR-TDDFT are conducted using the unit cell given the computational cost of using the supercell.

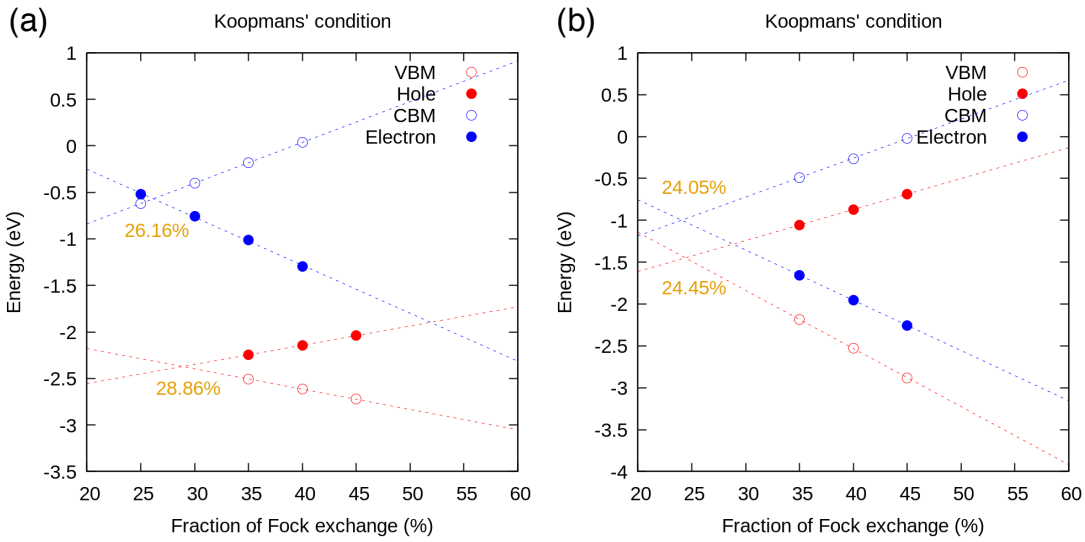

Figure 2.12 – Band edges and single-particle electron polaron (blue) and hole polaron (red) in RuTBPZn-OH as a function of the Hartree Fock exchange α used in the PBE0-TC-LRC. The intersection points are the α values for the Koopmans' condition. The dashed lines are extrapolations of energy levels to regions where the charge is not well localized. Using the (a) unit celland (b) considering a 2 x 1 x 1 supercell extending the ruthenium backbone.

2.6.5 Size effects supercell calculations

Table 2.4 shows the relaxation energy of the electron polaron in RuTBPZn-Cl systems considering the unit cell and a 2x1x1 supercell. The relaxation energy difference in the supercell case is minimum since in both functionals the electron polaron is localized (Self-trapped). The unit cell calculations differ since at the PBE0 level, the electron polaron has a 50%-50% occupation in the two Ru-backbone chains, respectively.

Table 2.4 – Relaxation energy of the electron polaron in the RuTBPZn-Cl periodic systems, using the unit cell and supercell at the PBE0 and PBE0 where generalized Koopmans' condition is enforced.

Functional	Unit Cell (eV)	Supercell (2×1×1) (eV)
PBE0	-0.129	-0.352
PBE0 Koopmans'	-0.271	-0.340

2.7 TDDFT optical spectra

2.7.1 Periodic calculations

The column Transition of the tables shows the percentage contribution from all orbitals involved in the excitations. P are the orbitals localized in the porphyrin core of the ligand and Ru are the orbitals localized in the ruthenium backbone. P+Ru represent orbitals that are

localized on both, i.e., the porphyrin core of the ligand and the ruthenium backbone.

Table 2.5 – Most intense excitation energies for the RuTBZn-Cl as obtained from the LR-TDDFT calculations.

State	Ω eV	Ω nm	f [b]	Transition % [c d]
S17	1.66319	745.460	0.00267	P → P 31.13 , Ru → Ru 66.09
S20	1.77068	700.606	0.00406	P → P 32.30 , Ru → Ru 55.75
S21	1.78173	695.864	0.01211	P → P 90.82 , P → Ru 3.6 , Ru → Ru 4.1
S22	1.81225	684.145	0.00415	P → P 79.24 , P → Ru 8.5 , Ru → Ru 6.59
S23	1.81983	681.295	0.01019	P → P 51.68 , P → Ru 21.49 , Ru → Ru 17.67
S26	1.89445	654.460	0.00303	P → P 32.58 , P → Ru 26.46 , Ru → Ru 22.54
S29	1.96060	632.378	0.00120	P → P 62.79 , P → Ru 4.97 , Ru → Ru 26.59
S32	2.05917	602.107	0.01064	P → P 11.19 , P → Ru 47.19 , Ru → Ru 25.18
S33	2.07785	596.694	0.00511	P → P 2.70 , P → Ru 51.43, Ru → Ru 33.98
S35	2.11018	587.551	0.00955	P → P 3.86, P → Ru 67.02 , Ru → Ru 8.93
S38	2.17223	570.769	0.00298	P → Ru 93.49
S39	2.19846	563.959	0.00320	P → P 6.98, P → Ru 69.80 , Ru → Ru 4.46

Table 2.6 – Most intense excitation energies for the RuTBZn-OH as obtained from the LR-TDDFT calculations.

State	Ω eV	Ω nm	f [a]	Transition % [b c]
S16	1.81876	681.696	0.00211	P → P 40.23 P → P+Ru 17.18 , Ru → Ru 14.13
S17	1.83185	676.825	0.01245	P → P 56.41 P → P+Ru 26.13 , Ru → Ru 16.76
S18	1.85652	667.831	0.00160	P → P 34.74 P → P+Ru 20.55 , Ru → Ru 23.28
S19	1.86236	665.737	0.00711	P → P 72.77 P → P+Ru 25.78
S20	1.88300	658.439	0.00749	P → P 75.97 P → P+Ru 22.55
S21	1.91010	649.097	0.00531	P → P 54.26 P → P+Ru 13.38 , Ru → Ru 11.73
S24	1.96850	629.841	0.00191	P → P 68.91, P → P+Ru 19.63 , Ru → Ru 8.90

2.7.2 Clusters calculations

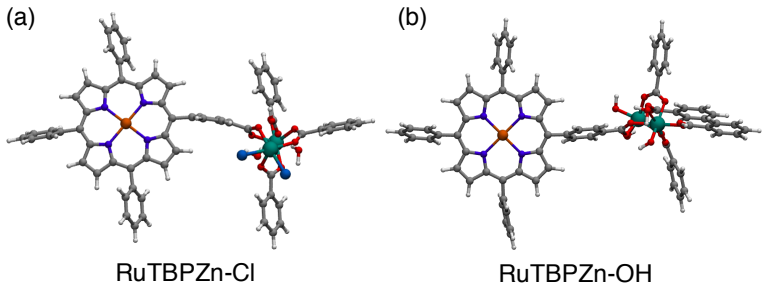

Figure 2.13 – Representative cluster models for (a) RuTBPZn-Cl , (b) RuTBPZn-OH. Oxygen atoms are shown in red, hydrogen in white , chlorine in blue, carbon in gray, zinc in orange and ruthenium in cyan.

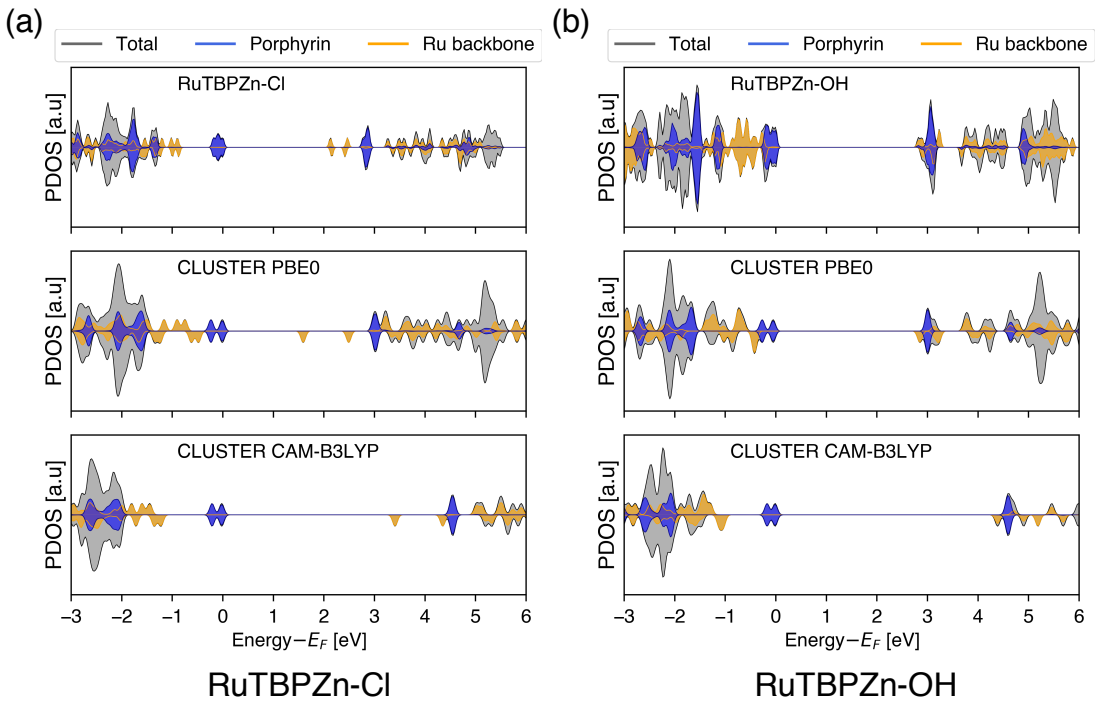

Figure 2.14 – Density of states comparison between the periodic crystal structure (Computed in CP2K) and the cluster model using PBE0 and CAM-B3LYP XC functionals (Computed in Gaussian).

Table 2.7 – Most intense excitation energies for the RuTBZn-Cl cluster model as obtained from the CAM-B3LYP LR-TDDFT calculations.

State	Ω eV	Ω nm	f [e]	S^2	Transition [f]
S16	2.2594	548.75	0.0248	2.008	Q
S17	2.2648	547.45	0.0099	2.008	Q
S22	2.5585	484.60	0.0172	2.086	CT
S24	2.5983	477.18	0.0027	2.079	CT
S27	2.7726	447.17	0.0011	2.070	CT
S45	3.3995	364.71	1.8047	2.040	B
S47	3.4318	361.28	1.4215	2.009	B

Table 2.8 – Most intense excitation energies for the RuTBZn-OH cluster model as obtained from the CAM-B3LYP LR-TDDFT calculations.

State	Ω eV	Ω nm	f [d]	S^2	Transition [e]
S13	2.2761	548.75	0.0183	2.006	Q
S14	2.2808	543.59	0.0052	2.006	Q
S34	3.4204	362.49	1.9179	2.014	B
S39	3.4553	358.82	1.2330	2.027	B

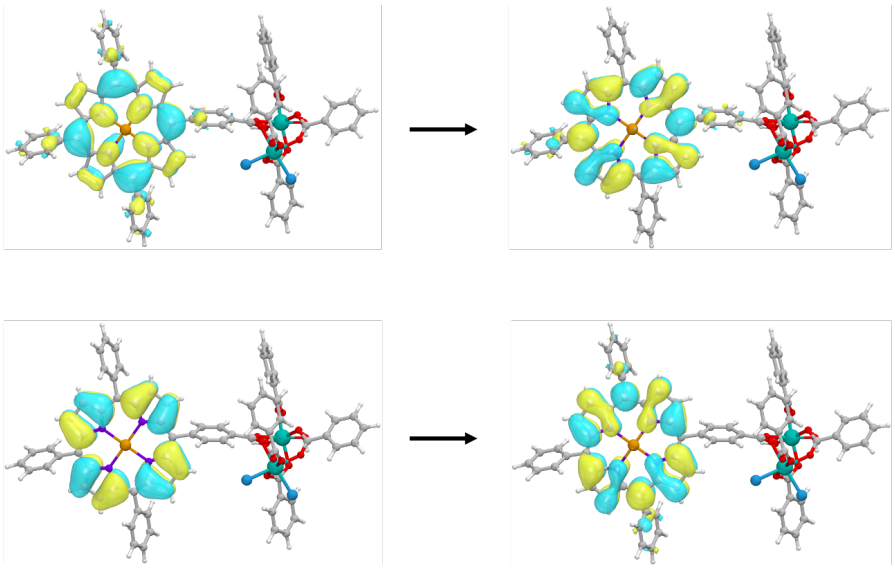

Figure 2.15 – Orbitals involved in the Q and Soret bands excitations in RuTBZn-Cl from the NTO analysis.

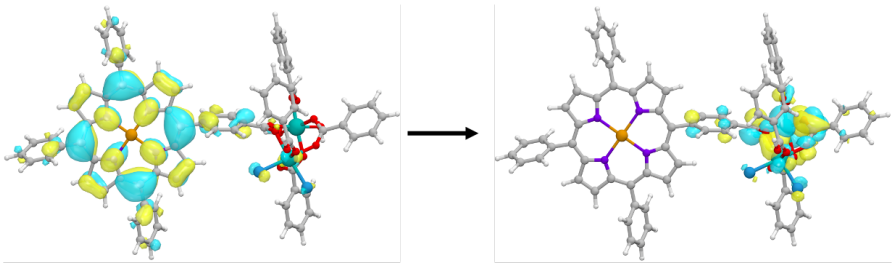

Figure 2.16 – Orbitals involved in the CT state excitations in RuTBZn-Cl from the NTO analysis.

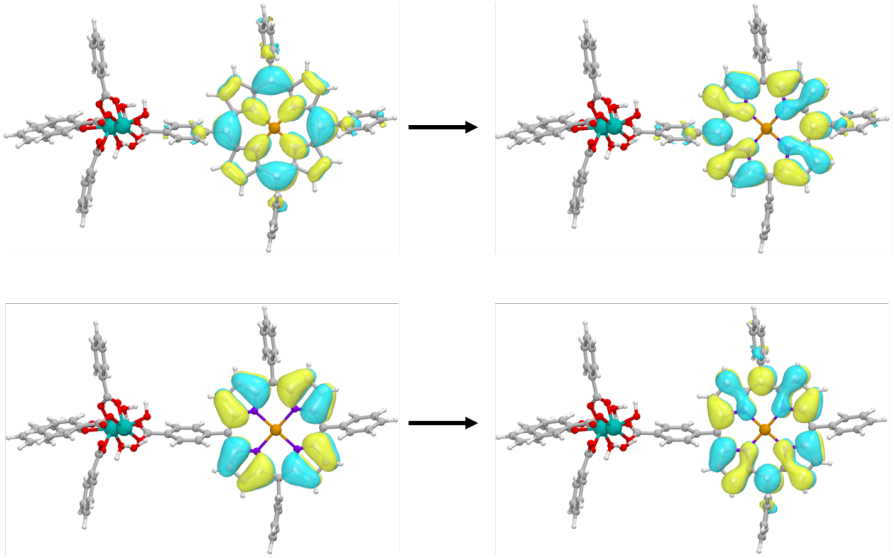

Figure 2.17 – Orbitals involved in the Q and Soret bands excitations in RuTBZn-OH from the NTO analysis.

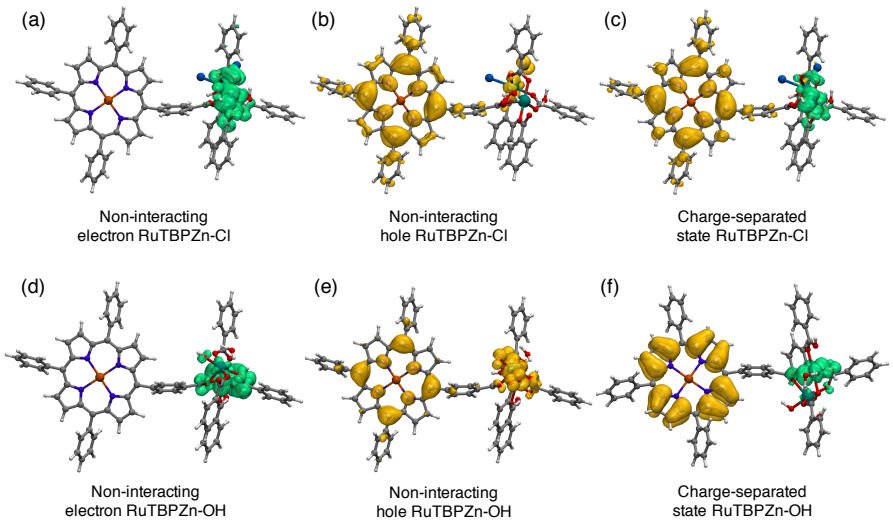

Figure 2.18 – Isosurface representation of the electron density of the electron (green) and hole (orange) in RuTBPZn-Cl and RuTBPZn-OH using the cluster models. (a), (b) and (d), (e) are the non-interacting geometry relaxations of the electron and hole, respectively. (c) and (d) are the interacting electron-hole TDDFT geometry optimization calculations at the PBE0 functional.

PBE0 vs CAM-B3LYP TDDFT spectra comparison

Figure 2.19a shows a comparison of the TDDFT spectra of the RuTBPZn-Cl cluster model computed with PBE0 and CAM-B3LYP. Both LR-TDDFT spectra are normalized to present a maximum theoretical absorbance of 1. It can be observed that the CAM-B3LYP Soret band is blue-shifted in comparison with the results from PBE0. On the other hand, the Q bands in CAM-B3LYP are red-shifted in contrast to the PBE0 calculations. Additionally, the LMCT from the porphyrin to the ruthenium dimer appears at the right side of the Q bands in the PBE0 calculations. This underestimation of a charge-transfer state is a known problem with PBE0 functionals[112]. The difference is the absorbance in the Q bands in both XC functionals comes from the different oscillator strength in the Soret band at the PBE0 and CAM-B3LYP. The latter one presents a higher oscillator strength causing the contrast between Soret and Q bands upon the normalization. The same differences of the Soret and Q bands are conserved in the isolated porphyrin ligand. Figure 2.19b presents a comparison of the experimental UV/Vis spectrum[165] and the TDDFT spectra at the PBE0 and CAM-B3LYP theory level. The theoretical spectra are normalized to match the experimental Soret peak absorbance (maximum peak).

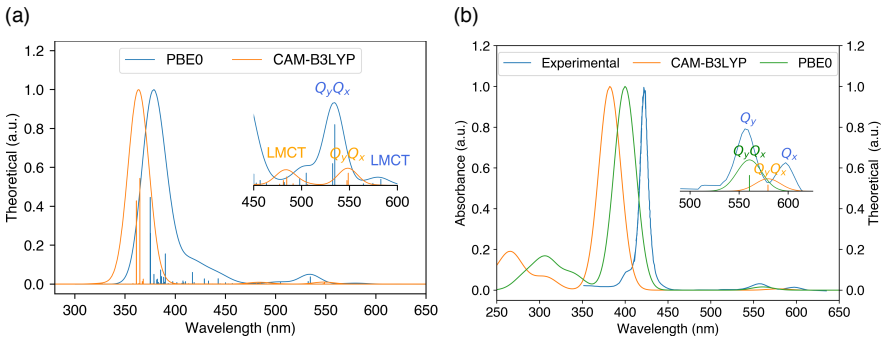

Figure 2.19 – (a) RuTBPZn-Cl cluster model TDDFT spectra using PBE0 and CAM-B3LYP XC functionals (b) Zinc meso-tetra(4-carboxyl-phenyl) porphyrin (ZnTCPP) molecule experimental spectrum (taken from Ref. [165]) vs TDDFT spectra using PBE0 and CAM-B3LYP XC. Insets: enlarged spectra of the Q and LMCT (porphyrin to Ru dimer) bands.

3 Charge Separation and Charge Carrier Mobility in Photocatalytic Metal-Organic Frameworks

[a]

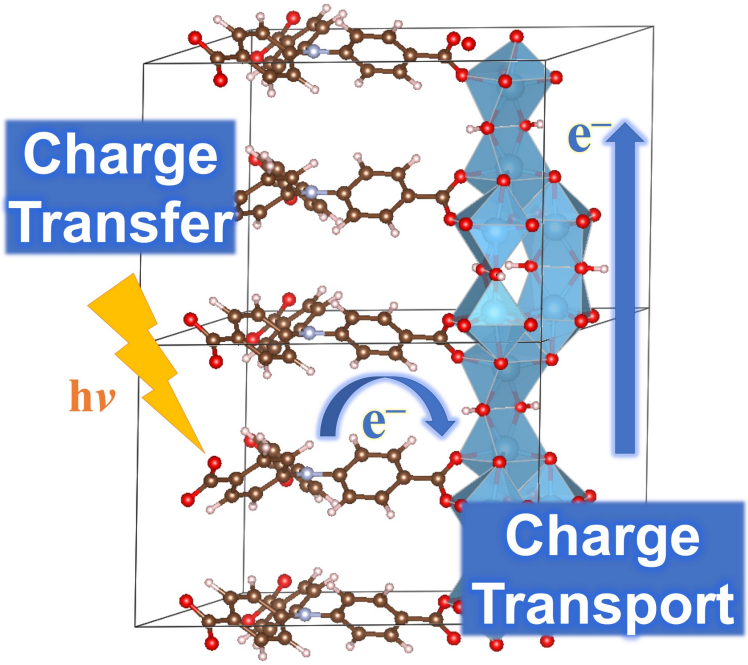

[a]postprint version of the article published as: Fumanal, M., Ortega-Guerrero, A., Jablonka, K. M., Smit, B., Tavernelli, I., Adv. Funct. Mater. 2020, 30, 2003792. https://doi.org/10.1002/adfm.202003792. A O-G contributed to the manuscript with the writing, calculation, and analysis of the bandstructures and charge mobility studies.

3.1 Abstract

Metal-Organic Frameworks (MOFs) are highly versatile materials owing to their vast structural and chemical tunability. These hybrid inorganic-organic crystalline materials offer an ideal platform to incorporate light-harvesting and catalytic centers and thus, exhibit a great potential to be exploited in solar-driven photocatalytic processes such as H_2 production and CO_2 reduction. To be photocatalytically active, UV-visible optical absorption and appropriate band alignment with respect to the target redox potential is required. Despite fulfilling these criteria, the photocatalytical performance of MOFs is still limited by their ability to produce long-lived electron-hole pairs and long-range charge transport. In this work, we establish a cost-effective computational strategy to address these two descriptors in MOF structures and translate them into charge transfer numbers and effective mass values. We apply our approach to 15 MOF structures from the literature that encompass the main strategies used in the design of efficient photocatalysts including different metals, ligands, and topologies. Our results capture the main characteristics previously reported for these MOFs and enable us to identify promising candidates. In the quest of novel photocatalytically active systems, high-throughput screening based on charge separation and charge mobility features is envisioned to be applied in large databases of both experimentally and in silico generated MOFs.

3.2 Introduction

The potential of MOFs as photocatalysts relies on the appropriate combination of visible-light-responsive organic ligands with oxidizing or reducing metal centers.[113] To be photocatalytically active, a MOF material must fulfill two energetic requirements, namely, visible-light absorbance and appropriate band-edge alignment with respect to the desired redox partners. These two characteristics can be associated with two energy-based descriptors that are accessible through electronic structure calculations. In particular, the light-absorption capabilities can be associated with the optical gap of the MOF material[86] and the band-edge energies can be efficiently estimated with respect to the vacuum potential evaluated at the center of the pore.[22]

While the capability of a MOF material to undergo photocatalysis is mainly determined by its visible-light absorbance and band-edge energies, its performance has been directly associated with the lifetime of the photo-generated charge carriers (electrons and holes), as well as with the charge-carriers mobility.[221] The main strategy used to increase the lifetime of the photo-generated charge carriers is to promote spatial charge separation in the low-lying excited states.[27] One possibility is to perform metal substitutions that result in low-lying unoccupied states localized in the metal nodes.[209, 184]

These substitutions lead to low-lying ligand-to-metal charge-transfer (LMCT) states when the highest occupied levels are localized in the organic ligand (Figure 3.1A). It is also possible to stabilize low-lying metal-to-ligand charge-transfer (MLCT) states by combining easily

oxidizable metals and reducible ligands (Figure 3.1B).[226, 95] In both cases, LMCT and MLCT, the photo-generated charges are spatially separated in either the ligand or the metal cluster of the MOF material in favor of long-lived lifetimes and low recombination rates. In contrast, low lying excitations toward ligand-centered (LC) and metal-centered (MC) states (Figure 3.1C,D, respectively) are associated with short and intense emission exploited in photo-luminescent applications.[163, 3] It is worth mentioning that light-induced ligand-to-ligand charge transfer (LLCT) (Figure 3.1E) and metal-to-metal charge transfer (MMCT) (Figure 3.1F) has been reported in MOFs[216, 125] and could also be exploited to enlarge the electron-hole lifetimes.

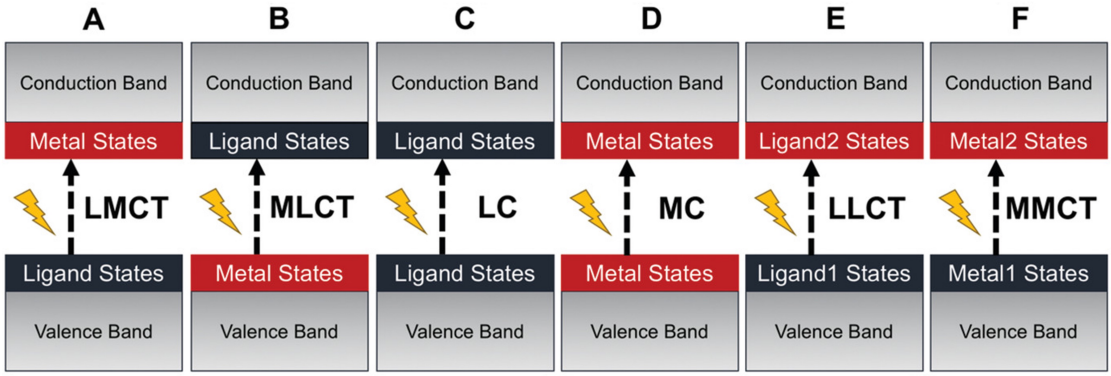

Figure 3.1 – Representation of the four types of low-lying excited states that can be found in MOFs. A ligand-to-metal charge transfer (LMCT), B metal-to-ligand charge transfer (MLCT), C ligand-centered (LC), D metal centered (MC), E ligand-to-ligand charge transfer (LLCT) and F metal-to-metal charge transfer (MMCT) states.

Efficient charge-carriers separation relies not only on the spatial separation of the photo-generated electron-hole pairs upon excitation but also on the available charge transport pathways, that is, photoconductivity. MOFs tend to be poor photoconductors as a result of their porosity and modular nature. The large voids usually lead to a large separation between the redox-active units in the MOF structure, which impedes the through-space interaction and thus, the (hopping) electron transport. In addition, poor organic–inorganic electronic conjugation may also hinder efficient through-bond charge-transport via delocalized conducting bands.[170] Currently, increasing efforts are devoted to developing highly conductive and photoconductive MOFs,[67, 183, 85] with conductivity values up to 103 S cm^{-1}. For instance, it has been shown that MOFs displaying 1D Ti-O chains will facilitate electron mobility.[198, 118] Similarly, high electrical conductivities have been reported for MOF materials consisting of metal ions connected into stacked 2D π-conjugated sheets.[173, 175] The outstanding performance of these systems originates in the dispersion of their electronic band structure,[36] which in turn can be directly related to the effective mass of the charge carriers.[139]

Elucidating the charge separation and charge carrier mobility from electronic structure calculations will not only provide insights into the fundamental properties of MOFs materials but also aid in the discovery of novel systems with improved characteristics for photocatalysis. In this context, high-throughput (HT) screening techniques become particularly useful to

encompass the almost unlimited number of hypothetical structures that can be synthesized from distinct metal-node and organic-linker combinations.[19, 39, 206] To date, tens of thousands of different experimental MOF structures have been reported and collected in extended databases.[137, 35] These databases provide the basis for computational studies devoted to identifying promising materials for different applications,[17] as well as to produce rich data to be exploited for machine-learning purposes.[84] HT screening procedures require the development of automatized computational protocols that translate the desired physicochemical properties into computable descriptors, such as distances, energies or any other quantifiable property. These descriptors need to be computed accurately to be predictive but also at a sufficiently low computational cost such that they are viable for HT screenings.

In a recent paper, a computational protocol was proposed to address visible-light absorbance and band-edge energies using cost-effective density-functional-theory (DFT) methods that can be applied for high-throughput screening of large databases of MOF structures.[61] In this work, we present a computational strategy to evaluate charge separation and charge-carrier mobility in MOF crystals from cost-effective DFT calculations. To do so, we selected 15 MOF structures that have been reported as promising candidates for photocatalysis. We first analyze their light absorption and photo-redox properties in terms of their optical band gap and band-edge energies. Then, we quantify light-induced charge separation by calculating the spatial overlap between the electron and hole densities of the lowest-lying singlet excited state,[156, 157, 155] and discuss three different strategies to estimate it from ground state calculations in large MOF databases. Finally, we address the evaluation of the charge carrier mobility using the electron and hole effective masses within the band transport model.[144] Altogether, our results elucidate the different electronic structure features at the basis of the most common strategies used in the design of MOFs for photocatalysis, namely, visible-light absorption, band-edge adequacy, charge separation, and electron mobility. By considering these four descriptors, we aim to provide a complete picture of the main characteristics required for efficient photocatalysis while presenting a computational procedure that can be used in HT screenings to accelerate the discovery of efficient photocatalytic MOFs.

3.3 Methods

3.3.1 MOF Structure Dataset

15 MOFs structures (herein labeled 15-set) were selected for which photocatalytic activity has been reported or that show promising features for photocatalysis. The chemical composition in terms of metal and ligand subunits, as well as the photocatalytic reaction for which they have been used, are collected in Table 3.1. In this dataset, non-magnetic semiconducting MOFs built from Al(III), Ti(IV), Zn(II), and Zr(IV) metal centers and 11 distinct ligands are considered. Chemically similar systems such as MIL125 and MIL125-NH_2 were included, that share the metal and structural topology but differ in the -NH_2 substitution of the 1,4-benzenedicarboxylate (bdc) ligand. The same applies to UiO66 and UiO66-NH_2, as well as

MOF5 and MOF5-NH2. At the same time, MIL125(-NH_2), UiO66(-NH_2) and MOF5(-NH_2) are built from the same bdc ligand but differ in their metal being Ti(IV), Zr(IV), and Zn(II), respectively. The latter implies also important changes in their structural motifs. MOFZn1 and MOF-74Zn are structurally similar MOFs showing a rod-like framework of Zn(II), but they have different ligands. ZSTU-1 and ZSTU-2 have also similar structural frameworks built from TiO2 1D channels but differ in their ligands. AlPMOF was included as a representative example of a porphyrin-based MOF. MUV11 and NTU-9 are Ti(IV)-based MOFs specifically designed for photocatalysis, as well as the pillared-layer NNU36 Zn(II)-MOF, built from a photo-active bipyridine-anthracene ligand. Finally, Zn_2TTFB was reported to exhibit high charge mobilities through TTF-stacked motifs. Altogether, the different metals, ligands, and topologies of the MOFs considered here cover the main strategies that have been used in the literature to improve the photocatalytic performance of MOFs.

3.3.2 Computational Details

Geometry optimization of the crystal coordinates and cell parameters of all MOFs was performed under periodic boundary conditions with DFT at PBE[158] level including D3 dispersion correction[71] using the CP2K program version 6.1.[97] In all calculations the Goedecker–Teter–Hutter pseudopotentials[69] was used with a density cutoff of 450 Ry and DZVP-MOLOPT basis set for non-metal atoms and TZVP-MOLOPT basis set for Al/Zn/Ti/Zr metal atoms.[189] The optimized cell parameters are collected and compared to the experimental values in Table 3.3, Supporting Information. They show good agreement in all cases. Energy calculations were performed upon the optimized structures at PBE0 level.[50] To reduce the computational cost, the auxiliary density matrix method[74] was used considering the pFIT3 auxiliary basis set for non-metal atoms (3 Gaussian exponents per valence orbital, includes polarization d-functions), the cFIT9 for Al atoms, and the cFIT11 for Zn/Ti/Zr atoms (contracted, 4 s, 3 p, and 3 d shells and 1 f shell in total).

3.3.3 Charge Separation

Linear-response-time-dependent-DFT calculations at PBE0 level were performed in periodic boundary conditions using the Tamm–Dancoff approximation as implemented in CP2K to evaluate the optical gap and to assess the charge separation in the lowest excited singlet state S_1. Only the first three states were computed. The charge separation (also named charge transfer) characterizing S_1 was calculated as the weighted average of the spatial overlap between the Kohn–Sham occupied and virtual orbitals involved in the excitation as [156, 157,

Table 3.1 – Photocatalytically active MOFs studied in this work, labeled as 15-set. Information about the metal and ligand constituent units is given, as well as its use for photocatalysis.

MOF	Metal	Ligand	Photocatalysis	Ref.
AlPMOF	Al(III)	Porphyrin	H2 production	[51]
MIL125	Ti(IV)	1,4-benzenedicarboxylate (bdc)	–	[42]
MIL125-NH_2	Ti(IV)	2-amino-1,4-benzenedicarboxylate	H2 production	[94]
MOF-74Zn	Zn(II)	2,5-dioxido-1,4-benzenedicarboxylate	–	[65]
MOF5	Zn(II)	1,4-benzenedicarboxylate	propene oxidation	[103]
MOF5-NH_2	Zn(II)	2-amino-1,4-benzenedicarboxylate	-	[194]
MOFZn1	Zn(II)	1,2,3-benzotriazole-5-carboxylate	CO2 methanation	[24]
MUV11	Ti(IV)	benzene-1,4-dihydroxamate	H2 production	[151]
NNU36	Zn(II)	9,10-bis(4'-pyridylethynyl)-anthracene and 4,4'-biphenyldicarboxylate	Cr(VI) reduction and dye degradation	[220]
NTU-9	Ti(IV)	2,5-dihydroxyterephthalate	dye degradation	[63]
UiO66	Zr(IV)	1,4-benzenedicarboxylate	-	[30]
UiO66-NH_2	Zr(IV)	2-amino-1,4-benzenedicarboxylate	H2 production	[174]
Zn_2TTFB	Zn(II)	tetrathiafulvalene(TTF)-tetrabenzoate	-	[140]
ZSTU-1	Ti(IV)	4,4',4"- nitrilotribenzoate	H2 production	[118]
ZSTU-2	Ti(IV)	1,3,5-tris(4-carboxyphenyl) benzene	H2 production	[118]

155]:

$$\Lambda = \frac{\sum_{i,a} \kappa_{ia}^2 O_{ia}}{\sum_{i,a} \kappa_{ia}^2} \tag{3.1}$$

where κ_{ia} are the coefficients or amplitudes associated with a given occupied-virtual pair

contribution and O_{ia} is the spatial overlap between these occupied and virtual orbitals, which is given by the inner product of the moduli of the two orbitals as

$$O_{ia} = \langle |\varphi_i| \, | \, |\varphi_a| \rangle = \int |\varphi_i(r)||\varphi_a(r)| dr \tag{3.2}$$

The spatial overlap O_{ia} has been also computed between the highest occupied crystal orbital (HOCO) and lowest unoccupied crystal orbital (LUCO) of the ground state singlet, triplet and charged doublets following the three schemes described in the Results.

3.3.4 Charge Carrier Effective Mass

To evaluate the photoconductive properties and the mobility of the charge carriers band structure calculations were performed for the 15-set structures at the PBE level in the CP2K implementation. The reciprocal space path within the first Brillouin zone (BZ) was computed connecting the high-symmetry points using the Seek-path package.[89] 50 points integrated between each high-symmetry point in the whole path were used. The integration of the BZ was conducted at the Γ-point. The band structure was also computed using a Monkhorst–Pack special Γ-centered k-point grid of 2 × 2 × 2 to sample the BZ. The results show no difference with the Γ-point band structure calculations (Figure 3.9, Supporting Information) indicating that Γ-point integration is a good approximation for materials like MOFs with large cell parameters.

The effective mass of the charge carriers, m*, was computed at the conduction band minima (CBM) and valence band maxima (VBM) for electron and holes, respectively, as the inverse of the electronic dispersion in the reciprocal space:

$$\frac{1}{m^*} = \frac{1}{\hbar^2} \times \frac{\delta^2 E}{\delta k^2} \tag{3.3}$$

Using this relationship, the data extracted from the band structure calculations was fitted to a parabola to obtain the effective mass values. All high-symmetry points of the band structure path were considered to compute the effective mass. Among the different values obtained, only the smallest effective mass at the CBM and VBM was discussed as the most favorable photoconductive pathway.

3.4 Results

3.4.1 Optical and Photo-Redox Properties

The potential of MOFs as photocatalysts is subject to their light-harvesting and photo-redox properties. These two features constitute the main characteristics that will discriminate between energetically capable and non-capable systems in large-scale screenings. By means of electronic structure calculations, the optical bandgap can be obtained from the energy of the lowest active excited state, while the photo-redox capabilities can be estimated from the band edge positions. The accuracy of the computed values will largely depend on the level of theory. For large-scale screenings, however, cost-effective strategies are needed. In a recent article, it is showed how DFT calculations at the PBE level can be empirically shifted to estimate more accurate PBE0 values for the accelerated screening of MOFs for photocatalysis.[61]

A comparison between the PBE and PBE0 bandgap values of the 15-set (see MOF dataset in Methods) is shown in Figure 3.2A. It can be seen that PBE systematically underestimates the electronic bandgap by ≈1.5 eV in comparison to the PBE0 values. This agrees with our previous studies[61] and with the well-known problem of generalized gradient approximation (GGA) functionals to correctly predict the bandgap in semiconductors.[31] In contrast, hybrid schemes such as PBE0 significantly improve the prediction.[162] A comparison between the experimental optical bandgap and the computed S_1 energies at the PBE0 level is shown in Figure 3.2B. The S_1 energies slightly overestimate the experimentally reported values (about 0.3 eV on average), however, the trends are properly captured. Certainly, the accurate prediction of the optical properties of MOF materials is still challenging and will largely benefit from the development of novel methods and computational strategies. For large-scale screenings, we found that an empirical shift of +0.85 eV applied to the PBE values provides reasonable estimates of the lowest absorption edge of MOF materials at a very low computational cost. This shift was parameterized based on the band gap computed for 132 MOFs.[61] Remarkably, this value is highly transferable to the 15-set studied here (Figure 3.2C) and thus, we believe can be applied to further MOF datasets.

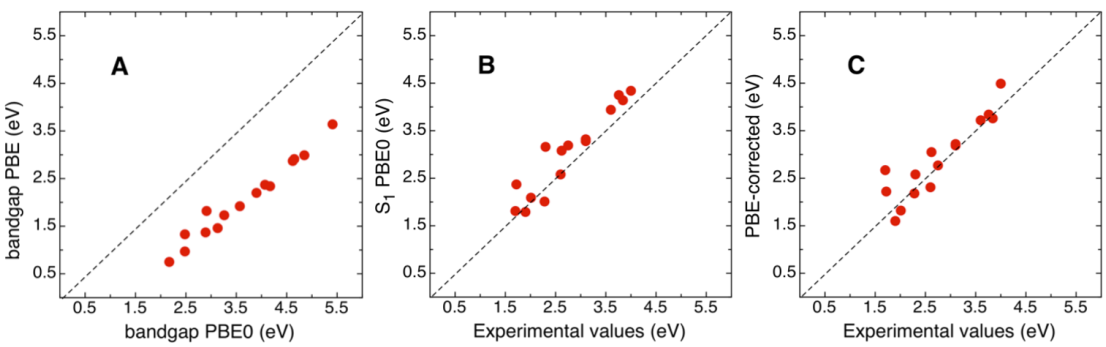

Figure 3.2 – Comparison between A) the PBE and PBE0 bandgaps, B) the experimental values and the S_1 (PBE0) energies, and C) the experimental values and the corrected PBE energies (+0.85 eV)[61] of the 15-set MOFs. Raw data is given in Table 3.4, Supporting Information.

The photo-redox properties of the 15-set have been addressed by means of estimating the absolute position of the conduction (CB) and valence (VB) band edges.[22, 61] The capability of a MOF to promote a particular redox reaction upon the absorption of light is then given by the position of the CBM (for reduction) and the VBM (for oxidation) relative to a target redox potential. In Figure 3.3, the CBM and VBM computed energies are shown with respect to the H^+/H_2 reduction and H_2O/O_2 oxidation potentials. In all cases, the CBM is placed above the H^+/H_2 indicating thermodynamic adequacy for hydrogen production. In contrast, some cases display VB edges above H_2O/O_2, which will prevent the oxidation of water and thus necessitates the use of a sacrificial agent. It is worth mentioning that only half of the 15-set systems (AlPMOF, MIL125(-NH_2), MUV11, UiO66(-NH_2), and ZSTU-) were originally targeted for H^+/H_2 reaction, while the others have been used for different photocatalytic reactions such as CO_2 reduction or organic degradation (Table 3.1). In this context, the band edges can be compared with the redox potential of the reactions of interest when performing computational screening of MOFs for photocatalysis. In principle, this option opens the possibility to avoid certain reactions and thus, promote selectivity in competitive photochemical processes.[57] Altogether, our computational strategy allows to easily estimate optical absorption and band energy alignment of MOF structures, which in turn enables to focus the experimental effort only toward the promising systems.

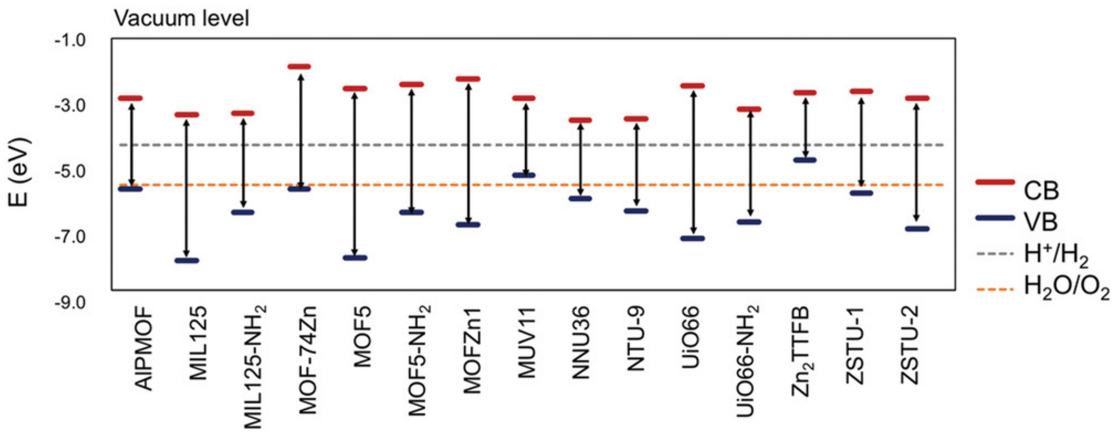

Figure 3.3 – Conduction band (CB) and valence band (VB) edge energies computed with PBE0 for the 15-set MOFs. The H^+/H_2 and H_2O/O_2 potentials are indicated. Raw data is given in Table 3.4

3.4.2 Charge Separation

Photo-generated charge separation is one of the crucial steps controlling the conversion efficiency in photocatalysis. A common scenario of a MOF photocatalytic system includes an electron-withdrawing co-catalyst and an easily oxidizable sacrificial agent.[99] In this way, the MOF acts as the photosensitizer and the electron-hole recombination is prevented by favoring charge transfer to the external components. However, the charge carrier lifetime needs to be long enough within the MOF to maximize the chances of electron(hole) injection

at the interfaces or to be directly transferred to the substrates. In this context, the formation of long-lived charge-transfer excited states in MOFs is a promising design target that can be exploited for large-scale computational screenings.

To evaluate the charge transfer (CT) character of an excited state, one possibility is to quantify the charge separation Λ as the spatial overlap between the photo-generated electron-hole pair densities (see Experimental Section). We assume that long-lived electron-hole pairs will decay to the lowest excited S_1 state.[101] The Λ values that characterized the S_1 state of the 15-set are collected in Table 3.2. They range from 0.11 to 0.76 and have been computed considering all relevant one-electron transitions involved in the S_1 state (see Experimental Section). Small $\Lambda(S_1)$ values indicate that the electron and hole densities do not spatially overlap and thus that S_1 is mainly a CT state. In contrast, large $\Lambda(S_1)$ values are associated with local excitations that can be either ligand- or metal-centered. Remarkably, the results show that the CT or local character of S_1 cannot be unequivocally assigned as 0 or 1, but that most of the systems show a partial character of both.

Table 3.2 – Charge separation coefficient Λ characterizing S_1 state obtained at PBE0 and charge carrier effective mass at the VBM (hole) and CBM (electron) using PBE, in electron rest mass (m_0) units.

	$\Lambda(S_1)$	m^*_{hole}	m^*_{elec}
AlPMOF	0.70	30.0	30.1
MIL125	0.33	–	0.9
MIL125-NH_2	0.24	84.2	4.2
MOF-74Zn	0.56	7.3	5.2
MOF5	0.40	–	217.1
MOF5-NH_2	0.32	62117.8	67.4
MOFZn1	0.64	–	3.3
MUV11	0.25	12.8	12.5
NNU36	0.76	1.2	3.7
NTU-9	0.58	1.1	1.6
UiO66	0.59	-	0.8
UiO66-NH_2	0.39	104.9	0.8
Zn_2TTFB	0.38	2.2	16.8
ZSTU-1	0.11	7.0	8.9
ZSTU-2	0.30	-	16.8

Interestingly, chemically and structurally similar MOFs such as MIL125 and MIL125-NH2 present non-equivalent $\Lambda(S_1)$ values, being slightly smaller for the -NH2 substituted one. This is also the case for MOF5 and MOF5-NH_2 as well as for UiO66 and UiO66-NH_2 thus clearly indicating the participation of the -NH_2 groups in the low lying states.[22, 27] Comparison between the Ti(IV)-, Zn(II)-, and Zr(IV)-based MOFs MIL125(-NH_2), MOF5(-NH_2), and UiO66(-NH_2), respectively, points also to the role of the metal in tuning the CT capabilities. Lower $\Lambda(S_1)$ values are obtained for the Ti(IV)-MIL125 MOF followed by the Zn(II)-MOF5 and the Zr(IV)-UiO66 cases. The predicted ability of MIL125-NH2 to undergo efficient photo-induced charge

separation agrees with previously reported experimental evidence from transient absorption spectroscopy.[134] Small $\Lambda(S_1)$ values are also obtained for the Ti(IV)- ZSTU- systems, for which charge separation was predicted based on their chemical composition and 1D structural motif.[61] In particular, ZSTU-1 showed a better photocatalytic performance than ZSTU-2 which could be in part due to a more favorable charge separation, as predicted by our $\Lambda(S_1)$ approach. From our results, we can conclude that both the ligand and the metal ion can be tuned to modify the CT character of the lowest state. Particularly promising are MOFs such as MIL125-NH_2, MUV11, and ZSTU-1 that combine Ti(IV) with oxidizable ligands leading to low-lying LMCT (Figure 3.1A).

Being able to quantify the photo-induced charge separation in MOFs is certainly a step forward into the characterization of their optical properties from electronic structure calculations, which was so far limited to the interpretation of the CB and VB character. Evaluating $\Lambda(S_1)$ however, implies the calculation of the lowest excited state S_1 and the spatial overlap between all the occupied-unoccupied orbital pairs that characterize it. This entails a large computational cost that cannot be afforded for HT screenings. For this reason, an alternative procedure to estimate Λ for many MOF structures needs to be established. To do so, we analyze three possible approximations to determine the electron-hole separation based on ground state (GS) calculations. One possibility is to consider the spatial overlap O_{ia} between the highest occupied crystal orbital (HOCO) and lowest occupied crystal orbital (LUCO) of the GS singlet state assuming that the lowest excitation will take place between the band-edge orbitals (Figure 3.4A). Another possibility is to evaluate the spatial overlap between the HOCO(α) and LUCO(β) of the lowest GS triplet (Figure 3.4B). This will assume that the lowest excited singlet S_1 and triplet T_1 states are equivalent. Finally, it is possible to consider the electron-hole pair as independent charges that coexist in a neutral state, therefore neglecting their interaction. In that case, the spatial overlap is evaluated between the HOCO(α) of the electron injection (Figure 3.4C) and the LUCO(β) of the hole injection (Figure 3.4D) both in their GS doublet. We have labeled the three strategies as GS0-S, GS-T, and GS-D, respectively.

Comparison between the computed $\Lambda(S_1)$ and the values obtained by means of the three aforementioned strategies (predicted Λ) is shown in Figure 3.5. The GS-S protocol predicts very small Λ in cases with large $\Lambda(S_1)$reference values, that is, it will erroneously predict low-lying CT excitations for systems characterized by a mainly local S_1 state. In contrast, the GS-T protocol overestimates Λ with respect to the $\Lambda(S_1)$ reference values in many cases, thus it would automatically discard promising CT candidates throughout screening. Finally, the GS-D strategy reproduces correctly the $\Lambda(S_1)$ trend with minor deviations in most cases, that is, considering the reduced and oxidized MOF in its GS we can estimate the locality of the e^- and the h^+ in S_1, respectively. In order to understand the different behavior of the GS-S, GS-T, and GS-D protocols we analyze the results of two test-cases in the following.

We have selected AlPMOF as a representative MOF displaying a low-lying local excitation with an $\Lambda(S_1)$ value of 0.70. This excitation corresponds to a π-π^* transition from the highest occupied molecular orbital to the lowest unoccupied molecular orbital (LUMO) of the

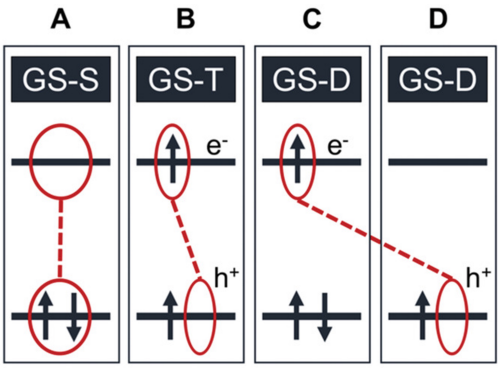

Figure 3.4 – Estimations considered to evaluate the CT character of S_1 from ground state calculations. A) Ground state singlet (GS-S), the spatial overlap is evaluated between the HOCO and the LUCO; B) GS triplet (GS-T), the spatial overlap is computed between the HOCO(α) and LUCO(β); C) GS doublet (GS-D) when injecting an electron (e^-); and D) GS doublet when injecting a hole (h^+), the spatial overlap is evaluated between the HOCO(α) of the e^- injection and the LUCO(β) of h^+ injection.

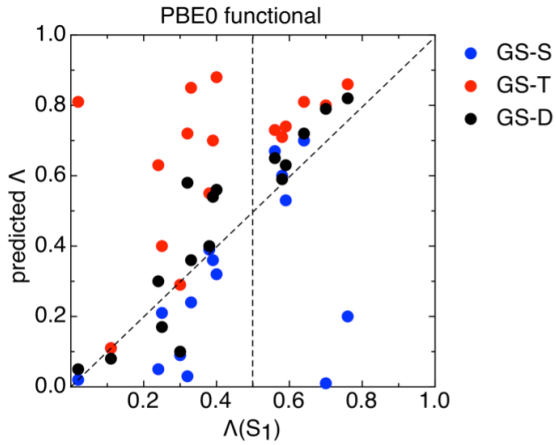

Figure 3.5 – Comparison between the computed $\Lambda(S_1)$ and the predicted Λ values obtained by means of the GS-S, GS-T, or GS-D protocol, as explained in the main text. A R^2 of 0.85 is obtained for the GS-D approach. Raw data is collected in Table 3.5, Supporting Information.

porphyrin ligand, also known as the Q bands.[115] The local character of the lowest state is well captured by the GS-T and GS-D strategies, which predict Λ values of 0.80 and 0.79, respectively. However, the GS-S protocol misleads this value to 0.01. These results can be explained by analyzing the different HOCO and LUCO obtained in each case (Figure 3.6). First, one has to notice that the unit cell contains four porphyrin units organized in two columns following eclipsed π-stacking motifs. In the GS-S, the crystal orbitals are delocalized along one or another column of the unit cell and therefore, the spatial overlap between them is negligible (Figure 3.6A). In contrast, the frontier crystal orbitals are both localized in a single porphyrin unit when evaluating the GS-T and thus, result in a large Λ (Figure 3.6B). Finally, delocalized orbitals in the four porphyrins are shown for the electron and hole injection states

in GS-D, which lead also to a large Λ (Figure 3.6C). The different (de)localization of the crystal orbitals in each approximation determines its ability to predict Λ and originates in the different electronic features that characterize the ground state singlet, triplet, and charged doublet states. On the one hand, the two spatially separated π-stacking motifs of the unit cell result in pseudo-degenerate HOCOs (and LUCOs) in the GS-S that would erroneously predict CT from one to another. On the other hand, both the GS-T and GS-D strategies will predict low-lying local excitations, but for very different reasons: while GS-T localizes the frontier crystal orbitals in the same porphyrin unit, in GS-D the injected charges delocalize them in the four porphyrin units of the unit cell.

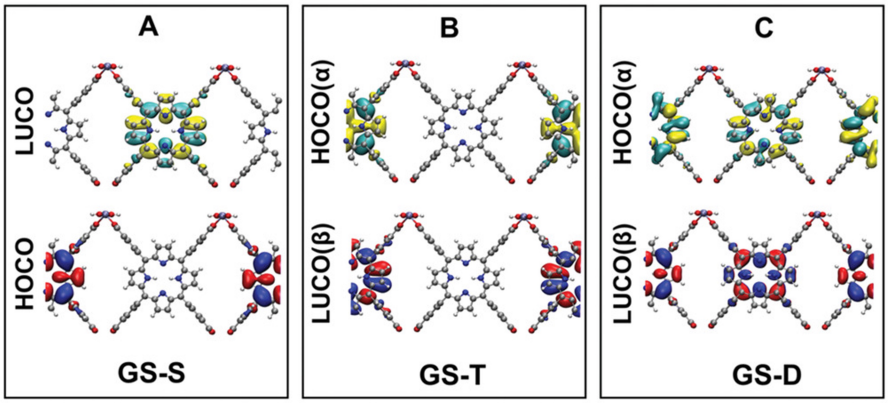

Figure 3.6 – HOCO and LUCO orbitals of AlPMOF computed at PBE0 level following the A) GS-S, B) GS-T, and C) GS-D protocols as explained in the main text.

We applied the same analysis for MIL125 as an example of MOF characterized by a low-lying CT excitation with an $\Lambda(S_1)$ value of 0.33. The latter involves an electronic transition from the bdc ligand to a hybrid ligand/Ti-cluster band.[86] In this case, both the GS-S and GS-D strategies predict a CT character for S_1 with an estimated Λ of 0.24 and 0.36, respectively, whereas GS-T will consider that the lowest state is local with an estimated Λ of 0.85. The frontier crystal orbitals obtained in each case are shown in Figure 3.7. Both GS-S and GS-D strategies represent correctly the different nature of the valence and conduction band edges. However, the GS-T minimizes its energy through fully localizing the frontier orbitals in one ligand unit. This example illustrates that the lowest triplet is not electronically equivalent to the lowest excited singlet, especially when local excitations and CT compete. This is because electronic exchange interactions play a crucial role in stabilizing local excitations and lead to large singlet-triplet energy splitting.[33] This conclusion would be of key importance when considering electrogenerated excited states in a optoelectronic application instead of light-induced excitations as in photocatalysis. In the former case, the statistical ratio of triplet and singlet excitons induced by the applied voltage is 3:1, while in the latter only singlet excitations are accessible in the absence of spin-orbit coupling effects.[213]

Our analysis on the AlPMOF and MIL125 examples illustrates that i) local excitations may not be well represented by the HOCO and LUCO of the GS-S due to orbital pseudo-degeneracies, ii)

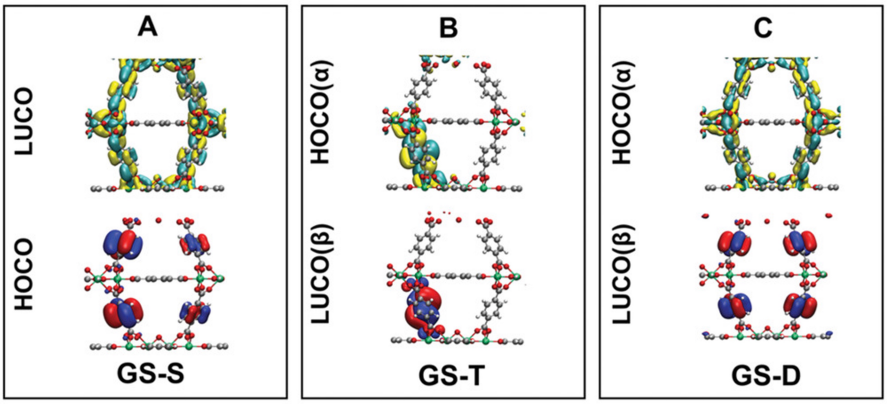

Figure 3.7 – HOCO and LUCO orbitals of MIL125 computed at PBE0 level following the A) GS-S, B) GS-T, and C) GS-D protocols as explained in the main text.

the GS-T might not be representative of the lowest excited singlet if the latter is characterized by a strong CT character, and iii) the independent injection of an electron and hole in their GS-D can be used to evaluate charge separation in S_1 and to discriminate between mainly local ($\Lambda > 0.5$) and mainly CT ($\Lambda < 0.5$) excitations. The conclusions (i) and (iii) equally apply when estimating $\Lambda(S_1)$ from ground state calculations performed with PBE functional, which is the preferred functional for HT screening.[61]Interestingly, the GS-T predictions when using PBE nicely follow the trend of the GS-D results and do not significantly deviate from the $\Lambda(S_1)$ reference values, as was shown by the PBE0 results (Figure 3.10, Supporting Information). This is a direct consequence of the lack of exact exchange in GGA functionals and, although they may miss the correct character of the triplet state, they are useful for the evaluation of the charge separation propensity of S_1 in large MOF databases via cost-effective ground state calculations.

3.4.3 Charge Mobility

In the band transport model, the mobility of the charge carriers is associated with the dispersion of the CB minimum and VB maximum. This is usually small in MOFs, for which most charge-transport studies reveal a hopping transport regime.[117, 26] In the latter, the charge carriers are localized on discrete sites of the MOFs and move from one site to another by means of thermally activated jumps. Generally, it is assumed that if the band-transport model predicts low mobility, that would be also the case when considering hopping.[144] That is, in the limit of the validity of the band transport mechanism, that is, when the band dispersion is zero, the hopping regime will also lead to small mobility values. Hence, we use herein the band transport model to evaluate the electron and hole mobilities in terms of their effective mass m^*. The effective mass is calculated directly from the band structure (see Experimental Section) and provides a measure of the photoconductive capabilities. Because m^* is inversely proportional to the charge mobility, large/small values of m* will be associated with poor/high photoconductive performance.

Band structure calculations were performed for the 15-set MOF structures at the PBE level (Figure 3.11, Supporting Information). To ensure that PBE functional provides reliable VBM and CBM bands, we compared the Projected Density of States (PDOS) of each MOF computed with PBE and PBE0. The results are plotted in Figure 3.12, Supporting Information and show that in most cases the only difference is a down-shift of the energy of the CBM that results in a smaller bandgap when using PBE as compared with PBE0. In those cases, both methods will provide a similar band dispersion at the VBM and CBM and thus, cost-effective PBE calculations are appropriate. In contrast, a drastic change in the nature of the VBM or CBM may affect the band dispersion and therefore, the estimated effective mass. This is the case of MIL125, MOF5, MOFZn1, UiO66, and ZSTU-2, for which the character of the VBM becomes significantly modified by changing the functional. For those MOFs, the addition of Hartree–Fock exchange within DFT causes a change in the contribution of the density in the valence band. The calculations with PBE showed contributions from the transition metal and oxygen atoms near the VBM, while when using PBE0 those contributions are reduced and shifted to lower energies. This disagreement affects the description of the VBM in 5 of the 15 studied cases, which corresponds to 17% of the effective mass computations. For this reason, the PBE approximation to the band structure needs to be perform with caution.

The smallest m^* computed at the VBM and CBM of the 15-set are collected in Table 3.2 given for the electron rest mass m_0, that is, m^*/m_0. The values obtained range from 0.8 to 6 × 104 thus encompass significantly different photoconductive capabilities. For instance, the electron effective masses obtained for Al-PMOF (30.1 m_0) and MIL-125 (0.9m_0) reflect the difference in their conduction band edge dispersion (Figure 3.11, Supporting Information). While Al-PMOF shows a localized porphyrin-based LUCO (Figure 3.6A), MIL125 presents a ligand/Ti-cluster delocalized LUCO (Figure 3.7A) that is translated into a more pronounced curvature of the CBM. Efficient electron mobility is also predicted for NNU36, NTU-9, and UiO66(-NH_2) materials, which all display a considerable dispersion in the CBM (Figure 3.11, Supporting Information). Interestingly, the addition of functional groups such as -NH_2 in materials like MIL125, MOF5, and UiO66 increases the hole effective mass up to $6 \times 10^4 m_0$. The -NH_2 substitution in MOFs is performed to improve the optical absorption properties,[86] however, the localized nature of the -NH_2 states results in flat bands at the VBM that may decrease their potential photoconductivity of holes (Table 3.2). Altogether, an appropriate electronic mixing of the organic and inorganic contributions in the VBM/CBM is desired to maximize charge mobilities. This metal-ligand orbital mixing can be favored for instance by promoting extended high-dimensional networks in the MOF topology, such as 1D or 2D metal-oxygen motifs.

An important question when addressing charge carriers mobilities is the spatial orientation of the most efficient photoconductive pathway. This information can be obtained from experimental measurements when a particular direction presents higher mobility than others. In our calculations, we obtain this information from the k-point path associated with the lowest effective mass (Table 3.6, Supporting Information). Figure 3.8 shows the direction in real space associated with the lowest hole effective mass computed for three representative

cases: Zn_2TTFB, ZSTU-1, and NTU-9. In the case of Zn_2TTFB, we found that the smallest hole effective mass ($2.2m_0$) is ascribed to the $Y \rightarrow \Gamma$ path (Table 3.6, Supporting Information), which in real space corresponds to the tetrathiafulvalene 1D-channel (FigureFigure 3.8a). This agrees with the previously reported experimental evidence, which showed high intrinsic mobilities in Zn_2TTFB along the helical π-stacking motif of TTF.[101, 153] This is also the case in ZSTU-1, for which the preferred direction of photoconductivity corresponds to the 1D-rod of π-stacked ligands (Figure 3.8b).[118] Certainly, the presence of 1D-channels in layered MOFs may facilitate the charge transport and is a promising strategy for the design of highly conductive materials.[31] However, other topologies such as 2D-like systems can also exhibit low effective masses when the through-bond hybridization is optimal. This is the case of NTU-9 material, which displays a 2D- hexagonal topology with high charge mobility along with the three equivalent ligand-to-Ti(IV) directions (Figure 3.8c). The strong bonding between the Ti(IV) and O atoms enables the band dispersion along the 2D plane, while remains minor in the stacking direction.[162] The characterization of the main photoconductive pathways in 3D MOFs is thus crucial to establish specific design strategies toward 1D or 2D topologies. In this context, our cost-effective computational strategy based on the effective mass approximation can capture these two structural features that promote photoconductivity. Thus, it can be applied to large-scale screening not only to identify potential photoconductive MOFs but also to characterize their charge transport motifs.

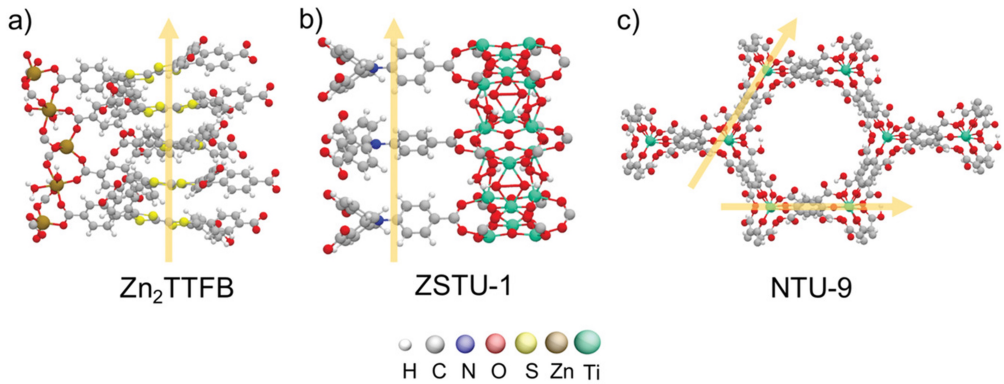

Figure 3.8 – Representation of the computed photoconductive pathways of the lightest hole carriers in a) Zn_2TTFB, along the benzoate-extended TTF stack, b) ZSTU-1, through the ligand staking direction, and c) NTU-9, along the honeycomb-like 2D layers of 2,5-dihydroxyterephthalate ligands.

3.5 Conclusions

The inherent tunability of MOFs makes them particularly attractive for the design of high-performance photocatalysts. In this context, increasing efforts are devoted to the design of new materials with long-lived charge separation and exceptional charge carrier's mobilities. These characteristics are by no means easily predictable and thus computational support is crucial. In this work, we propose two computational strategies, namely the analysis of

charge separation and charge mobility, to easily address these properties in MOF structures. Based on cost-effective DFT calculations at the PBE level, our protocol can be applied to large databases of MOF structures and serve as a fast and comprehensive step that guide the experimental synthesis toward the most promising systems. On the one hand, our results show that the charge separation that characterizes the low-lying singlet excited state can be estimated from the spatial overlap between the HOCO(α) and LUCO(β) of the ground state doublet of the electron and hole injection states, respectively. This approximation can be further extended to the HOCO(α)-LUCO(β) spatial overlap of the ground state triplet state when using local GGA PBE functional. On the other hand, charge carriers mobilities of MOFs can be associated with the effective mass m^* computed from the band structure at the VBM and CBM. The later strategy provides quantitative values to m^* and elucidates the most favorable photoconductive pathway for charge transport. This computational strategy can correctly predict the charge separation and the effective mass of 15 representative MOF structures promising for photocatalysis in agreement with the literature. From our analysis, we show that those systems combining low-lying unoccupied metal states, light-harvesting ligands and extended metal-oxygen networks display all the optoelectronic characteristics to be efficient photocatalysts.

3.6 Supplementary Information

Table 3.3 – Experimental cell parameters reported for the 15 selected MOF structures. For the -NH_2 structures (MIL125-NH_2, MOF5-NH_2 and UiO66-NH_2) we considered as initial parameters for cell-optimization the experimental values of the non-substituted (-H) structures. The PBE-optimized values are given below (see Computational Details).

Name	Metal	a(Å)	b(Å)	c(Å)	α (∘)	β (∘)	γ(∘)
AlPMOF[a]	13.227	31.881	16.808	90.00	90.00	90.00	
		13.424	31.775	17.161	90.00	90.00	90.00
MIL125	Ti(IV)	19.082	19.082	18.127	90.00	90.00	90.00
		19.058	19.058	18.058	90.00	90.00	90.00
MIL125-NH_2	Ti(IV)	19.082	19.082	18.127	90.00	90.00	90.00
		19.041	18.994	18.121	90.09	89.95	90.00
MOF-74Zn[b]	Zn(II)	25.932	25.932	13.673	90.00	90.00	120.00
		26.101	26.066	13.917	89.94	90.05	119.73
MOF5	Zn(II)	25.832	25.832	25.832	90.00	90.00	90.00
		26.126	26.126	26.126	90.00	90.00	90.00
MOF5-NH_2	Zn(II)	25.832	25.832	25.832	90.00	90.00	90.00
		26.057	26.063	26.087	90.06	90.03	90.08
MOFZn1	Zn(II)	19.262	9.984	11.085	90.00	90.25	90.00
		19.344	10.044	11.142	89.76	90.03	89.95
MUV11	Ti(IV)	18.123	18.123	11.224	90.00	90.00	120.00
		18.192	18.171	11.450	89.99	90.02	120.06
NNU36[a]	Zn(II)	15.646	19.980	17.118	90.00	91.09	90.00
		15.510	20.059	17.437	90.21	90.60	89.82
NTU-9	Ti(IV)	14.620	14.620	11.698	90.00	90.00	120.00
		14.837	14.932	11.679	89.01	90.55	120.18
UiO66	Zr(IV)	14.509	14.509	14.509	60.00	60.00	60.00
		14.779	14.791	14.790	59.89	60.06	60.06
UiO66-NH_2	Zr(IV)	14.509	14.509	14.509	60.00	60.00	60.00
		14.790	14.818	14.777	59.99	60.02	60.03
Zn_2TTFB	Zn(II)	19.293	19.293	20.838	90.00	90.00	120.00
		19.458	19.458	20.705	90.01	89.99	120.06
ZSTU-1	Ti(IV)	17.273	17.273	11.758	90.00	90.00	120.00
		17.484	15.155	11.966	90.00	90.00	119.91
ZSTU-2	Ti(IV)	20.160	20.160	11.758	90.00	90.00	120.00
		20.088	20.089	11.925	90.00	90.00	120.03

[a] Cell parameters considering a supercell duplicated along a vector.
[b] Cell parameters considering a supercell duplicated long c vector.

Table 3.4 – Computed band gap at PBE and PBE0 level, S1 energies obtained with LR-TDDFT at PBE0 level and experimentally reported optical band gap values. Valence and conduction band edges with respect to vacuum level are also given. All values are in eV.

MOF	PBE	PBE0	PBE0(S_1)	Exp.[a]	CB	VB
AlPMOF	1.82	2.91	1.81	1.70	-2.877	-5.788
MIL125	2.87	4.62	3.94	3.60	-3.437	-8.059
MIL125-NH_2	1.46	3.13	2.58	2.60	-3.383	-6.517
MOF-74Zn	2.20	3.90	3.08	2.62	-1.878	-5.775
MOF5	3.64	5.41	4.34	4.00	-2.578	-7.988
MOF5-NH_2	2.37	4.07	3.28	3.10	-2.435	-6.508
MOFZn1	2.91	4.65	4.14	3.84	-2.265	-6.919
MUV11	0.97	2.48	2.09	2.01	-2.887	-5.364
NNU36	1.33	2.48	2.01	2.28	-3.608	-6.088
NTU-9	1.37	2.89	2.37	1.72	-3.572	-6.462
UiO66	2.99	4.85	4.25	3.76	-2.487	-7.338
UiO66-NH_2	1.92	3.57	3.19	2.75	-3.247	-6.812
Zn_2TTFB	0.75	2.17	1.79	1.90	-2.702	-4.874
ZSTU-1	1.73	3.26	3.16	2.30	-2.658	-5.922
ZSTU-2	2.34	4.17	3.32	3.10	-2.879	-7.049

[a] Experimental values extracted from the references indicated in Table 3.1

Table 3.5 – Spatial orbital overlap Λ characterizing the S_1 state computed with PBE0 and considering the three approximations GS-S, GS-T and GS-D discussed in the main text at PBE0 and PBE level.

	PBE0				PBE		
	$\Lambda(S_1)$	Λ(GS-S)	Λ(GS-T)	Λ(GS-D)	Λ(GS-S)	Λ(GS-T)	Λ(GS-D)
AlPMOF	0.70	0.01	0.80	0.79	0.17	0.81	0.79
MIL125	0.33	0.24	0.85	0.36	0.28	0.44	0.42
MIL125-NH_2	0.24	0.05	0.63	0.30	0.06	0.41	0.39
MOF-74Zn	0.56	0.67	0.73	0.65	0.67	0.67	0.64
MOF5	0.40	0.32	0.88	0.56	0.52	0.62	0.61
MOF5-NH_2	0.32	0.03	0.72	0.58	0.02	0.63	0.61
MOFZn1	0.64	0.70	0.81	0.72	0.31	0.77	0.62
MUV11	0.25	0.21	0.40	0.17	0.26	0.40	0.35
NNU36	0.76	0.20	0.86	0.82	0.21	0.85	0.83
NTU-9	0.58	0.60	0.71	0.59	0.61	0.64	0.63
UiO66	0.59	0.53	0.74	0.63	0.40	0.59	0.61
UiO66-NH_2	0.39	0.36	0.70	0.54	0.33	0.60	0.60
Zn_2TTFB	0.38	0.39	0.55	0.40	0.42	0.46	0.45
ZSTU-1	0.11	0.11	0.11	0.08	0.12	0.22	0.18
ZSTU-2	0.30	0.09	0.29	0.10	0.41	0.41	0.27

AlPMOF

PATH	VBM	m^*_{hole}	CBM	$m^*_{electron}$
$\Gamma \rightarrow$ X	-0.56	5060.7	1.27	49686.8
Y $\rightarrow \Gamma$	-0.56	137.1	1.27	247.5
$\Gamma \rightarrow$ Z	-0.56	30.0	1.27	30.1
R $\rightarrow$ Z	0.56	61.6	1.27	48.8
$\Gamma \rightarrow$ T	-0.56	56.2	1.27	45.2
U $\rightarrow \Gamma$	0.56	35.8	1.27	35.9
$\Gamma \rightarrow$ V	-0.56	159.8	1.27	299.9

MIL125

PATH	VBM	m^*_{hole}	CBM	$m^*_{electron}$
$\Gamma \rightarrow$ X	-0.56	171.9	2.31	16.1
Y $\rightarrow \Gamma$	-0.56	183.7	2.31	25.0
$\Gamma \rightarrow$ Z	-0.56	16.9	2.31	0.9
R $\rightarrow$ Z	0.56	33.9	2.31	2.7
$\Gamma \rightarrow$ T	-0.56	27.3	2.31	1.7
U $\rightarrow \Gamma$	0.56	26.9	2.31	1.7
$\Gamma \rightarrow$ V	-0.56	166.2	2.31	1145.5

MIL125-NH2

PATH	VBM	m^*_{hole}	CBM	$m^*_{electron}$
$\Gamma \rightarrow$ X	-0.28	2922.7	1.18	122.7
Y $\rightarrow \Gamma$	-0.28	84.2	1.18	44.3
$\Gamma \rightarrow$ Z	-0.28	92.4	1.18	4.2
$R_2 \rightarrow \Gamma$	-0.28	132.0	1.18	12.5
$\Gamma \rightarrow T_2$	-0.28	85.6	1.18	7.7
$U_2 \rightarrow \Gamma$	-0.28	188.9	1.18	8.9
$\Gamma \rightarrow V_2$	-0.28	159.1	1.18	72.9

MOF74-Zn

PATH	VBM	m^*_{hole}	CBM	$m^*_{electron}$
$\Gamma \rightarrow$ X	-0.13	143.8	2.07	5.2
Y $\rightarrow \Gamma$	-0.13	9.4	2.07	6.9
$\Gamma \rightarrow$ Z	-0.13	11.5	2.07	6.8
$R \rightarrow \Gamma$	-0.13	23.9	2.07	6.1
$\Gamma \rightarrow T$	-0.13	7.3	2.07	7.9
$U \rightarrow \Gamma$	-0.13	30.9	2.07	5.7
$\Gamma \rightarrow V$	-0.13	28.6	2.07	5.8

MOF5

PATH	VBM	m^*_{hole}	CBM	$m^*_{electron}$

$\Gamma \rightarrow$ X	-1.76	287.8	1.88	259.7
Y $\rightarrow \Gamma$	-1.76	291.3	1.88	217.1
$\Gamma \rightarrow$ Z	-1.76	570.2	1.88	492.7
$R_2 \rightarrow \Gamma$	-1.76	498.3	1.88	973.2
$\Gamma \rightarrow T_2$	-1.76	401.6	1.88	338.4
$U_2 \rightarrow \Gamma$	-1.76	706.1	1.88	17837.1
$\Gamma \rightarrow V_2$	-1.76	296.9	1.88	222.4

MOF5-NH_2

PATH	VBM	m^*_{hole}	CBM	$m^*_{electron}$
$\Gamma \rightarrow$ X	-0.01	320105.8	2.36	71.6
Y $\rightarrow \Gamma$	-0.01	517349.9	2.36	270.0
$\Gamma \rightarrow$ Z	-0.01	62117.8	2.36	67.4
$R_2 \rightarrow \Gamma$	-0.01	333694.2	2.36	160.9
$\Gamma \rightarrow T_2$	-0.01	108308.7	2.36	211.9
$U_2 \rightarrow \Gamma$	-0.01	129137.9	2.36	318.4
$\Gamma \rightarrow V_2$	-0.01	178287.4	2.36	78.7

MOFZn1

PATH	VBM	m^*_{hole}	CBM	$m^*_{electron}$
$\Gamma \rightarrow$ X	-1.16	55.7	1.75	3.3
Y $\rightarrow \Gamma$	-1.12	4.4	1.75	9.3
$\Gamma \rightarrow$ Z	-1.16	4.9	1.75	25.3
$R_2 \rightarrow \Gamma$	-1.12	10.5	1.75	5.3
$\Gamma \rightarrow T_2$	-1.12	9.3	1.75	5.2
$U_2 \rightarrow \Gamma$	-1.16	77.1	1.75	5.4
$\Gamma \rightarrow V_2$	-1.12	5.9	1.75	7.4

MUV11

PATH	VBM	m^*_{hole}	CBM	$m^*_{electron}$
$\Gamma \rightarrow$ X	-0.49	12.8	0.46	12.5
Y $\rightarrow \Gamma$	-0.49	87.2	0.48	4.9
$\Gamma \rightarrow$ Z	-0.49	95.3	0.48	4.4
$R_2 \rightarrow \Gamma$	-0.49	20.3	0.48	8.9
$\Gamma \rightarrow T_2$	-0.49	89.6	0.48	3.8
$U_2 \rightarrow \Gamma$	-0.49	20.0	0.48	8.6
$\Gamma \rightarrow V_2$	-0.49	20.5	0.48	9.1

NNU36

PATH	VBM	m^*_{hole}	CBM	$m^*_{electron}$
$\Gamma \rightarrow$ X	-0.71	1.2	0.62	3.7
Y $\rightarrow \Gamma$	-0.71	95.9	0.62	154.7

$\Gamma \rightarrow$ Z	-0.71	90.3	0.62	47.2
$R \rightarrow \Gamma$	-0.71	2.8	0.62	8.7
$\Gamma \rightarrow T$	-0.71	121.1	0.62	65.9
$U \rightarrow \Gamma$	-0.71	2.1	0.62	6.5
$\Gamma \rightarrow V$	-0.71	1.9	0.62	5.8

NTU9

PATH	VBM	m^*_{hole}	CBM	$m^*_{electron}$
$\Gamma \rightarrow$ X	-0.67	4.9	0.7002	11.5
Y $\rightarrow \Gamma$	-0.67	1.2	0.7002	2.5
$\Gamma \rightarrow$ Z	-0.67	1.1	0.7002	2.4
$R_2 \rightarrow \Gamma$	-0.67	2.3	0.7002	3.7
$\Gamma \rightarrow T_2$	-0.67	1.3	0.7002	1.6
$U_2 \rightarrow \Gamma$	-0.67	2.0	0.7002	5.8
$\Gamma \rightarrow V_2$	-0.67	2.0	0.7002	5.3

UiO66

PATH	VBM	m^*_{hole}	CBM	$m^*_{electron}$
$\Gamma \rightarrow$ X	-2.11	2216.9	0.88	0.8
Y $\rightarrow \Gamma$	-2.11	127.5	0.88	0.8
$\Gamma \rightarrow$ Z	-2.11	66.3	0.88	0.8
$R \rightarrow \Gamma$	-2.11	213.4	0.88	0.8
$\Gamma \rightarrow T$	-2.11	7.2	0.88	0.8
$U \rightarrow \Gamma$	-2.11	47.6	0.88	0.8
$\Gamma \rightarrow V$	-2.11	94.1	0.88	0.8

UiO66-NH_2

PATH	VBM	m^*_{hole}	CBM	$m^*_{electron}$
$\Gamma \rightarrow$ X	-0.35	104.9	1.57	0.8
Y $\rightarrow \Gamma$	-0.35	165.7	1.57	0.8
$\Gamma \rightarrow$ Z	-0.35	1125.3	1.57	0.8
$R \rightarrow \Gamma$	-0.35	678.1	1.57	0.9
$\Gamma \rightarrow T$	-0.35	388.7	1.57	0.8
$U \rightarrow \Gamma$	-0.35	342.1	1.57	0.8
$\Gamma \rightarrow V$	-0.35	982.65	1.57	0.8

Zn_2TTFB

PATH	VBM	m^*_{hole}	CBM	$m^*_{electron}$
$\Gamma \rightarrow$ X	-0.56	37.2	0.19	16.8
Y $\rightarrow \Gamma$	-0.56	2.2	0.20	8.9
$\Gamma \rightarrow$ Z	-0.56	37.2	0.19	18.9
$R_2 \rightarrow \Gamma$	-0.56	5.0	0.20	73.3

$\Gamma \rightarrow T_2$	-0.56	4.9	0.20	71.6
$U_2 \rightarrow \Gamma$	-0.56	40.3	0.19	19.9
$\Gamma \rightarrow V_2$	-0.56	4.9	0.20	93.5

ZSTU-1

PATH	VBM	m^*_{hole}	CBM	$m^*_{electron}$
$\Gamma \rightarrow$ X	-0.25	7.1	1.47	76.9
Y $\rightarrow \Gamma$	-0.25	11.9	1.47	8.9
$\Gamma \rightarrow$ Z	-0.25	7.1	1.47	76.1
$R_2 \rightarrow \Gamma$	-0.25	9.4	1.47	13.9
$\Gamma \rightarrow T_2$	-0.25	9.5	1.47	13.6
$U_2 \rightarrow \Gamma$	-0.25	7.0	1.47	68.7
$\Gamma \rightarrow V_2$	-0.25	9.5	1.47	13.6

ZSTU-2

PATH	VBM	m^*_{hole}	CBM	$m^*_{electron}$
$\Gamma \rightarrow$ X	-0.26	1.9	2.06	16.8
Y $\rightarrow \Gamma$	-0.28	17.9	2.06	3093.3
$\Gamma \rightarrow$ Z	-0.28	317.0	2.06	2177.8
$R_2 \rightarrow \Gamma$	-0.26	3.1	2.06	27.7
$\Gamma \rightarrow T_2$	-0.28	317.6	2.06	2268.3
$U_2 \rightarrow \Gamma$	-0.26	3.1	2.06	27.0
$\Gamma \rightarrow V_2$	-0.26	3.1	2.06	27.3

Table 3.6 – Effective mass of electron ($m^*_{electron}$) computed at the Conduction Band Minima (CBM) and effective mass of the hole (m^*_{hole}) at the Valence Band Maxima (VBM) given in electron rest mass units of the 15-set of MOFs computed using the PBE functional at each trace in the k-point path. The VBM and CBM energies are given in eV.

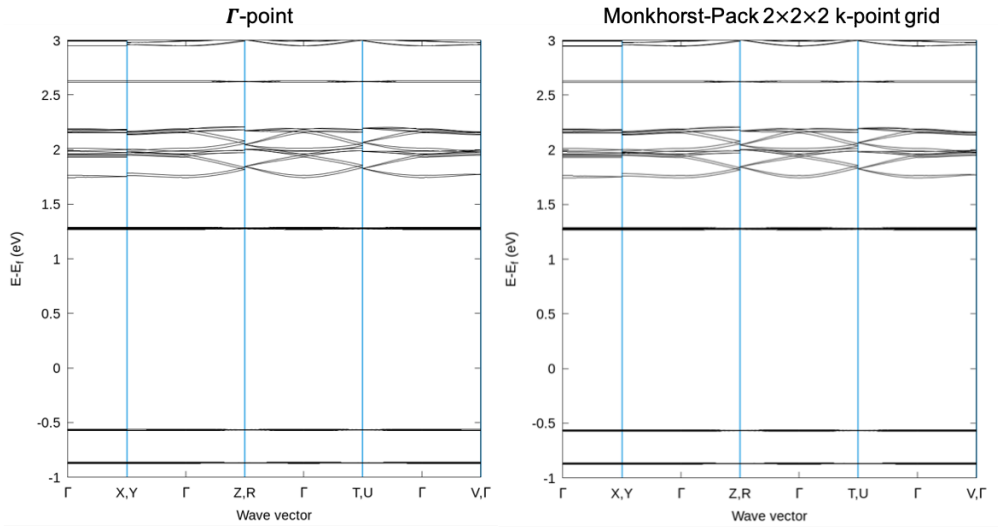

Figure 3.9 – Band structure comparison using Γ-point vs Monkhorst-Pack 2×2×2 k-point grid for Al-PMOF.

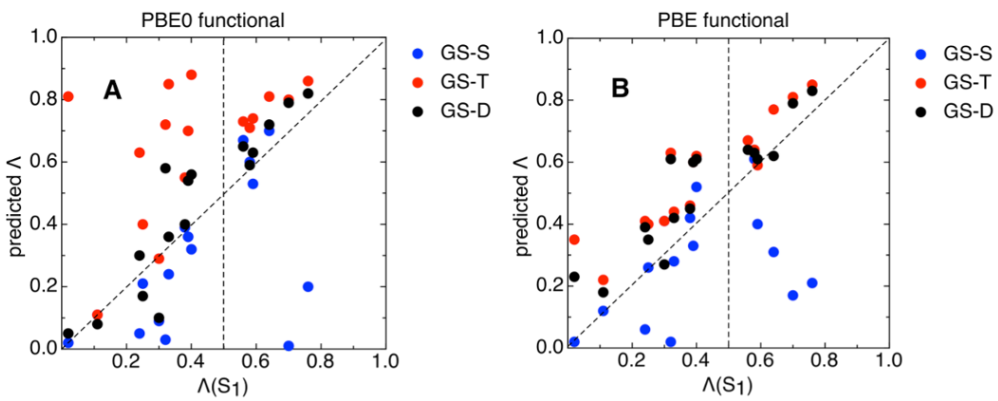

Figure 3.10 – Comparison between the computed $\Lambda(S_1)$ and the predicted Λ values obtained by means of the GS-S, GS-T or GS-D protocol, as explained in the main text, at A) PBE0 and B) PBE level. Raw data is collected in Table 3.5.

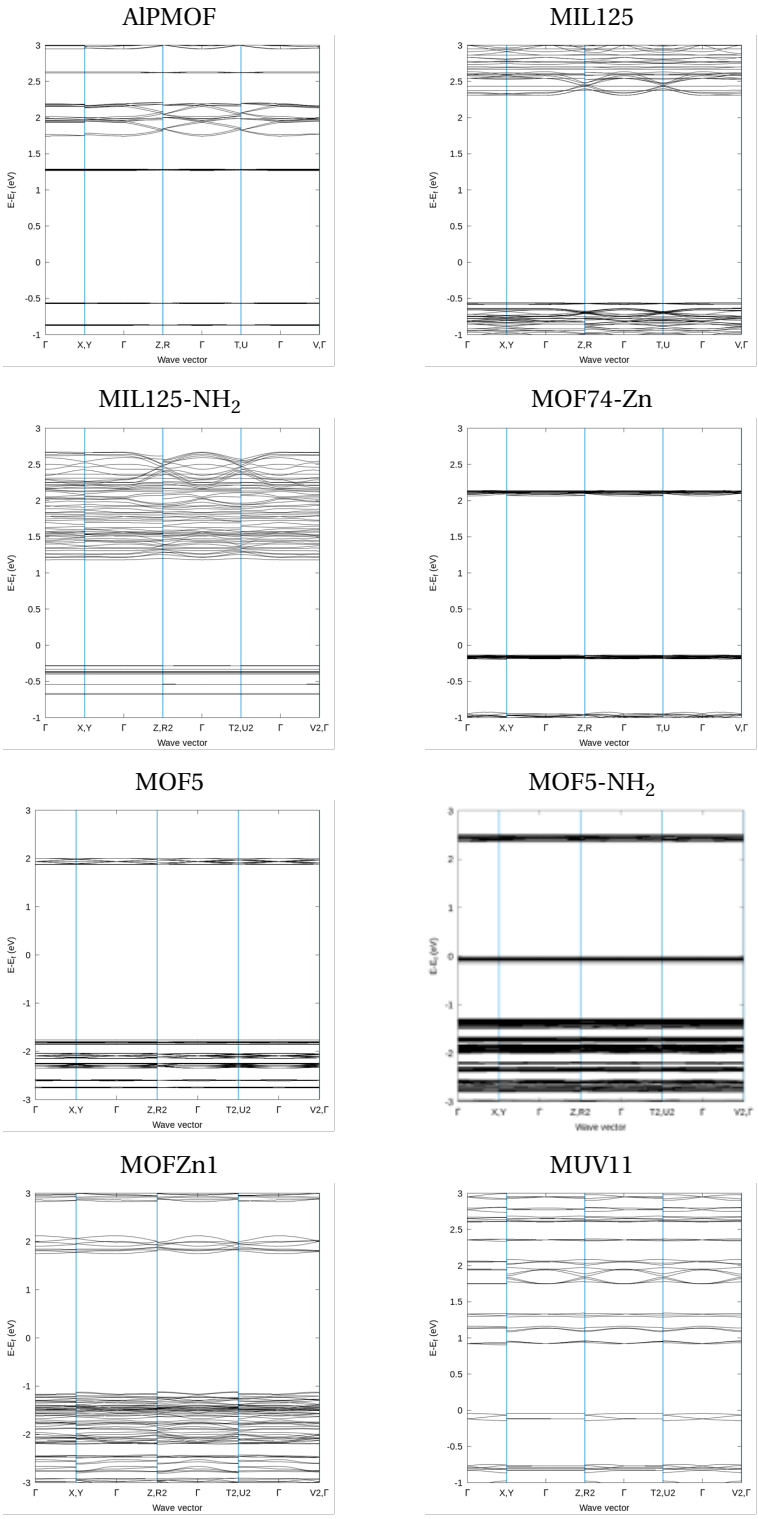

Figure 3.11 – Band structure of the 15-set of MOFs computed with the PBE functional.

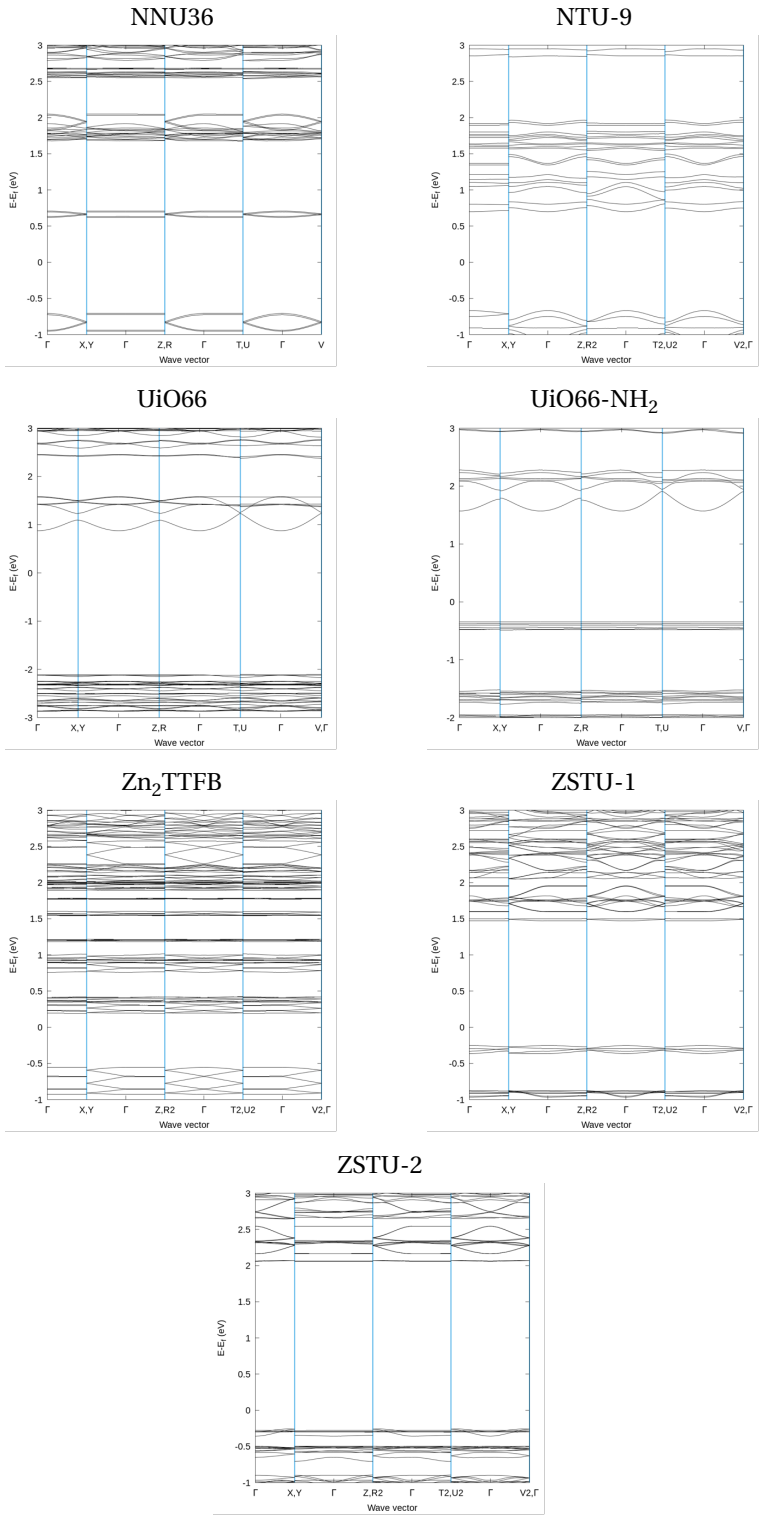

Figure 3.11 – Band structure of the 15-set of MOFs computed with the PBE functional (Cont).

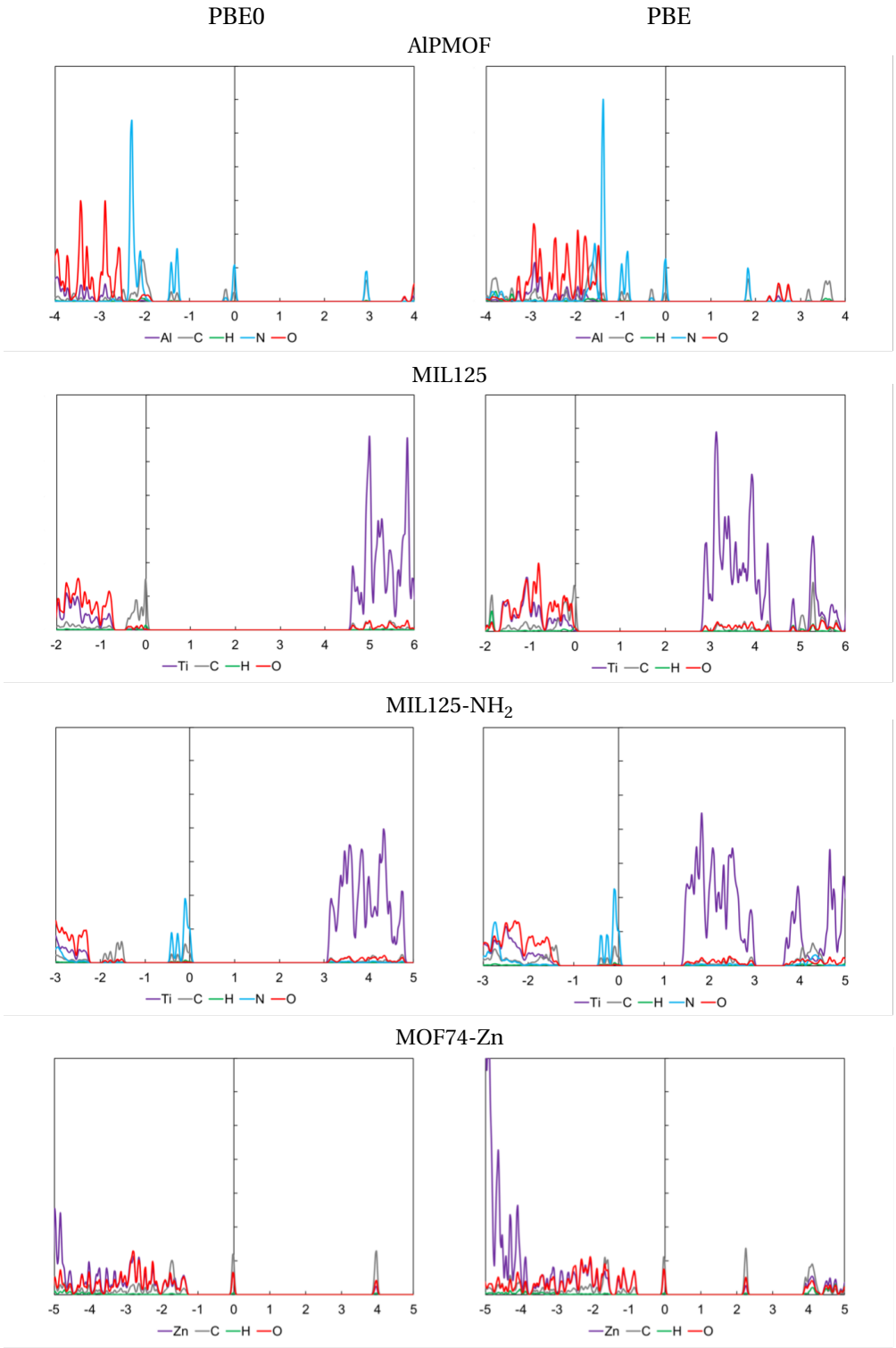

Figure 3.12 – PBE0 and PBE projected density of states (PDOS) of the studied MOFs (in eV).

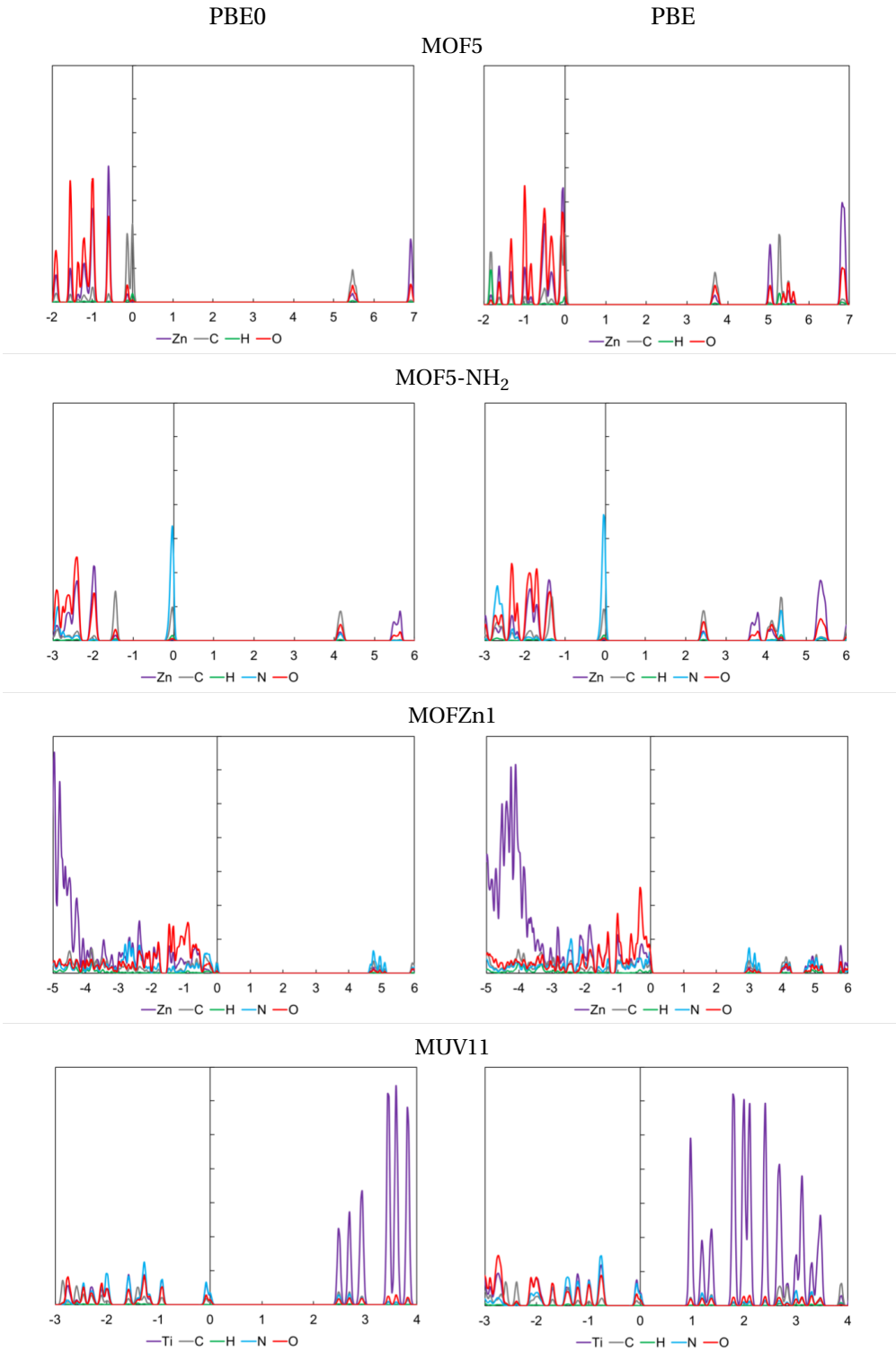

Figure 3.12 – PBE0 and PBE projected density of states (PDOS) of the studied MOFs (in eV), Continuation.

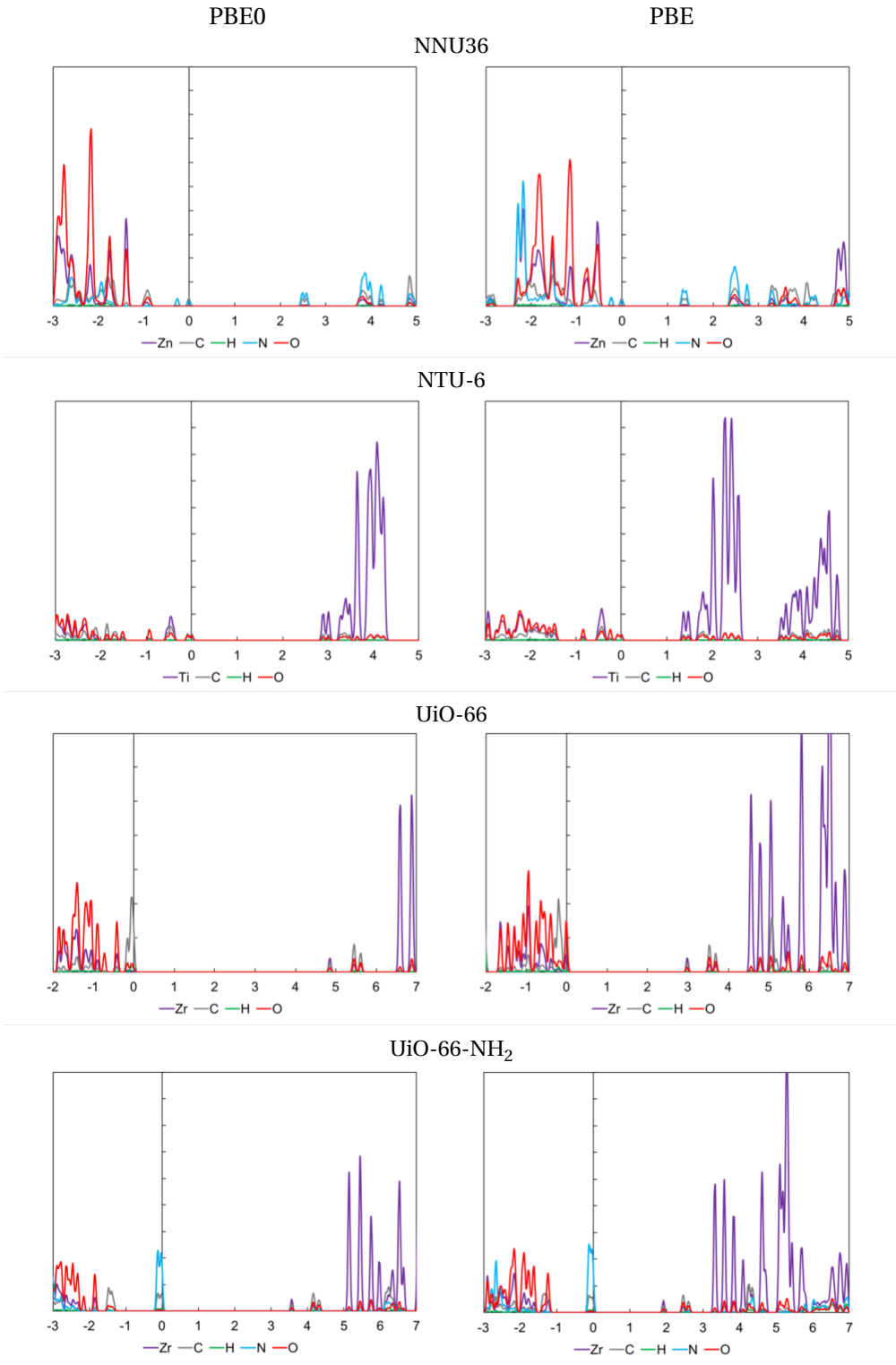

Figure 3.12 – PBE0 and PBE projected density of states (PDOS) of the studied MOFs (in eV), Continuation.

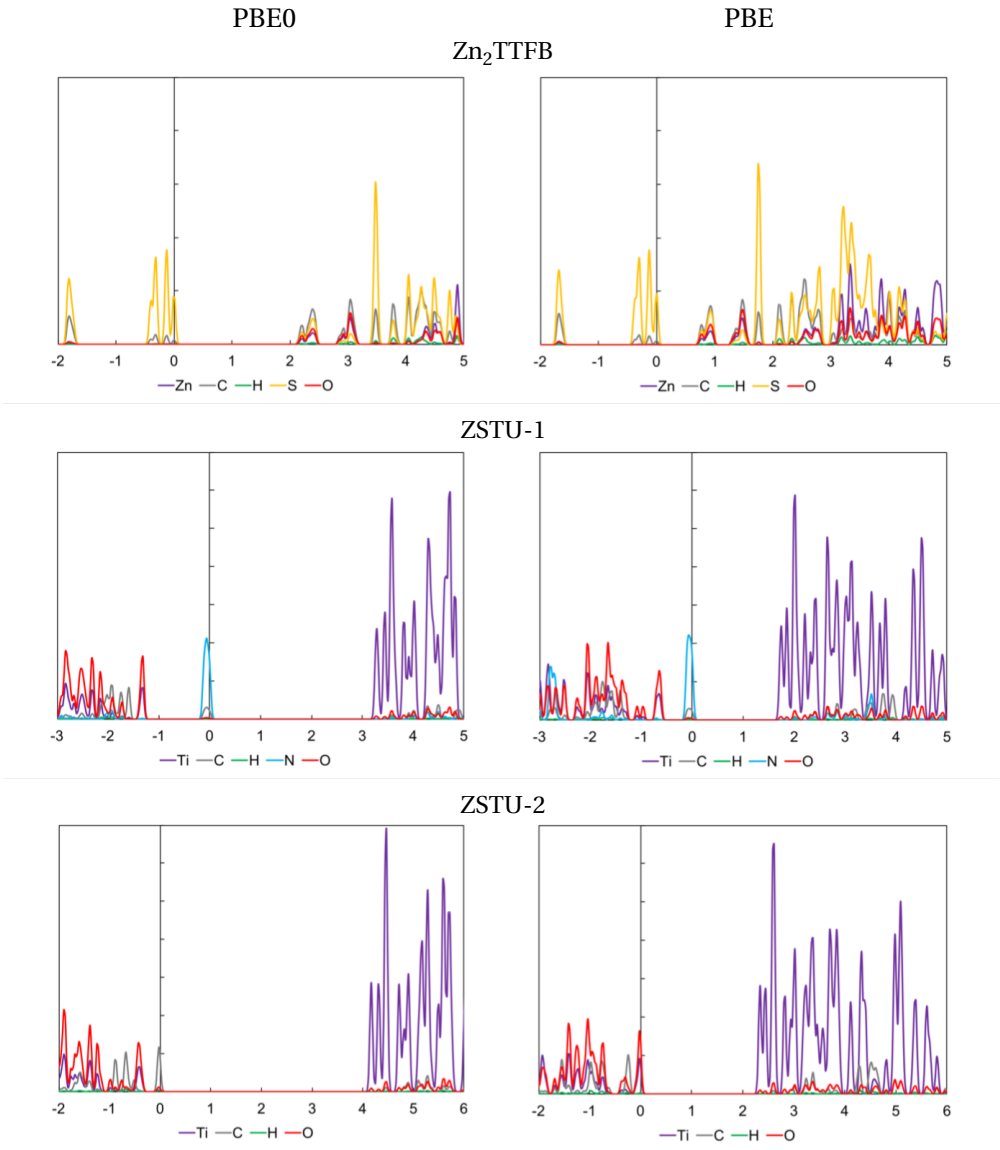

Figure 3.12 – PBE0 and PBE projected density of states (PDOS) of the studied MOFs (in eV), Continuation.

4 Towards optimal photocatalytic hydrogen generation from water using pyrene-based metal-organic frameworks[a]

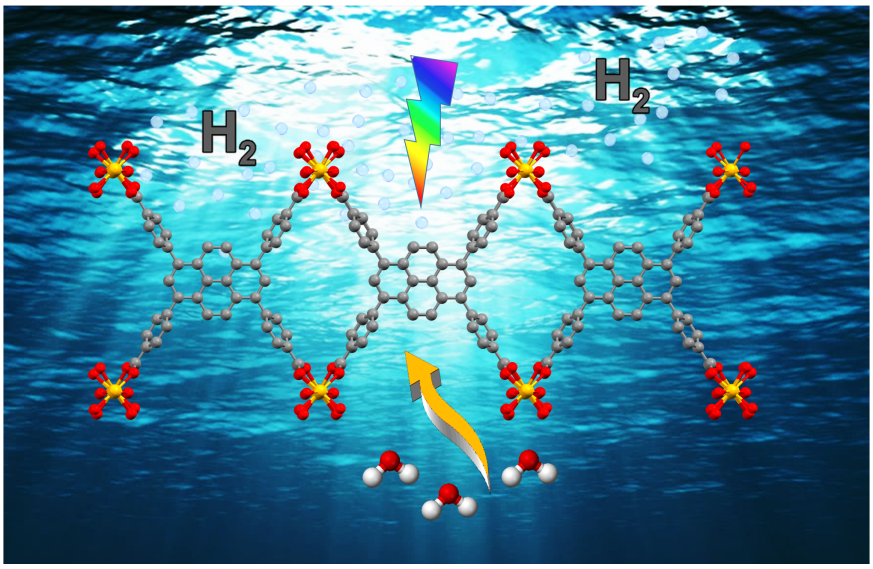

[a]This chapter is based from the preprint version of the submitted manuscript: F. Pelin Kinik, Andres Ortega-Guerrero, Fatmah Mish Ebrahim, Christopher P. Ireland, Ozge Kadioglu, Amber Mace, Mehrdad Asgari, and Berend Smit. A O-G performed and analyzed the ab-initio calculations of the electronic and optical properties of the materials, and together with FPK and BS wrote the manuscript with the help of the other coauthors. FPK and A O-G contributed equally to this work.

4.1 Abstract

Metal organic frameworks (MOFs) have been promising candidates for the photocatalytic H_2 evolution reaction (HER) from water, thanks to their advantageous optical, electronic and structural properties. As yet, the main criteria for MOFs to be considered as “photocatalysts" have mostly been their light absorption capability, optical band gap and band alignment. In this study, we present the synergy between the experiments and computational calculations to show that there are other aspects to take into consideration. We investigated three isostructural pyrene-based MOFs (M-TBAPy, where M = Sc, Al, and In), which have similar band gap energies. Despite all being isostructural MOFs, Sc-TBAPy performed better in H_2 generation compared to its Al and In counterparts. Our investigation allowed us to identify the effect of metal-related characteristics, and the effect of morphology, on the photocatalytic HER rate. We conclude that all the aforementioned aspects should be studied together for the optimization of photocatalytic activity, and the knowledge obtained in this study can be transferred to other MOFs.

4.2 Introduction

Photocatalytic H_2 evolution reaction (HER) from water is one of the promising catalytic applications for MOFs. Thanks to their advantageous characteristics such as *(i)* adjustable light absorption, *(ii)* porous structure shortening the charge transfer path and improving the separation of electron-hole pairs, and *(iii)* possibility of incorporating different co-catalysts or photosensitizers to promote the separation of electron-hole pairs.[124, 223, 210, 185] Depending on the design principles of the MOFs, they can produce H_2 from water under UV or UV-visible light. The UV light irradiation conditions correspond to only 3–5% of the solar spectrum,[146] therefore the development of visible-light active MOFs have been of importance by the careful selection of the ligand.

To design MOFs for photocatalytic HER from water, it is important to understand the factors contributing to the overall performance. Like any photocatalytic material, the HER photocatalytic activity of a MOF relies on having a material with adequate light absorption capability, optical band gap, and band alignment.[201] In addition, Guo *et al.*[76] demonstrated that different morphologies of the same MOFs can have strikingly different performances. Nasalevich *et al.*[141] showed that MOFs having different electronic properties perform differently toward photocatalytic HER. However, the lack of a systematic study investigating all these effects together makes it difficult to compare the relative importance of these different factors. We believe that isostructural MOFs are a good platform for this investigation, thanks to their similar crystal structures.

In this work, we present a combined experimental and computational study on a family of pyrene-based isostructural MOFs. We systematically investigate different factors that contribute to the photocatalytic HER from water. In particular, we study *(i)* the effect of metal

coordinated in the MOF, causing differences in electronic and optical properties, and *(ii)* the effect of morphological characteristics. We show how these insights can be used to tune different factors that can be affecting the HER performance of MOFs, and can be generalized to other photocatalytic MOFs.

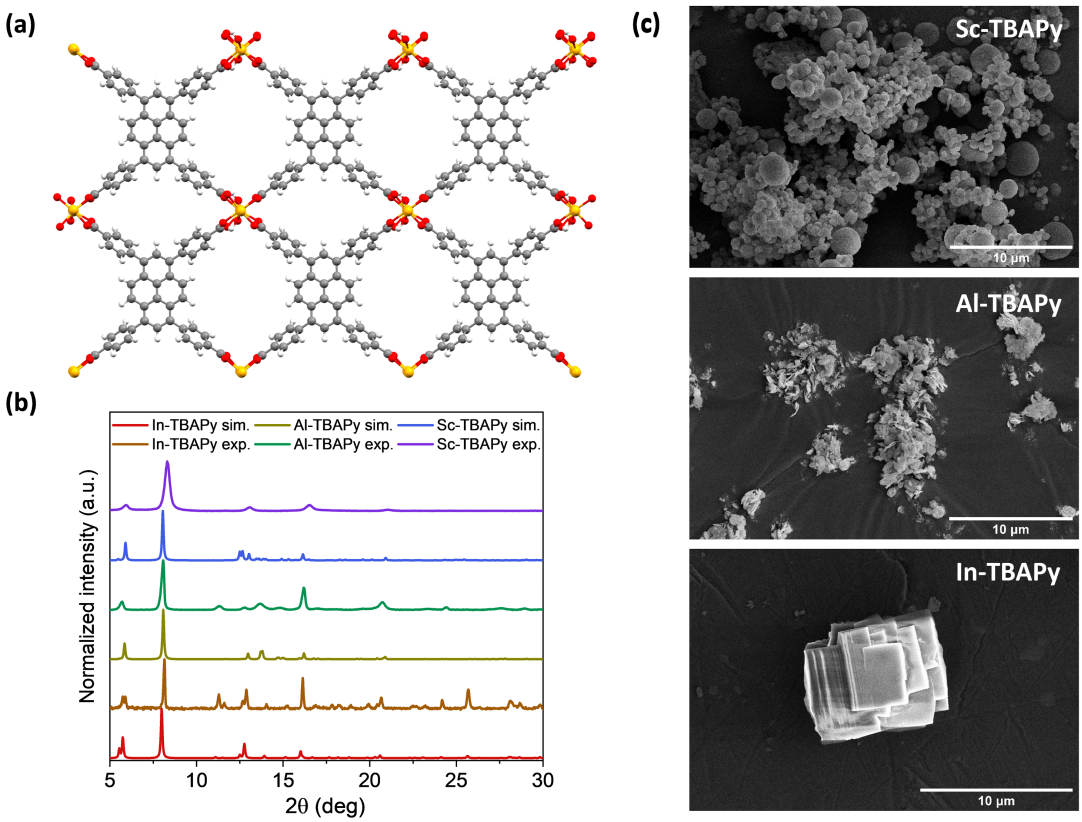

Figure 4.1 – (a) Crystal structure of M-TBAPy (where M = Sc, Al, and In) MOFs. Color code: M: yellow, O: red, C: gray, H: white. (b) Powder X-ray diffraction (PXRD) patterns of isostructural M-TBAPy MOFs, showing a good match between the individual experimental and simulated patterns. (c) SEM images of Sc-TBAPy (top), Al-TBAPy (middle) and In-TBAPy (bottom), demonstrating different structural characteristics of the MOFs.

For our study we compared the performance of HER for a family of isostructural pyrene-based TBAPy MOFs, which we refer to as "M-TBAPy" (M = Al, In, and Sc, Figure 4.1(a)). Pyrene exhibits favorable intense visible-light absorption, energy-transfer ability, and a long excited-state lifetime with successful electron hole-pair dissociation, which is the reason for the selection of TBAPy as the ligand.[54, 104] AlPyrMOF[18] and ROD-7[181] were synthesized using the procedures from the literature. In this work we refer to these two materials as Al-TBAPy and In-TBAPy, respectively. We synthesized the novel isostructural Sc version of the M-TBAPy MOFs, Sc-TBAPy (for more details, see "Material Synthesis and Characterization"). The framework of Sc-TBAPy is based on chains of octahedral $ScO_4(OH)_2$ units, where each Sc(III) is bound to four TBAPy ligands and two μ_2 trans hydroxide anions (Figure 4.1(a)).

Comparison of the simulated and experimental PXRD patterns show that for each of the three materials we obtained the desired structure (Figure 4.1(b)).

Scanning electron microscopy (SEM) images revealed that, although the synthesis conditions for all three MOFs are the same (85 °C for 12 h, in a mixture of DMF/dioxane/H_2O), the metal has a pronounced effect on the crystal morphology. Sc-, Al-, and In-TBAPy form spherical crystals, circular discs, and intergrown rectangular plates, respectively (Figure 4.1(c)). The size of Al-TBAPy crystals is close to the Sc-TBAPy crystals, while the size of In-TBAPy crystals is an order of magnitude bigger.

Cadiau *et al.*[25] reported the synthesis of the Ti version, ACM-1, which we refer to as Ti-TBAPy. Our synthesis attempts for Ti-TBAPy were not successful, which we attributed to the complexity of Ti chemistry and its sensitivity to synthesis conditions to isolate crystalline Ti-MOFs.[199, 142] As for Ti-TBAPy detailed HER experiments have been reported, in our comparison of the different properties we therefore used the data reported by Cadiau *et al.*

This family of M-TBAPy MOFs allows us to systematically study the effect of metal on the HER activity. In addition, we investigate in detail how the metal impacts the different factors contributing to the HER, such as the electronic structure of the MOF and the optical characteristics.

4.3 Results

4.3.1 Photocatalytic Performances

The photocatalytic HER performances of Sc-, Al-, and In-TBAPy MOFs were investigated under visible-light irradiation using a 300W Xe lamp, with a 420 nm cut off filter to remove any UV light. Reactions were performed in the presence of triethylamine (TEA) as the sacrificial reagent. The same conditions (17 mg MOF in 17 ml photocatalytic solution in a 25 ml reactor, 3 hours of reaction) were established for all MOFs for the comparability of the photocatalytic performances. Figure 4.2 shows that all three MOFs are capable of producing H_2 from water under specified conditions. The HER rates of In-TBAPy (4.7 $\mu mol\, g^{-1}\, h^{-1}$) and Al-TBAPy (6.3 $\mu mol\, g^{-1}\, h^{-1}$) are comparable, while Sc-TBAPy has a higher HER rate of 32.8 $\mu mol\, g^{-1}\, h^{-1}$. The HER rate of Sc-TBAPy was found to be less than that of Ti-TBAPy, 147.5 $\mu mol\, g^{-1}\, h^{-1}$).[25] Our experiments are not done at exactly the same conditions with that of Ti-TBAPy, but these differences are not expected to change the ranking.

4.3.2 Electronic Characteristics

There can be different factors that can explain the effect of the metal on the photocatalytic HER performance. One of these factors is the position of the band edges with respect to the redox potential of water. A thermodynamic requirement is the proper alignment of the band edges of the materials with the reduction and oxidation potential for water splitting,

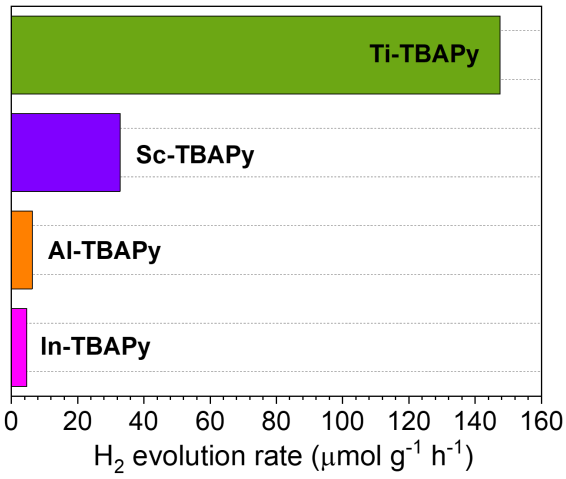

Figure 4.2 – Photocatalytic HER rates of Sc-, Al- and In-TBAPy MOFs, under visible light irradiation ($\lambda \geq 420$ nm, 3h reaction). Ti-TBAPy was included for comparison, where photocatalysis was conducted under visible light irradiation ($\lambda \geq 380$ nm, data from Cadiau et al.[25]).

i.e., the conduction band minimum (CBM) being above the H^+/H_2 reduction potential for HER and the valence band maximum (VBM) below the H_2O/O_2 oxidation potential for oxygen evolution reaction (OER).

To analyze the positions of these band edges of the M-TBAPy MOFs (M= Al, In, Sc, and Ti), we carried out density functional theory (DFT) calculations. In these calculations, we optimized the structures with the PBE0 functional using the *Cmmm* space group symmetry (see “Methods"). Figure 4.3 shows that for all materials this requirement is fulfilled. The alignment of the VBM in Ti-TBAPy is lower than in the other materials despite their similarities, which can be associated with the difference in the coordination of the μ_2-OH groups in Al-, In-, and Sc-TBAPy MOF to μ_2-O in Ti-TBAPy.

Our DFT calculations also provide us with the band structures. From the shape of the band structure, we can obtain some insights into the photoconductive properties and the mobility of the charge carriers. Likewise, the effective mass of the carriers is proportional to the inverse of the electronic dispersion in the reciprocal space (curvature) at the band structure edges[60]. This effective mass is inversely proportional to definition of charge mobility according to the Bardeen–Shockley mobility model[139]. Therefore, the curvature of the CBM and VBM will be related to the mobility of the photo-excited electrons and holes, respectively. The flatter the shape of the band, the higher the effective mass, and as a high effective mass can be associated with a low charge mobility, such a flat shape can be associated with poor photoconductivity.

Figure 4.5 shows the band structure calculations of the different M-TBAPy MOFs (M = Sc, Al, In, and Ti) together with a visualization of the CBM and VBM orbitals. All MOFs show a similar flat band for the VBM, but for the CBM we see a large effect of the metals. For

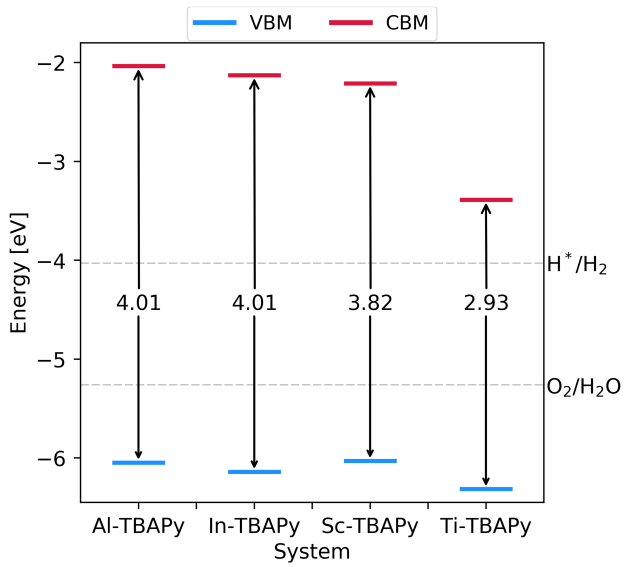

Figure 4.3 – Energy diagrams of fundamental band gaps and the band edge positions with respect to the vacuum potential computed at the pore centre for Al-TBAPy, In-TBAPy, Sc-TBAPy, and Ti-TBAPy. The dashed lines are redox potentials of water splitting.

Al-TBAPy and In-TBAPy the CBM orbitals are located on the pyrene core of the TBAPy ligands, while for Sc-TBAPy and Ti-TBAPy these are localized along with the coordination complex, involving the metal and phenyl groups. For all four materials, the valence band is the result of the contribution of pyrene π orbitals, hence in these crystals the VBM orbital is localized (Figure 4.5). The metals do impact the shape of the conduction band. Al-TBAPy and In-TBAPy have a flat band for the CBM and have the same band gap. For Al-TBAPy and In-TBAPy the VBM and CBM are both localized on the π and π^* pyrene orbitals of the TBAPy ligands, respectively. [149] As the band gap for those materials is dominated by the pyrene orbitals of the ligand, the calculation will predict the same values for band gaps. In contrast, Sc-TBAPy and Ti-TBAPy have a CBM placed below the pyrene orbitals leading to smaller band gaps. Sc-TBAPy presents a slightly smaller band gap than Al and In MOFs, since the CBM composed by orbitals of the Sc and phenyl groups is placed just below the pyrene orbitals (Figure 4.5(c)). The former are the ones associated with the one-dimensional Sc metal-rod-like structure form in the topology of the M-TBAPy MOFs. This leads to a CBM with more electronic dispersion in the reciprocal space. Ti-TBAPy has the smallest band gap of the four materials, since its CBM is localized only in the Ti d orbitals and it has a more pronounced dispersion among the four materials (Figure 4.5(d)).

Unlike Al- and In-TBAPy, Sc-TBAPy shows the proximity of other bands touching the CBM in different points of the reciprocal space (Figure 4.5(c)). This suggests that Sc-TBAPy conduction band presents the contribution of different orbitals of the MOF. Figure 4.4(a) shows the contribution of the electronic density of states of the four materials around the band edges. Despite Sc-TBAPy CBM shows the presence of Sc orbitals, its contribution is minimal. This is not the case in Ti-TBAPy where the Ti orbitals contribute the most in the CBM. Likewise, Sc-TBAPy

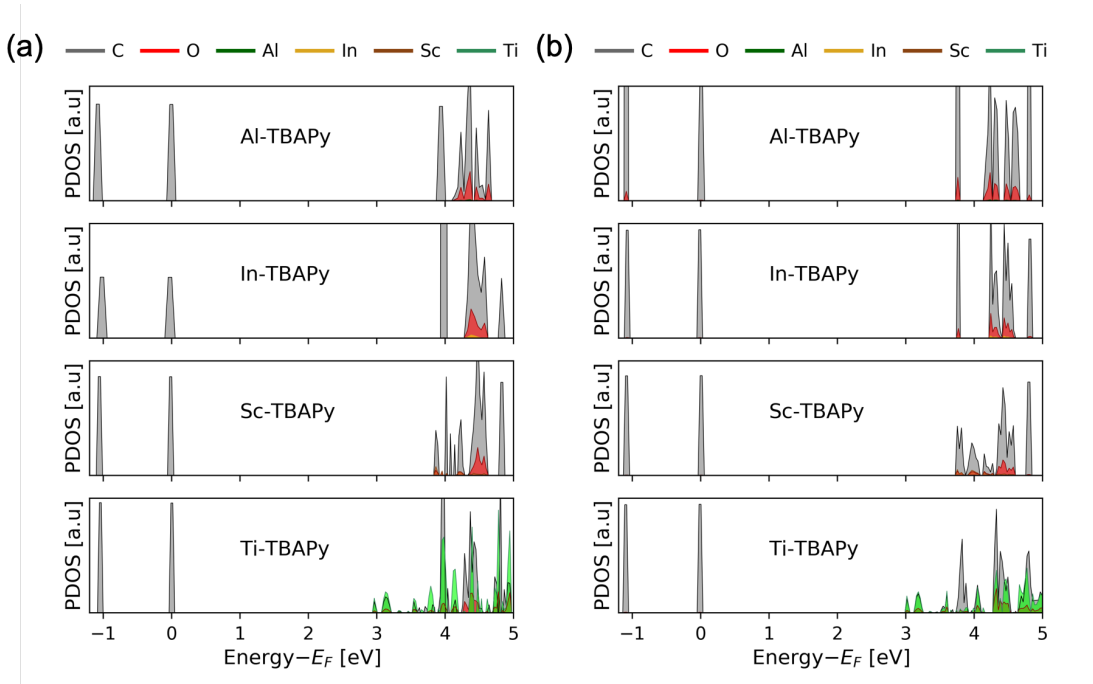

Figure 4.4 – Projected density of states of (a) the high-symmetry structure and (b) the phenyl rotated structures of Al-TBAPy, In-TBAPy, Sc-TBAPy, and Ti-TBAPy with PBE0 functional, CRYSTAL17 calculations.

CBM presents a relatively small energy gap between the higher energy states (compared to Al- and In-TBAPy MOFs) as a result of its electronic dispersion.

In this scenario, Ti-TBAPy (curved) band structure depicts a system with higher electron mobility among the four MOFs. In the case of Al-TBAPy and In-TBAPy, due to having a low dispersion (flat bands), and having carriers localized on the pyrene, carrier mobility is through a much slower hopping transport regime. In the case of Sc-TBAPy, its CBM presents less curvature than that of Ti-TBAPy, yet it suggests a better electron photoconductivity than its Al and In counterparts. Sc-TBAPy conduction band suggests a better participation from the pyrene and the Sc metal-rod orbitals in the mobility of the photogenerated electrons. However, the contribution of Sc orbitals in the CBM is small unlike the case of Ti-TBAPy, where the Ti d orbitals present most of the contribution (Figure 4.4(a)). The above depicts ligand to metal charge transfer (LMCT) in the case of Ti-TBAPy as it was reported by Cadiau *et al.*[25]

Sc-TBAPy is particularly interesting from a theoretical point of view because of the proximity of the CBM to the orbitals of the pyrene ligand. This proximity makes the calculations very sensitive to the exact orientation of the phenyl groups in the ligands.[154] The optimized ground state structure of Sc-TBAPy is with high symmetry. We conducted vibrational frequencies calculation on Sc-TBAPy, where the vibrational mode of the phenyl rotations has a vibration temperature of 48.9 K. Figure 4.22 shows the energy as a function of the orientation of the phenyl groups by scanning the geometry along this vibrational mode. To investigate the

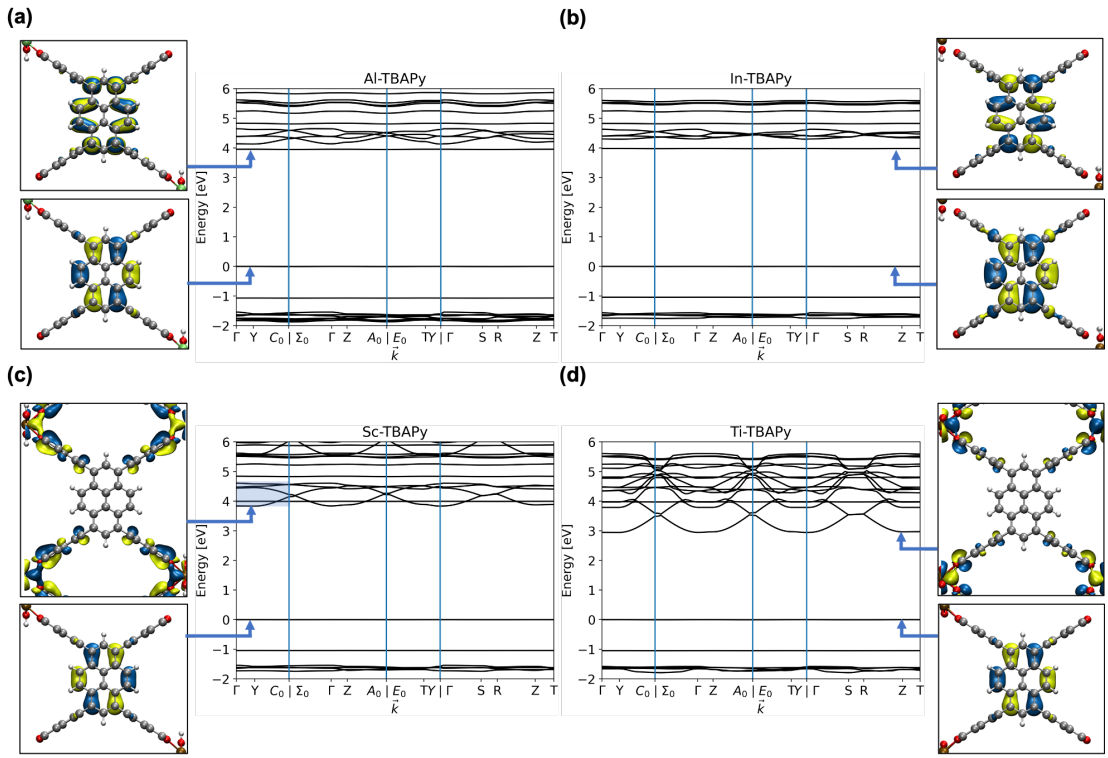

Figure 4.5 – Band structure calculations and CBM and VBM crystal orbitals of the pyrene-based MOFs using PBE0 functional with *Cmmm* space group (symmetrical structure). (a) Al-TBAPy , (b) In-TBAPy , (c) Sc-TBAPy, and (d) Ti-TBAPy. The blue square highlights the conduction bands in Sc-TBAPy.)

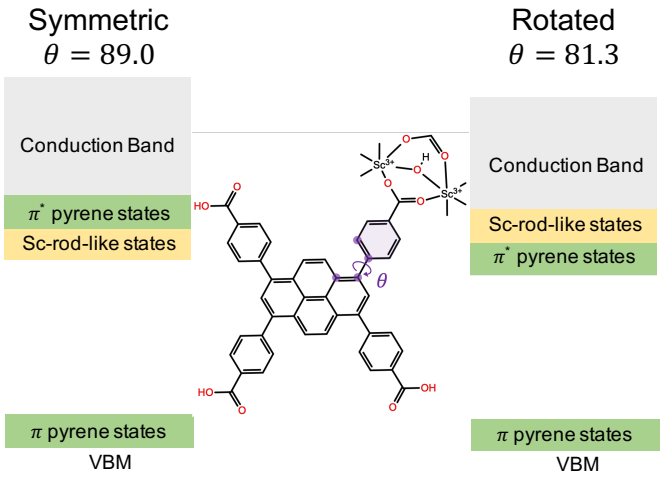

Figure 4.6 – Representation of the different character of the valence band and conduction band edges in Sc-TBAPy for the Symmetric and Rotated structures. The rotation angle (Θ) of the phenyl group is represented as the dihedral between the four highlight carbon atoms.

effect of the rotation of the phenyl groups on the electronic structure, we conducted PBE0 geometrical relaxations calculation on all four M-TBAPys in both the symmetric and the rotated position of the phenyl rings. We refer to these as “symmetrical" and “rotated," respectively. Sc-TBAPy has a local minimum, with an energy that is slightly higher than the ground state. In this local minimum the phenyl groups have a rotation angle of 8°. The energy barrier between the ground state and this local minimum is relatively low ($\approx$ 3.35 meV). Therefore, it can be expected that because of the thermal fluctuations, the phenyl groups can be found in both orientations.

Figures 4.5 and 4.20 show the band structures of the symmetrical and rotated systems, respectively. For Al- and In-TBAPy systems, we see that the rotated case causes the CBM orbital to be at a lower energy. The rotation changes the localization of the pyrene core orbitals, causing the π^*-orbitals to move down, hence we see a small decrease in the band gap. As for Ti-TBAPy, the CBM is dominated by the orbitals on Ti, these rotations of the phenyl group have therefore little impact. In contrast, Sc-TBAPy around the CBM there are contributions from both the ligand as well as the metal orbitals. In the rotated case, the CBM is localized on the π^* orbital of the pyrene ligand and the Sc metal orbitals lies above, but in the symmetric case, this description was the opposite (see Figure 4.6 and Figure 4.19). If we now take the thermal fluctuations (or the presence of solvent, see Figures 4.21) into account, then the CBM of Sc-TBAPy consists of contributions from both the orbitals on the Sc-rod and the π^* pyrene orbitals. This result suggests that the probability of Sc-rod crystal orbital states being populated in the excited-states dynamics of the Sc-TBAPy system is higher than in the Al- and In- counterparts, given their proximity to the pyrene orbitals.

Since Sc-TBAPy CBM contains contributions from both the ligand as well from the Sc orbitals,

it is important to establish whether the mechanism of the optical excitations is LMCT, ligand-centered (LC), or both. For this, we first computed the optical band gap (or the first optical excitation) of the four materials to establish the nature of the optical transition. For these calculations, we use linear-response time-dependent DFT (LR-TDDFT). Table 4.1 shows the values of the ground state and optical band gaps in both the symmetric and rotated cases. It can be seen, that in Al-, In- and Sc-TBAPy MOFs the nature of the optical band gap is the π - π^* optical transition (LC transition). The rotated cases present smaller optical band gaps than the symmetric cases, keeping the same behavior as the one described before for the ground state band gaps. Although the symmetric case of Sc-TBAPy has a CBM with a contribution of the Sc orbitals, the first optical transition is associated with a LC transition, despite the pyrene orbitals being higher in energy. This is a result of the excitonic effects (originated from the electron–hole Coulombic interactions) in MOFs.[150] On the other hand, Ti-TBAPy's first excitation is an LMCT excitation from the pyrene to the Ti orbitals as it was reported as well by Cadiau *et al.*[25]. The experimental measurement of the optical bandgaps in Al-, In- and Sc-TBAPy MOFs was determined via Tauc plots (see Figure 4.13). The experimental optical bandgaps are 2.68, 2.63 and 2.58eV for Al-TBAPy, In-TBAPy, and Sc-TBAPy, respectively. The optical bandgaps values obtained via LR-TDDFT are higher than the experimental values. The theoretical optical bandgaps for the Symmetric and Rotated models are 0.7 and 0.5 eV higher than the experimental optical bandgap values, respectively. Although this difference can appear significant, it is noteworthy to mention that the experiments are performed at room temperature while our calculations are performed at 0 K. Our calculations do not consider the thermal effects and the quantum motion of the nuclei contributions on the bandgap. The inclusion of these effects has shown a decrease in the calculated bandgaps and better agreement with experiments [27]. On the other hand, Ti-TBAPy can suffer the limitations of using PBE0 functional. Such limitation is expected given the difficulties of LR-TDDFT for describing the optical transition energies in charge-transfer states when using pure hybrid functionals.

We also investigated the possibility of Sc-TBAPy trapping an electron in the Sc orbitals in the form of a polaron. For this, we added an electron to our system and we computed the interactions of this extra electron with the material (i.e., electron polaron) in the four materials. Polarons can appear because of doping or charge injection, or be created through the separation of an exciton formed through electronic excitation.[66] We considered the calculation of the symmetric and the rotated structures of the M-TBAPy MOFs. The polarons are localized in their respective CBM orbitals: π^* pyrene orbitals for Al- and In-TBAPy, and the d orbital of a Ti atom in Ti-TBAPy (Figure 4.23). The electron polarons of Al-, In-, and Ti-TBAPy MOFs are not affected by the presence of the phenyl rotations. For Al- and In- the polaron is trapped on the ligand, hence a LC transition. For Ti-, the electron polaron trapping on the d orbitals of the metal leads to a Ti(III) oxidation and hence an LMCT mechanism. Sc-TBAPy presents an electron polaron localized in the π^* pyrene orbitals for the rotated structure (Figure 4.23(c)), and in the Sc and phenyl orbitals from the rod in the symmetric structure (Figure 4.24(b)). The latter resulted in a more delocalized electron polaron given

Table 4.1 – Comparison between the theoretical ground state E_{gs} and optical E_{opt} bandgaps and the experimental optical bandgaps E_{exp}. The calculations are conducted using the symmetrical and phenyl rings rotated structures with PBE0 exchange-correlation functional. The nature of the optical transition excitations are included as well.

	Symmetric			Rotated			
System	E_{gs} (eV)	E_{opt} (eV)	Transition [a]	E_{gs}(eV)	E_{opt} (eV)	Transition [a]	E_{exp} (eV)
Al-TBAPy	4.01	3.40	LC	3.76	3.18	LC	2.68
In-TBAPy	4.01	3.41	LC	3.72	3.14	LC	2.63
Sc-TBAPy	3.82	3.40	LC	3.77	3.21	LC	2.58
Ti-TBAPy	2.93	2.86	LMCT	2.94	2.82	LMCT	2.30 [b]

[a] LC stands for "Ligand-centered" transition and LMCT stands for "Ligand to Metal Charge Transfer". [b] Data from Cadiau et al.[25].

the crystal orbital and the dispersion of the band structure. The Mulliken charge distribution analysis indicates that even in the symmetric case there is no electron trapping on the Sc atoms leading to an Sc(II) oxidation state, discarding the possibility of LMCT for both the symmetric and rotated case.

From our electronic structure calculations we can conclude that Sc-TBAPy and Ti-TBAPy coordination promote a better CBM dispersion. In the case of Ti-, LMCT leads to beneficial electronic properties for HER than the ones with Al- and In-. Sc-TBAPy's electronic properties are different from the other isoreticular M-TBAPy MOFs due to the presence of the ligand as well as the metal orbitals near the CBM which leads to a better electron mobility compared compared to Al- and In-TBAPy.

4.3.3 Optical Characteristics

For the photocatalytic activity it is important that the MOFs absorb light at the desired frequencies. The differences between the M-TBAPy MOFs in terms of their light absorption can be seen from the diffuse reflectance ultraviolet-visible (UV-vis) spectra shown in Figure 4.7. The UV-vis spectra of Al-TBAPy exhibits a broad light absorption ranging from 250 to 475 nm, with two main peaks at 278 and 350 nm. The absorbance maxima are red-shifted for both In-TBAPy (375 nm) and Sc-TBAPy (415 nm) compared to that of Al-TBAPy at 350 nm. This result shows that Sc-TBAPy absorbs better in the visible light region than the other two MOFs, which contributes to its better HER rate. Although the absorption maxima of Ti-TBAPy is similar to that of Sc-TBAPy, its visible light absorption is slightly extended (up to ≈ 550 nm) [25] than that of Sc-TBAPy (up to ≈ 500 nm).

Whereas the absorption spectra give us information on which photons are absorbed, the apparent quantum yields (AQYs) gives us fraction of photons arriving on the sample that cause a chemical reaction to take place.[20] The AQYs of Al-TBAPy and Sc-TBAPy were measured by ferrioxalate actinometry at 400 and 450 nm, respectively (Table 4.2).[81, 110, 100] While both MOFs showed similar AQY yields at 400 nm irradiation (≈ 0.076%), Sc-TBAPy showed better

AQY (0.364%) compared to that of Al-TBAPy (negligible) at 450 nm.

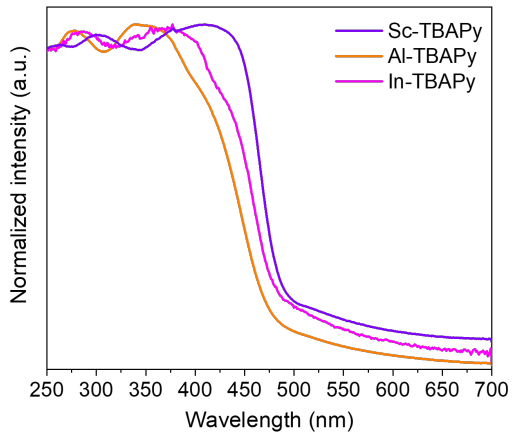

Figure 4.7 – UV-Vis spectra of M-TBAPy MOFs.

Another important quantity for the analysis of the efficient HER is the life times of the photo excited electrons. Therefore, we performed time-resolved photoluminescence measurements to record the duration of the decay of the photo-excited electrons. The photoluminescence lifetimes of Sc-, Al-, and In-TBAPy show two decay features, with the longer lifetime (t_2) feature corresponding to decay localized on the pyrene core, and the shorter lifetime (t_1) corresponding to the rotation of the phenyl rings.[23] Table 4.3 shows that Sc-TBAPy has a shorter photoluminescence lifetime ((t_1) = 2.40 and (t_2) = 11.70 ns) than its Al- ((t_1) = 2.72 and (t_2) = 13.42) and In- ((t_1) = 2.84 and (t_2) = 12.18 ns) counterparts. The shorter lifetime of Sc-TBAPy can be attributed to the localization of the CBM around the phenyl rings and Sc rods rather than on the pyrene core, resulting in an overall shorter-lived excited state.[23] These results present an interesting example of the complexity of photocatalytic HER. If we would only consider the photoluminescence lifetime, one would conclude that those MOFs with the long photoluminescence lifetimes are those with an efficient charge separation and are thus often directly linked to better HER performance[193, 25, 219]. The case of Sc-TBAPy, however, demonstrates that different mechanisms can propose different explanations for lifetimes.

To gain further insights in the mechanism that causes these differences in photoluminescence lifetimes, we carried out nanosecond transient absorption spectroscopy (nTAS) analysis. nTAS is a pump-probe technique which is used to measure dynamic changes in the absorption of a photo-excited sample [12]. A broad-spectrum probe light illuminates the sample at nanosecond time intervals, before and after it has been photo-excited by a pump pulse. By plotting the difference in the sample's absorbance before and after photo-excitation as a function of wavelength and time, we gain insights into the dynamics of photo-excited charge carriers. For example, as molecules are promoted to the excited state through the pump pulse, the number of ground-state molecules decreases. Consequently, the ground-state absorption in the excited sample is less than that in the non-excited sample. This creates a negative signal in the absorption spectrum, which is known as ground state bleach (GSB).[12]

Figure 4.8(a-c) shows the GSB of M-TBAPy MOFs at the two absorption bands, around 300 nm and 500 nm. As expected, the shape of the GSB reflects the steady-state UV-Vis absorption spectra of the MOFs, with Sc-TBAPy exhibiting a broad single peak from 450 - 550 nm, and In- and Al-TBAPy exhibiting slightly blue-shifted peak maxima around 425 nm, and as well as a broad shoulder above 450 nm. The GSB recovery of the three MOFs matches their photoluminescence lifetimes, with Sc-TBAPy having the shortest recovery, followed by In-TBAPy and then Al-TBAPy.

A key characteristic of the In- and Al-TBAPy nTAS profiles, in particular, is the clear red-shifting of the principal 425 nm peak with time, indicated by the black arrows in Figure 4.8(b) and (c). Such a red-shift is typically indicative of non-radiative, vibrational losses, from the higher vibrational S_1 energy states to the CBM, that lower the energy of the excited state with time, and are typically seen in photoexcited pyrene.[135, 55] In the case of Al-TBAPy and In-TBAPy MOFs, the transient red-shift can be seen over a longer timescale than what is typically observed due to vibrational decays.[135] This is likely due to inter-ligand interactions in the Al- and In-TBAPy MOFs. Since the CBM in both these structures is localised on the pyrene core, it is expected that electrons from adjacent pyrene cores will interact in the excited state, to form excimers.[68, 23] The decay of these excimers presumably adds a long lifetime component to the vibrational red-shift of the GSB. We can therefore conjecture that while localization of the CBM on the phenyl rings in Sc-TBAPy results in a shorter lifetime and a single prominent feature in its transient and steady-state absorption spectra, the distribution of charges around the pyrene core in In- and Al-TBAPy accounts for their longer excited-state lifetimes and the distinct vibrational features in their TAS profiles.

Comparing the UV-Vis absorption of the three MOFs with their respective excitation spectra further supports the hypothesis that Al- and In-TBAPy suffer from more non-radiative, vibrational losses than Sc-TBAPy.[23] As seen in Figure 4.8(d-f), when probing the 500 nm emitting S_1 state, the excitation spectrum of Sc-TBAPy (shaded region) closely follows its UV-vis absorption spectrum (solid line). This suggests that absorbed photons are efficiently populating on the S_1 excited state of the MOF. This is less evident in In- and Al-TBAPy, where a discrepancy between the absorption profiles and excitation spectra suggests that a portion of photoexcited electrons are undergoing vibrational decay.

Studies of pyrene suggest that the vibrationally unrelaxed state of pyrene molecules tends to be the active state for energy or charge transfer to a nearby acceptor.[135, 102] Therefore, the absence of vibrational features in the Sc-TBAPy spectra implies that its photoexcited electrons are maintained in a vibrationally unrelaxed state, where they are in an energetically favorable position for water reduction. The combination of enhanced absorption, spatial localization of the CBM, and efficient photoexcitation of the active excited state, all contribute to the superior performance of Sc-TBAPy as a photocatalyst. Our optical investigation thus highlights these three critical points: *(i)* LMCT is not a requisite for MOFs with high rates of HER, *(ii)* photoluminescence lifetime is not the only decisive parameter for photocatalytic HER and distribution of charges in the MOF structure should be also considered, and *(iii)*

vibrational losses due to the localization of charges in the core of TBAPy may depopulate the active state for water reduction in photocatalytic active pyrene MOFs.

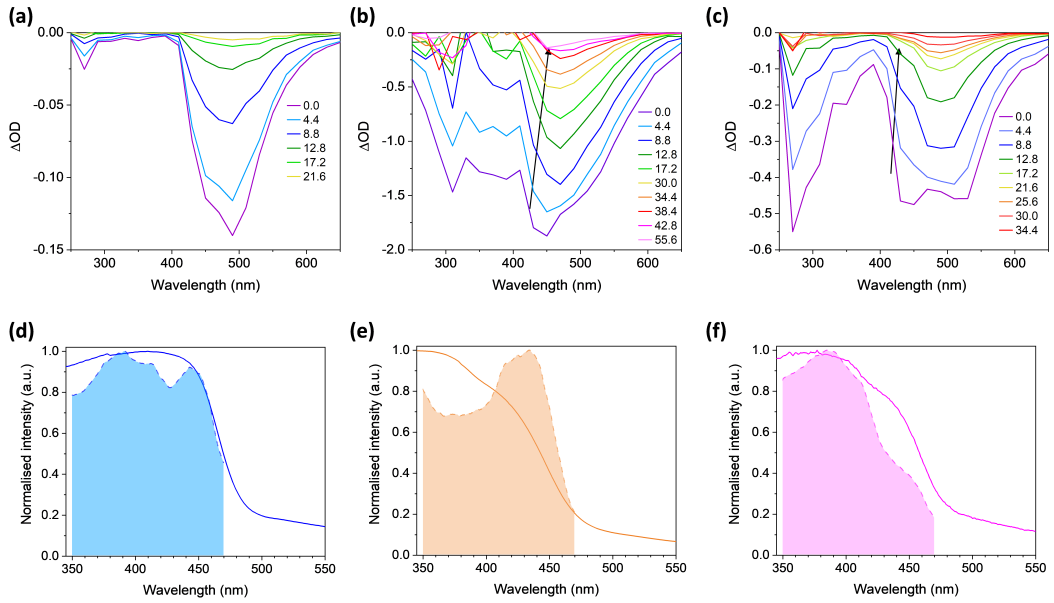

Figure 4.8 – Upper panel: nanosecond transient absorption spectra (TAS) of (a) Sc-TBAPy, (b) Al-TBAPy and (c) In-TBAPy (upon excitation at 420 nm). Lower panel: steady-state UV-vis absorption spectra (solid lines) and excitation spectra (shaded regions) of (d) Sc-TBAPy, (e) Al-TBAPy, and (f) In-TBAPy.

4.3.4 Investigation of Morphological Characteristics

Our findings showed that the combination of its electronic and optical characteristics made Sc-TBAPy favorable toward photocatalytic HER compared to its Al and In counterparts. Nonetheless, it should be kept in mind that the structural characteristics should not be neglected when exploring photocatalytic activity of MOFs.[76, 34] Sc-TBAPy was selected as the case study and different syntheses conditions were applied to obtain different morphologies.

A structure-capping surfactant (cetyltrimethylammonium bromide (CTAB)) was used during the syntheses, to allow the formation of different morphological characteristics.[76] It was observed that when the synthesis temperature was increased to 120°C and the synthesis was performed for 72 h, the spherical particles of Sc-TBAPy were evolved to rectangular rods (named as “Sc-2", Figure 4.9(a)). When the same synthesis condition for Sc-2 was performed in the absence of the modulator (HCl), smaller rectangular-shaped crystals were obtained (named as “Sc-3", Figure 4.9(b)). PXRD patterns showed that Sc-2 and Sc-3 have comparable patterns to that of Sc-TBAPy (Figure 4.9(c)). Light absorption characteristics of Sc-TBAPy samples were investigated by UV-Vis spectroscopy, demonstrating that all 3 materials have similar visible-light absorption (Figure 4.17).

Sc-2 and Sc-3 samples were investigated as photocatalysts for HER using the same photocatalytic conditions as mentioned before. Sc-3 performed the highest hydrogen evolution rate (82.5 $\mu mol\, g^{-1}\, h^{-1}$), followed by Sc-2 (60.6 $\mu mol\, g^{-1}\, h^{-1}$) and Sc-TBAPy (32.8 $\mu mol\, g^{-1}\, h^{-1}$) (Figure 4.9(d)). Catalytic activity of MOFs can be directly related to the catalyst size where MOFs with the smallest sizes can tend to exhibit superior photocatalytic performance.[77, 123] Previous studies showed that the fraction of catalytic sites on edges and corners mainly determines the electron transfer efficiency, where smaller particles have higher density of these sites.[77, 202] The shape and the facet of MOFs exposed to the catalysis is another important parameter.[76, 126, 34] Therefore, the better performance of Sc-3 might be attributed to the combination of its smallest size among all Sc-TBAPy MOFs, in addition to its exposed facet to the photocatalytic HER.

To compare the degree of crystallinity of Sc-TBAPy and Sc-3 samples, the peak shape were fitted using Gaussian and Lorentzian functions as implemented in TOPAS5, while keeping the other peak shape parameters associated to instrumental effects same for both simulated patterns. From the comparison of Figure 4.11 and Figure 4.15, the average crystalline region size obtained based on the LeBail analysis were 25.2(2) and 41.5(3) nm for samples Sc-TBAPy and Sc-3, respectively. The larger size of crystalline region for Sc-3 compared to Sc-TBAPy confirms its higher degree of long-range order, intuitively known as “higher crystallinity", which can be another factor for a better photocatalytic HER rate.

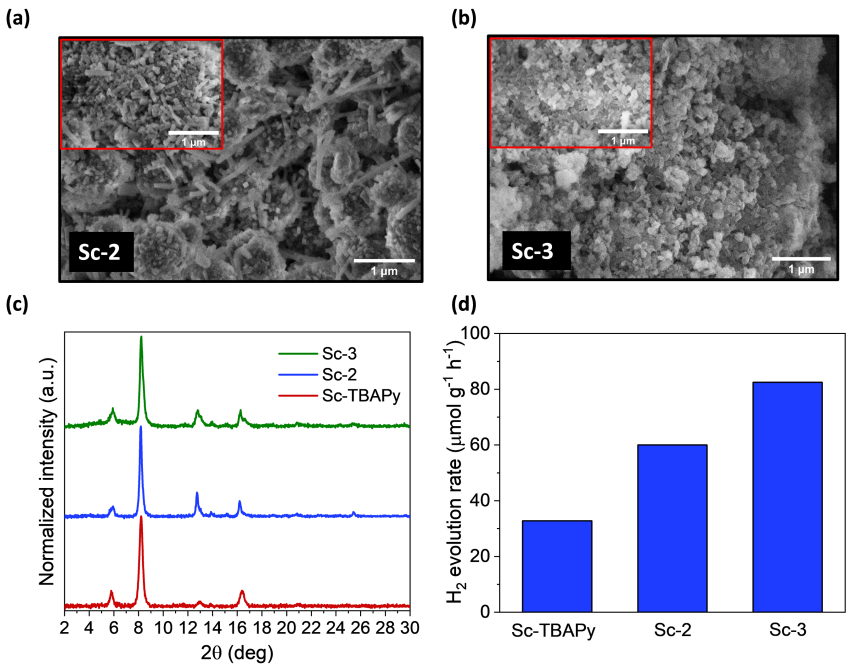

Figure 4.9 – SEM images of (a) Sc-2 and (b) Sc-3 MOFs. (c) PXRD patterns of Sc-2 and Sc-3, showing that all 3 samples have the same crystallographical identity. (d) Photocatalytic HER rates of Sc-TBAPy, Sc-2 and Sc-3.

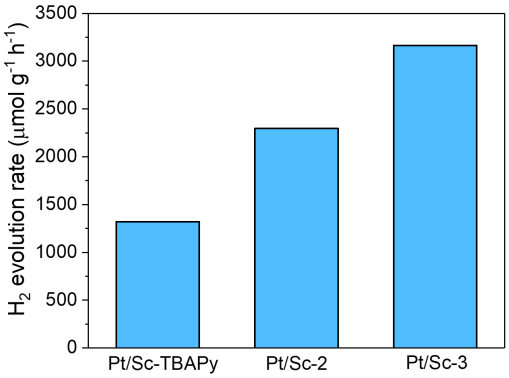

Figure 4.10 – Photocatalytic HER rates of Sc-TBAPy, Sc-2 and Sc-3 in the presence of 3 wt% Pt co-catalyst, showing the improvement in the photocatalytic activity compared to bare MOFs. It can be deduced that the excited electrons are efficiently trapped by Pt co-catalyst, increasing the HER rate.

4.4 Concluding Remarks

In this study, we synthesized a new TBAPy-based MOF with Sc(III) metal centers, which is isostructural to previously reported Al-, In- and Ti-TBAPy MOFs. Sc-TBAPy performs a better photocatalytic HER rate (32.8 $\mu mol\, g^{-1}\, h^{-1}$) compared to its Al and In counterparts (6.3 and 4.7 $\mu mol\, g^{-1}\, h^{-1}$, respectively). Our ab-initio calculations showed that there are some distinctions in the band alignments and band structures of M-TBAPy MOFs. Sc-rod orbitals are found to be located in the CBM in Sc-TBAPy, unlike the cases of its Al and In counterparts, where the CBM is localized on the pyrene orbitals. Interestingly, it was found that the vibrational rotations of the phenyl groups in TBAPy can modify the nature of the CBM in Sc-TBAPy. Our calculations indicated that Sc and Ti metals promote a better electron dispersion around the CBM in the band structure. Optical investigations demonstrated that Sc-TBAPy has an extended visible light absorption compared to Al- and In-TBAPy. nTAS measurements combined with the UV-Vis absorption and the respective excitation spectra inferred that Al- and In-TBAPy suffer from more non-radiative, vibrational losses than Sc-TBAPy. Along with the electronic and optical investigation, morphological characteristics of Sc-TBAPy were modified to optimize the HER performance. With the optimized synthesis conditions of Sc-3, it is possible to increase the HER rate to 82.5 $\mu mol\, g^{-1}\, h^{-1}$.

Different chemical and structural factors come together to determine the photocatalytic HER rates of MOFs. Our study has addressed the understanding of various aspects and these are linked with the HER performances of M-TBAPy MOFs. The isoreticular nature of the selected M-TBAPy MOFs allowed us to explore the impact of using different transition metal elements on the resulting properties of MOFs. Our electronic structure investigation, optical characterization, and photocatalytic HER rates confirm how Sc-TBAPy excels among Al- and

In-TBAPy.

A key factor in the HER performance of the materials was the morphological study. Sc-TBAPy performance was improved considerably by the modification of the shape of the Sc-TBAPy crystals. A similar observation was described by Fan *et al*[76], where the change of morphology of MIL-125 crystals led to higher HER rates. Such enhancement was ascribed primarily to the exposure of specific facets of the crystals. This finding signifies the importance of controlled synthesis conditions for the desired morphological characteristics, that can be impactful for photocatalytic HER efficiency.

The main motivation of this work was to obtain a systematic understanding of the different factors that contribute to the HER. It is therefore interesting to see if we can use this knowledge to improve the catalytic performance of these MOFs. The most interesting case is Sc versus Ti. Our study shows that Sc-TBAPy has the potential to be good HER catalyst but the most likely bottleneck is that the electrons do not reach the water molecules as efficiently as for Ti-TBAPy. A solution to this would be the addition of a co-catalyst. A co-catalyst can attract the excited electrons and reducing the possibility of electron-hole recombination. To test this hypothesis, we combined Pt nanoparticles with the different morphologies of the Sc-TBAPy. We observed that the photocatalytic HER rate of Sc-MOFs can be improved further by their combination with Pt nanoparticles. When Sc-3 was combined with 3 wt% Pt, the HER rate was increased to 3164 $\mu mol\, g^{-1}\, h^{-1}$ (Figure 4.10) and the HER rate even exceeded that of Pt/Ti-TBAPy (1675 $\mu mol\, g^{-1}\, h^{-1}$).[25] Although we have an activity that is almost a factor of two higher than for Pt/Ti-TBAPy, one has to be careful as these two studies have not been performed at exactly the same conditions. Also for Ti-TBAPy, one could expect that changes of the morphology may give higher rates. Nevertheless, it is encouraging to see how our systematic study can show the way on how to improve the catalytic performance of a material that initially (see Figure 4.9) did not look that promising compared to Ti-TBAPy.

We believe that our strategy can be translated to the investigation of other efficient MOFs for photocatalytic HER studies. The exploration of the morphological and electronic properties is of great interest for this proposal hence there is a need for combining such studies. Likewise, the selection of isoreticular MOFs allowed us to explore the effect of different metals, yet this investigation should be extended to different ligands, which can potentially eventuate new MOF chemistry. Based on our observations, we can envision future efforts to have facet-controlled growth of MOF crystals as well as the interaction study with different co-catalyst for the optimization in photocatalytic HER applications.

4.5 Methods

4.5.1 Material Synthesis and Characterization

The synthesis of 4, 4', 4", 4"'-(pyrene-1,3,6,8-tetrayl)tetrabenzoic acid (TBAPy) ligand was performed based on the previously reported procedure.[200] Al-TBAPy and In-TBAPy were

synthesized according to the synthesis methods reported previously.[18, 181] The synthesis for Sc-TBAPy was performed in 12 mL Pyrex reactor, where TBAPy (0.015 mmol, 10 mg) and $Sc(NO_3)_3 \cdot xH_2O$ (0.03 mmol, 6.9 mg) were added to 4 mL of DMF/dioxane/H_2O mixture (2:1:1) followed by adding 10 µl of concentrated HCl. The suspension was sonicated for 15 minutes for the complete dissolution of ligand. The reaction mixture was heated at 85 °C for 12 h, with a heating rate of 2 °C/ min and then cooled to room temperature at a rate of 0.2 °C/ min. The solid was recovered by centrifuge, and washed with DMF in order to remove any recrystallized TBAPy ligand. After drying, the as-made Sc-TBAPy MOF was obtained as a yellow solid powder. The peak indexation of Sc-TBAPy showed that the MOF has an orthorhombic unit cell with experimental cell parameters of a=30.25(8) Å, b= 7.13(1) Å, c=15.32(4) Å, which are in agreement with the reported cell parameters of Ti-TBAPy and In-TBAPy.[25, 181] Le Bail analysis of the collected powder pattern was carried out using TOPAS5 software.[38] The profile fits confirmed that Sc-TBAPy is isostructural to the other M-TBAPy MOFs, with the space group of *Cmmm* (no. 65) (Figure 4.11). Thermogravimetric analysis (TGA) reveals that Sc-TBAPy is stable up to 500 °C (Figure 4.12(a)). Nitrogen adsorption-desorption analysis at 77 K showed that Sc-TBAPy has a Brunauer-Emmett-Teller (BET) surface area of 1197 $m^2 g^{-1}$ (Figure 4.12(b)), which is close to those of Ti-TBAPy (1212 $m^2 g^{-1}$)[25] and In-TBAPy (1189 $m^2 g^{-1}$)[181].

For the synthesis of Sc-2, the same amount of TBAPy (0.015 mmol, 10 mg) and $Sc(NO_3)_3 \cdot xH_2O$ (0.03 mmol, 6.9 mg) were added to 4 ml of DMF/dioxane/H_2O mixture (2:1:1), followed by adding 10 µl of concentrated HCl and 4.38 mg of CTAB. In the case of Sc-3, all the amounts remained the same except from the modulator (HCl), which is excluded from the synthesis. The suspensions were sonicated for 15 min for the complete dissolution of ligand. The reaction mixtures were heated at 120 °C for 72 h, with a heating rate of 2 °C/ min and then cooled to room temperature at a rate of 0.2 °C/ min. Yellow powder samples were recovered by centrifuge, and washed with DMF in order to remove any recrystallized TBAPy ligand.

4.5.2 Computational details

The periodic structures of M-TBAPy (M = Al, In, Sc and Ti) MOFs were optimized using the 65 space group (*Cmmm*) symmetry in CRYSTAL17 code[46]. All the structures were optimized using the PBE0 XC functional along with D3BJ dispersion corrections. Likewise, we further optimized the atomic coordinates of the structures considering the rotation of the benzene groups in the MOFs. Double-ζ basis set pob-DZVP was used to described the organic atoms, while triple-ζ pop-TZVP basis was used to described the metal atoms. The shrinking factors for the diagonalization of the Kohn-Sham matrix in the reciprocal space has been set to 4 for the Monkhorst-Pack and 4 for the Gilat nets. Bandstructures calculations were computing using the reciprocal space path within the first Brillouin zone (BZ) in the primitive cell using the Seek-path package[89] using the primitive cell.

The study of the optical excitations and electron polarons in the periodic structures was per-

formed in the CP2K code[111]. All structures were optimized initially with the PBE functional followed by second optimization using the PBE0 exchange and correlation (XC) functional with the D3BJ dispersion correction in both cases. The double-ζ polarization MOLOPT basis sets were used to describe organic atoms, while a triple-ζ was used for metal atoms. The PBE0 calculations used the auxiliary MOLOPT-ADMM basis functions: cFIT8 for Al, cFIT12 for In , Sc and Ti, and pFIT3 for non-metal atoms. The Truncated Coulomb operator with a long-range correction was employed for the Hartree-Fock exchange of hybrid calculations. Both symmetric and rotated phenyl structures were considered as well using a 1x3x1 super cell of the conventional cell and a 4x1x1 of the primitive cell, respectively. The use of 2x2x2 Monkhorst-Pack scheme in the initial PBE optimation guarantees the symmetrical orientation of the phenyl groups as an starting point for the PBE0 optimizations. On the other hand, the starting configuration of the rotated structure for the PBE0 optimization is obtained by rotating the phenyl groups and without the use of K-points during the PBE optimization. The truncation radius is half of the smallest edge of the unit cell (7.5 Å), and the long-range part of the exchange is computed using the PBE exchange. All calculations conducted with PBE0 used the orbital transformation (OT) method. Electron polaron geometries calculations were conducted using 45% of Hartree-Fock in order to impose localization of the electron. The LR-TDDFT scheme including the Tamm-Dancoff approximation was used to predict the optical bandgap of the systems. To align the conduction and valence band energies with vacuum, the methodology proposed by Butler *et al* [22] was used to calculate the vacuum level in the periodic systems. This method consists of evaluating the average potential within a small sphere at the pore centre.

4.6 Supplementary Information

4.6.1 Apparent quantum yield (AQY) determination

To calculate AQY values, first the photocatalytic reactions were carried out using the same photocatalytic solution and setup which was mentioned previously. The hydrogen evolution was investigated under 400 and 450 nm radiation by using relative band pass filters with the 300 W Xenon lamp. Below, the moles of hydrogen generated for each sample (in 3 hours) are given:

Table 4.2 – Hydrogen evolution performances of M-TBAPy MOFs irradiated at 400 and 450 nm

Hydrogen generation in 3 hours (mol)		
MOF Name	**400 nm**	**450 nm**
In-TBAPy	negligible	negligible
Al-TBAPy	negligible	$6.450 * 10^{-8}$
Sc-TBAPy	$6.550 * 10^{-8}$	$3.270 * 10^{-7}$

AQY values were calculated based on the formula below:

$$AQY\,(\%) = 2 * \frac{\frac{n_{rate}}{min}}{\frac{n_{photons}}{min}} * 100$$

AQY values for Sc-TBAPy and Al-TBAPy can be found as 0.076% and 0.076%, and 0.364% and negligible at 400 nm and 405 nm, respectively.

4.6.2 Characterizations and photocatalytic experiments

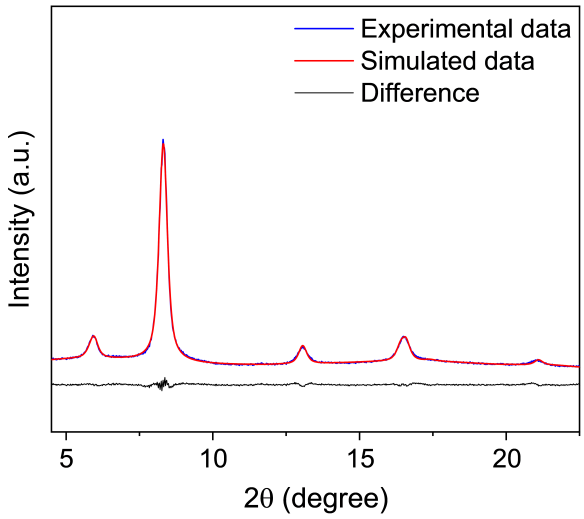

Figure 4.11 – Le Bail fit obtained from the PXRD data of Sc-TBAPy MOF. Orthorhombic space group *Cmmm* (no. 65), a = 30.25(8) Å, b = 7.13(1) Å, c = 15.32(4) Å, V = 3305(14) Å^3. GOF parameters: wRp = 0.024, Rp = 0.019.

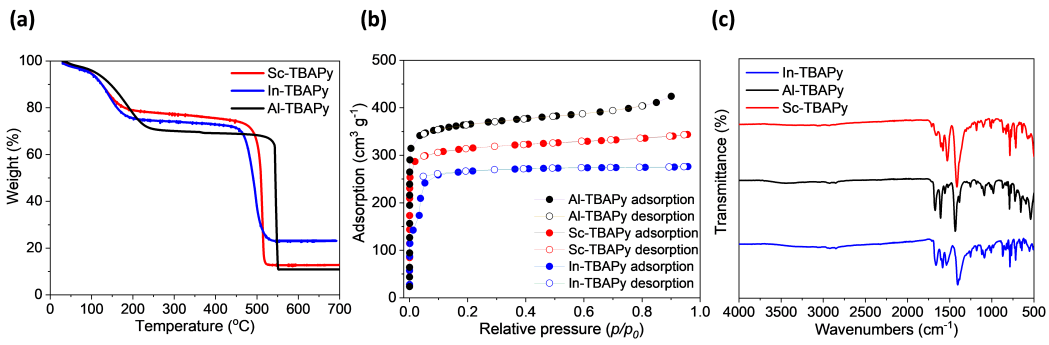

Figure 4.12 – (a) Thermogravimetric analysis (TGA) curves, (b) N_2 adsorption and desorption isotherms (at 77 K), and (c) Fourier transform infrared (FTIR) spectra of Sc-TBAPy, In-TBAPy and Al-TBAPy.

Table 4.3 – Photoluminescence lifetimes (t_1) and (t_2) of M-TBAPy MOFs recorded at 500 nm wavelength, based on the photoluminescence emission peaks of the MOFs.

MOF	t_1 (ns)	t_2 (ns)
Al-TBAPy	2.72	13.42
In-TBAPy	2.84	12.18
Sc-TBAPy	2.40	11.70

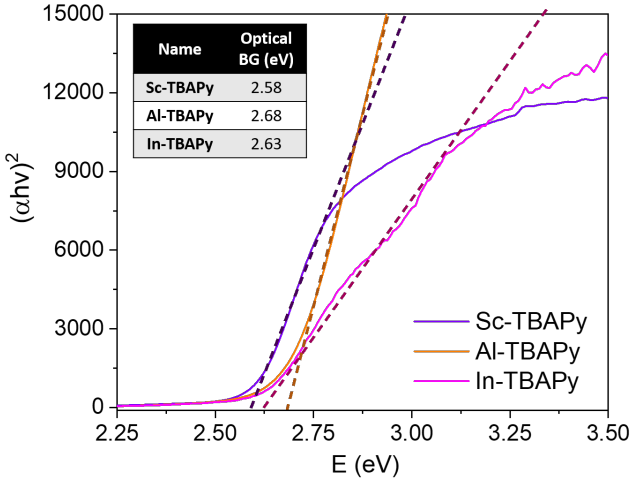

Figure 4.13 – Tauc plots of the three M-TBAPy MOFs.

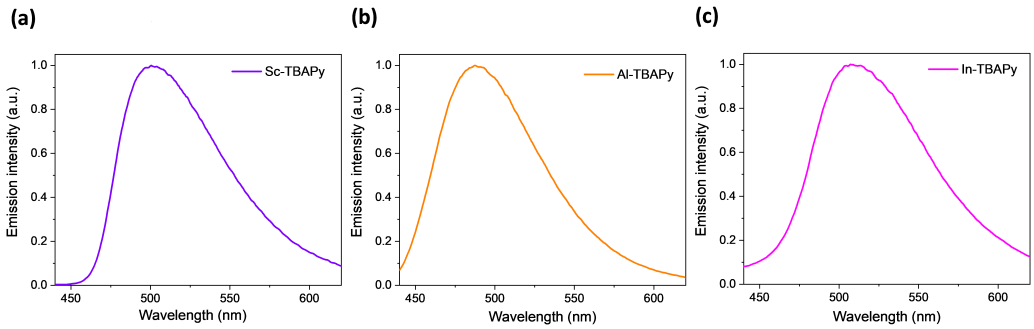

Figure 4.14 – PL spectra of (a) Sc-TBAPy, (b) Al-TBAPy and (c) In-TBAPy. The MOFs were suspended in acetonitrile and excited at 420 nm.

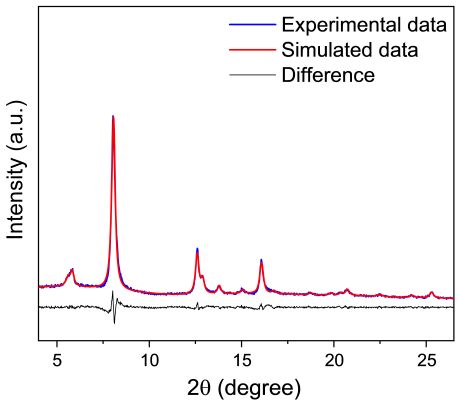

Figure 4.15 – Le Bail fit obtained from the PXRD of Sc-3 MOF. Orthorhombic space group *Cmmm* (no. 65), a = 30.62(4) Å, b = 7.25(1) Å, c = 15.96 (2) Å, V = 3544(7) Å^3. GOF parameters: wRp = 0.055, Rp = 0.042.

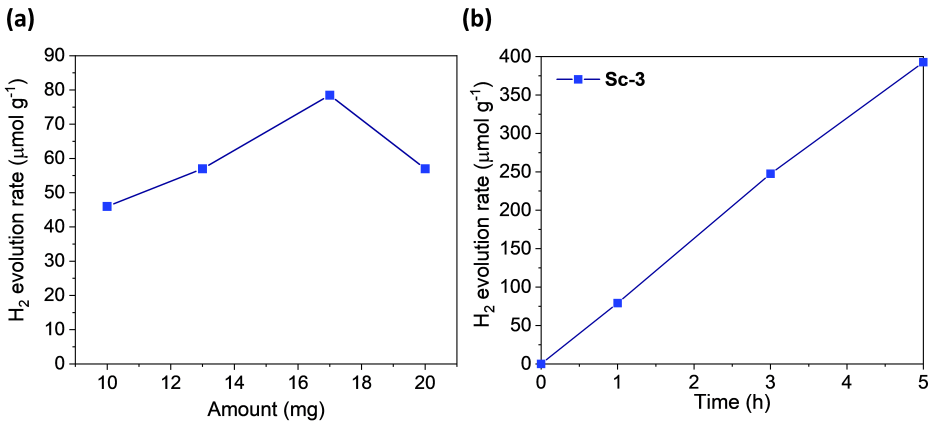

Figure 4.16 – (a) Optimization of the amount of Sc-3 used in HER, upon visible light exposure ($\lambda \geq 420$ nm). Reaction conditions: 13.93 ml acetonitrile, 2.79 ml TEA and 0.279 ml H_2O. The experiment duration was 5 h. The optimized amount (17 mg) was used for all other M-TBAPy MOFs. (b) The HER rate of Sc-3 for 5 h of photocatalytic reaction.

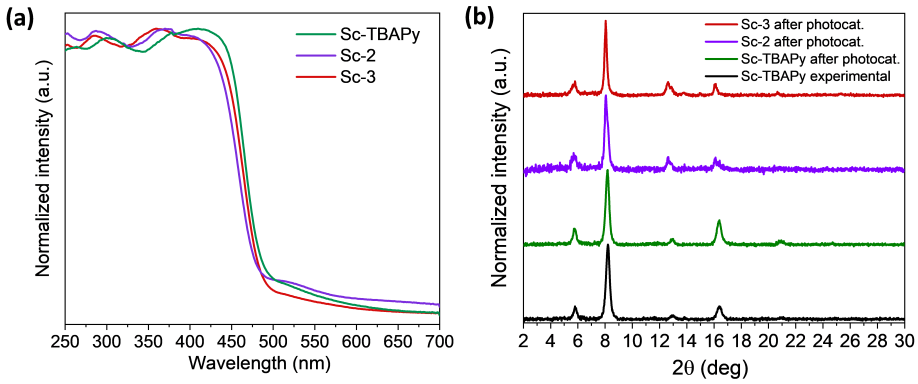

Figure 4.17 – (a) UV-Vis spectra of Sc-TBAPy, Sc-2 and Sc-3 samples, showing their similar light absorption capability. (b) PXRD patterns of Sc-TBAPy, Sc-2, and Sc-3 samples after photocatalysis, showing that all 3 MOFs are stable after the HER.

4.6.3 Band structure calculations

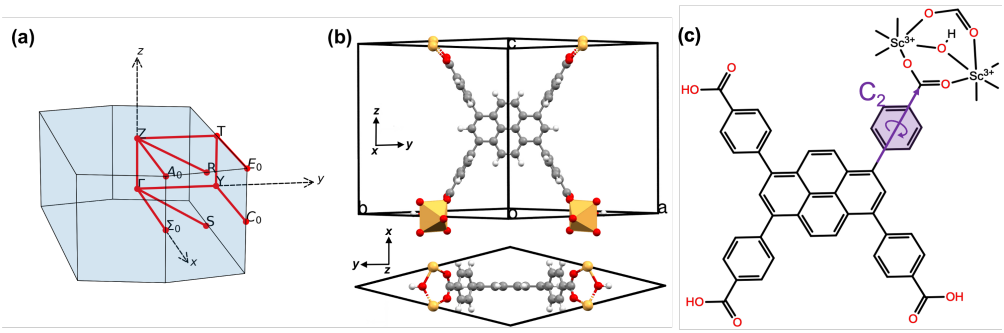

Figure 4.18 – (a) First Brillouin zone of the reticular pyrene-based MOFs. The high symmetrical points and paths are represented in red. (b) Two side views of the primitive cell representation of the pyrene-based MOFs using the *Cmmm* space group. The Cartesian vectors are depicted in all figures to correlate the high-symmetry path and the atomic coordinates. (c) Rotational axis of the phenyl group in the TBAPy ligand in the M-TBAPy MOFs.

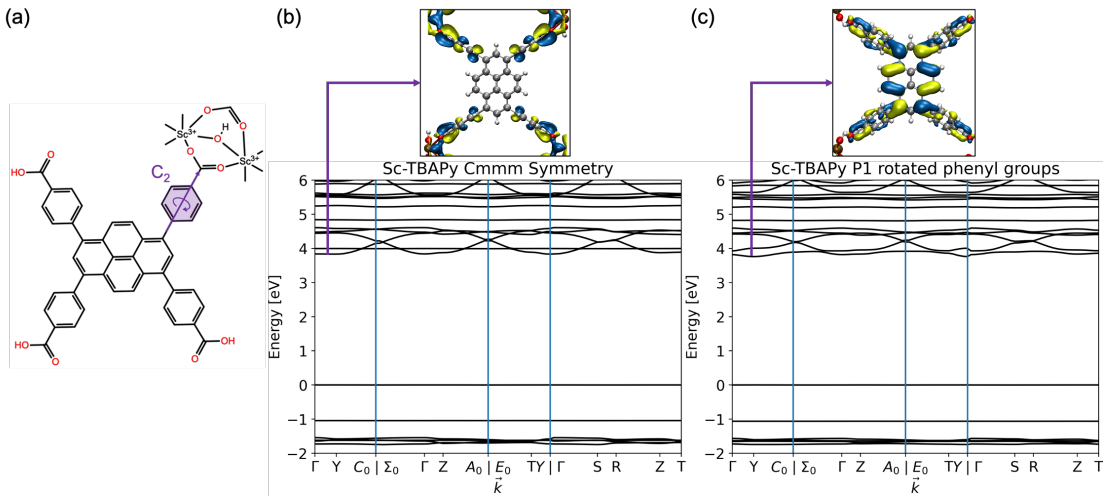

Figure 4.19 – (a) Rotational axis of the phenyl group in the TBAPy ligand in the Sc-TBAPy MOF. Band structure calculations and Conduction band minimum crystal orbital of Sc-TPBAPy with (b) Cmmm space group (Symmetrical structure) and (c) Phenyl rings rotated structure.

4.6.4 Vibrational mode of the phenyl rotations

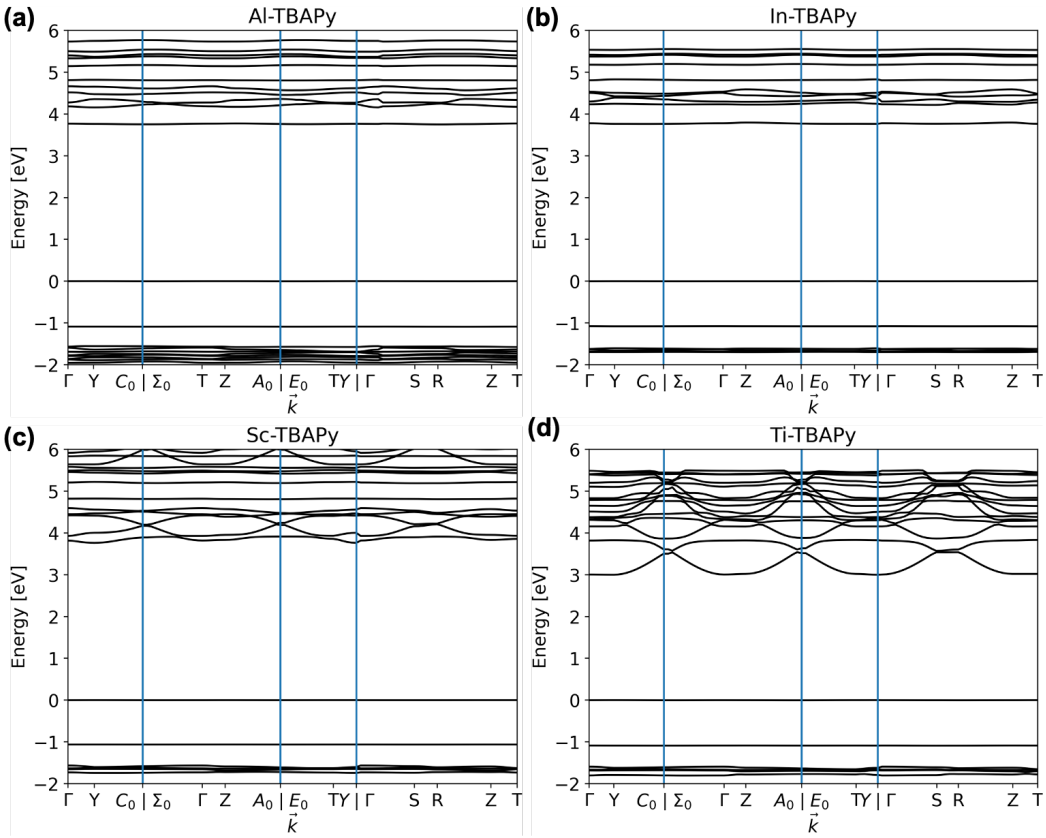

Figure 4.20 – Band structure calculations of the pyrene-based MOFs using PBE0 functional (CRYSTAL17) with phenyl rings rotated structure. (a) Al-TBAPy , (b) In-TBAPy , (c) Sc-TBAPy and (d) Ti-TBAPy.

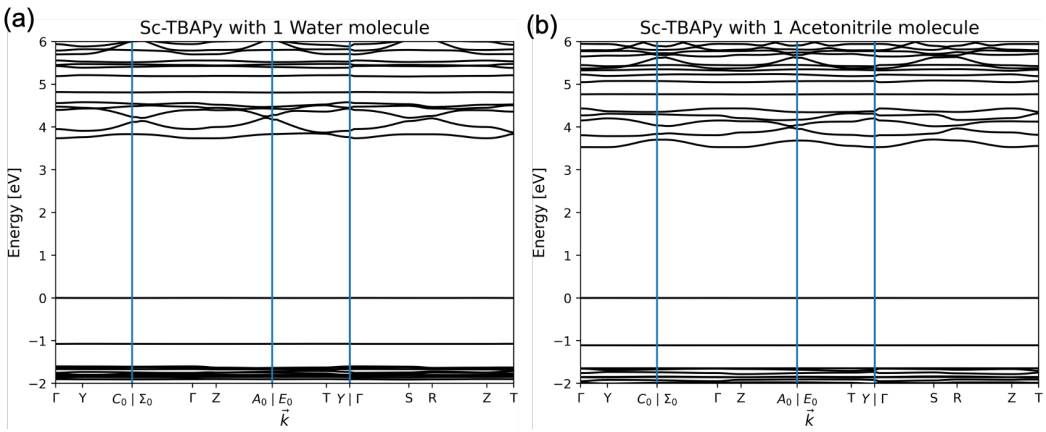

Figure 4.21 – Band structure calculations of the geometrical optimization of Sc-TBAPy structure containing one molecule of (a) H_2O and (b) Acetonitrile in the pore.

4.6.5 Electron polarons in M-TBAPy MOFs

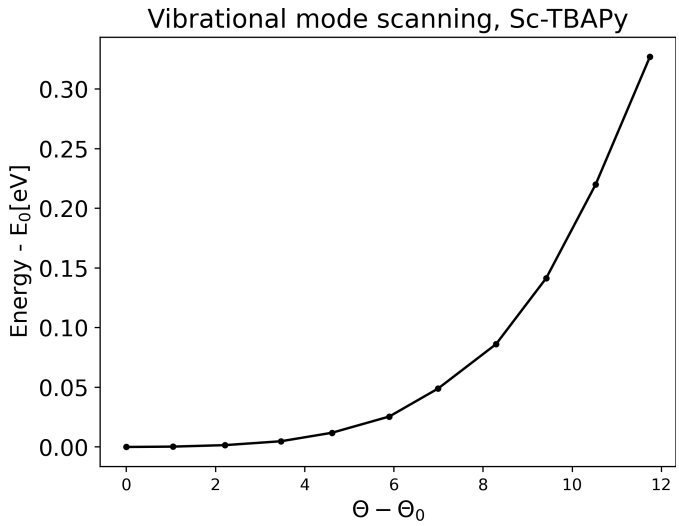

Figure 4.22 – Vibrational mode scanning displacement involving the phenyl rotation. E_0 is the ground state minimum energy with a rotational angle $\Theta_0 = 89.0$

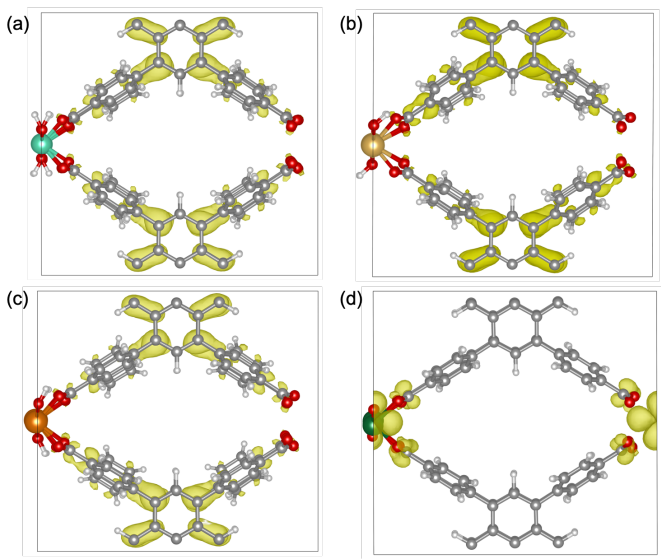

Figure 4.23 – Electron polaron crystal orbital in (a) Al-TBAPy , (b) In-TBAPy , (c) Sc-TBAPy , and (d) Ti-TBAPy. PBE0 functional where the Hartree-Fock percentage is set to 45 %.

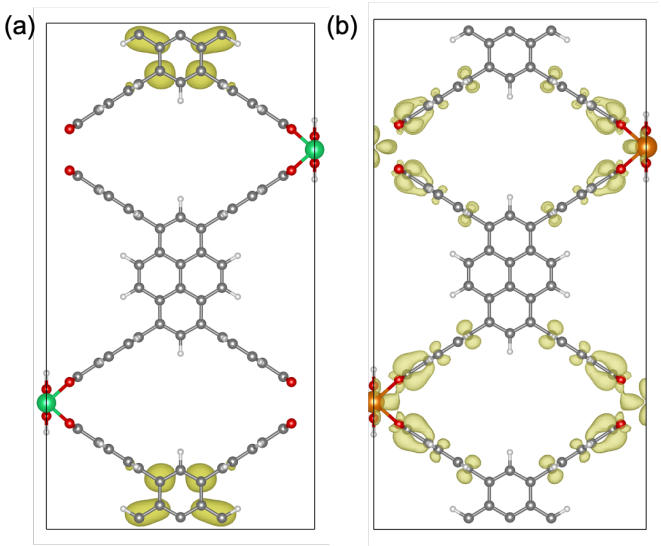

Figure 4.24 – Electron polaron crystal orbital of the Cmmm space group structures of (a) Al-TBAPy and (b) Sc-TBAPy. PBE0 functional where the Hartree-Fock percentage is set to 45 %.

5 Conclusions and Future Research

The increasing interest in MOFs for photocatalytic applications faces the challenge of discovering optimal materials among millions of possibilities, given MOFs' intrinsic modular nature. The main problem for such a purpose is understanding and predicting the photochemical and photophysical properties of MOFs. This challenge is not unique to MOFs since theoretical chemistry faces the same difficulties describing the fundamental physics and chemistry for excited-state processes. Yet, current computational chemistry methods can still provide descriptors for the appropriate questions involving the phenomena of interest. In this thesis, we have investigated the photophysical properties of MOFs involving the three main steps in photocatalysis (light absorption, charge separation, and charge transfer) using DFT/LR-TDDFT calculations.

The calculation of the electronic properties of solids is restricted to generalized gradient approximation (GGA) functionals within DFT. Hybrid and meta-GGA functional, although computationally costly, can be used as well. The use of more advanced approximations of the exchange-correlation functional brings more accuracy to the description of the electronic problem. In this regard, MOFs' inorganic-organic nature poses a challenge for DFT. The presence of transition metal atoms requires the use of hybrid functionals to get an accurate description and to avoid artifacts from GGA functionals. On the other hand, the organic ligand orbitals can have a strong effect on the fundamental band gap of a MOF. This effect can place the HOMO and LUMO orbitals of the ligand in the valence and conduction band of the periodic MOF, respectively. If this is the case, GGA and hybrid functionals will predict the fundamental band gap value of the MOF as one of the isolated organic ligands. This behavior is due to the lack of GGA and hybrid functionals to capture the gap re-normalization of going from an isolated molecule to a periodic crystal. One strategy to overcome such drawbacks can be to include the effect of the dielectric response along with optimally tuned range-separated functionals. These functionals display the correct gap-renormalization description of the band gap when used in organic crystals. Future developments should focus on the implementation of these functionals and tuning strategies in current DFT packages for periodic systems.

DFT provides some reliability of the ground states properties of MOFs, however the picture is

different when excited states are involved. When it comes to the light absorption of MOFs, LR-TDDFT provides a formally exact description of excited states at a reasonable computational cost. The presence of organic ligand in MOFs leads to localized excitons displaying strong excitonic effects. The use of GGA functional with LR-TDDFT in MOFs suffers from the wrong description of excitonic effects. This problem can be solved by considering hybrid functionals which capture such excitonic effects. Yet, there can be more artifacts from the choice of approximations used. The unique photophysics of MOFs can easily display charge transfer states, which LR-TDDFT can yield substantial errors with GGA and hybrid functionals. One simple solution to mitigate these errors is the use of range-separated functionals. However, due to current implementation, LR-TDDFT range-separated functionals for MOFs usage are restricted to representative cluster models. This restriction can be a limiting factor since not all the MOFs can be reduced to a representative cluster depending on the crystal topology. We envisioned the future development of LR-TDDFT for periodic crystals with range-separated functional for this restriction.

MOFs' electronic structure is different from inorganic semiconductors. Typical MOFs, have a low atomic density and strong localization of the electronic wave function (characteristic of Werner-type coordination complexes). This localization causes the MOFs to present little or no band dispersion behaving as insulators, and in the case of photocatalysis, this could be a problem. One dimensional topology for the metal clusters displays curve dispersion. The exploration of metal clusters with this topology could be an attempt to introduce band dispersion on MOFs. Likewise, the combination of different coordination chemistry and binary transition metal atoms should be considered as well. Such a combination can lead to the discovery of MOF-photocatalyst with improved dispersion properties. The development of computational strategies for in-silico generation of MOFs structures can play an important role. Another topology to consider is two-dimensional MOFs. This topology has also shown more band dispersion and even metallic behavior on MOFs. Likewise, this topology can be important from a technology point of view since it can be integrated into thin-film technology. Current, visible light-responsive photocatalytic MOFs are in powder form, which limits their industrial applications. Therefore, computational studies should also address the study of 2D MOFs with the combination of other 2D materials like COFs.

Most of the photocatalytic properties of MOFs described in this thesis are limited to the electronic and photophysical properties. However, there are more aspects to explore for MOF-based photocatalysts. For instance, the need for sacrificial agents for the photocatalytic reaction. Hence, there is a need to develop computational methodologies to aid the prediction of MOF-based systems without needing additive sacrificial agents. To accomplish such property it might be necessary to explore MOF-based photocatalysts having bi-functionality (different ligands and/or metal nodes) or to be combined with other MOFs or COFs. There is still another computational challenge for photocatalysis in MOFs. This challenge is the final fundamental step of photocatalysis, the reaction. The study of the reduction (or oxidation) reaction in the excited states is a fundamental question related to the dynamical properties of photoexcited systems. Computational chemistry methods developed for such phenomena are

still limited to a reduced number of atoms. On the other hand, the quantum mechanical nature of the dynamics of the excited states might require the inclusion of nonadiabatic interactions. Hence, the size and number of atoms of MOFs represent an immense computational cost for methods for excited states dynamics. Nevertheless, the computational study of photochemical properties of MOFs is needed for discovering efficient photocatalysts. Future developments should address photoinduced phenomena in MOFs at a reasonable computational cost where accuracy and efficiency are balanced.

Andrés Adolfo Ortega Guerrero

Cell phone: +41 77 966 52 64 Home phone: +57 2 3048269
email: andres.ortegaguerrero@epfl.ch
Born: December 15, 1990—Cali, Colombia

Education

2008-2014 *Bachelor of Electronics Engineering*, Universidad del Valle, Cali, Colombia
Thesis: "Simulation of the interaction between a carbon nanotube and an ion channel". Thesis Advisors: Prof. Jaime Velasco-Medina and John Michael Espinosa-Duran

2015-2017 *Erasmus Mundus Master of Nanoscience and Nanotechnology*, Major: Biophysics, Katholieke Universiteit Leuven, Leuven, Belgium and Technische Universität Dresden, Dresden, Germany
Thesis: "Computational study of a monomer for 2D polymers confined on the surface of water". Thesis Advisors: Prof. Gianaurelio Cuniberti and Prof. Michel Houssa.

Nov 2017 - currently *Doctoral program in chemistry and chemical engineering* , Swiss Federal Institute of Technology in Lausanne (EPFL), Switzerland
Thesis: "Computational studies for the description of electronic and optical properties for photocatalysis in Metal Organic Frameworks", Advisor: Prof. Berend Smit.

Research Interests

Computational chemistry simulations for optical and electronic properties of Metal-organic frameworks for photocatalysis applications.
Computational chemistry simulations using embedding methods for adsorption and catalysis in metal-organic frameworks.
Computational nanoscale theory modelling of biological and inorganic materials for nanotechnology and bionanotechnology applications.

Awards and Honors

2015-2017 *Erasmus Mundus Master of Nanoscience and Nanotechnology Consortium Scholarship*
2014 *Laureated Thesis*, Thesis Title "Simulation of the interaction between a carbon nanotube and an ion channel", Universidad del Valle.
Full academic scholarship based on academic merit, Universidad del Valle (Semesters: II,IV, V)

Research Experience

2012-2014 *Universidad de Valle*, School of Electrical and Electronics Engineering, Bionanoelectronics Research Group, Advisor: Jaime Velasco-Medina, Desig of drug- delivery nanosystems based on carbon nanotubes, Activities: Molecular dynamics simulation exploring the interaction of a CNT and the TRPV1 ion channel and the diffusion of an anticancer drug molecule through TRPV1.

Feb 2015 - Sep 2015 *Universidad ICESI (Cali,Colombia)*, School of Engineering, i2T Research Group, Advisor: Carlos Alberto Arce Lopera, Activities: Acoustical study of the Aedes Aegypti mosquito, Data acquisition, Machine learning techniques and processing of Mosquito Wingbeat.

Feb 2016 - Jun 2016 *KU Leuven (Leuven,Belgium)*, Lab Project Work, Advisor: Prof. Dr. Michel Houssa, Activities: Defects and oxidation of monolayer SnS_2: A first-principles study.

Oct 2016 - August 2017 *Technische Universität Dresden (Dresden,Germany)*, Chair of Materials Science and Nanotechnology, Advisor: Dr. Alexander Croy, Activities: Implementation of a Valence Force Field for Phospherene in LAMMPS, Computational study of building-blocks of 2D polymers confined on the surface of water (Master Thesis).

Teaching Experience

Sept. 2012 – Jul. 2014 *Universidad del Valle*, School of Electrical and Electronics Engineering. Teaching Assistant: Courses on (1) "Electronic circuits", (2) "Power electronics", (3) "Electronic Instrumentation" (4) "Operational amplifier circuits" for undergraduate electronics technology students.

Mar. 2015 - Apr. 2015 *Universidad del Valle*, School of Electrical and Electronics Engineering. Teaching Assistant: Nanoengineering and Nanotechnology (Master graduate course), Professor: Jaime Velasco-Medina.

2018 - 2020 *Swiss Federal Institute of Technology in Lausanne, EPFL* Teaching Assistant: "Understanding advanced molecular simulation"(Master graduate course), Fall semesters, Professor: Berend Smit.

Papers – Peer-Reviewed Journals

Google Scholar
Andres Ortega-Guerrero

Skills

Computer

Molecular Modelling and Simulation: CP2k, Quantum-Espresso, Gaussian, Gromacs, SIESTA, CRYSTAL, DFTB+, LAMMPS
Operative Systems: Linux, Windows, Mac OS.
Programming: Python, C++, MATLAB.

Language

Spanish (Mother tongue).
English (Level: Proficient)

Last updated: September 10, 2021 •

Bibliography

[1] Carlo Adamo and Vincenzo Barone. "Toward reliable density functional methods without adjustable parameters: The PBE0 model". In: *J. Chem. Phys.* 110.13 (1999), pp. 6158–6170. DOI: 10.1063/1.478522. eprint: https://doi.org/10.1063/1.478522. URL: https://doi.org/10.1063/1.478522.

[2] Alexandre S. Alexandrov and Jozef T. Devreese. "Bipolaron". In: *Advances in Polaron Physics*. Berlin, Heidelberg: Springer Berlin Heidelberg, 2010, pp. 97–113. ISBN: 978-3-642-01896-1. DOI: 10.1007/978-3-642-01896-1_4. URL: https://doi.org/10.1007/978-3-642-01896-1_4.

[3] M. D. Allendorf et al. "Luminescent metal-organic frameworks". In: *Chem. Soc. Rev.* 38 (5 2009), pp. 1330–1352. DOI: 10.1039/B802352M. URL: http://dx.doi.org/10.1039/B802352M.

[4] Cigdem Altintas, Ilknur Erucar, and Seda Keskin. "High-Throughput Computational Screening of the Metal Organic Framework Database for CH4/H2 Separations". In: *ACS Applied Materials & Interfaces* 10.4 (2018). PMID: 29313343, pp. 3668–3679. DOI: 10.1021/acsami.7b18037. eprint: https://doi.org/10.1021/acsami.7b18037. URL: https://doi.org/10.1021/acsami.7b18037.

[5] Samantha L. Anderson et al. "Taking lanthanides out of isolation: tuning the optical properties of metal–organic frameworks". In: *Chem. Sci.* 11 (2020), pp. 4164–4170. DOI: 10.1039/D0SC00740D. URL: http://dx.doi.org/10.1039/D0SC00740D.

[6] Edwin Argueta et al. "Molecular Building Block-Based Electronic Charges for High-Throughput Screening of Metal–Organic Frameworks for Adsorption Applications". In: *Journal of Chemical Theory and Computation* 14.1 (2018). PMID: 29227644, pp. 365–376. DOI: 10.1021/acs.jctc.7b00841. eprint: https://doi.org/10.1021/acs.jctc.7b00841. URL: https://doi.org/10.1021/acs.jctc.7b00841.

[7] Alex Aziz et al. "Porphyrin-based metal-organic frameworks for solar fuel synthesis photocatalysis: band gap tuning via iron substitutions". In: *J. Mater. Chem. A* 5 (2017), pp. 11894–11904. DOI: 10.1039/C7TA01278K. URL: http://dx.doi.org/10.1039/C7TA01278K.

[8] E. J. Baerends. "From the Kohn–Sham band gap to the fundamental gap in solids. An integer electron approach". In: *Phys. Chem. Chem. Phys.* 19 (2017), pp. 15639–15656. DOI: 10.1039/C7CP02123B. URL: http://dx.doi.org/10.1039/C7CP02123B.

[9] E. J. Baerends, O. V. Gritsenko, and R. van Meer. "The Kohn–Sham gap, the fundamental gap and the optical gap: the physical meaning of occupied and virtual Kohn–Sham orbital energies". In: *Phys. Chem. Chem. Phys.* 15 (2013), pp. 16408–16425. DOI: 10.1039/C3CP52547C. URL: http://dx.doi.org/10.1039/C3CP52547C.

[10] E.J Baerends et al. "A DFT/TDDFT interpretation of the ground and excited states of porphyrin and porphyrazine complexes". In: *Coord. Chem. Rev.* 230.1 (2002), pp. 5–27. ISSN: 0010-8545. DOI: https://doi.org/10.1016/S0010-8545(02)00093-0. URL: http://www.sciencedirect.com/science/article/pii/S0010854502000930.

[11] Alankriti Bajpai et al. "Single Crystal-to-Single Crystal Site-Selective Postsynthetic Metal Exchange in a Zn–MOF Based on Semi-Rigid Tricarboxylic Acid and Access to Bimetallic MOFs". In: *Chemistry – A European Journal* 21.7 (2014), pp. 2759–2765. DOI: 10.1002/chem.201406098. eprint: https://onlinelibrary.wiley.com/doi/pdf/10.1002/chem.201406098. URL: https://onlinelibrary.wiley.com/doi/abs/10.1002/chem.201406098.

[12] Rudi Berera, Rienk van Grondelle, and John TM Kennis. "Ultrafast transient absorption spectroscopy: principles and application to photosynthetic systems". In: *Photosynthesis research* 101.2 (2009), pp. 105–118.

[13] Luca Bertini et al. "Quantum Chemical Investigations of Reaction Paths of Metalloenzymes and BiomimeticModels – The Hydrogenase Example". In: *Atomistic Approaches in Modern Biology: From Quantum Chemistry to Molecular Simulations.* Ed. by Markus Reiher. Berlin, Heidelberg: Springer Berlin Heidelberg, 2007, pp. 1–46. ISBN: 978-3-540-38085-6. DOI: 10.1007/128_2006_080. URL: https://doi.org/10.1007/128_2006_080.

[14] Srijana Bhandari et al. "Fundamental Gaps of Condensed-Phase Organic Semiconductors from Single-Molecule Calculations using Polarization-Consistent Optimally Tuned Screened Range-Separated Hybrid Functionals". In: *J. Chem. Theory Comput.* 14.12 (2018), pp. 6287–6294. DOI: 10.1021/acs.jctc.8b00876. eprint: https://doi.org/10.1021/acs.jctc.8b00876. URL: https://doi.org/10.1021/acs.jctc.8b00876.

[15] P. J. Boddy. "Oxygen Evolution on Semiconducting TiO[sub 2]". In: *Journal of The Electrochemical Society* 115.2 (1968), p. 199. DOI: 10.1149/1.2411080. URL: https://doi.org/10.1149/1.2411080.

[16] David N. Bowman et al. "Excited-state absorption in tetrapyridyl porphyrins: comparing real-time and quadratic-response time-dependent density functional theory". In: *Phys. Chem. Chem. Phys.* 19 (2017), pp. 27452–27462. DOI: 10.1039/C7CP04567K. URL: http://dx.doi.org/10.1039/C7CP04567K.

[17] Peter G Boyd, Yongjin Lee, and Berend Smit. "Computational development of the nanoporous materials genome". In: *Nature Reviews Materials* 2.8 (2017), pp. 1–15.

[18] Peter G Boyd et al. "Data-driven design of metal–organic frameworks for wet flue gas CO_2 capture". In: *Nature* 576.7786 (2019), pp. 253–256.

[19] Peter G. Boyd and Tom K. Woo. "A generalized method for constructing hypothetical nanoporous materials of any net topology from graph theory". In: *CrystEngComm* 18 (21 2016), pp. 3777–3792. DOI: 10.1039/C6CE00407E. URL: http://dx.doi.org/10.1039/C6CE00407E.

[20] Silvia E Braslavsky. "Glossary of terms used in photochemistry, (IUPAC Recommendations 2006)". In: *Pure Appl. Chem.* 79.3 (2007), pp. 293–465.

[21] Giovanni Bussi, Davide Donadio, and Michele Parrinello. "Canonical sampling through velocity rescaling". In: *The Journal of Chemical Physics* 126.1 (2007), p. 014101. DOI: 10.1063/1.2408420. eprint: https://doi.org/10.1063/1.2408420. URL: https://doi.org/10.1063/1.2408420.

[22] Keith T. Butler, Christopher H. Hendon, and Aron Walsh. "Electronic Chemical Potentials of Porous Metal–Organic Frameworks". In: *Journal of the American Chemical Society* 136.7 (2014). PMID: 24447027, pp. 2703–2706. DOI: 10.1021/ja4110073. eprint: https://doi.org/10.1021/ja4110073. URL: https://doi.org/10.1021/ja4110073.

[23] Elena Caballero-Mancebo et al. "Unravelling Why and to What Extent the Topology of Similar Ce-Based MOFs Conditions their Photodynamic: Relevance to Photocatalysis and Photonics". In: *Adv. Sci.* 6.19 (2019), p. 1901020.

[24] María Cabrero-Antonino et al. "Design of cost-efficient and photocatalytically active Zn-based MOFs decorated with Cu2O nanoparticles for CO2 methanation". In: *Chem. Commun.* 55 (73 2019), pp. 10932–10935. DOI: 10.1039/C9CC04446A. URL: http://dx.doi.org/10.1039/C9CC04446A.

[25] Amandine Cadiau et al. "A Titanium Metal–Organic Framework with Visible-Light-Responsive Photocatalytic Activity". In: *Angew. Chem.* 132.32 (2020), pp. 13570–13574.

[26] Joaquín Calbo, Matthias J. Golomb, and Aron Walsh. "Redox-active metal–organic frameworks for energy conversion and storage". In: *J. Mater. Chem. A* 7 (28 2019), pp. 16571–16597. DOI: 10.1039/C9TA04680A. URL: http://dx.doi.org/10.1039/C9TA04680A.

[27] Gloria Capano et al. "On the Electronic and Optical Properties of Metal–Organic Frameworks: Case Study of MIL-125 and MIL-125-NH2". In: *J. Phys. Chem. C* 124.7 (2020), pp. 4065–4072. DOI: 10.1021/acs.jpcc.9b09453. eprint: https://doi.org/10.1021/acs.jpcc.9b09453. URL: https://doi.org/10.1021/acs.jpcc.9b09453.

[28] M.E. Casida, A. Ipatov, and F. Cordova. "Linear-Response Time-Dependent Density Functional Theory for Open-Shell Molecules". In: *Time-Dependent Density Functional Theory*. Ed. by Miguel A.L. Marques et al. Berlin, Heidelberg: Springer Berlin Heidelberg, 2006, pp. 243–257. ISBN: 978-3-540-35426-0. DOI: 10.1007/3-540-35426-3_16. URL: https://doi.org/10.1007/3-540-35426-3_16.

[29] Mark E. Casida. "Time-Dependent Density Functional Response Theory for Molecules". In: *Recent Advances in Density Functional Methods*. Ed. by Delano P Chong. Singapore: World Scientific, 1995. Chap. Time-Dependent Density Functional Response Theory for Molecules, pp. 155–192. DOI: 10.1142/9789812830586_0005. eprint: https://www.worldscientific.com/doi/pdf/10.1142/9789812830586_0005. URL: https://www.worldscientific.com/doi/abs/10.1142/9789812830586_0005.

[30] Jasmina Hafizovic Cavka et al. "A New Zirconium Inorganic Building Brick Forming Metal Organic Frameworks with Exceptional Stability". In: *Journal of the American Chemical Society* 130.42 (2008). PMID: 18817383, pp. 13850–13851. DOI: 10.1021/ja8057953. eprint: https://doi.org/10.1021/ja8057953. URL: https://doi.org/10.1021/ja8057953.

[31] M. K. Y. Chan and G. Ceder. "Efficient Band Gap Prediction for Solids". In: *Phys. Rev. Lett.* 105 (19 2010), p. 196403. DOI: 10.1103/PhysRevLett.105.196403. URL: https://link.aps.org/doi/10.1103/PhysRevLett.105.196403.

[32] Agisilaos Chantzis et al. "Is the Tamm-Dancoff Approximation Reliable for the Calculation of Absorption and Fluorescence Band Shapes?" In: *J. Chem. Theory Comput.* 9.10 (2013), pp. 4517–4525. DOI: 10.1021/ct400597f. eprint: https://doi.org/10.1021/ct400597f. URL: https://doi.org/10.1021/ct400597f.

[33] Ting Chen et al. "Understanding the control of singlet-triplet splitting for organic exciton manipulating: a combined theoretical and experimental approach". In: *Scientific reports* 5.1 (2015), pp. 1–11.

[34] Xiao-Mei Cheng et al. "Enhanced Photocatalytic CO_2 Reduction Activity over NH2-MIL-125(Ti) by Facet Regulation". In: *ACS Catal.* 11 (2020), pp. 650–658.

[35] Yongchul G. Chung et al. "Computation-Ready, Experimental Metal–Organic Frameworks: A Tool To Enable High-Throughput Screening of Nanoporous Crystals". In: *Chemistry of Materials* 26.21 (2014), pp. 6185–6192. DOI: 10.1021/cm502594j. eprint: https://doi.org/10.1021/cm502594j. URL: https://doi.org/10.1021/cm502594j.

[36] Andrew J. Clough et al. "Metallic Conductivity in a Two-Dimensional Cobalt Dithiolene Metal–Organic Framework". In: *Journal of the American Chemical Society* 139.31 (2017). PMID: 28704606, pp. 10863–10867. DOI: 10.1021/jacs.7b05742. eprint: https://doi.org/10.1021/jacs.7b05742. URL: https://doi.org/10.1021/jacs.7b05742.

[37] Andrew J. Clough et al. "Room Temperature Metallic Conductivity in a Metal–Organic Framework Induced by Oxidation". In: *Journal of the American Chemical Society* 141.41 (2019). PMID: 31553621, pp. 16323–16330. DOI: 10.1021/jacs.9b06898. eprint: https://doi.org/10.1021/jacs.9b06898. URL: https://doi.org/10.1021/jacs.9b06898.

[38] Alan A Coelho. "TOPAS and TOPAS-Academic: an optimization program integrating computer algebra and crystallographic objects written in C++". In: *J. Appl. Crystallogr.* 51.1 (2018), pp. 210–218.

[39] Yamil J. Colón, Diego A. Gómez-Gualdrón, and Randall Q. Snurr. "Topologically Guided, Automated Construction of Metal–Organic Frameworks and Their Evaluation for Energy-Related Applications". In: *Crystal Growth & Design* 17.11 (2017), pp. 5801–5810. DOI: 10.1021/acs.cgd.7b00848. eprint: https://doi.org/10.1021/acs.cgd.7b00848. URL: https://doi.org/10.1021/acs.cgd.7b00848.

[40] Yuanjing Cui et al. "Photonic functional metal–organic frameworks". In: *Chem. Soc. Rev.* 47 (2018), pp. 5740–5785. DOI: 10.1039/C7CS00879A. URL: http://dx.doi.org/10.1039/C7CS00879A.

[41] Basile F. E. Curchod and Todd J. Martínez. "Ab Initio Nonadiabatic Quantum Molecular Dynamics". In: *Chemical Reviews* 118.7 (2018). PMID: 29465231, pp. 3305–3336. DOI: 10.1021/acs.chemrev.7b00423. eprint: https://doi.org/10.1021/acs.chemrev.7b00423. URL: https://doi.org/10.1021/acs.chemrev.7b00423.

[42] Meenakshi Dan-Hardi et al. "A New Photoactive Crystalline Highly Porous Titanium(IV) Dicarboxylate". In: *Journal of the American Chemical Society* 131.31 (2009). PMID: 19621926, pp. 10857–10859. DOI: 10.1021/ja903726m. eprint: https://doi.org/10.1021/ja903726m. URL: https://doi.org/10.1021/ja903726m.

[43] Tianyu Deng et al. "TDDFT investigation on the solvent effect of methanol on the electronic structure and luminescence of metal organic framework CdL2". In: *Chem. Phys.* 523 (2019), pp. 70–74. ISSN: 0301-0104. DOI: https://doi.org/10.1016/j.chemphys.2019.03.014. URL: http://www.sciencedirect.com/science/article/pii/S0301010419300710.

[44] Pravas Deria et al. "Topology-dependent emissive properties of zirconium-based porphyrin MOFs". In: *Chem. Commun.* 52 (88 2016), pp. 13031–13034. DOI: 10.1039/C6CC07343C. URL: http://dx.doi.org/10.1039/C6CC07343C.

[45] Aleksandra B. Djurišić, Yanling He, and Alan M. C. Ng. "Visible-light photocatalysts: Prospects and challenges". In: *APL Materials* 8.3 (2020), p. 030903. DOI: 10.1063/1.5140497. eprint: https://doi.org/10.1063/1.5140497. URL: https://doi.org/10.1063/1.5140497.

[46] Roberto Dovesi et al. "Quantum-mechanical condensed matter simulations with CRYSTAL". In: *WIREs Comput. Mol. Sci.* 8.4 (2018), e1360. DOI: https://doi.org/10.1002/wcms.1360. eprint: https://onlinelibrary.wiley.com/doi/pdf/10.1002/wcms.1360. URL: https://onlinelibrary.wiley.com/doi/abs/10.1002/wcms.1360.

[47] David A. Egger et al. "Outer-valence Electron Spectra of Prototypical Aromatic Heterocycles from an Optimally Tuned Range-Separated Hybrid Functional". In: *J. Chem. Theory Comput.* 10.5 (2014), pp. 1934–1952. DOI: 10.1021/ct400956h. eprint: https://doi.org/10.1021/ct400956h. URL: https://doi.org/10.1021/ct400956h.

[48] David Emin. "INTERACTIONS BETWEEN SMALL-POLARONIC PARTICLES IN SOLIDS**This work was supported by the U. S. Department of Energy, DOE, under Contract DE-AC04-76-DP00789." In: *The Physics of MOS Insulators.* Ed. by GERALD LUCOVSKY, SOKRATES T. PANTELIDES, and FRANK L. GALEENER. New York: Pergamon Press Inc., 1980, pp. 39–43. ISBN: 978-0-08-025969-7. DOI: https://doi.org/10.1016/B978-

0-08-025969-7.50010-5. URL: http://www.sciencedirect.com/science/article/pii/B9780080259697500105.

[49] Emma S. E. Eriksson and Leif A. Eriksson. "Predictive power of long-range corrected functionals on the spectroscopic properties of tetrapyrrole derivatives for photodynamic therapy". In: *Phys. Chem. Chem. Phys.* 13 (2011), pp. 7207–7217. DOI: 10.1039/C0CP02792H. URL: http://dx.doi.org/10.1039/C0CP02792H.

[50] Matthias Ernzerhof and Gustavo E. Scuseria. "Assessment of the Perdew–Burke–Ernzerhof exchange-correlation functional". In: *The Journal of Chemical Physics* 110.11 (1999), pp. 5029–5036. DOI: 10.1063/1.478401. eprint: https://doi.org/10.1063/1.478401. URL: https://doi.org/10.1063/1.478401.

[51] Alexandra Fateeva et al. "A Water-Stable Porphyrin-Based Metal–Organic Framework Active for Visible-Light Photocatalysis". In: *Angew. Chem. Int. Ed.* 51.30 (2012), pp. 7440–7444. DOI: 10.1002/anie.201202471. eprint: https://onlinelibrary.wiley.com/doi/pdf/10.1002/anie.201202471. URL: https://onlinelibrary.wiley.com/doi/abs/10.1002/anie.201202471.

[52] Liang Feng et al. "Catalytic Porphyrin Framework Compounds". In: *Trends Chem.* 2.6 (2020), pp. 555–568. ISSN: 2589-5974. DOI: https://doi.org/10.1016/j.trechm.2020.01.003. URL: http://www.sciencedirect.com/science/article/pii/S2589597420300289.

[53] Xuanyu Feng et al. "Metal–Organic Frameworks Significantly Enhance Photocatalytic Hydrogen Evolution and CO2 Reduction with Earth-Abundant Copper Photosensitizers". In: *J. Am. Chem. Soc.* 142.2 (2020), pp. 690–695. DOI: 10.1021/jacs.9b12229. eprint: https://doi.org/10.1021/jacs.9b12229. URL: https://doi.org/10.1021/jacs.9b12229.

[54] Teresa M Figueira-Duarte and Klaus Mullen. "Pyrene-based materials for organic electronics". In: *Chem. Rev.* 111 (2011), pp. 7260–7314. ISSN: 0009-2665.

[55] Paolo Foggi et al. "Transient absorption and vibrational relaxation dynamics of the lowest excited singlet state of pyrene in solution". In: *J. Phys. Chem. C* 99.19 (1995), pp. 7439–7445.

[56] M. J. Frisch et al. *Gaussian~16 Revision C.01*. Gaussian Inc. Wallingford CT. 2016.

[57] Junwei Fu et al. "Product selectivity of photocatalytic CO2 reduction reactions". In: *Materials Today* 32 (2020), pp. 222–243. ISSN: 1369-7021. DOI: https://doi.org/10.1016/j.mattod.2019.06.009. URL: https://www.sciencedirect.com/science/article/pii/S1369702119304389.

[58] Yanghe Fu et al. "An Amine-Functionalized Titanium Metal–Organic Framework Photocatalyst with Visible-Light-Induced Activity for CO2 Reduction". In: *Angewandte Chemie International Edition* 51.14 (2012), pp. 3364–3367. DOI: 10.1002/anie.201108357. eprint: https://onlinelibrary.wiley.com/doi/pdf/10.1002/anie.201108357. URL: https://onlinelibrary.wiley.com/doi/abs/10.1002/anie.201108357.

[59] AKIRA FUJISHIMA and KENICHI HONDA. "Electrochemical Photolysis of Water at a Semiconductor Electrode". In: *Nature* 238.5358 (July 1972), pp. 37–38. ISSN: 1476-4687. DOI: 10.1038/238037a0. URL: https://doi.org/10.1038/238037a0.

[60] Maria Fumanal et al. "Charge Separation and Charge Carrier Mobility in Photocatalytic Metal-Organic Frameworks". In: *Adv. Func. Mater.* 30.49 (2020), p. 2003792. DOI: https://doi.org/10.1002/adfm.202003792. eprint: https://onlinelibrary.wiley.com/doi/pdf/10.1002/adfm.202003792. URL: https://onlinelibrary.wiley.com/doi/abs/10.1002/adfm.202003792.

[61] Maria Fumanal et al. "Energy-based descriptors for photo-catalytically active metal–organic framework discovery". In: *J. Mater. Chem. A* 8 (2020), pp. 4473–4482. DOI: 10.1039/C9TA13506E. URL: http://dx.doi.org/10.1039/C9TA13506E.

[62] Filipp Furche and Reinhart Ahlrichs. "Adiabatic time-dependent density functional methods for excited state properties". In: *The Journal of Chemical Physics* 117.16 (2002), pp. 7433–7447. DOI: 10.1063/1.1508368. eprint: https://doi.org/10.1063/1.1508368. URL: https://doi.org/10.1063/1.1508368.

[63] Junkuo Gao et al. "A p-type Ti(iv)-based metal–organic framework with visible-light photo-response". In: *Chem. Commun.* 50 (29 2014), pp. 3786–3788. DOI: 10.1039/C3CC49440C. URL: http://dx.doi.org/10.1039/C3CC49440C.

[64] Alejandro J. Garza and Gustavo E. Scuseria. "Predicting Band Gaps with Hybrid Density Functionals". In: *The Journal of Physical Chemistry Letters* 7.20 (2016), pp. 4165–4170. DOI: 10.1021/acs.jpclett.6b01807. eprint: https://doi.org/10.1021/acs.jpclett.6b01807. URL: https://doi.org/10.1021/acs.jpclett.6b01807.

[65] Stephen J. Geier et al. "Selective adsorption of ethylene over ethane and propylene over propane in the metal–organic frameworks M2(dobdc) (M = Mg, Mn, Fe, Co, Ni, Zn)". In: *Chem. Sci.* 4 (5 2013), pp. 2054–2061. DOI: 10.1039/C3SC00032J. URL: http://dx.doi.org/10.1039/C3SC00032J.

[66] Dibyajyoti Ghosh et al. "Polarons in Halide Perovskites: A Perspective". In: *The Journal of Physical Chemistry Letters* 11.9 (2020). PMID: 32216360, pp. 3271–3286. DOI: 10.1021/acs.jpclett.0c00018. eprint: https://doi.org/10.1021/acs.jpclett.0c00018. URL: https://doi.org/10.1021/acs.jpclett.0c00018.

[67] Gonzalo Givaja et al. "Electrical conductive coordination polymers". In: *Chem. Soc. Rev.* 41 (1 2012), pp. 115–147. DOI: 10.1039/C1CS15092H. URL: http://dx.doi.org/10.1039/C1CS15092H.

[68] Andrzej Gładysiak et al. "Temperature-dependent interchromophoric interaction in a fluorescent pyrene-based metal–organic framework". In: *Chemical science* 10.24 (2019), pp. 6140–6148.

[69] S. Goedecker, M. Teter, and J. Hutter. "Separable dual-space Gaussian pseudopotentials". In: *Phys. Rev. B* 54 (1996), pp. 1703–1710. DOI: 10.1103/PhysRevB.54.1703. URL: https://link.aps.org/doi/10.1103/PhysRevB.54.1703.

[70] Martin Gouterman, Georges H. Wagnière, and Lawrence C. Snyder. "Spectra of porphyrins: Part II. Four orbital model". In: *J. Mol. Spectrosc.* 11.1 (1963), pp. 108–127. ISSN: 0022-2852. DOI: https://doi.org/10.1016/0022-2852(63)90011-0. URL: http://www.sciencedirect.com/science/article/pii/0022285263900110.

[71] Stefan Grimme et al. "A consistent and accurate ab initio parametrization of density functional dispersion correction (DFT-D) for the 94 elements H-Pu". In: *J. Chem. Phys.* 132.15 (2010), p. 154104. DOI: 10.1063/1.3382344. eprint: https://doi.org/10.1063/1.3382344. URL: https://doi.org/10.1063/1.3382344.

[72] Colin R. Groom et al. "The Cambridge Structural Database". In: *Acta Crystallographica Section B* 72.2 (2016), pp. 171–179. DOI: 10.1107/S2052520616003954. URL: https://doi.org/10.1107/S2052520616003954.

[73] Shi-Wei Gu and Meng-Yan Shen. "Binding Energy of Excitons in a Polar Crystal Slab". In: *physica status solidi (b)* 142.2 (1987), pp. 473–479. DOI: 10.1002/pssb.2221420217. eprint: https://onlinelibrary.wiley.com/doi/pdf/10.1002/pssb.2221420217. URL: https://onlinelibrary.wiley.com/doi/abs/10.1002/pssb.2221420217.

[74] Manuel Guidon, Jürg Hutter, and Joost VandeVondele. "Auxiliary Density Matrix Methods for Hartree-Fock Exchange Calculations". In: *J. Chem. Theory Comput.* 6.8 (2010), pp. 2348–2364. DOI: 10.1021/ct1002225. eprint: https://doi.org/10.1021/ct1002225. URL: https://doi.org/10.1021/ct1002225.

[75] Manuel Guidon, Jürg Hutter, and Joost VandeVondele. "Robust Periodic Hartree-Fock Exchange for Large-Scale Simulations Using Gaussian Basis Sets". In: *J. Chem. Theory Comput.* 5.11 (2009), pp. 3010–3021. DOI: 10.1021/ct900494g. eprint: https://doi.org/10.1021/ct900494g. URL: https://doi.org/10.1021/ct900494g.

[76] Fan Guo et al. "Facet-dependent photocatalytic hydrogen production of metal–organic framework NH_2-MIL-125(Ti)". In: *Chem. Sci.* 10.18 (2019), pp. 4834–4838.

[77] Fan Guo et al. "Size engineering of metal–organic framework MIL-101(Cr)–Ag hybrids for photocatalytic CO_2 reduction". In: *ACS Catal.* 9.9 (2019), pp. 8464–8470.

[78] Qing Guo et al. "Fundamentals of TiO2 Photocatalysis: Concepts, Mechanisms, and Challenges". In: *Advanced Materials* 31.50 (2019), p. 1901997. DOI: https://doi.org/10.1002/adma.201901997. eprint: https://onlinelibrary.wiley.com/doi/pdf/10.1002/adma.201901997. URL: https://onlinelibrary.wiley.com/doi/abs/10.1002/adma.201901997.

[79] Said Hamad et al. "Electronic structure of porphyrin-based metal–organic frameworks and their suitability for solar fuel production photocatalysis". In: *J. Mater. Chem. A* 3 (2015), pp. 23458–23465. DOI: 10.1039/C5TA06982C. URL: http://dx.doi.org/10.1039/C5TA06982C.

[80] Said Hamad et al. "Electronic structure of porphyrin-based metal–organic frameworks and their suitability for solar fuel production photocatalysis". In: *J. Mater. Chem. A* 3 (2015), pp. 23458–23465. DOI: 10.1039/C5TA06982C. URL: http://dx.doi.org/10.1039/C5TA06982C.

[81] CG Hatchard and C A_ Parker. "A new sensitive chemical actinometer-II. Potassium ferrioxalate as a standard chemical actinometer". In: *P. Roy. Soc. A - Mat. Phys.* 235.1203 (1956), pp. 518–536.

[82] K. Hattori. "Exciton Binding Energies in Polar Crystals". In: *physica status solidi (b)* 76.1 (1976), pp. 281–287. DOI: 10.1002/pssb.2220760129. eprint: https://onlinelibrary.wiley.com/doi/pdf/10.1002/pssb.2220760129. URL: https://onlinelibrary.wiley.com/doi/abs/10.1002/pssb.2220760129.

[83] P. Jeffrey Hay and Willard R. Wadt. "Ab initio effective core potentials for molecular calculations. Potentials for the transition metal atoms Sc to Hg". In: *The Journal of Chemical Physics* 82.1 (1985), pp. 270–283. DOI: 10.1063/1.448799. eprint: https://doi.org/10.1063/1.448799. URL: https://doi.org/10.1063/1.448799.

[84] Yuping He et al. "Metallic Metal–Organic Frameworks Predicted by the Combination of Machine Learning Methods and Ab Initio Calculations". In: *The Journal of Physical Chemistry Letters* 9.16 (2018). PMID: 30052453, pp. 4562–4569. DOI: 10.1021/acs.jpclett.8b01707. eprint: https://doi.org/10.1021/acs.jpclett.8b01707. URL: https://doi.org/10.1021/acs.jpclett.8b01707.

[85] Christopher H. Hendon, Davide Tiana, and Aron Walsh. "Conductive metal–organic frameworks and networks: fact or fantasy?" In: *Phys. Chem. Chem. Phys.* 14 (38 2012), pp. 13120–13132. DOI: 10.1039/C2CP41099K. URL: http://dx.doi.org/10.1039/C2CP41099K.

[86] Christopher H. Hendon et al. "Engineering the Optical Response of the Titanium-MIL-125 Metal–Organic Framework through Ligand Functionalization". In: *Journal of the American Chemical Society* 135.30 (2013). PMID: 23841821, pp. 10942–10945. DOI: 10.1021/ja405350u. eprint: https://doi.org/10.1021/ja405350u. URL: https://doi.org/10.1021/ja405350u.

[87] Kevin Hendrickx et al. "Exploring Lanthanide Doping in UiO-66: A Combined Experimental and Computational Study of the Electronic Structure". In: *Inorganic Chemistry* 57.9 (2018). PMID: 29659259, pp. 5463–5474. DOI: 10.1021/acs.inorgchem.8b00425. eprint: https://doi.org/10.1021/acs.inorgchem.8b00425. URL: https://doi.org/10.1021/acs.inorgchem.8b00425.

[88] Kevin Hendrickx et al. "Understanding Intrinsic Light Absorption Properties of UiO-66 Frameworks: A Combined Theoretical and Experimental Study". In: *Inorg. Chem.* 54.22 (2015), pp. 10701–10710. DOI: 10.1021/acs.inorgchem.5b01593. eprint: https://doi.org/10.1021/acs.inorgchem.5b01593. URL: https://doi.org/10.1021/acs.inorgchem.5b01593.

[89] Yoyo Hinuma et al. "Band structure diagram paths based on crystallography". In: *Computational Materials Science* 128 (2017), pp. 140–184. ISSN: 0927-0256. DOI: https://doi.org/10.1016/j.commatsci.2016.10.015. URL: https://www.sciencedirect.com/science/article/pii/S0927025616305110.

[90] So Hirata and Martin Head-Gordon. "Time-dependent density functional theory within the Tamm–Dancoff approximation". In: *Chem. Phys. Lett.* 314.3 (1999), pp. 291–299. ISSN: 0009-2614. DOI: https://doi.org/10.1016/S0009-2614(99)01149-5. URL: http://www.sciencedirect.com/science/article/pii/S0009261499011495.

[91] Takashi Hisatomi, Jun Kubota, and Kazunari Domen. "Recent advances in semiconductors for photocatalytic and photoelectrochemical water splitting". In: *Chem. Soc. Rev.* 43 (22 2014), pp. 7520–7535. DOI: 10.1039/C3CS60378D. URL: http://dx.doi.org/10.1039/C3CS60378D.

[92] P. Hohenberg and W. Kohn. "Inhomogeneous Electron Gas". In: *Phys. Rev.* 136 (3B Nov. 1964), B864–B871. DOI: 10.1103/PhysRev.136.B864. URL: https://link.aps.org/doi/10.1103/PhysRev.136.B864.

[93] Nico Holmberg and Kari Laasonen. "Efficient Constrained Density Functional Theory Implementation for Simulation of Condensed Phase Electron Transfer Reactions". In: *Journal of Chemical Theory and Computation* 13.2 (2017). PMID: 28009515, pp. 587–601. DOI: 10.1021/acs.jctc.6b01085. eprint: https://doi.org/10.1021/acs.jctc.6b01085. URL: https://doi.org/10.1021/acs.jctc.6b01085.

[94] Yu Horiuchi et al. "Visible-Light-Promoted Photocatalytic Hydrogen Production by Using an Amino-Functionalized Ti(IV) Metal–Organic Framework". In: *The Journal of Physical Chemistry C* 116.39 (2012), pp. 20848–20853. DOI: 10.1021/jp3046005. eprint: https://doi.org/10.1021/jp3046005. URL: https://doi.org/10.1021/jp3046005.

[95] Ren-Wu Huang et al. "Hypersensitive dual-function luminescence switching of a silver-chalcogenolate cluster-based metal-organic framework". In: *Nature chemistry.* 9.7 (2017). ISSN: 1755-4330.

[96] Seong Huh, Sung-Jin Kim, and Youngmee Kim. "Porphyrinic metal–organic frameworks from custom-designed porphyrins". In: *CrystEngComm* 18 (2016), pp. 345–368. DOI: 10.1039/C5CE02106E. URL: http://dx.doi.org/10.1039/C5CE02106E.

[97] Jürg Hutter et al. "cp2k: atomistic simulations of condensed matter systems". In: *Wiley Interdiscip. Rev.: Comput. Mol. Sci.* 4.1 (2014), pp. 15–25. DOI: 10.1002/wcms.1159. eprint: https://onlinelibrary.wiley.com/doi/pdf/10.1002/wcms.1159. URL: https://onlinelibrary.wiley.com/doi/abs/10.1002/wcms.1159.

[98] Artur F. Izmaylov and Gustavo E. Scuseria. "Why are time-dependent density functional theory excitations in solids equal to band structure energy gaps for semilocal functionals, and how does nonlocal Hartree-Fock-type exchange introduce excitonic effects?" In: *J. Chem. Phys.* 129.3 (2008), p. 034101. DOI: 10.1063/1.2953701. eprint: https://doi.org/10.1063/1.2953701. URL: https://doi.org/10.1063/1.2953701.

[99] Stavroula Kampouri et al. "Concurrent Photocatalytic Hydrogen Generation and Dye Degradation Using MIL-125-NH2 under Visible Light Irradiation". In: *Advanced Functional Materials* 28.52 (2018), p. 1806368. DOI: https://doi.org/10.1002/adfm.201806368. eprint: https://onlinelibrary.wiley.com/doi/pdf/10.1002/adfm.201806368. URL: https://onlinelibrary.wiley.com/doi/abs/10.1002/adfm.201806368.

[100] Stavroula Kampouri et al. "Photocatalytic hydrogen generation from a visible-light responsive metal–organic framework system: the impact of nickel phosphide nanoparticles". In: *J. Mater. Chem. A* 6 (6 2018), pp. 2476–2481. DOI: 10.1039/C7TA10225A. URL: http://dx.doi.org/10.1039/C7TA10225A.

[101] Michael Kasha. "Characterization of electronic transitions in complex molecules". In: *Discuss. Faraday Soc.* 9 (0 1950), pp. 14–19. DOI: 10.1039/DF9500900014. URL: http://dx.doi.org/10.1039/DF9500900014.

[102] Tomomi Kawakami et al. "Ultrafast capture of electrons ejected by photoionization leading to the formation of a charge-separated state at a high energy level". In: *Phys. Chem. Chem. Phys.* 22.31 (2020), pp. 17472–17481.

[103] Hossein Khajavi et al. "Unraveling the Optoelectronic and Photochemical Behavior of Zn4O-Based Metal Organic Frameworks". In: *The Journal of Physical Chemistry C* 115.25 (2011), pp. 12487–12493. DOI: 10.1021/jp201760s. eprint: https://doi.org/10.1021/jp201760s. URL: https://doi.org/10.1021/jp201760s.

[104] F Pelin Kinik et al. "Pyrene-based metal organic frameworks: from synthesis to applications". In: *Chem. Soc. Rev.* (2021).

[105] W. Kohn and L. J. Sham. "Self-Consistent Equations Including Exchange and Correlation Effects". In: *Phys. Rev.* 140 (4A Nov. 1965), A1133–A1138. DOI: 10.1103/PhysRev.140.A1133. URL: https://link.aps.org/doi/10.1103/PhysRev.140.A1133.

[106] Sebastian Kokott et al. "First-principles supercell calculations of small polarons with proper account for long-range polarization effects". In: *New Journal of Physics* 20.3 (2018), p. 033023. DOI: 10.1088/1367-2630/aaaf44. URL: https://doi.org/10.1088%2F1367-2630%2Faaaf44.

[107] Nikolay Kornienko et al. "Metal–Organic Frameworks for Electrocatalytic Reduction of Carbon Dioxide". In: *J. Am. Chem. Soc.* 137.44 (2015), pp. 14129–14135. DOI: 10.1021/jacs.5b08212. eprint: https://doi.org/10.1021/jacs.5b08212. URL: https://doi.org/10.1021/jacs.5b08212.

[108] Leeor Kronik and Stephan Kümmel. "Dielectric Screening Meets Optimally Tuned Density Functionals". In: *Advanced Materials* 30.41 (2018), p. 1706560. DOI: 10.1002/adma.201706560. eprint: https://onlinelibrary.wiley.com/doi/pdf/10.1002/adma.201706560. URL: https://onlinelibrary.wiley.com/doi/abs/10.1002/adma.201706560.

[109] Leeor Kronik et al. "Excitation Gaps of Finite-Sized Systems from Optimally Tuned Range-Separated Hybrid Functionals". In: *J. Chem. Theory Comput.* 8.5 (2012), pp. 1515–1531. DOI: 10.1021/ct2009363. eprint: https://doi.org/10.1021/ct2009363. URL: https://doi.org/10.1021/ct2009363.

[110] HJ Kuhn, SE Braslavsky, and R Schmidt. "Chemical actinometry (IUPAC technical report)". In: *Pure Appl. Chem.* 76.12 (2004), pp. 2105–2146.

[111] Thomas D. Kühne et al. "CP2K: An electronic structure and molecular dynamics software package - Quickstep: Efficient and accurate electronic structure calculations". In: *J. Chem. Phys.* 152.19 (2020), p. 194103. DOI: 10.1063/5.0007045. eprint: https://doi.org/10.1063/5.0007045. URL: https://doi.org/10.1063/5.0007045.

[112] Stephan Kümmel. "Charge-Transfer Excitations: A Challenge for Time-Dependent Density Functional Theory That Has Been Met". In: *Adv. Energy Mater.* 7.16 (2017), p. 1700440. DOI: 10.1002/aenm.201700440. eprint: https://onlinelibrary.wiley.com/doi/pdf/10.1002/aenm.201700440. URL: https://onlinelibrary.wiley.com/doi/abs/10.1002/aenm.201700440.

[113] Guangxu Lan et al. "Electron Injection from Photoexcited Metal–Organic Framework Ligands to Ru2 Secondary Building Units for Visible-Light-Driven Hydrogen Evolution". In: *J. Am. Chem. Soc.* 140.16 (2018), pp. 5326–5329. DOI: 10.1021/jacs.8b01601. eprint: https://doi.org/10.1021/jacs.8b01601. URL: https://doi.org/10.1021/jacs.8b01601.

[114] Mark A. W. Lawrence, Jimmie L. Bullock, and Alvin A. Holder. "Basic Coordination Chemistry of Ruthenium". In: *Ruthenium Complexes: Photochemical and Biomedical Applications*. Weinheim, Germany: Wiley-VCH Verlag GmbH & Co. KGaA, 2017. Chap. 2, pp. 25–41. ISBN: 9783527695225. DOI: 10.1002/9783527695225.ch2. eprint: https://onlinelibrary.wiley.com/doi/pdf/10.1002/9783527695225.ch2. URL: https://onlinelibrary.wiley.com/doi/abs/10.1002/9783527695225.ch2.

[115] M. W. Lee et al. "Synthesis, Optical and Photovoltaic Properties of Porphyrin Dyes". In: *J. Macromol. Sci., Part A: Pure Appl.Chem.* 46.7 (2009), pp. 730–737. DOI: 10.1080/10601320902938558. eprint: https://doi.org/10.1080/10601320902938558. URL: https://doi.org/10.1080/10601320902938558.

[116] Fucheng Leng et al. "Boosting Photocatalytic Hydrogen Production of Porphyrinic MOFs: The Metal Location in Metalloporphyrin Matters". In: *ACS Catalysis* 8.5 (2018), pp. 4583–4590. DOI: 10.1021/acscatal.8b00764. eprint: https://doi.org/10.1021/acscatal.8b00764. URL: https://doi.org/10.1021/acscatal.8b00764.

[117] Chanel F Leong, Pavel M Usov, and Deanna M D'Alessandro. "Intrinsically conducting metal–organic frameworks". In: *MRS Bulletin* 41.11 (2016), pp. 858–864.

[118] Changqing Li et al. "Tunable titanium metal–organic frameworks with infinite 1D Ti–O rods for efficient visible-light-driven photocatalytic H2 evolution". In: *J. Mater. Chem. A* 7 (19 2019), pp. 11928–11933. DOI: 10.1039/C9TA01942A. URL: http://dx.doi.org/10.1039/C9TA01942A.

[119] Hao Li et al. "Recent advances in gas storage and separation using metal–organic frameworks". In: *Materials Today* 21.2 (2018), pp. 108–121. ISSN: 1369-7021. DOI: https://doi.org/10.1016/j.mattod.2017.07.006. URL: https://www.sciencedirect.com/science/article/pii/S1369702117302407.

[120] Ying Li et al. "Metal–organic frameworks for photocatalysis". In: *Phys. Chem. Chem. Phys.* 18 (11 2016), pp. 7563–7572. DOI: 10.1039/C5CP05885F. URL: http://dx.doi.org/10.1039/C5CP05885F.

[121] Meng-Sheng Liao et al. "Electronic structure, absorption spectra, and hyperpolarisabilities of some novel push–pull zinc porphyrins. A DFT/TDDFT study". In: *Molecular Physics* 106.1 (2008), pp. 147–160. DOI: 10.1080/00268970701870991. eprint: https://doi.org/10.1080/00268970701870991. URL: https://doi.org/10.1080/00268970701870991.

[122] M. Lions et al. "Insights into the mechanism of electrocatalysis of the oxygen reduction reaction by a porphyrinic metal organic framework". In: *Chem. Commun.* 53 (2017), pp. 6496–6499. DOI: 10.1039/C7CC02113E. URL: http://dx.doi.org/10.1039/C7CC02113E.

[123] Lin Liu et al. "Robust Molecular Bowl-Based Metal–Organic Frameworks with Open Metal Sites: Size Modulation To Increase the Catalytic Activity". In: *Inorg. Chem.* 54.8 (2015), pp. 3719–3721.

[124] Shengjun Liu et al. "Design of metal-organic framework-based photocatalysts for hydrogen generation". In: *Coord. Chem. Rev.* 413 (2020), p. 213266.

[125] Tao Liu et al. "Water-Switching of Spin Transitions Induced by Metal-to-Metal Charge Transfer in a Microporous Framework". In: *Angewandte Chemie International Edition* 49.46 (2010), pp. 8645–8648. DOI: https://doi.org/10.1002/anie.201002881. eprint: https://onlinelibrary.wiley.com/doi/pdf/10.1002/anie.201002881. URL: https://onlinelibrary.wiley.com/doi/abs/10.1002/anie.201002881.

[126] Yali Liu et al. "Shape-and size-dependent catalysis activities of iron-terephthalic acid metal-organic frameworks". In: *Sci. China Chem.* 58.10 (2015), pp. 1553–1560.

[127] Per-Olov Löwdin. "On the Non-Orthogonality Problem Connected with the Use of Atomic Wave Functions in the Theory of Molecules and Crystals". In: *J. Chem. Phys.* 18.3 (1950), pp. 365–375. DOI: 10.1063/1.1747632. eprint: https://doi.org/10.1063/1.1747632. URL: https://doi.org/10.1063/1.1747632.

[128] Javeed Mahmood et al. "An efficient and pH-universal ruthenium-based catalyst for the hydrogen evolution reaction". In: *Nature Nanotechnology* 12 (2017), p. 441. URL: https://doi.org/10.1038/nnano.2016.304%20http://10.0.4.14/nnano.2016.304%20https://www.nature.com/articles/nnano.2016.304%7B%5C#%7Dsupplementary-information.

[129] Richard L. Martin. "Natural transition orbitals". In: *The Journal of Chemical Physics* 118.11 (2003), pp. 4775–4777. DOI: 10.1063/1.1558471. eprint: https://doi.org/10.1063/1.1558471. URL: https://doi.org/10.1063/1.1558471.

[130] Simon Mathew et al. "Dye-sensitized solar cells with 13% efficiency achieved through the molecular engineering of porphyrin sensitizers". In: *Nat. Chem.* 6.3 (2014), pp. 242–247. DOI: 10.1038/nchem.1861. URL: https://doi.org/10.1038/nchem.1861.

[131] R. van Meer, O. V. Gritsenko, and E. J. Baerends. "Physical Meaning of Virtual Kohn–Sham Orbitals and Orbital Energies: An Ideal Basis for the Description of Molecular Excitations". In: *J. Chem. Theory Comput.* 10.10 (2014), pp. 4432–4441. DOI: 10.1021/ct500727c. eprint: https://doi.org/10.1021/ct500727c. URL: https://doi.org/10.1021/ct500727c.

[132] Yu Meng et al. "When Density Functional Approximations Meet Iron Oxides". In: *Journal of Chemical Theory and Computation* 12.10 (2016). PMID: 27532639, pp. 5132–5144. DOI: 10.1021/acs.jctc.6b00640. eprint: https://doi.org/10.1021/acs.jctc.6b00640. URL: https://doi.org/10.1021/acs.jctc.6b00640.

[133] Giacomo Miceli et al. "Nonempirical hybrid functionals for band gaps and polaronic distortions in solids". In: *Phys. Rev. B* 97 (12 2018), p. 121112. DOI: 10.1103/PhysRevB.97.121112. URL: https://link.aps.org/doi/10.1103/PhysRevB.97.121112.

[134] Maykel de Miguel et al. "Evidence of Photoinduced Charge Separation in the Metal–Organic Framework MIL-125(Ti)-NH2". In: *ChemPhysChem* 13.16 (2012), pp. 3651–3654. DOI: https://doi.org/10.1002/cphc.201200411. eprint: https://chemistry-europe.onlinelibrary.wiley.com/doi/pdf/10.1002/cphc.201200411. URL: https://chemistry-europe.onlinelibrary.wiley.com/doi/abs/10.1002/cphc.201200411.

[135] Hiroshi Miyasaka, Hiroshi Masuhara, and Noboru Mataga. "Picosecond absorption spectra and relaxation processes of the excited singlet state of pyrene in solution". In: *Laser Chem.* 1.5 (1983), pp. 357–386.

[136] Jonas Moellmann and Stefan Grimme. "DFT-D3 Study of Some Molecular Crystals". In: *The Journal of Physical Chemistry C* 118.14 (2014), pp. 7615–7621. DOI: 10.1021/jp501237c. eprint: https://doi.org/10.1021/jp501237c. URL: https://doi.org/10.1021/jp501237c.

[137] Peyman Z. Moghadam et al. "Development of a Cambridge Structural Database Subset: A Collection of Metal–Organic Frameworks for Past, Present, and Future". In: *Chemistry of Materials* 29.7 (2017), pp. 2618–2625. DOI: 10.1021/acs.chemmater.7b00441. eprint: https://doi.org/10.1021/acs.chemmater.7b00441. URL: https://doi.org/10.1021/acs.chemmater.7b00441.

[138] N F Mott and A M Stoneham. "The lifetime of electrons, holes and excitons before self-trapping". In: *Journal of Physics C: Solid State Physics* 10.17 (1977), pp. 3391–3398. DOI: 10.1088/0022-3719/10/17/022. URL: https://doi.org/10.1088%2F0022-3719%2F10%2F17%2F022.

[139] Christoph Muschielok and Harald Oberhofer. "Aspects of semiconductivity in soft, porous metal-organic framework crystals". In: *The Journal of Chemical Physics* 151.1 (2019), p. 015102. DOI: 10.1063/1.5108995. eprint: https://doi.org/10.1063/1.5108995. URL: https://doi.org/10.1063/1.5108995.

[140] Tarun C. Narayan et al. "High Charge Mobility in a Tetrathiafulvalene-Based Microporous Metal–Organic Framework". In: *Journal of the American Chemical Society* 134.31 (2012). PMID: 22827709, pp. 12932–12935. DOI: 10.1021/ja3059827. eprint: https://doi.org/10.1021/ja3059827. URL: https://doi.org/10.1021/ja3059827.

[141] Maxim A Nasalevich et al. "Electronic origins of photocatalytic activity in d^0 metal organic frameworks". In: *Sci. Rep.* 6.1 (2016), pp. 1–9.

[142] Ha L Nguyen. "Perspectives on titanium-based metal–organic frameworks". In: *Journal of Physics: Energy* 3.2 (2021), p. 021003.

[143] Nagapradeep Nidamanuri and Sourav Saha. "Chapter 6 Metal-organic Frameworks with Tunable Electrical and Optical Properties". In: *Functional Supramolecular Materials: From Surfaces to MOFs*. The Royal Society of Chemistry, 2017, pp. 217–246. ISBN: 978-1-78262-540-7. DOI: 10.1039/9781788010276-00217. URL: http://dx.doi.org/10.1039/9781788010276-00217.

[144] Harald Oberhofer, Karsten Reuter, and Jochen Blumberger. "Charge Transport in Molecular Materials: An Assessment of Computational Methods". In: *Chemical Reviews* 117.15 (2017). PMID: 28644623, pp. 10319–10357. DOI: 10.1021/acs.chemrev.7b00086. eprint: https://doi.org/10.1021/acs.chemrev.7b00086. URL: https://doi.org/10.1021/acs.chemrev.7b00086.

[145] Samuel O. Odoh et al. "Quantum-Chemical Characterization of the Properties and Reactivities of Metal–Organic Frameworks". In: *Chemical Reviews* 115.12 (2015). PMID: 25872949, pp. 6051–6111. DOI: 10.1021/cr500551h. eprint: https://doi.org/10.1021/cr500551h. URL: https://doi.org/10.1021/cr500551h.

[146] B Ohtani. "Photocatalysis A to Z — What we know and what we do not know in a scientific sense". In: *J. Photochem. Photobiol. C* 11.4 (2010), pp. 157–178.

[147] Joseph F. Olorunyomi et al. "Metal–organic frameworks for chemical sensing devices". In: *Mater. Horiz.* (2021), pp. -. DOI: 10.1039/D1MH00609F. URL: http://dx.doi.org/10.1039/D1MH00609F.

[148] Daniele Ongari et al. "Building a Consistent and Reproducible Database for Adsorption Evaluation in Covalent-Organic Frameworks". In: *ACS Central Science* 5.10 (2019), pp. 1663–1675. DOI: 10.1021/acscentsci.9b00619. eprint: https://doi.org/10.1021/acscentsci.9b00619. URL: https://doi.org/10.1021/acscentsci.9b00619.

[149] Andres Ortega-Guerrero et al. "From Isolated Porphyrin Ligands to Periodic Al-PMOF: A Comparative Study of the Optical Properties Using DFT/TDDFT". In: *J. Phys. Chem. C* 124.39 (2020), pp. 21751–21760. DOI: 10.1021/acs.jpcc.0c06885. eprint: https://doi.org/10.1021/acs.jpcc.0c06885. URL: https://doi.org/10.1021/acs.jpcc.0c06885.

[150] Andres Ortega-Guerrero et al. "Insights into the Electronic Properties and Charge Transfer Mechanism of a Porphyrin Ruthenium-Based Metal–Organic Framework". In: *Chem. Mater.* 32.10 (2020), pp. 4194–4204. DOI: 10.1021/acs.chemmater.0c00356. eprint: https://doi.org/10.1021/acs.chemmater.0c00356. URL: https://doi.org/10.1021/acs.chemmater.0c00356.

[151] Natalia M. Padial et al. "Hydroxamate Titanium–Organic Frameworks and the Effect of Siderophore-Type Linkers over Their Photocatalytic Activity". In: *Journal of the American Chemical Society* 141.33 (2019). PMID: 31319033, pp. 13124–13133. DOI: 10.1021/jacs.9b04915. eprint: https://doi.org/10.1021/jacs.9b04915. URL: https://doi.org/10.1021/jacs.9b04915.

[152] Hyunwoong Park et al. "Photoinduced charge transfer processes in solar photocatalysis based on modified TiO2". In: *Energy Environ. Sci.* 9 (2 2016), pp. 411–433. DOI: 10.1039/C5EE02575C. URL: http://dx.doi.org/10.1039/C5EE02575C.

[153] Sarah S. Park et al. "Cation-Dependent Intrinsic Electrical Conductivity in Isostructural Tetrathiafulvalene-Based Microporous Metal–Organic Frameworks". In: *Journal of the American Chemical Society* 137.5 (2015). PMID: 25597934, pp. 1774–1777. DOI: 10.1021/ja512437u. eprint: https://doi.org/10.1021/ja512437u. URL: https://doi.org/10.1021/ja512437u.

[154] Sameer Patwardhan and George C. Schatz. "Theoretical Investigation of Charge Transfer in Metal Organic Frameworks for Electrochemical Device Applications". In: *J. Phys. Chem. C* 119.43 (2015), pp. 24238–24247. DOI: 10.1021/acs.jpcc.5b06065. eprint: https://doi.org/10.1021/acs.jpcc.5b06065. URL: https://doi.org/10.1021/acs.jpcc.5b06065.

[155] Michael J. G. Peach and David J. Tozer. "Overcoming Low Orbital Overlap and Triplet Instability Problems in TDDFT". In: *J. Phys. Chem. A* 116.39 (2012), pp. 9783–9789. DOI: 10.1021/jp308662x. eprint: https://doi.org/10.1021/jp308662x. URL: https://doi.org/10.1021/jp308662x.

[156] Michael J. G. Peach et al. "Excitation energies in density functional theory: An evaluation and a diagnostic test". In: *The Journal of Chemical Physics* 128.4 (2008), p. 044118. DOI: 10.1063/1.2831900. eprint: https://doi.org/10.1063/1.2831900. URL: https://doi.org/10.1063/1.2831900.

[157] Michael J. G. Peach et al. "TDDFT diagnostic testing and functional assessment for triazene chromophores". In: *Phys. Chem. Chem. Phys.* 11 (22 2009), pp. 4465–4470. DOI: 10.1039/B822941D. URL: http://dx.doi.org/10.1039/B822941D.

[158] John P. Perdew, Kieron Burke, and Matthias Ernzerhof. "Generalized Gradient Approximation Made Simple". In: *Phys. Rev. Lett.* 77 (1996), pp. 3865–3868. DOI: 10.1103/PhysRevLett.77.3865. URL: https://link.aps.org/doi/10.1103/PhysRevLett.77.3865.

[159] John P. Perdew, Matthias Ernzerhof, and Kieron Burke. "Rationale for mixing exact exchange with density functional approximations". In: *J. Chem. Phys.* 105.22 (1996), pp. 9982–9985. DOI: 10.1063/1.472933. eprint: https://doi.org/10.1063/1.472933. URL: https://doi.org/10.1063/1.472933.

[160] John P. Perdew et al. "Density-Functional Theory for Fractional Particle Number: Derivative Discontinuities of the Energy". In: *Phys. Rev. Lett.* 49 (23 1982), pp. 1691–1694. DOI: 10.1103/PhysRevLett.49.1691. URL: https://link.aps.org/doi/10.1103/PhysRevLett.49.1691.

[161] John P. Perdew et al. "Restoring the Density-Gradient Expansion for Exchange in Solids and Surfaces". In: *Phys. Rev. Lett.* 100 (13 2008), p. 136406. DOI: 10.1103/PhysRevLett.100.136406. URL: https://link.aps.org/doi/10.1103/PhysRevLett.100.136406.

[162] John P. Perdew et al. "Understanding band gaps of solids in generalized Kohn–Sham theory". In: *Proceedings of the National Academy of Sciences* 114.11 (2017), pp. 2801–2806. ISSN: 0027-8424. DOI: 10.1073/pnas.1621352114. eprint: https://www.pnas.org/content/114/11/2801.full.pdf. URL: https://www.pnas.org/content/114/11/2801.

[163] John J. Perry IV et al. "Connecting structure with function in metal-organic frameworks to design novel photo- and radioluminescent materials". In: *J. Mater. Chem.* 22 (20 2012), pp. 10235–10248. DOI: 10.1039/C2JM16627E. URL: http://dx.doi.org/10.1039/C2JM16627E.

[164] G. A. Petersson et al. "A complete basis set model chemistry. I. The total energies of closed-shell atoms and hydrides of the first-row elements". In: *J. Chem. Phys.* 89.4 (1988), pp. 2193–2218. DOI: 10.1063/1.455064. eprint: https://doi.org/10.1063/1.455064. URL: https://doi.org/10.1063/1.455064.

[165] *Por-Lab, Porphyrin-Laboratories GmbH.* 5,10,15,20-Tetrakis-(4-carboxyphenyl)-porphine-Zn(II). https://porphyrin-laboratories.com/eng/catalog/ (Accessed: Oct 30, 2019).

[166] Saied Md Pratik and Christopher J. Cramer. "Predicted Efficient Visible-Light Driven Water Splitting and Carbon Dioxide Reduction Using Photoredox-Active UiO-NDI Metal Organic Framework". In: *The Journal of Physical Chemistry C* 123.32 (2019), pp. 19778–19785. DOI: 10.1021/acs.jpcc.9b05693. eprint: https://doi.org/10.1021/acs.jpcc.9b05693. URL: https://doi.org/10.1021/acs.jpcc.9b05693.

[167] Benjamin P. Pritchard et al. "New Basis Set Exchange: An Open, Up-to-Date Resource for the Molecular Sciences Community". In: *J. Chem. Inf. Model.* 59.11 (2019), pp. 4814–4820. DOI: 10.1021/acs.jcim.9b00725. eprint: https://doi.org/10.1021/acs.jcim.9b00725. URL: https://doi.org/10.1021/acs.jcim.9b00725.

[168] Kyle G. Reeves and Yosuke Kanai. "Theoretical oxidation state analysis of Ru-(bpy)3: Influence of water solvation and Hubbard correction in first-principles calculations". In: *The Journal of Chemical Physics* 141.2 (2014), p. 024305. DOI: 10.1063/1.4886406. eprint: https://doi.org/10.1063/1.4886406. URL: https://doi.org/10.1063/1.4886406.

[169] Sivan Refaely-Abramson et al. "Gap renormalization of molecular crystals from density-functional theory". In: *Phys. Rev. B* 88 (2013), p. 081204. DOI: 10.1103/PhysRevB.88.081204. URL: https://link.aps.org/doi/10.1103/PhysRevB.88.081204.

[170] Akinori Saeki et al. "Comprehensive Approach to Intrinsic Charge Carrier Mobility in Conjugated Organic Molecules, Macromolecules, and Supramolecular Architectures". In: *Accounts of Chemical Research* 45.8 (2012). PMID: 22676381, pp. 1193–1202. DOI: 10.1021/ar200283b. eprint: https://doi.org/10.1021/ar200283b. URL: https://doi.org/10.1021/ar200283b.

[171] Giovanni Scalmani et al. "Geometries and properties of excited states in the gas phase and in solution: Theory and application of a time-dependent density functional theory polarizable continuum model". In: *The Journal of Chemical Physics* 124.9 (2006), p. 094107. DOI: 10.1063/1.2173258. eprint: https://doi.org/10.1063/1.2173258. URL: https://doi.org/10.1063/1.2173258.

[172] R. D. Shannon and C. T. Prewitt. "Effective ionic radii in oxides and fluorides". In: *Acta Crystallographica Section B* 25.5 (1969), pp. 925–946. DOI: 10.1107/S0567740869003220. URL: https://doi.org/10.1107/S0567740869003220.

[173] Dennis Sheberla et al. "High Electrical Conductivity in Ni3(2,3,6,7,10,11-hexaiminotriphenylene)2, a Semiconducting Metal–Organic Graphene Analogue". In: *Journal of the American Chemical Society* 136.25 (2014). PMID: 24750124, pp. 8859–8862. DOI: 10.1021/ja502765n. eprint: https://doi.org/10.1021/ja502765n. URL: https://doi.org/10.1021/ja502765n.

[174] Cong-Cong Shen et al. "Boosting visible-light photocatalytic H2 evolution via UiO-66-NH2 octahedrons decorated with ultrasmall NiO nanoparticles". In: *Dalton Trans.* 47 (33 2018), pp. 11705–11712. DOI: 10.1039/C8DT02681E. URL: http://dx.doi.org/10.1039/C8DT02681E.

[175] Grigorii Skorupskii et al. "Efficient and tunable one-dimensional charge transport in layered lanthanide metal–organic frameworks". In: *Nature chemistry* 12.2 (2020), pp. 131–136.

[176] Daniel G. A. Smith et al. "Revised Damping Parameters for the D3 Dispersion Correction to Density Functional Theory". In: *The Journal of Physical Chemistry Letters* 7.12 (2016). PMID: 27203625, pp. 2197–2203. DOI: 10.1021/acs.jpclett.6b00780. eprint: https://doi.org/10.1021/acs.jpclett.6b00780. URL: https://doi.org/10.1021/acs.jpclett.6b00780.

[177] Monica C. So et al. "Metal–organic framework materials for light-harvesting and energy transfer". In: *Chem. Commun.* 51 (2015), pp. 3501–3510. DOI: 10.1039/C4CC09596K. URL: http://dx.doi.org/10.1039/C4CC09596K.

[178] Ho-Jin Son et al. "Light-Harvesting and Ultrafast Energy Migration in Porphyrin-Based Metal–Organic Frameworks". In: *J. Am. Chem. Soc.* 135.2 (2013), pp. 862–869. DOI: 10.1021/ja310596a. eprint: https://doi.org/10.1021/ja310596a. URL: https://doi.org/10.1021/ja310596a.

[179] Piyush Kumar Sonkar et al. "Co(ii)-porphyrin-decorated carbon nanotubes as catalysts for oxygen reduction reactions: an approach for fuel cell improvement". In: *J. Mater. Chem. A* 5 (2017), pp. 6263–6276. DOI: 10.1039/C6TA10482G. URL: http://dx.doi.org/10.1039/C6TA10482G.

[180] Ivo Stassen et al. "An updated roadmap for the integration of metal–organic frameworks with electronic devices and chemical sensors". In: *Chem. Soc. Rev.* 46 (2017), pp. 3185–3241. DOI: 10.1039/C7CS00122C. URL: http://dx.doi.org/10.1039/C7CS00122C.

[181] Kyriakos C Stylianou et al. "A guest-responsive fluorescent 3D microporous metal-organic framework derived from a long-lifetime pyrene core". In: *J. Am. Chem. Soc.* 132.12 (2010), pp. 4119–4130.

[182] Haitao Sun et al. "Ionization Energies, Electron Affinities, and Polarization Energies of Organic Molecular Crystals: Quantitative Estimations from a Polarizable Continuum Model (PCM)-Tuned Range-Separated Density Functional Approach". In: *J. Chem. Theory Comput.* 12.6 (2016), pp. 2906–2916. DOI: 10.1021/acs.jctc.6b00225. eprint: https://doi.org/10.1021/acs.jctc.6b00225. URL: https://doi.org/10.1021/acs.jctc.6b00225.

[183] Lei Sun, Michael G. Campbell, and Mircea Dincă. "Electrically Conductive Porous Metal–Organic Frameworks". In: *Angewandte Chemie International Edition* 55.11 (2016), pp. 3566–3579. DOI: https://doi.org/10.1002/anie.201506219. eprint: https://onlinelibrary.wiley.com/doi/pdf/10.1002/anie.201506219. URL: https://onlinelibrary.wiley.com/doi/abs/10.1002/anie.201506219.

[184] Maria A. Syzgantseva et al. "Metal Substitution as the Method of Modifying Electronic Structure of Metal–Organic Frameworks". In: *Journal of the American Chemical Society* 141.15 (2019). PMID: 30915844, pp. 6271–6278. DOI: 10.1021/jacs.8b13667. eprint: https://doi.org/10.1021/jacs.8b13667. URL: https://doi.org/10.1021/jacs.8b13667.

[185] Sehar Tasleem, Muhammad Tahir, and Wesam Alsayeh Khalifa. "Current trends in structural development and modification strategies for metal-organic frameworks (MOFs) towards photocatalytic H_2 production: A review". In: *Int. J. Hydrog. Energy* (2021).

[186] Stephen J. Tereniak and Connie C. Lu. "Group 8 Metal–Metal Bonds". In: *Molecular Metal-Metal Bonds: Compounds, Synthesis, Properties*. Ed. by Stephen T. Liddle. Weinheim, Germany: Wiley-VCH Verlag GmbH & Co. KGaA, 2015. Chap. 8, pp. 225–278. ISBN: 9783527673353. DOI: 10.1002/9783527673353.ch8. eprint: https://onlinelibrary.wiley.com/doi/pdf/10.1002/9783527673353.ch8. URL: https://onlinelibrary.wiley.com/doi/abs/10.1002/9783527673353.ch8.

[187] C. Ullrich. *Time-Dependent Density-Functional Theory: Concepts and Applications*. Oxford Graduate Texts. OUP Oxford, 2012. ISBN: 9780199563029. URL: https://books.google.ch/books?id=hCNNsC4sEtkC.

[188] Joost VandeVondele and Jürg Hutter. "An efficient orbital transformation method for electronic structure calculations". In: *J. Chem. Phys.* 118.10 (2003), pp. 4365–4369. DOI: 10.1063/1.1543154. eprint: https://doi.org/10.1063/1.1543154. URL: https://doi.org/10.1063/1.1543154.

[189] Joost VandeVondele and Jürg Hutter. "Gaussian basis sets for accurate calculations on molecular systems in gas and condensed phases". In: *The Journal of Chemical Physics* 127.11 (2007), p. 114105. DOI: 10.1063/1.2770708. eprint: https://doi.org/10.1063/1.2770708. URL: https://doi.org/10.1063/1.2770708.

[190] Ivan I. Vrubel et al. "Electronic Structure and Optical Response of Zn-Based Metal–Organic Frameworks". In: *Adv. Theory Simul.* 1.9 (2018), p. 1800049. DOI: 10.1002/adts.201800049. eprint: https://onlinelibrary.wiley.com/doi/pdf/10.1002/adts.201800049. URL: https://onlinelibrary.wiley.com/doi/abs/10.1002/adts.201800049.

[191] Michael G. Walter et al. "Solar Water Splitting Cells". In: *Chemical Reviews* 110.11 (2010). PMID: 21062097, pp. 6446–6473. DOI: 10.1021/cr1002326. eprint: https://doi.org/10.1021/cr1002326. URL: https://doi.org/10.1021/cr1002326.

[192] Dewen Wang et al. "Single-atom ruthenium based catalyst for enhanced hydrogen evolution". In: *Applied Catalysis B: Environmental* 249 (2019), pp. 91–97. ISSN: 0926-3373. DOI: https://doi.org/10.1016/j.apcatb.2019.02.059. URL: http://www.sciencedirect.com/science/article/pii/S0926337319301833.

[193] Guanzhi Wang et al. "A Bismuth-Based Metal–Organic Framework as an Efficient Visible-Light-Driven Photocatalyst". In: *Chem. Eur. J.* 21.6 (2015), pp. 2364–2367.

[194] Meng Wang, Lin Guo, and Dapeng Cao. "Amino-Functionalized Luminescent Metal–Organic Framework Test Paper for Rapid and Selective Sensing of SO2 Gas and Its Derivatives by Luminescence Turn-On Effect". In: *Analytical Chemistry* 90.5 (2018). PMID: 29405067, pp. 3608–3614. DOI: 10.1021/acs.analchem.8b00146. eprint: https://doi.org/10.1021/acs.analchem.8b00146. URL: https://doi.org/10.1021/acs.analchem.8b00146.

[195] Qi Wang and Didier Astruc. "State of the Art and Prospects in Metal–Organic Framework (MOF)-Based and MOF-Derived Nanocatalysis". In: *Chemical Reviews* 120.2 (2020). PMID: 31246430, pp. 1438–1511. DOI: 10.1021/acs.chemrev.9b00223. eprint: https://doi.org/10.1021/acs.chemrev.9b00223. URL: https://doi.org/10.1021/acs.chemrev.9b00223.

[196] Qian Wang and Kazunari Domen. "Particulate Photocatalysts for Light-Driven Water Splitting: Mechanisms, Challenges, and Design Strategies". In: *Chemical Reviews* 120.2 (2020). PMID: 31393702, pp. 919–985. DOI: 10.1021/acs.chemrev.9b00201. eprint: https://doi.org/10.1021/acs.chemrev.9b00201. URL: https://doi.org/10.1021/acs.chemrev.9b00201.

[197] Sujing Wang et al. "A phase transformable ultrastable titanium-carboxylate framework for photoconduction". In: *Nature Communications* 9.1 (2018), p. 1660. ISSN: 2041-1723. DOI: 10.1038/s41467-018-04034-w. URL: https://doi.org/10.1038/s41467-018-04034-w.

[198] Sujing Wang et al. "A phase transformable ultrastable titanium-carboxylate framework for photoconduction". In: *Nature communications* 9.1 (2018), pp. 1–9.

[199] Sujing Wang et al. "Toward a rational design of titanium metal-organic frameworks". In: *Matter* 2.2 (2020), pp. 440–450.

[200] Timothy C Wang et al. "Scalable synthesis and post-modification of a mesoporous metal-organic framework called NU-1000". In: *Nat. Protoc.* 11.1 (2016), pp. 149–162.

[201] Wei Wang et al. "Recent progress in metal-organic frameworks for applications in electrocatalytic and photocatalytic water splitting". In: *Adv. Sci.* 4.4 (2017), p. 1600371.

[202] Wei-Ning Wang et al. "Size and structure matter: enhanced CO_2 photoreduction efficiency by size-resolved ultrafine Pt nanoparticles on TiO_2 single crystals". In: *J. Am. Chem. Soc.* 134.27 (2012), pp. 11276–11281.

[203] Yong-Sheng Wei et al. "Metal–Organic Framework-Based Catalysts with Single Metal Sites". In: *Chemical Reviews* 120.21 (2020). PMID: 32356657, pp. 12089–12174. DOI: 10.1021/acs.chemrev.9b00757. eprint: https://doi.org/10.1021/acs.chemrev.9b00757. URL: https://doi.org/10.1021/acs.chemrev.9b00757.

[204] Julia Wiktor et al. "Comprehensive modeling of the band gap and absorption spectrum of $BiVO_4$". In: *Phys. Rev. Mater.* 1 (2017), p. 022401. DOI: 10.1103/PhysRevMaterials.1.022401. URL: https://link.aps.org/doi/10.1103/PhysRevMaterials.1.022401.

[205] Liam Wilbraham, François-Xavier Coudert, and Ilaria Ciofini. "Modelling photophysical properties of metal–organic frameworks: a density functional theory based approach". In: *Phys. Chem. Chem. Phys.* 18 (2016), pp. 25176–25182. DOI: 10.1039/C6CP04056J. URL: http://dx.doi.org/10.1039/C6CP04056J.

[206] Christopher E Wilmer et al. "Large-scale screening of hypothetical metal–organic frameworks". In: *Nature chemistry* 4.2 (2012), p. 83.

[207] Randall Q. Wilmer Christopher E.and Snurr. "Large-Scale Generation and Screening of Hypothetical Metal-Organic Frameworks for Applications in Gas Storage and Separations". In: *Prediction and Calculation of Crystal Structures: Methods and Applications.* Cham: Springer International Publishing, 2014, pp. 257–289. ISBN: 978-3-319-05774-3. DOI: 10.1007/128_2013_490. URL: https://doi.org/10.1007/128_2013_490.

[208] Xin-Ping Wu, Indrani Choudhuri, and Donald G. Truhlar. "Computational Studies of Photocatalysis with Metal–Organic Frameworks". In: *Energy Environ. Mater.* 2.4 (2019), pp. 251–263. DOI: 10.1002/eem2.12051. eprint: https://onlinelibrary.wiley.com/doi/pdf/10.1002/eem2.12051. URL: https://onlinelibrary.wiley.com/doi/abs/10.1002/eem2.12051.

[209] Xin-Ping Wu, Laura Gagliardi, and Donald G. Truhlar. "Cerium Metal–Organic Framework for Photocatalysis". In: *Journal of the American Chemical Society* 140.25 (2018). PMID: 29807431, pp. 7904–7912. DOI: 10.1021/jacs.8b03613. eprint: https://doi.org/10.1021/jacs.8b03613. URL: https://doi.org/10.1021/jacs.8b03613.

[210] Juan-Ding Xiao and Hai-Long Jiang. "Metal–organic frameworks for photocatalysis and photothermal catalysis". In: *Acc. Chem. Res.* 52.2 (2018), pp. 356–366.

[211] Juan-Ding Xiao and Hai-Long Jiang. "Metal–Organic Frameworks for Photocatalysis and Photothermal Catalysis". In: *Acc. Chem. Res.* 52.2 (2019), pp. 356–366. DOI: 10.1021/acs.accounts.8b00521. eprint: https://doi.org/10.1021/acs.accounts.8b00521. URL: https://doi.org/10.1021/acs.accounts.8b00521.

[212] Lilia S. Xie, Grigorii Skorupskii, and Mircea Dincă. "Electrically Conductive Metal–Organic Frameworks". In: *Chem. Rev.* 120.16 (2020), pp. 8536–8580. DOI: 10.1021/acs.chemrev.9b00766. eprint: https://doi.org/10.1021/acs.chemrev.9b00766. URL: https://doi.org/10.1021/acs.chemrev.9b00766.

[213] Hui Xu et al. "Recent progress in metal–organic complexes for optoelectronic applications". In: *Chem. Soc. Rev.* 43 (10 2014), pp. 3259–3302. DOI: 10.1039/C3CS60449G. URL: http://dx.doi.org/10.1039/C3CS60449G.

[214] Takeshi Yanai, David P Tew, and Nicholas C Handy. "A new hybrid exchange–correlation functional using the Coulomb-attenuating method (CAM-B3LYP)". In: *Chem. Phys. Lett.* 393.1 (2004), pp. 51–57. ISSN: 0009-2614. DOI: https://doi.org/10.1016/j.cplett.2004.06.011. URL: http://www.sciencedirect.com/science/article/pii/S0009261404008620.

[215] Jie Yang and Ying-Wei Yang. "Metal–Organic Frameworks for Biomedical Applications". In: *Small* 16.10 (2020), p. 1906846. DOI: https://doi.org/10.1002/smll.201906846. eprint: https://onlinelibrary.wiley.com/doi/pdf/10.1002/smll.201906846. URL: https://onlinelibrary.wiley.com/doi/abs/10.1002/smll.201906846.

[216] Xiao-Dong Yang et al. "Phototriggered Mechanical Movement in A Bipyridinium-based Coordination Polymer Powered by Electron Transfer". In: *Inorganic Chemistry* 57.5 (2018). PMID: 29424529, pp. 2724–2729. DOI: 10.1021/acs.inorgchem.7b03108. eprint: https://doi.org/10.1021/acs.inorgchem.7b03108. URL: https://doi.org/10.1021/acs.inorgchem.7b03108.

[217] Xiaogang Yang and Dunwei Wang. "Photocatalysis: From Fundamental Principles to Materials and Applications". In: *ACS Applied Energy Materials* 1.12 (2018), pp. 6657–6693. DOI: 10.1021/acsaem.8b01345. eprint: https://doi.org/10.1021/acsaem.8b01345. URL: https://doi.org/10.1021/acsaem.8b01345.

[218] Angel Zhang, Lydia Kwan, and Martin J. Stillman. "The spectroscopic impact of interactions with the four Gouterman orbitals from peripheral decoration of porphyrins with simple electron withdrawing and donating groups". In: *Org. Biomol. Chem.* 15 (2017), pp. 9081–9094. DOI: 10.1039/C7OB01960B. URL: http://dx.doi.org/10.1039/C7OB01960B.

[219] Jijie Zhang et al. "Metal–Organic-Framework-Based Photocatalysts Optimized by Spatially Separated Cocatalysts for Overall Water Splitting". In: *Adv. Mater.* 32.49 (2020), p. 2004747.

[220] Hongmei Zhao et al. "Construction of Pillared-Layer MOF as Efficient Visible-Light Photocatalysts for Aqueous Cr(VI) Reduction and Dye Degradation". In: *ACS Sustainable Chemistry & Engineering* 5.5 (2017), pp. 4449–4456. DOI: 10.1021/acssuschemeng.7b00641. eprint: https://doi.org/10.1021/acssuschemeng.7b00641. URL: https://doi.org/10.1021/acssuschemeng.7b00641.

[221] Shu-Na Zhao et al. "Metal Organic Frameworks Based Materials for Heterogeneous Photocatalysis". In: *Molecules* 23.11 (2018). ISSN: 1420-3049. DOI: 10.3390/molecules23112947. URL: https://www.mdpi.com/1420-3049/23/11/2947.

[222] Hong-Cai Zhou, Jeffrey R. Long, and Omar Yaghi M. "Introduction to Metal–Organic Frameworks". In: *Chemical Reviews* 112.2 (2012). PMID: 22280456, pp. 673–674. DOI: 10.1021/cr300014x. eprint: https://doi.org/10.1021/cr300014x. URL: https://doi.org/10.1021/cr300014x.

[223] Bingjun Zhu, Ruqiang Zou, and Qiang Xu. "Metal–organic framework based catalysts for hydrogen evolution". In: *Adv. Energy Mater.* 8.24 (2018), p. 1801193.

[224] Bingjun Zhu, Ruqiang Zou, and Qiang Xu. "Metal–Organic Framework Based Catalysts for Hydrogen Evolution". In: *Advanced Energy Materials* 8.24 (2018), p. 1801193. DOI: 10.1002/aenm.201801193. eprint: https://onlinelibrary.wiley.com/doi/pdf/10.1002/aenm.201801193. URL: https://onlinelibrary.wiley.com/doi/abs/10.1002/aenm.201801193.

[225] Li Zhu et al. "Metal–Organic Frameworks for Heterogeneous Basic Catalysis". In: *Chemical Reviews* 117.12 (2017). PMID: 28541694, pp. 8129–8176. DOI: 10.1021/acs.chemrev.7b00091. eprint: https://doi.org/10.1021/acs.chemrev.7b00091. URL: https://doi.org/10.1021/acs.chemrev.7b00091.

[226] Jian-Ping Zou et al. "Two Novel Metal-Organic Frameworks (MOFs) with (3,6)-Connected Net Topologies: Syntheses, Crystal Structures, Third-Order Nonlinear Optical and Luminescent Properties". In: *Crystal Growth & Design* 10.6 (2010), pp. 2613–2619. DOI: 10.1021/cg100104t. eprint: https://doi.org/10.1021/cg100104t. URL: https://doi.org/10.1021/cg100104t.